

## University of Southampton Research Repository ePrints Soton

Copyright © and Moral Rights for this thesis are retained by the author and/or other copyright owners. A copy can be downloaded for personal non-commercial research or study, without prior permission or charge. This thesis cannot be reproduced or quoted extensively from without first obtaining permission in writing from the copyright holder/s. The content must not be changed in any way or sold commercially in any format or medium without the formal permission of the copyright holders.

When referring to this work, full bibliographic details including the author, title, awarding institution and date of the thesis must be given e.g.

AUTHOR (year of submission) "Full thesis title", University of Southampton, name of the University School or Department, PhD Thesis, pagination

University of Southampton

**TEMPORAL CHANGES IN THE RED SEA CIRCULATION AND  
ASSOCIATED WATER MASSES**

By

Turki Metabe Alraddadi

A thesis submitted for the degree of Doctor of Philosophy

Faculty of Engineering, Science and Mathematics  
School of Ocean and Earth Sciences  
University of Southampton,  
United Kingdom

January 2013

ABSTRACT

FACULTY OF ENGINEERING, SCIENCE AND MATHEMATICS  
SCHOOL OF OCEAN AND EARTH SCIENCES

Doctor of Philosophy

THE CHANGES IN THE RED SEA CIRCULATION AND ASSOCIATED WATER  
MASSES

By Turki Metabe Alraddadi

Long-term variability of the Red Sea deep water (RSDW) properties was investigated using hydrographic data stretching back to the beginning of the 19<sup>th</sup> century. The analysis of the potential temperature and salinity indicate that there is a signal of cooling and freshening trends between 1950 to 2011 in the RSDW by an average of  $35.5 \times 10^{-4} \pm 5.6 \times 10^{-4} \text{ } ^\circ\text{C yr}^{-1}$  and  $13.8 \times 10^{-4} \pm 2.8 \times 10^{-4} \text{ psu yr}^{-1}$  respectively. Both trends of cooling and freshening are statistically significant with a confidence level of more than 95%. These cooling and freshening trends are consistent with the net heat loss trend in the three source regions for the deep water formation of the Red Sea by an average of  $-1.12 \pm 0.49 \text{ Wm}^{-2}$ ,  $-1.75 \pm 0.49 \text{ Wm}^{-2}$  and  $-1.58 \pm 0.47 \text{ Wm}^{-2}$  for the northern part of the Red Sea and the Gulfs of Suez and Aqaba respectively. The results suggest that the potential temperature and salinity seem to have decreased between 1950 and 2011 by as much as  $0.12 \text{ } ^\circ\text{C}$  and  $0.13 \text{ psu}$  respectively. These changes observed in the potential temperature and salinity in the RSDW are consistent throughout the Red Sea basin (subdivided into  $2^\circ$  grids) for the last three decades (1977-2011).

An inverse box model of the Red Sea is constructed using two hydrographic sections in the southern basin during August 2001 from research vessel (R/V) Maurice Ewing to provide quantification of the summer field fluxes (volume, heat and salt). The results show that the volume transport of the Red Sea outflow water (RSOW) to the Indian Ocean through the Strait of Bab el Mandeb is  $0.11 \pm 0.06 \text{ Sv}$  ( $1 \text{ Sv} = 10^6 \text{ m}^3 \text{ s}^{-1}$ ). There is a heat loss by advection with a magnitude of  $23.5 \pm 5.7 \text{ W m}^{-2}$  during a summer month (August) that fits well with the previous estimate by Patzert (1974b) with magnitude of  $21.81 \text{ W m}^{-2}$  and with magnitude of  $-22 \text{ Wm}^{-2}$  based on data from

Sofianos et al. (2002). There is a salt loss by advection with a magnitude of  $0.98 \times 10^9$   $\text{kg s}^{-1}$  this estimate is supported by the analysis of Tragou et al. (1999) which gives a magnitude of  $0.8 \times 10^9$   $\text{kg s}^{-1}$ .

# Contents

|                  |   |           |
|------------------|---|-----------|
| <b>Chapter 1</b> | <b>Literature review .....</b>  | <b>1</b>  |
| 1.1              | Introduction.....   | 1         |
| 1.2              | Geography.....  | 2         |
| 1.3              | Meteorological conditions .....   | 3         |
| 1.4              | Hydrographic properties .....   | 7         |
| 1.5              | Circulation.....  | 12        |
| 1.5.1            | Wind driven circulation .....   | 12        |
| 1.5.2            | Deep circulation and formation .....  | 13        |
| 1.6              | Exchanges between the Red Sea and Gulf of Aden at the Strait of Bab el Mandeb | 15        |
| 1.7              | Aim of this thesis .....  | 17        |
| <b>Chapter 2</b> | <b>Dataset.....</b>   | <b>18</b> |
| 2.1              | Introduction.....   | 18        |
| 2.2              | Hydrographic data.....  | 20        |
| 2.2.1            | Data source.....  | 20        |
| 2.3              | Quality control .....   | 26        |
| 2.3.1            | Preliminary QC .....  | 27        |
| 2.3.2            | Assessing data quality (accuracy).....  | 28        |
| 2.4              | Comparison to World Ocean Atlas 2009 Database .....                           | 34        |
| 2.5              | Surface heat flux data.....   | 38        |
| 2.5.1            | National Oceanography Centre, Southampton flux dataset.....                   | 40        |
| 2.5.2            | Accuracy of the surface heat flux data.....                                   | 43        |
| 2.6              | Conclusion .....  | 45        |
| <b>Chapter 3</b> | <b>Decadal changes in the Red Sea Deep Water properties.....</b>              | <b>46</b> |
| 3.1              | Introduction.....   | 46        |
| 3.2              | Data and method .....   | 47        |
| 3.3              | Results.....  | 49        |
| 3.3.1            | Long-term trends in the variability of the RSDW .....                         | 49        |
| 3.3.2            | Influence of the spatial variability .....                                    | 53        |
| 3.4              | Air-Sea interaction in the Red Sea.....                                       | 63        |
| 3.5              | Discussion and conclusion.....  | 68        |

|                  |  |            |
|------------------|--|------------|
| <b>Chapter 4</b> | <b>Heat and salt storage in the Red Sea</b> .....                                    | <b>74</b>  |
| 4.1              | Introduction.....  | 74         |
| 4.2              | Data and method .....  | 75         |
| 4.3              | Heat and salt storage of the Red Sea Water.....                                      | 75         |
| 4.4              | Results.....   | 77         |
| 4.4.1            | Heat and salt storage variability in the upper layers .....                          | 77         |
| 4.4.2            | Heat and salt storage variability in the deep layers.....                            | 79         |
| 4.5              | Discussion and conclusion.....   | 83         |
| <b>Chapter 5</b> | <b>Box inverse model</b> .....   | <b>88</b>  |
| 5.1              | Introduction.....  | 88         |
| 5.2              | The theory of the box inverse model .....  | 89         |
| 5.2.1            | Basic inverse model .....  | 89         |
| 5.2.2            | Weighting and uncertainties .....  | 92         |
| 5.2.3            | Diapycnal mixing.....  | 94         |
| 5.2.4            | Ekman volume transport.....  | 95         |
| 5.2.5            | Final inversion form.....  | 95         |
| 5.3              | Conclusion .....   | 96         |
| <b>Chapter 6</b> | <b>Hydrographic characteristics of the southern Red Sea</b> .....                    | <b>97</b>  |
| 6.1              | Introduction.....  | 97         |
| 6.2              | Section description.....   | 97         |
| 6.2.1            | Bathymetry of the southern Red Sea region .....                                      | 98         |
| 6.2.2            | Hydrographic properties .....  | 99         |
| 6.2.3            | Water masses .....   | 105        |
| 6.3              | Thermohaline properties of the southern Red Sea region.....                          | 106        |
| 6.3.1            | Surface layers (RSSW, surface-24.4 $\sigma_\theta$ ).....                            | 107        |
| 6.3.2            | Intermediate layers (GAIW, 24.4- 27 $\sigma_\theta$ ) .....                          | 111        |
| 6.3.3            | Deep layers (RSOW, 27-28.33 $\sigma_\theta$ and RSDW, $\sigma_\theta > 28.33$ )..... | 111        |
| 6.4              | Conclusion .....   | 112        |
| <b>Chapter 7</b> | <b>Setup of the standard inverse box model</b> .....                                 | <b>114</b> |
| 7.1              | Introduction.....  | 114        |
| 7.2              | Setup of the standard inverse box model .....  | 114        |
| 7.3              | Conservation constraints.....  | 116        |
| 7.4              | Initial geostrophic velocity field .....   | 117        |
| 7.4.1            | A priori reference level and reference velocity.....                                 | 117        |

|                   |   |            |
|-------------------|---|------------|
| 7.4.2             | Bottom triangle .....                                   | 118        |
| 7.4.3             | Initial geostrophic velocity and transport field .....  | 120        |
| 7.4.4             | Choice of a priori uncertainties .....                  | 124        |
| 7.5               | Other unknowns parameters .....                         | 126        |
| 7.5.1             | Diapycnal mixing .....                                  | 126        |
| 7.5.2             | Ekman transport .....                                   | 127        |
| 7.6               | Conclusion .....  | 129        |
| <b>Chapter 8</b>  | <b>The standard model and solution .....</b>            | <b>130</b> |
| 8.1               | Introduction .....                                      | 130        |
| 8.2               | Standard inverse box model .....                        | 131        |
| 8.2.1             | Choice of the solution degree .....                     | 131        |
| 8.2.2             | Description of the model solution .....                 | 133        |
| 8.3               | Inverse box model sensitivity .....                     | 138        |
| 8.3.1             | Choice of the rank .....                                | 138        |
| 8.3.2             | Sensitivity to the number of constraints .....          | 139        |
| 8.3.3             | Sensitivity to a priori errors on the constraints ..... | 142        |
| 8.3.4             | Sensitivity to the number of layers .....               | 143        |
| 8.3.5             | Sensitivity to inclusion of diapycnal velocities .....  | 147        |
| 8.3.6             | Sensitivity to choice of the initial velocities .....   | 147        |
| 8.3.7             | Sensitivity to the bottom triangle .....                | 151        |
| 8.4               | Conclusion .....  | 153        |
| <b>Chapter 9</b>  | <b>Circulation in the southern Red Sea region .....</b> | <b>154</b> |
| 9.1               | Introduction .....                                      | 154        |
| 9.2               | Geostrophic velocity field .....                        | 154        |
| 9.3               | Summer circulation of the southern Red Sea .....        | 160        |
| 9.3.1             | Full-depth volume transports .....                      | 160        |
| 9.3.2             | Upper waters .....                                      | 161        |
| 9.3.3             | Intermediate waters .....                               | 162        |
| 9.3.4             | Deep waters .....                                       | 164        |
| 9.4               | Interior diapycnal mixing .....                         | 171        |
| 9.5               | Heat and salt fluxes .....                              | 175        |
| 9.6               | Conclusion .....  | 178        |
| <b>Chapter 10</b> | <b>Summary and Conclusion .....</b>                     | <b>179</b> |
| 10.1              | Overview .....  | 179        |

|                   |   |     |
|-------------------|---|-----|
| 10.2              | Decadal changes in the Red Sea deep water properties..... | 180 |
| 10.3              | Circulation in the southern Red Sea region .....          | 182 |
| 10.4              | Conclusion .....  | 184 |
| <b>References</b> | <b>185</b>  |     |
| <b>Appendix A</b> | <b>196</b>  |     |

# List of Figures

|   |    |
|---|----|
| Figure 1-1: Bathymetry map of the Red Sea basin (Smith & Sandwell, 1997).....   | 4  |
| Figure 1-2: Climatological monthly mean wind stress (14 year averages from 1980 to 1993 from NOCS.1 (max arrow = $0.068 \text{ Nm}^{-2}$ )) .....   | 6  |
| Figure 1-3: Monthly mean climatology of the Red Sea for the months January, April, July and October from Levitus94 (World Ocean Atlas, 1994). Sea surface temperature in $^{\circ}\text{C}$ (upper panel), sea surface salinity (middle panel) and $\sigma_{\theta}$ (lower panel).....                   | 9  |
| Figure 1-4: Hydrographic section along the main axis of the Red Sea for a) potential temperature in $^{\circ}\text{C}$ , b) salinity and c) $\sigma_{\theta}$ from the cruise of Commandant Robert Giraud during January-February 1963 .....  | 10 |
| Figure 1-5: Hydrographic section along the main axis of the Red Sea for a) potential temperature in $^{\circ}\text{C}$ , b) salinity and c) $\sigma_{\theta}$ from the cruise of R/V Maurice Ewing in August 2001 .....   | 11 |
| Figure 1-6: Schematic of the circulation patterns in the upper layers (single arrows), upper deep layers (double arrows, driven by open ocean convection) and deep layers (bold arrows, driven by plume convection) in the Red Sea (Quadfasel, 2001). Dotted topography represents the Gulf of Aqaba..... | 14 |
| Figure 1-7: Sketch of two circulation patterns in the Strait of Bab el Mandeb during the winter and summer seasons. SW represents the surface water, GAIW represents Gulf of Aden intermediate water and RSOW represents Red Sea outflow water (Smeed, 2000).....   | 17 |
| Figure 2-1: Distribution of the hydrographic data for the Red Sea (the codes are explained in Table 2-3) .....  | 24 |
| Figure 2-2: Distribution of the hydrographic data for the Red Sea (the codes are explained in Table 2-3) .....  | 25 |
| Figure 2-3: Position errors in the hydrographic data from GBOT and NIOSD .....  | 27 |
| Figure 2-4: $\theta$ -S diagram for CTD data from the R/V <i>Maurice Ewing</i> cruise on August 2001. Main water masses, Red Sea Surface Water (RSSW), Gulf of Aden Intermediate Water (GAIW), Red Sea Outflow Water (RSOW) and Red Sea Deep Water (RDSW).....  | 29 |

|  |    |
|--|----|
| Figure 2-5: $\theta$ -S diagram for all CTD data. The blue dot represents the mean value of each profile below depth 300 m; a solid red line indicates $\pm 3$ standard deviations from the mean (red dot) of all profiles. The box indicates the statistical mean and standard deviation for potential temperature (PT), salinity (S) and $\sigma_\theta$ (PD) .....  | 30 |
| Figure 2-6: Examples of suspicious bottle data from the R/V A.I. Voeykov cruise on September 1959 (upper panel) and the R/V A.A. Nesmeyanov cruise on July 1982 (lower panel) to be removed from our data. The whole profile data (right panel) and data below 300 m depth (left panel).....   | 31 |
| Figure 2-7: $\theta$ -S diagrams for NIOSD data for the whole profiles (left panel) and deep layer (right panel) after the statistical range check step. The box represents the reference mean with 3 standard deviations from CTD data .....  | 32 |
| Figure 2-8: As in Figure 2-7 but for MBOT .....  | 33 |
| Figure 2-9: As in Figure 2-7 but for ABOT.....   | 33 |
| Figure 2-10: Mean salinity and potential temperature below 300 m from Argo float 69008.....  | 34 |
| Figure 2-11: $\theta$ -S diagram for the climatology annual mean of WOD09 for upper layers in the left panel and deep layers in the right panel for three regions of the Red Sea (northern (red), central (green) and southern (cyan)). The circle represents the mean with its three standard deviations from the annual mean of WOD09. The data grid resolution is $0.25^\circ \times 0.25^\circ$ .....  | 35 |
| Figure 2-12: $\theta$ -S diagram for the climatology annual mean and the means of the winter, summer, spring and autumn seasons of WOD09 for upper layers in the left panel and deep layers in the right panel for three regions of the Red Sea (northern (red), central (green) and southern (cyan)). The circle represents the mean with its three standard deviations from the annual mean of WOD09. The data grid resolution is $0.25^\circ \times 0.25^\circ$ ..... | 36 |
| Figure 2-13: Annual NOCS v2.0 climatological mean fields of the different surface heat flux components (shortwave (SW), longwave (LW), latent heat flux (LHF), sensible heat flux (SHF) and net heat flux (NHF)) over the period 1973 to 2006. Positive values indicate heat gained by the sea .....   | 41 |
| Figure 2-14: Monthly mean of NHF anomalies from NOCS v2.0 over the Red Sea region (for the box $14-28^\circ\text{N}$ , $32-43.5^\circ\text{E}$ ) from 1973 to 2006.....  | 42 |
| Figure 2-15: Monthly mean of evaporation anomalies from NOCS v2.0 over the Red Sea region (for the box $14-28^\circ\text{N}$ , $32-43.5^\circ\text{E}$ ) from 1973 to 2006.....  | 42 |

|   |    |
|---|----|
| Figure 2-16: Comparison of surface heat flux from the surface mooring Marine Light-Mixed Layer experiment in the sub-Arctic North Atlantic in the summer of 1991. NOCS v2.0 (dark blue), NOCS v2.0 with height adjustment but without bias adjustment (blue), NCEP1 (cyan), NCEP2 (yellow), ERA40 (orange) and OAFlux (brown) (Berry & Kent, 2009) .....                            | 43 |
| Figure 3-1: Typical profiles along the Red Sea axis for the potential temperature ( $^{\circ}$ C) and salinity and their locations based on data from R/V Maurice Ewing during August 2001 (Sofianos & Johns, 2007) .....   | 48 |
| Figure 3-2: a, b and c: Properties of RSDW at a depth of 300 m to a maximum depth of each profile for the area between latitude 14 and 27.9 $^{\circ}$ N. Each point represents an average per profile per cruise per year with its standard deviation .....  | 51 |
| Figure 3-3: a, b and c: Properties of RSDW at a depth of 300 m to a maximum depth of each profile for the area between latitude 14 and 27.885 $^{\circ}$ N. Each point represents an average per profile per cruise per year with its standard deviation.....   | 52 |
| Figure 3-4: Location of the hydrographic sections along the Red Sea axis.....   | 53 |
| Figure 3-5: Differences of the thermohaline properties along the Red Sea basin: a, potential temperature differences in 1963-1962; b, salinity differences in 1963-1962; c, potential temperature differences in 1983-1982; d, salinity differences in 1983-1982 .....  | 57 |
| Figure 3-6: As in Figure 3-5 but for a, potential temperature differences in 1982-1963; b, salinity differences in 1982-1963; c, potential temperature differences in 2001-1983; d, salinity differences in 2001-1983 .....   | 58 |
| Figure 3-7: As in Figures 3-5 but for a, potential temperature differences in 2001-1962; b, salinity differences in 2001-1962.....  | 59 |
| Figure 3-8: Vertical meridional averaged thermohaline properties differences plotted plus/minus one standard deviation for a, potential temperature differences in 1963-1962; b, salinity differences in 1963-1962; c, potential temperature differences in 1983-1982; d, salinity differences in 1983-1982 along the Red Sea basin. Note that the x-axis scales are different..... | 61 |
| Figure 3-9: Vertical meridional averaged thermohaline properties differences plotted plus/minus one standard deviation for a, potential temperature differences in 1982-1963; b, salinity differences in 1982-1963; c, potential temperature differences in 2001-1983; d, salinity differences in 2001-1983 along the Red Sea basin. Note that the x-axis scales are different..... | 62 |

|   |    |
|---|----|
| Figure 3-10: Vertical meridional averaged thermohaline properties differences plotted plus/minus one standard deviation for a, potential temperature differences in 2001-1962; b, salinity differences in 2001-1962 along the Red Sea basin. Note that the x-axis scales are different.....   | 63 |
| Figure 3-11: Monthly net heat flux anomalies over a, the Red Sea (RS); b, the northern Red Sea (NRS); c, the Gulf of Suez (GS) and d, the Gulf of Aqaba (GA) derived from the NOCS v2.0 dataset with a six month running mean represented by solid black with a regression line and a three month running mean by a solid green line (+ gained, - loss) .....   | 65 |
| Figure 3-12: Monthly sea surface temperature anomalies over a, the Red Sea (RS); b, the northern Red Sea (NRS); c, the Gulf of Suez (GS); and d, the Gulf of Aqaba (GA) derived from the NOCS v2.0 dataset with a six month running mean represented by solid blue with a regression line and a three month running mean represented by a solid cyan line ..... | 66 |
| Figure 3-13: Monthly evaporation anomalies over a, the Red Sea (RS); b, the northern Red Sea (NRS); c, the Gulf of Suez (GS) and d, the Gulf of Aqaba (GA) derived from the NOCS v2.0 dataset with a six month running mean represented by solid black with a regression line and a three month running mean represented by a solid green line.....             | 67 |
| Figure 3-14: Schematic of the processes important for the deep water formation in the northern of the Red Sea according to (Woelk & Quadfasel, 1996).....   | 70 |
| Figure 3-15: a, b and c: Properties of the RSDW for different sub-regions in the Red Sea from CTD data .....  | 73 |
| Figure 4-1: Distribution of the stations used for a) upper layers (0-300m) (left) and b) deep layers (300-1000m) (right) in the Red Sea.....  | 77 |
| Figure 4-2: Mean heat storage ( $Jm^{-2}$ ) in the upper layers in each 100 m layer from the surface to 300 m depth in the Red Sea. Vertical bars represent one standard deviation and the dashed lines represent a linear regression. Note that the y-axis scales are different .....  | 80 |
| Figure 4-3: Mean salt storage ( $kg/m^2$ ) in the upper layers in each 100 m layer from the surface to 300 m depth in the Red Sea. Vertical bars represent one standard deviation and the dashed lines represent a linear regression. Note that the y-axis scales are different .....   | 81 |

Figure 4-4: Linear regression for the properties of RSDW from 300 m to 1000 m depth for (a) heat storage ( $J/m^2$ ) and (b) salt storage ( $kg/m^2$ ). Vertical bars represent one standard deviation and the dashed lines represent a linear regression..... 82

Figure 5-1: Inverse model structure reproduced from Ganachaud and Wunsch (2003). The volume of the ocean is closed by two hydrographic sections (S1 and S2) and land boundaries ..... 89

Figure 6-1: Bathymetry of the southern Red Sea (Smith & Sandwell, 1997). The two transects used to construct the box (in blue and red) and the other sections used to study the thermohaline properties of the southern of the Red Sea (section D in cyan and E in green). SBM: Strait of Bab el Mandeb and GA: Gulf of Aden ..... 98

Figure 6-2: Vertical distribution of potential temperature along the rim of the box in the southern Red Sea. Upper panel: upper 300 m. Lower panel: whole profile from the surface to the bottom. The station numbers are shown in white along the lower axis and the white lines represent the boundaries of the water mass. Longitudes are shown over the two zonal transects ..... 101

Figure 6-3: Vertical distribution of salinity along the rim of the box in the southern Red Sea. Upper panel: upper 300 m. Lower panel: whole profile from the surface to the bottom. The station numbers are shown in white along the lower axis and the white lines represent the boundaries of the water mass. Longitudes are shown over the two zonal transects ..... 102

Figure 6-4: Vertical distribution of potential density along the rim of the box in the southern Red Sea. Upper panel: upper 300 m. Lower panel: whole profile from the surface to the bottom. The station numbers are shown in white along the lower axis and the white lines represent the boundaries of the water mass. Longitudes are shown over the two zonal transects ..... 103

Figure 6-5: Vertical distribution of dissolved oxygen concentration along the rim of the box in the southern Red Sea. Upper panel: upper 300 m. Lower panel: whole profile from the surface to the bottom. The station numbers are shown in white along the lower axis and the white lines represent the boundaries of the water mass. Longitudes are shown over the two zonal transects..... 104

Figure 6-6:  $\theta$ -S diagrams of sections C (blue lines) and F (red lines) in the southern region of the Red Sea.  $\sigma_\theta$  boundaries of the main water masses (dotted lines). The main water masses are labelled..... 105

Figure 6-7:  $\theta$ -S diagrams of all the profiles over the box (C, D, E and F) in the southern Red Sea (left panel) and their corresponding stations are shown (right panel).  $\sigma_\theta$

|  |     |
|--|-----|
| boundaries of the main water masses (dotted lines). SBM: Strait of Bab el Mandeb and GA: Gulf of Aden.....   | 108 |
| Figure 6-8: $\theta$ -S diagrams of main water masses found in section C (left panel) and their corresponding stations are shown (right panel) .....   | 108 |
| Figure 6-9: $\theta$ -S diagrams of main water masses found in section D (left panel) and their corresponding stations are shown (right panel) .....   | 109 |
| Figure 6-10: $\theta$ -S diagrams of main water masses found in section E (left panel) and their corresponding stations are shown (right panel).....   | 109 |
| Figure 6-11: $\theta$ -S diagrams of main water masses found in section F (left panel) and their corresponding stations are shown (right panel).....   | 110 |
| Figure 6-12: $\theta$ -S diagrams of main water masses found along the eastern side of the basin (left panel) and their corresponding stations are shown (right panel) .....   | 110 |
| Figure 6-13: Circulation scheme for the southern Red Sea based on results from the geostrophic circulation. The major water masses (see Table 6-1). RSSW for Red Sea Water mass, GAIW for Gulf of Aden Water mass, RSOW for Red Sea Outflow Water mass and RSDW for Red Sea Water mass. SBM represents the Strait of Bab el Mandeb region and GA the Gulf of Aden region. The dots indicate the hydrographic data from R/V Maurice Ewing (2001) for section C (blue), section D (green), section E (cyan) and section F (red)..... | 113 |
| Figure 7-1: Two transects used to build the box (blue circles (section C) and red circles (section F)) and the axis station used to calculate the property mean in the layer of each interface (cyan circles). SBM: Strait of Bab el Mandeb, GA: Gulf of Aden .....  | 115 |
| Figure 7-2: Comparison of the velocity profiles from the two methods showing that they differ only below DCL. The two computation methods are constant velocity (blue) and shear scaled by the vertical density gradient (green).....  | 120 |
| Figure 7-3: <i>A priori</i> geostrophic velocity along the rim of the box with water mass boundaries (the black dashed lines). Positive velocities are directed into the box. Stations are shown in red along the x-axis. Longitudes are also shown.....   | 122 |
| Figure 7-4: <i>A priori</i> cumulative volume transport along the rim of the box with <i>a priori</i> cumulative uncertainties (shaded area). Longitudes are also shown .....  | 123 |
| Figure 7-5: Initial residual of the volume, potential temperature ( $\theta$ ) anomaly and salinity anomaly in individual model layers. The full-depth residual and units are indicated beneath each graph .....   | 124 |

|  |     |
|--|-----|
| Figure 7-6: <i>A priori</i> volume, potential temperature and salinity anomaly uncertainties .....   | 125 |
| Figure 7-7: Climatology mean of the wind stress magnitude for August over the box in the southern region of the Red Sea. Wind stress ( $\text{Nm}^{-2}$ ) is shown by colour and wind direction by vectors.....  | 128 |
| Figure 8-1: Full-depth volume residual as a function of the rank solution (red) and the full-depth volume residual for the initial solution (blue).....  | 132 |
| Figure 8-2: Standard solution residual of volume, potential temperature ( $\theta$ ) anomaly, and salinity (S) anomaly in individual layers (red). One <i>a posteriori</i> standard deviation uncertainty (blue) .....   | 132 |
| Figure 8-3: Comparison between the <i>a priori</i> standard deviation (red) and the <i>a posteriori</i> standard deviation (blue) for the volume, potential temperature anomaly and salinity anomaly .....   | 133 |
| Figure 8-4: Upper panel: Gain of information ( $\sigma_s - \sigma_0 / \sigma_0$ ) with $\sigma_s$ the <i>a posteriori</i> standard deviation and $\sigma_0$ the <i>a priori</i> standard deviation. Lower panel: Reference velocity after the inversion for each station pair. One <i>a priori</i> standard deviation is shown in the shaded area .....  | 135 |
| Figure 8-5: Upper panel: differences between the <i>a priori</i> and the <i>a posteriori</i> full-depth cumulative volume transport (Sv) along the rim of the box. Middle panel: comparison between the <i>a priori</i> (red) and the <i>a posteriori</i> (blue) full-depth cumulative volume transport (Sv) along the rim of the box. The shaded area gives accumulated <i>a posteriori</i> uncertainty in the full-depth transport. Lower panel: geostrophic velocities ( $\text{m s}^{-1}$ ) diagnosed by the inverse box model. The sign convection (+) is directed into the box and (-) is directed out of the box..... | 136 |
| Figure 8-6: <i>A posteriori</i> solution (blue) and <i>a priori</i> solution (red) cumulative volume transport (Sv) for each water mass RSSW, GAIW, RSOW and RSDW in each section. The shaded area represents <i>a posteriori</i> cumulative uncertainties.....  | 137 |
| Figure 8-7: Cumulative volume transport (Sv) along the rim of the box for simulation with the different ranks 2, 4, 8, 10 and 14 (red circle, green dashed line, cyan circle, black dashed line and magenta dashed line) and for the selected solution (blue).....   | 140 |
| Figure 8-8: Cumulative transport (Sv) along the rim of the box for volume conservation only (green), for volume and salinity conservation (red) and for the selected solution (blue).....  | 141 |

|  |     |
|--|-----|
| Figure 8-9: Cumulative volume transport ( $S_v$ ) along the rim of the box when weighting is not included, for row weighting (RW, red line), column weighting (CW, green dashed line), row and column weighting (cyan line) for the selected solution (blue line) and for the initial solution (black dashed line) .....   | 144 |
| Figure 8-10: Cumulative transport ( $S_v$ ) along the rim of the box when the <i>a priori</i> uncertainties about the volume conservation are constant ( $0.2 S_v$ ) (red) and for the selected solution (blue). The <i>a posteriori</i> cumulative error is shown in the grey shaded area.....  | 145 |
| Figure 8-11: Cumulative volume transport ( $S_v$ ) along the rim of the box when the number of the layers is increased to 6 (red) and for the selected solution (blue). The <i>a posteriori</i> cumulative error is shown in the grey shaded area.....   | 146 |
| Figure 8-12: Cumulative volume transport ( $S_v$ ) along the rim of the box when the diapycnal velocities are not included (red) and for the selected solution (blue). The <i>a posteriori</i> cumulative error is shown in the grey shaded area .....   | 148 |
| Figure 8-13: Cumulative volume transport ( $S_v$ ) along the rim of the box when the <i>a priori</i> uncertainties for diapycnal velocity are increased ( $10^{-3}$ ) (red) and for the selected solution (blue). The <i>a posteriori</i> cumulative error is shown in the grey shaded area.....   | 149 |
| Figure 8-14: Cumulative volume transport ( $S_v$ ) along the rim of the box when the <i>a priori</i> uncertainties for reference velocity are constant at $0.04 \text{ ms}^{-1}$ (red) and for the selected solution (blue). The <i>a posteriori</i> cumulative error is shown in the grey shaded area.....  | 150 |
| Figure 8-15: Cumulative volume transport ( $S_v$ ) along the rim of the box when the bottom triangles are not included (red) and for the selected solution (blue). The <i>a posteriori</i> cumulative error is shown in the grey shaded area .....   | 152 |
| Figure 9-1: Geostrophic velocity (in $\text{m s}^{-1}$ ) of the inverse model solution, with water mass boundaries (dashed lines). For simplicity the two sections were taken from the west-east direction. Positive velocities (red) are directed into the box and negative velocities (blue) are going out of the box. The station numbers are shown in red at the bottom of each panel. The map indicates the location of the two sections in the southern Red Sea region ..... | 157 |
| Figure 9-2: Mean winter (left panel) and summer (right panel) surface circulation from MICOM simulation. The results represent the last 9 years of simulation (Sofianos & Johns, 2003).....  | 158 |

|   |     |
|---|-----|
| Figure 9-3: Cumulative full-depth volume transport (in Sv, positive into the box) for each section (black dashed lines). Accumulated volume transport for each layer is plotted for RSSW (green), GAIW (blue), RSOW (red) and RSDW (magnetic). The <i>a posteriori</i> cumulative error is shown in the grey shaded area.....   | 159 |
| Figure 9-4: Circulation scheme for the southern Red Sea based on results from the geostrophic circulation. The major water masses (see Table 6-1). RSSW represents Red Sea Water mass, SBM the Strait of Bab el Mandeb region and GA the Gulf of Aden region. The dots indicate the hydrographic data from R/V Maurice Ewing (2001) for section C (blue), section D (green), section E (cyan) and section F (red) .....   | 162 |
| Figure 9-5: As in Figure 9-4 but for Gulf of Aden intermediate water (GAIW).....  | 164 |
| Figure 9-6: As in Figure 9-4 but for Red Sea Outflow Water (RSOW).....  | 166 |
| Figure 9-7: As in Figure 9-4 but for Red Sea Deep Water (RSDW).....   | 167 |
| Figure 9-8: Volume transport (Sv) for each station pair at section C, calculated from the standard solution, for a) full-depth volume transports (layer 5), b) present volume transports for RSSW (layer 1, $\sigma_\theta < 24.4$ ), c) present volume transports for GAIW (layer 2, $24.4 < \sigma_\theta < 27$ ), d) present volume transports for RSOW (layer 3, $27 < \sigma_\theta < 28.33$ ) and e) present volume transports for RSDW (layer 4, $\sigma_\theta > 28.33$ ). Positive values indicate transport directed into the box and negative values indicate transport going out of the box.....  | 169 |
| Figure 9-9: Volume transport (Sv) for each station pair in section F, calculated from the standard solution, for a) full-depth volume transports (Layer 5), b) present volume transports for RSSW (layer 1, $\sigma_\theta < 24.4$ ), c) present volume transports for GAIW (layer 2, $24.4 < \sigma_\theta < 27$ ), d) present volume transports for RSOW (layer 3, $27 < \sigma_\theta < 28.33$ ) and e) presents volume transports for RSDW (layer 4, $\sigma_\theta > 28.33$ ). Positive values indicate transport directed into the box and negative values indicate transport going out of the box..... | 170 |
| Figure 9-10: Residual for volume transport for each layer of the model in sections C and F. Positive values indicate transport directed northward and negative values indicate transport directed southward .....   | 171 |
| Figure 9-11: Interior diapycnal velocity and associated diapycnal volume transport for the model domain in the solution. Positive velocity or transport is directed upward. Water masses are labelled and their boundaries indicated by horizontal dotted lines. The <i>a posteriori</i> uncertainty is shown by error bar.....   | 173 |

Figure 9-12: Interior diapycnal velocity and associated diapycnal potential temperature anomaly transport for the model domain in the solution. Positive velocity or transport is directed upward. Water masses are labelled and their boundaries indicated by horizontal dotted lines. The black dashed line indicates the conurbation from the effective diffusion where the contribution of the diapycnal volume has been removed. The a posteriori uncertainty is shown by error bar .. 174

Figure 9-13: Interior diapycnal velocity and associated diapycnal salinity anomaly transport for the model domain in the solution. Positive velocity or transport is directed upward. Water masses are labelled and their boundaries indicated by horizontal dotted lines. The black dashed line indicates the conurbation from the effective diffusion where the contribution of the diapycnal volume has been removed. The a posteriori uncertainty is shown by error bar ..... 174

Figure 9-14: Heat fluxes ( $10^{12}$  W) for individual layers in section C (left panel), in section F (middle panel) and over the whole box (right panel). Positive values indicate net heat towards the box..... 177

Figure 9-15: Salt fluxes ( $\text{kg s}^{-1}$ ) for individual layers in section C (left panel), in section F (middle panel) and over the whole box (right panel). Positive values indicate net salt towards the box ..... 177

Figure 10-1: Schematic of the general circulation for the RSDW according to Cember (1988)..... 183

# List of Tables

|  |    |
|--|----|
| Table 1-1: Summary of available evaporation rate estimates for the Red Sea (after Sofianos et al. (2002)).....   | 3  |
| Table 1-2: Summary of available residence time and rate of formation estimates for the Red Sea ( $1Sv= 10^6 m^3 s^{-1}$ ) .....  | 15 |
| Table 2-1: Available CTD data for the Red Sea from the NODC dataset (N1CTD) ...  | 22 |
| Table 2-2: Available bottle data for the Red Sea from the NODC dataset (N1OSD) ...   | 23 |
| Table 2-3: Available data for the Red Sea region from different sources with their codes .....   | 26 |
| Table 2-4: Statistical values of the thermohaline properties of the Red Sea deep water ( $\geq 300$ m) with their standard deviations for potential temperature (PT), salinity (S) and $\sigma_\theta$ from climatology data of WOA09 .....  | 35 |
| Table 2-5: Number of profiles discarded and accepted from the hydrographic data of the Red Sea from different sources .....  | 37 |
| Table 3-1: Potential temperature ( $\theta$ ), salinity (S) and potential density ( $\sigma_\theta$ ) in the RSDW below 300 m depth. The results represent averages per cruise per year; N indicates the number of the observations on which the averages were based .....   | 50 |
| Table 3-2: Results are presented for the potential temperature ( $\theta$ ) and salinity (S) for the RSDW (300-1000) and Net heat fluxes and evaporation anomalies over the Red Sea (RS) and the sources region: Northern of the Red Sea (NRS), Gulf of Suez (GS) and Gulf of Aqaba (GA); the linear trend and the standard error are also presented ..... | 69 |
| Table 3-3: Potential temperature ( $\theta$ ), salinity (S) and potential density ( $\sigma_\theta$ ) in the Red Sea deep water below 300 m depth; results represent averages per cruise per year .....  | 72 |
| Table 4-1: Results are presented for the heat ( $*10^6 J m^{-2}$ ) and salt ( $kg m^{-2}$ ) storage for upper (0-300m) and deep layers (300-1000); the linear trend and the standard error are also presented .....  | 78 |
| Table 4-2: Results are presented for the heat ( $*10^6 J m^{-2}$ ) and salt ( $kg m^{-2}$ ) storage for the RSDW (300-1000) and Net heat fluxes ( $Wm^{-2}$ ) and evaporation ( $myr^{-1}$ ) anomalies over the Red Sea (RS) and the sources region: Northern of the Red Sea   |    |

|  |     |
|--|-----|
| (NRS), Gulf of Suez (GS) and Gulf of Aqaba (GA); the linear trend and the standard error are also presented.....   | 87  |
| Table 6-1: $\sigma_\theta$ boundaries of the main water mass used in the entire thesis .....   | 106 |
| Table 7-1: Layers used in the model defined by the $\sigma_\theta$ surface (potential density minus 1000 kg m <sup>-3</sup> in reference to the surface).....  | 116 |
| Table 7-2: Constraints applied to the inverse box model (standard solution). Each constraint represents a conservation equation for the flux (volume, salinity or temperature) constrained to zero.....                                  | 117 |
| Table 7-3: Initial volume transports ( $S_v$ ) for each section (C and F) and for each layer (in each section and along the rim of the box). The sign convection (+) is into the box and (-) is out of the box.....                      | 121 |
| Table 7-4: <i>A priori</i> errors in the volume conservation equations for model layers and the layer mean and standard deviation of potential temperature ( $\theta$ ) and salinity anomalies .....                                     | 125 |
| Table 7-5: Uncertainties for reference velocities for each station pair .....  | 126 |
| Table 7-6: The initial solution for the model layer interfaces derived from CTD data and then included in the inversion. The area is the total area of each potential density ( $\sigma_\theta$ ) interface over the whole box.....      | 127 |
| Table 7-7: Ekman volume transport ( $S_v$ ) calculated from SCOW August average climatology. For the whole box, positive transport indicates a convergence over the box.....   | 128 |
| Table 8-1: Volume transports ( $S_v$ ) for each section (C and F) along the rim of the box and for each layer (the initial and final solutions of the inversion). The sign convection (+) is into the box and (-) is out of the box..... | 135 |
| Table 8-2: Volume transport estimates ( $S_v$ ) for the southern Red Sea for the selected solution and the alternative models, run with different ranks.....   | 139 |
| Table 8-3: Volume transport ( $S_v$ ) estimates for the initial solution, selected solution, alternative model runs (no row weight (RW), no column weight (CW) and no row-column weight (RW-CW) included in the selected solution).....  | 143 |
| Table 9-1: Volume transports ( $S_v$ ) for each section (C and F) and for each layer (after the inversion). The sign convection (+) is into the box and (-) is out of the box.   | 164 |

# Declaration of authorship

I, Turki Metabe Alraddadi declare that the thesis entitled

Temporal Changes in the Red Sea Circulation and associated water masses

and the work presented in the thesis are both my own, and have been generated by me as the result of my own original research. I confirm that:

- this work was done wholly or mainly while in candidature for a research degree at this University;
- where any part of this thesis has previously been submitted for a degree or any other qualification at this University or any other institution, this has been clearly stated;
- where I have consulted the published work of others, this is always clearly attributed;
- where I have quoted from the work of others, the source is always given. With the exception of such quotations, this thesis is entirely my own work;
- I have acknowledged all main sources of help;
- where the thesis is based on work done by myself jointly with others, I have made clear exactly what was done by others and what I have contributed myself;
- none of this work has been published before submission.

Signed: .....

Date:.....

# Acknowledgements

I would like to express my gratitude to my supervisor Dr. Neil C. Wells and Dr. Loïc Jullion for their wonderful supervision and for the patient guidance, encouragement and advice they have provided throughout my time as their student. I would like to express my deepest appreciation to my panel committee, Prof. Harry Bryden, Dr. David Smeed and Dr. Kate Stansfield, for their encouragement and insightful comments.

I would like to thank King Abdulaziz University for funding this work and the purchase of the Argo float. I would like to thank Dr Brian King for his supporting purchasing and deploying the Argo float in the Red Sea. I also thank Justin Buck of the British Oceanographic Data Centre for his support in deploying the float. I would like to thank Dr. Amy Bower and Dr. Abdulaziz Al Suwailem for giving me an opportunity to participate in the Red Sea cruise in March of 2010.

I would like to thank Prof. Detlef Quadfasel, Dr. Maren Walter, William Johns and Dr. Sarantis Sofianos for providing hydrographic data.

I take this opportunity to express my deep gratitude to my parents, brothers and lovely sister Manal. I wish to express my deepest appreciation to my lovely wife Rana for her patience and support, to my daughters Wala and Lana and to my little son Bander.

Finally, I would like to thank and express appreciation and gratitude to all the people who have contributed to the completion of this thesis. Many thanks to my friends Muhammed Qurban, Thamier Alrshiedi, Turki Alsaeed, Amer Deaf, Anna Kaczmarska, Aurelie Persechino, Khairul Nizam Mohamed, Aldo Aquino-Cruiz, Sudipta Sarkar and Ibrahim Muhammed and many others for their friendship during my PhD life.

# Definitions and abbreviations used

|          |   |
|----------|---|
| ADCP     | Acoustic Doppler Current Profiler                       |
| AODC     | Australian Oceanographic Data Centre                    |
| BODC     | Oceanographic Data Centre                               |
| COARE    | Coupled Ocean-Atmosphere Response Experiment            |
| CTD      | Conductivity-Temperature-Depth                          |
| DCL      | Deepest Common Level                                    |
| GA       | Gulf of Aden  |
| GAIW     | Gulf of Aden Intermediate Water                         |
| GCM      | General Circulation Model                               |
| ICOADS   | International Comprehensive Ocean-Atmosphere Data Set   |
| IIOE     | International Indian Ocean Expedition                   |
| KAU      | King Abdulaziz University                               |
| LADCP    | Lowered Acoustic Doppler Current Profiler               |
| NCEP     | National Centers for Environmental Prediction           |
| MICOM    | Miami Isopycnic Coordinate Ocean Model                  |
| NE       | Northeast   |
| NNW      | North-northwest   |
| NOAA     | National Oceanic and Atmospheric Administration         |
| NOCS     | National Oceanography Centre, Southampton               |
| NODC     | National Oceanographic Data Center                      |
| OAFlux   | Objective analysed air-sea fluxes dataset               |
| OSD      | Ocean Station Data                                      |
| PFL      | Profiling Float   |
| PI       | Principal Investigator                                  |
| QC       | Quality Control   |
| QuikScat | Satellite with a dedicated scatterometer mission (NASA) |
| R/V      | Research Vessel   |
| RSW      | Red Sea Water   |
| RSIW     | Red Sea Intermediate Water                              |
| RSSW     | Red Sea Surface Water                                   |

|       |  |
|-------|--|
| RSDW  | Red Sea Deep Water                       |
| RSOW  | Red Sea Outflow Water                    |
| SCOW  | Scatterometer Climatology of Ocean Winds |
| SSE   | South-southeast                          |
| SST   | Sea Surface Temperature                  |
| STD   | Salinity-Temperature-Depth               |
| SVD   | Singular Value Decomposition             |
| SW    | Southwest                                |
| VOS   | Voluntary Observing Ship                 |
| WHOI  | Woods Hole Oceanographic Institution     |
| WMDW  | Western Mediterranean Deep Water         |
| WOA09 | World Ocean Atlas 2009                   |
| WOD09 | World Ocean Database 2009                |

# Chapter 1 Literature review

## 1.1 Introduction

The Red Sea, like the Mediterranean Sea, is a semi-enclosed sea, connected to the Indian Ocean via the narrow and shallow Strait of Bab el Mandeb. It has an area of about one-fifth of the Mediterranean Sea and a very high evaporation rate which exceeds 2 m/yr (Sofianos et al., 2002). The Red Sea outflow water is considered one of the most important intermediate water masses in the Indian Ocean due to its significant impact on thermohaline circulation of the Indian Ocean. The Red Sea intermediate water (RSIW) has been mapped spreading eastwards from 50° E in the northern Indian Ocean to near the coast of Sumatra, southwards through the Mozambique Channel and into the Agulhas Current (Wyrki, 1971; Shapiro & Meschanov, 1991; Beal et al., 2000) and into the Cape Basin and the South Atlantic Ocean (Valentine et al., 1993).

The structure of this thesis is organised as follows. Chapter 1 gives general introductory information about geography, meteorological conditions, hydrography, circulation and exchange between the Red Sea Gulf of Aden at the Strait of Bab el Mandeb. Chapter 2 gives a detailed description of the data used in this study and their sources, as well as the quality control (QC) procedure. Chapter 3 gives detailed analysis of historical data (time series) and main results are presented. Chapter 4 gives a detailed analysis of heat and salt storage over the Red Sea. Chapter 5 gives a description of the inverse box modelling used in this study. Chapter 6 describes the hydrographic characteristics of the southern Red Sea. A setup of the standard inverse box model is presented in Chapter 7. A study of the sensitivity of the inverse box model and discussion of its errors are presented in Chapter 8. A description and discussion of the main results of the inverse box model are presented in Chapter 9. Chapter 10 gives a summary and conclusion.

## 1.2 Geography

The Red Sea forms a long, narrow semi-enclosed basin which separates the African and Asian continents, oriented north-northwest (NNW) south-southeast (SSE), and located between 12° 44' and 30° N, and 32° and 44° E. The basin is roughly 1932 km long with an average width of 280 km (Morcos, 1970). The depth varies from a maximum of 2500 m in the main basin to 160 m at the sill (13° 44' N), with an average depth of 450 m (Degens & Ross, 1969). The area of the Red Sea is  $0.46 \times 10^6 \text{ km}^2$  and its volume is  $0.251 \times 10^6 \text{ km}^3$  (Figure 1-1).

The Red Sea can be suitably divided into three regions, namely the main basin, the Strait of Bab el Mandeb, and the Gulfs of Aqaba and Suez.

1. The main basin is located in the central part of the Red Sea and extends from the Strait of Bab el Mandeb in the south to the Sinai Peninsula in the north. The main trough, extending along the axis, contains the deepest regions, down to approximately 2000 m in places. In this region the hot brine, topographic depression, which has very high temperature water (60 °C) and high salinity water (300 psu), are found near 21°10' N and 21°30' N (Morcos, 1970).
2. In the southern region, the Strait of Bab el Mandeb is located around 15° N, where the Red Sea joins the Indian Ocean by the Gulf of Aden. It extends over a southern entry point off Perim Island to the Hanish Islands in the northwest (Murray & Johns, 1997). There is a shallow sill at 13°41' N, where the water depth is only about 160 m. The strait is divided into two channels by Perim Island, the eastern strait and the southwest strait. The eastern strait is smaller, being approximately 4 km wide and 26 m deep; the western strait is 20 km wide and 300 m deep. Away from the straits, the bottom slopes down to the Gulf of Aden on the southern side of the Strait of Bab el Mandeb (Morcos, 1970) and into the Red Sea at the northern end.
3. North of 28°N, the Red Sea is divided into two narrow gulfs: the Gulf of Aqaba in the northeast and the Gulf of Suez in the northwest. The Gulf of Aqaba is a deep, narrow channel (with a depth of about 1400 m, a width of 16 km and a length of 150 km). It is separated from the main basin by a shallow sill (300 m deep). The Gulf of Suez is longer and wider than the

Gulf of Aqaba as it is about 250 km long and 36 km wide but it is relatively shallow when compared with the Gulf of Aqaba, being only about 70 m deep (Morcos, 1970).

### 1.3 Meteorological conditions

The climate of the Red Sea area is extremely arid with an average annual rainfall of less than 250 mm. The rate of evaporation in the Red Sea is higher than in most oceans and seas and it exceeds the precipitation rate (Patzert, 1974b). The average annual evaporation in the Red Sea has been estimated either by indirect calculation (conservation of volume and salt) or by using the bulk formula (see Table 1-2). There is no river runoff into the Red Sea.

| <b>Author</b>             | <b>Method</b>                   | <b>E (my<sup>-1</sup>)</b> |
|---------------------------|---------------------------------|----------------------------|
| (Vercelli, 1925)          | Pan measurements                | 3.5                        |
| (Yegorov, 1950)           | Bulk formula                    | 2.3                        |
| (Neumann, 1952)           | Bulk formula                    | 2.15                       |
| (Wust, 1954)              | Correction to Vercelli, 1925    | 1.9                        |
| (Privett, 1959)           | Bulk formula                    | 1.83                       |
| (Morcos, 1970)            | Average of previous estimations | 2.1                        |
| (Hastenrath & Lamb, 1979) | Bulk formula                    | 1.54                       |
| (Bunker et al., 1982)     | Bulk formula                    | 2.3                        |
| (Ahmad & Sultan, 1987)    | Bulk formula                    | 2.07                       |
| (Ahmad & Sultan, 1989)    | Bulk formula                    | 2.13                       |
| (Osman, 1985)             | Bulk formula                    | 2.04                       |
| (da Silva et al., 1994)   | Bulk formula                    | 1.5                        |
| (Tragou et al., 1999)     | Volume and salt conservation    | 1.75                       |
| (Sofianos et al., 2002)   | Volume and salt conservation    | 2.1                        |

Table 1-1: Summary of available evaporation rate estimates for the Red Sea (after Sofianos et al. (2002))

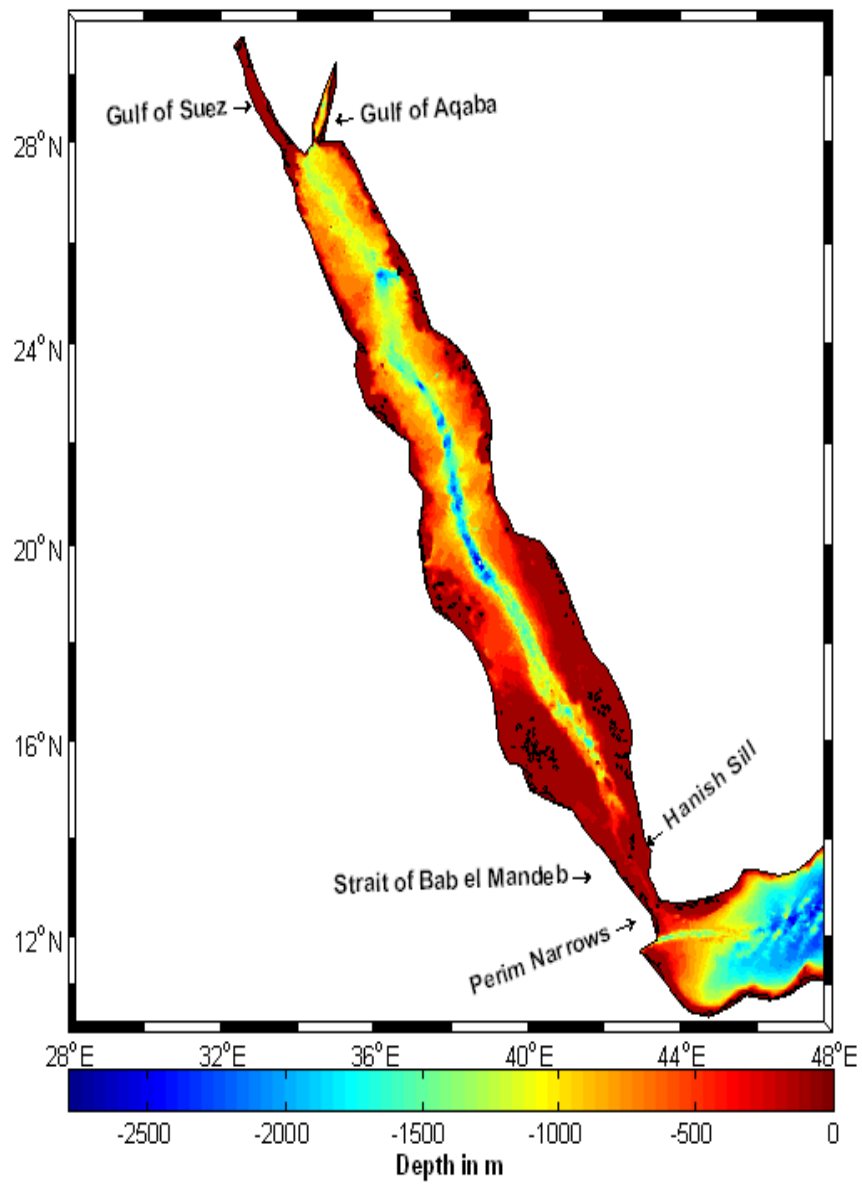


Figure 1-1: Bathymetry map of the Red Sea basin (Smith & Sandwell, 1997)

The wind field over the Red Sea flows parallel to the Sea axis as a result of high mountains and plateaus on either side of the basin (Patzert, 1974a). Throughout the year, winds blow from north-northwest in the northern part of the Red Sea (north of 20° N). And in the southern part (south of 20° N) the winds are influenced by the monsoons of the Arabian Sea (northeast (NE) and southwest (SW) monsoons), which reverse their direction twice per year (Quadfasel & Baudner, 1993). During the SW monsoon (June-September) the NNW winds are dominant in the southern part of the Red Sea. In contrast, during the NE monsoon and transition periods (October-May) the winds reverse from NNW to SSE. As shown in Figure 1-2, the monthly mean wind stress over the Red Sea region is directed along the main axis of the basin. The data were obtained from the NOC1.1 flux climatology, determined from in situ meteorological reports from Comprehensive Ocean-Atmosphere Data Set Release 1a (Sloyan & Rintoul, 2000) with extensions, which covers the period 1980-1993. During the period from October to December there is an intermediate zone created approximately in the middle of the Red Sea (20° N) due to the strong SSE winds (6.7-9.3 ms<sup>-1</sup>) in the southern part and the weak NNW winds (2.4-4.4 ms<sup>-1</sup>) in the northern part. This intermediate zone gradually moves southwards until June, when the whole of the Red Sea is dominated by NNW winds (Patzert, 1974a) (see Figure 1-2). Overall, the winds over the Red Sea region during the winter months are stronger than during the summer months.

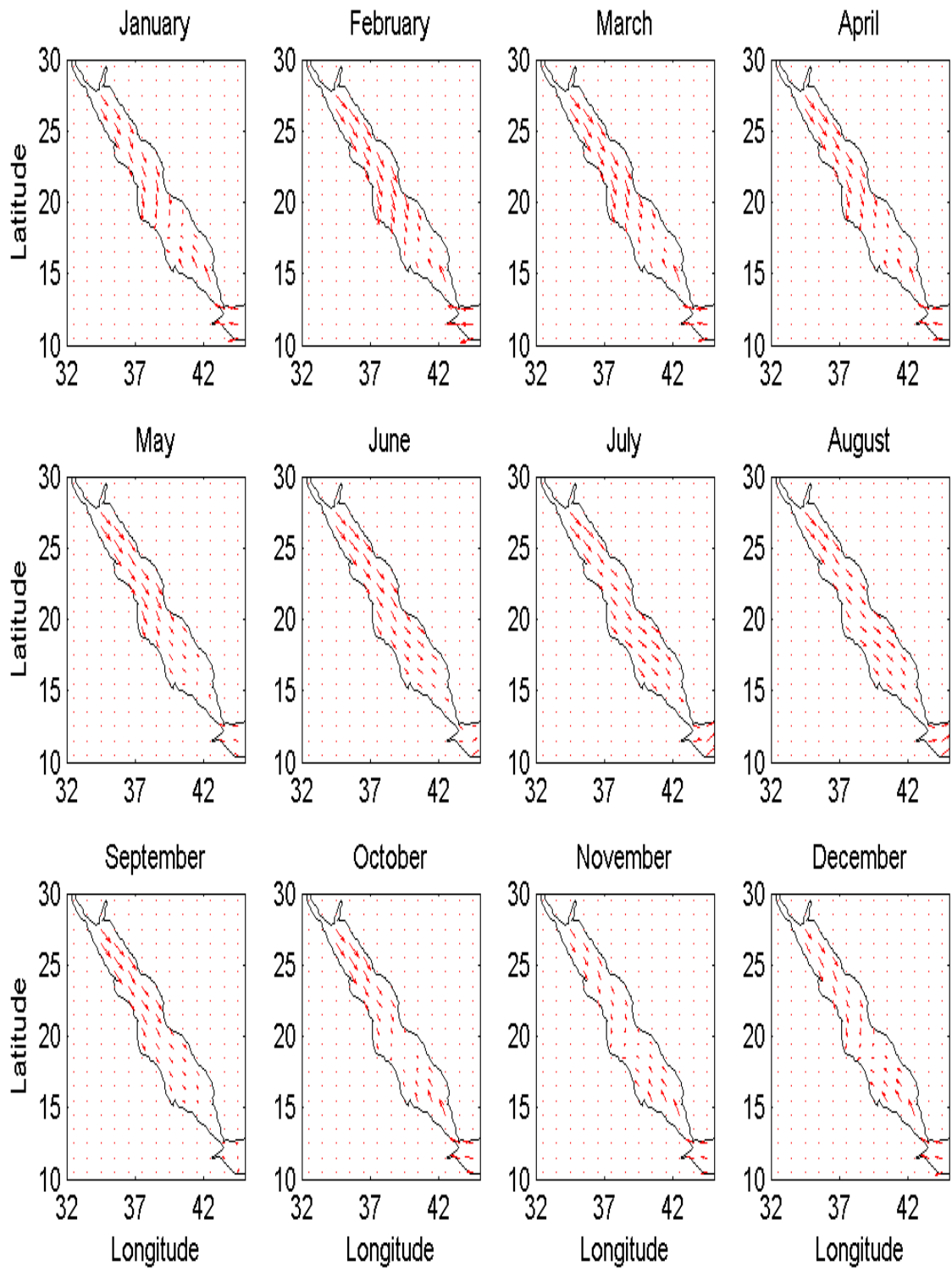


Figure 1-2: Climatological monthly mean wind stress (14 year averages from 1980 to 1993 from NOCS.1 (max arrow =  $0.068 \text{ Nm}^{-2}$ ))

## 1.4 Hydrographic properties

In general, the distribution of the sea surface temperature (SST) in the Red Sea is affected by the air temperature. Both increase southwards down to nearly 14° N and then decrease towards the Strait of Bab el Mandeb (Buchan, 1895; Morcos, 1970). (Figure 1-3). A zone of maximum SST (31°C) occurs in late summer to about 14° N and decreases (25 °C) and migrates northwards in winter (20° N) (Patzert, 1974a; Maillard & Soliman, 1986; Eshel et al., 1994). These seasonal changes are attributed to the monsoons (Morcos, 1970). The seasonal variation of the SST varies meridionally to 8°C in the northern Red Sea and 5°C in the Strait of Bab el Mandeb. The SST on the east coast of the Red Sea is higher than on the west coast in the winter and this is attributed to cyclonic circulation, while the situation is reversed in the summer. In summer when the winds blow from NNW along the axis of the Red Sea a clockwise circulation occurs at right angles to the direction of the winds, which is due to the piling up of surface warm water along the west coast and the upwelling of deeper water moving in an easterly direction. In winter, the opposite is true when the winds blow from SSE (Thompson, 1939; Morcos, 1970; Robinson, 1974). Generally, at all depths along the east coast the temperature is higher than on the west coast except in the wind convergence zone between 18 and 19° N where the opposite is true (Robinson, 1974).

The Red Sea has the most saline water of all the world's oceans (Morcos, 1970) due to its strong evaporation rate. Generally, the sea surface salinity of the Red Sea increases from the south at about 36.5 psu near the Strait of Bab el Mandeb, to the north at about 41-40 psu, at the southern tip of the Sinai Peninsula (Vercelli, 1927; Morcos, 1970; Edwards & Head, 1987) (see Figure 1-3). The annual variation of the salinity increases from the south to the north, going from about 0.5 (psu) in the south to more than 1 (psu) in the north (Morcos, 1970). The potential density in figure 1-3 through out of the year shows a strong north-south difference up to 4 kg m<sup>-3</sup> where the maximum density observed during winter time at the northern end of the Red Sea has a magnitude of  $\sigma_{\theta}$  28 or more.

The vertical distribution of the hydrographic properties is shown in Figure 1-4 and Figure 1-5. These hydrographic properties were taken along the main axis of the Red Sea for potential temperature and salinity from two different cruises, of R/V Maurice Ewing during August 2001 and Commandant Robert Giraud during January-February 1963.

In the upper layers, the potential temperature and salinity distribution changes substantially between the two monsoon seasons as a result of varying atmospheric forcing. During summer, the cool and fresh water layer from the Gulf of Aden flows below the shallow warm and saline mixed layer, causing unstable stratification. In contrast, during the winter season, the vertical temperature stratification is stable throughout the basin with the inflow of a warm and fresh water layer at the surface and the outflow of a cool and saline water layer at the bottom (Quadfasel, 2001).

Below the thermocline, the temperature decreases gradually to a minimum of 21.6°C at a depth of around 600 m and then increases adiabatically to more than 21.8°C at the bottom, which is higher than that in the world's oceans. The temperature in the bottom layer of 1000-2000 m varies by less than 0.5°C in the Red Sea (21.5-22°C) due to being disconnected from the Gulf of Aden by the sill at a depth of 160 m in the southern region. At the same depth in the Gulf of Aden, the temperature decreases steadily from 10°C to 3°C as result of free connection with the Indian Ocean (Morcos, 1970).

The whole Red Sea basin is filled below about 300 m with water of an extremely homogenous temperature, salinity and potential density of about 21.5-21.6°C, 40.5-40.6 psu and 28.6 kg m<sup>-3</sup> respectively (Wyrski, 1971; Edwards & Head, 1987). However, a notable changes in the RSDW characteristics in northern of the Red Sea (north of 26 °N) has been observed by Woelk and Quadfasel (1996) between 1982 and 1983. The characteristics of the new deep water (cooler and fresher) originate from the Gulf of Suez from vertical convection and mixing with fresher surface water masses.

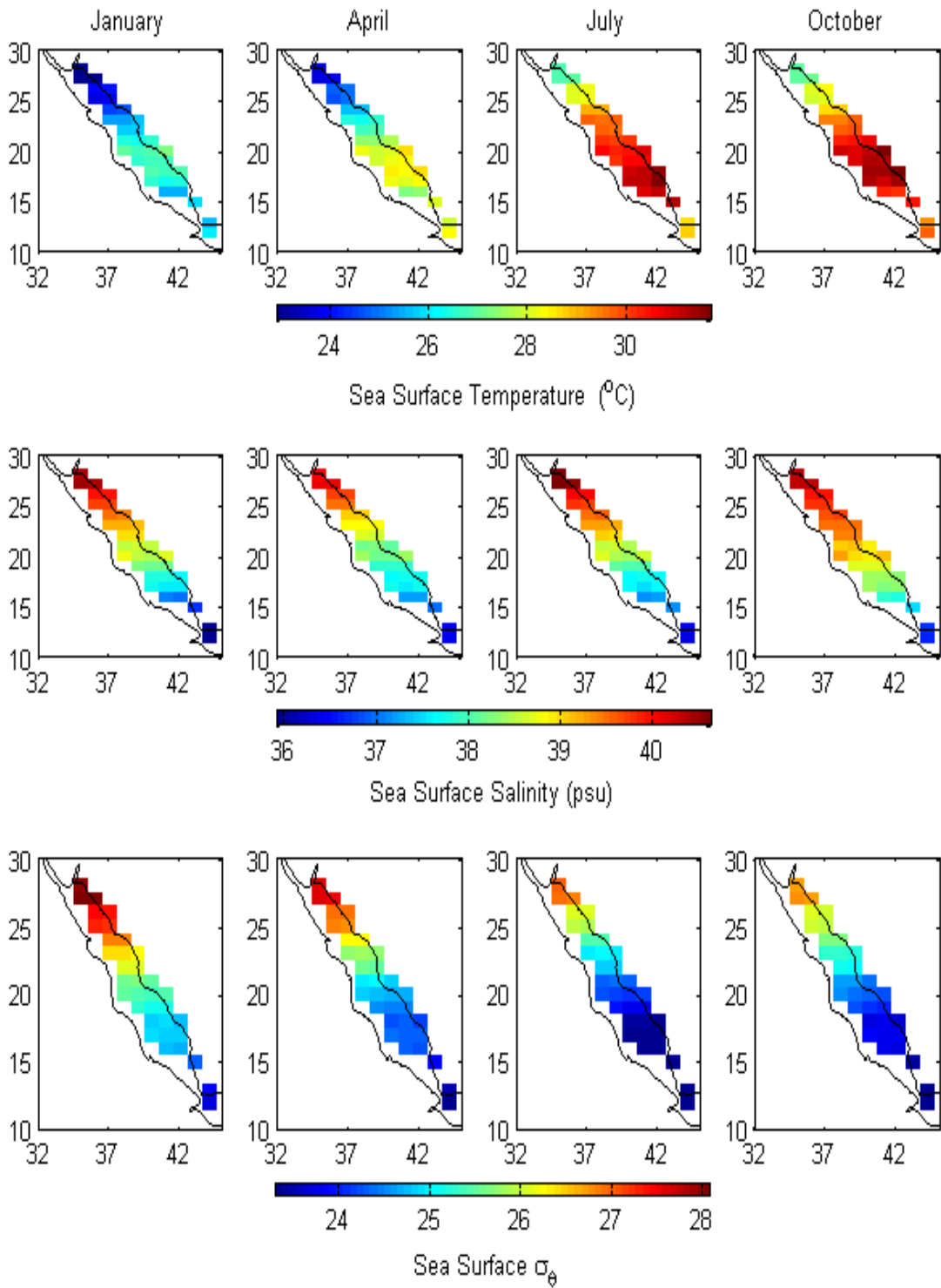


Figure 1-3: Monthly mean climatology of the Red Sea for the months January, April, July and October from Levitus94 (World Ocean Atlas, 1994). Sea surface temperature in °C (upper panel), sea surface salinity (middle panel) and  $\sigma_\theta$  (lower panel)

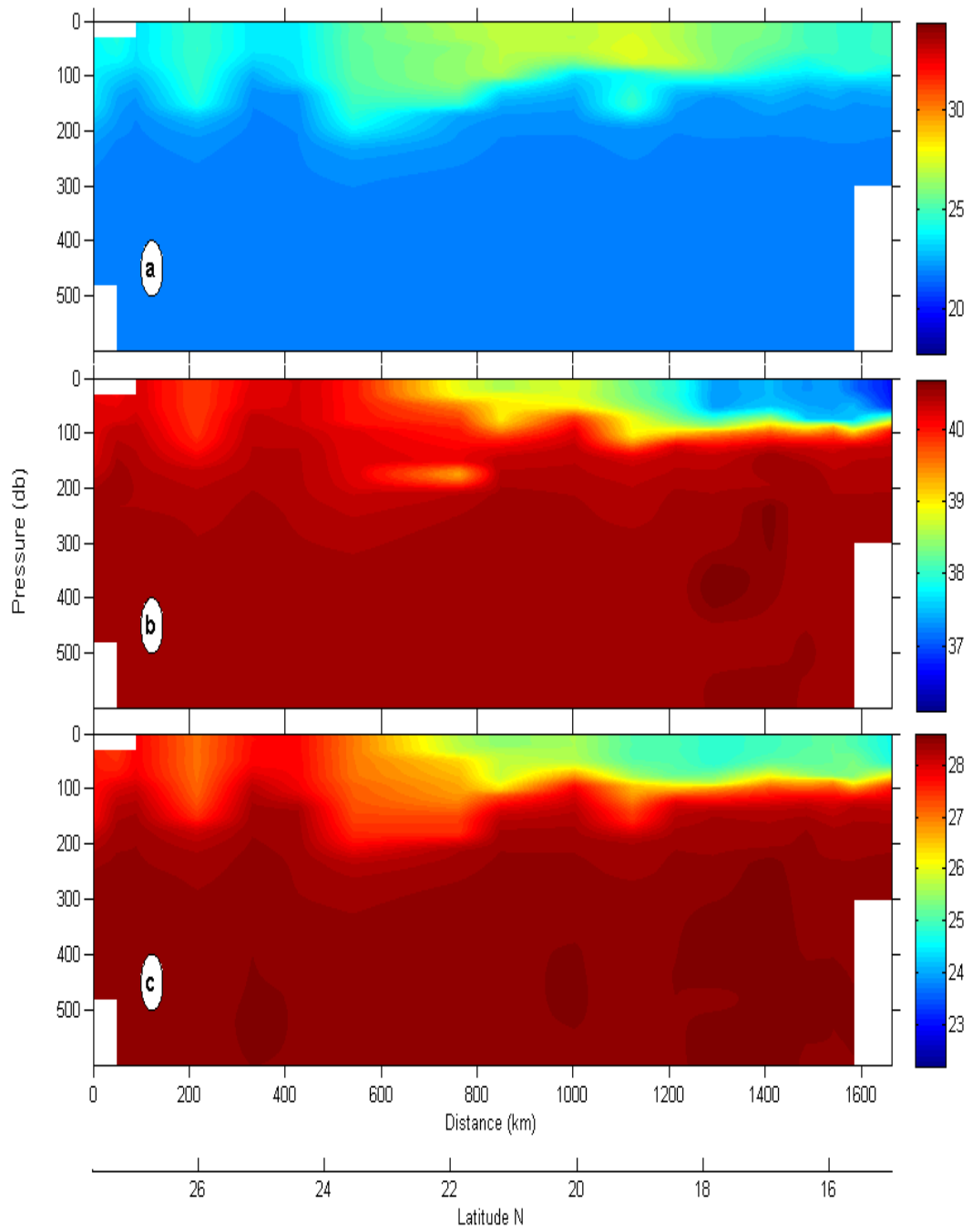


Figure 1-4: Hydrographic section along the main axis of the Red Sea for a) potential temperature in °C, b) salinity and c)  $\sigma_t$  from the cruise of Commandant Robert Giraud during January-February 1963

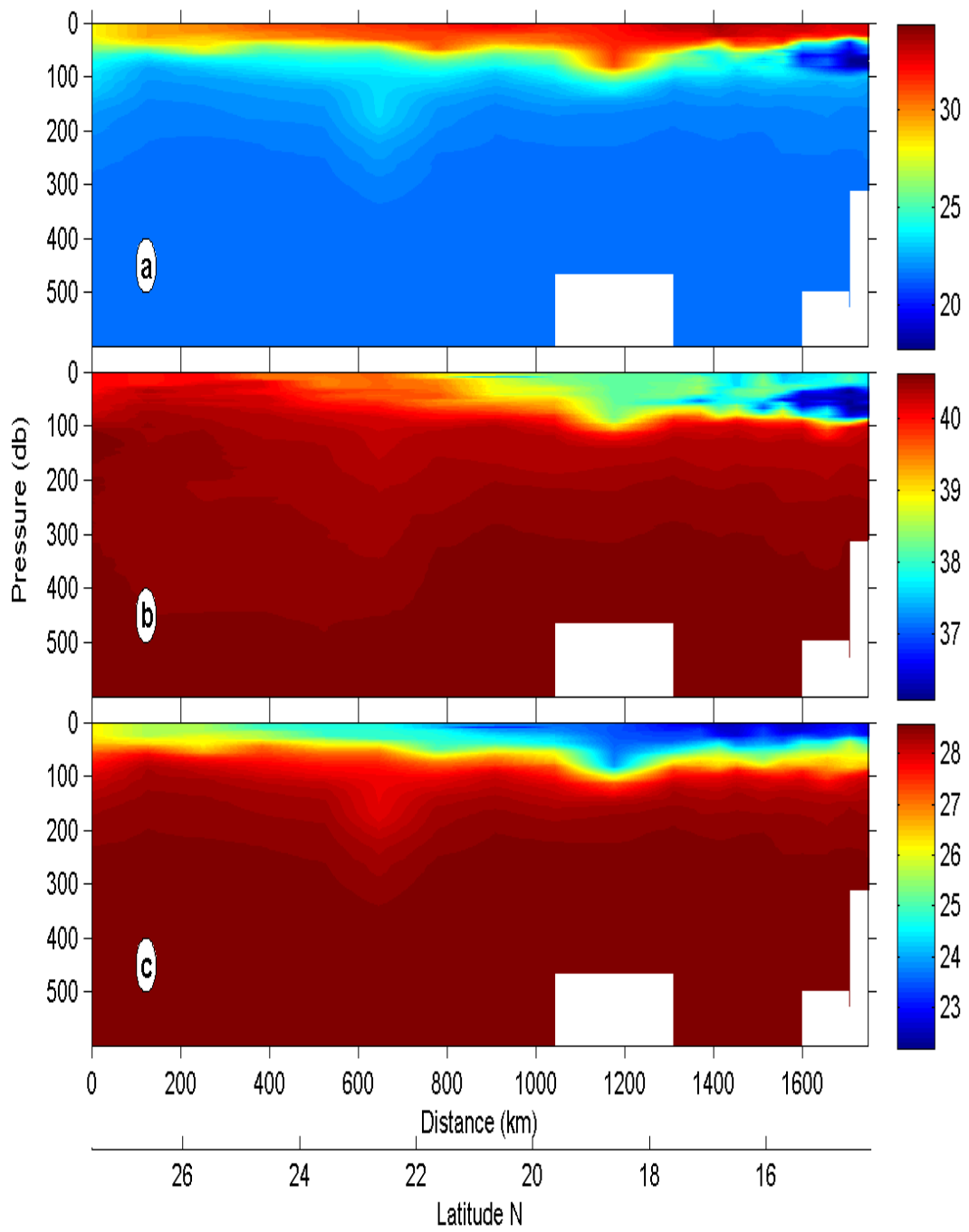


Figure 1-5: Hydrographic section along the main axis of the Red Sea for a) potential temperature in °C, b) salinity and c)  $\sigma_t$  from the cruise of R/V Maurice Ewing in August 2001

## 1.5 Circulation

Current measurements in the Red Sea are sparse, the few data available being for the strait regions (the Strait of Bab el Mandeb and the mouth of the Gulf of Aqaba) (Vercelli, 1927; Maillard & Soliman, 1986; Murray & Johns, 1997). There are two important factors controlling the water circulation in the Red Sea, namely the wind and the thermohaline forcing. The wind forcing governs the horizontal circulation in the upper layer (Patzert, 1974a; Ahmad & Sultan, 1987), while the overturning circulation is driven by thermohaline forcing (air-sea heat and mass exchanges) (Wyrтки, 1974)

### *1.5.1 Wind driven circulation*

The surface currents in the Red Sea are influenced by the winds which vary with the monsoon blowing in from the Arabian Sea (Edwards & Head, 1987). The surface currents flow southwards to reach the Strait of Bab el Mandeb during the SW monsoon (June-September). The mean surface currents flow to the southeast towards the Gulf of Aden through the Strait of Bab el Mandeb. In late summer, the speed of the south southeast current in the north of the Red Sea (north of 26° N) increases due to the strong NNW winds. However, the winds over the southern Red Sea region are weak during July and August and there are strong surface currents flowing south in the central region of the Red Sea between 18° and 20° N. The strongest outflowing surface current is found to be over 20 cm s<sup>-1</sup> in early July in the Strait of Bab el Mandeb (Patzert, 1974a).

Monthly mean currents in the southern region of the Red Sea are weak and most variable during the transition period of the monsoon winds (May-June and September-October). As a result of the decrease in the strength of the south-southeast winds in early June in the southern region of the Red Sea, the currents change direction from south-southeast to north-northwest. In addition, in the central region, the current reverses and flows southwards. These changes in the current direction are approximately in phase with changes in the direction of the winds. However, the current in the southern region lags one month behind the change in the wind direction in early September (Patzert, 1974a; Maillard & Soliman, 1986).

The SSE winds in the southern region (south of 20° N) increase in strength during the winter and drive the surface water from the Gulf of Aden into the Red Sea

through the Strait of Bab el Mandeb with a mean surface flow of 15-20 cm s<sup>-1</sup>. The current flows northwards against the weak NNW winds in the northern region (Patzert, 1974a; Bethoux, 1988; Shapiro & Meschanov, 1991).

The circulation in the upper layer of the basin is considered to be mainly due to wind forcing. However, Neumann and McGill (1961) and Phillips (1966) argued that circulation in the upper layer could be attributed to thermohaline forcing. As the fresh warm water flows from the Gulf of Aden into the Red Sea through the strait which moves northwards, it cools, mostly due to the high evaporation in the northern region. This water becomes more saline, becoming denser as a result, and it sinks and flows out of the Red Sea over the shallow (160 m depth) sill of Bab el Mandeb (Figure 1-6).

### *1.5.2 Deep circulation and formation*

As there are no direct deep current measurements in the Red Sea the major source of the information regarding subsurface and deep circulation is based on tracer budgets. Eshel et al. (1994) noted that circulation in the Red Sea is mostly driven by thermohaline forcing, which is more important than wind forcing. They estimated the general circulation by using a linear inverse model based on the conservation of heat, salt, and <sup>3</sup>He. Their model produced two modes of winter deep water formation in the extreme north of the Red Sea. These modes are the convection mode (annual mean of bottom formation water of 0.04 Sv) and the isopycnal mode (renewal of the top layer of deep water mass of 100-200 m with an annual rate of about 0.02-0.04 Sv). There are three different sources for the formation of deep water in the Red Sea. The first is the Gulf of Suez, where salinity is higher (about 42 psu) than salinity in the deep basin (40.5 psu). During winter the temperature decreases to less than 20°C, producing high density water at the surface which leaves the shallow Gulf of Suez and sinks into the Red Sea. The second source is the outflow of dense water from the Gulf of Aqaba over the shallow sill (300 m depth) of the Strait of Tiran. The third is the open-ocean deep convection at the northern end of the Red Sea, south of the Sinai Peninsula (Wyrki, 1974; Maillard & Soliman, 1986; Cember, 1988; Eshel et al., 1994).

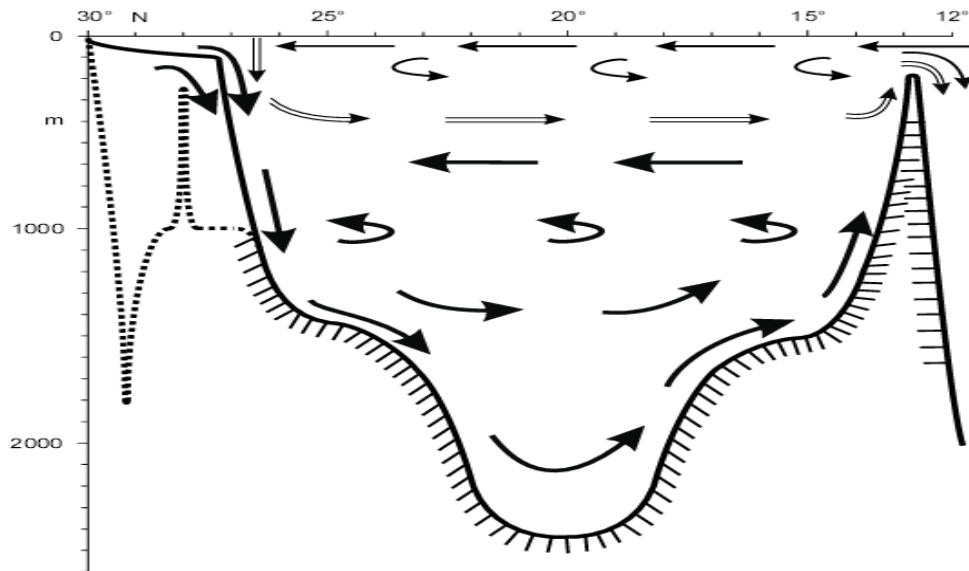


Figure 1-6: Schematic of the circulation patterns in the upper layers (single arrows), upper deep layers (double arrows, driven by open ocean convection) and deep layers (bold arrows, driven by plume convection) in the Red Sea (Quadfasel, 2001). Dotted topography represents the Gulf of Aqaba

Morcos (1970), Manins (1973), Wyrcki (1974) and Cember (1988) showed that the formation of deep water in the Red Sea occurs in the north basin. During winter in the southern part of the Sinai Peninsula, the surface water sinks to the bottom as result of an increase in its density when evaporation and cooling are both at a maximum (Privett, 1959). This newly formed water feeds the current of deep water flowing to the south. Part of the bottom upwells back to the upper layer. The upwelled water returns to the north at a depth of around 500 m and reaches the far north of the basin where it sinks again to the bottom to restart the loop of deep circulation (Figure 1-6).

Maillard (1974) argued that the deep water of the Red Sea is an equal mixture of the high dense outflow from the mouth of the Gulf of Suez and the water in the upper layers (0-150 m) formed during the winter. Her evidence was based on temperature and salinity measurements in the winter season.

Cember (1988) noted, by using data of  $^{14}\text{C}$  and  $^3\text{He}$  distributions below a 200 m depth from the GEOSECS Indian Ocean Expedition, that the upwelling of the deep water along the Red Sea basin maintains the sharp pycnocline with its base near the depth of the sill in the Strait of Bab el Mandeb. There is a variety of estimated rates for the annual mean deep water formation and the renewal time from a few decades to a century (Table 1-2).

| Author                       | Method                                       | Residence time<br>(year) | Rate of<br>formation (Sv) |
|------------------------------|--|--------------------------|---------------------------|
| (Manins, 1973)               | Hydrological model                           | 320                      | -                         |
| (Maillard, 1974)             | Hydrography                                  | 100                      | 0.04                      |
| (Wyrтки, 1974)               | Oxygen budget                                | 72                       | 0.06                      |
| (Kuntz, 1985)                | Tritium, <sup>3</sup> He (multibox-model)    | 40                       | 0.016                     |
| (Cember, 1988)               | <sup>14</sup> C, <sup>3</sup> He (box model) | 36                       | 0.16                      |
| (Eshel et al., 1994)         | T, S, <sup>3</sup> He (box model)            | 35                       | 0.16                      |
| (Woelk & Quadfasel, 1996)    | Hydrography                                  | 40-90                    | 0.05-0.08                 |
| (Jean-Baptiste et al., 2004) | <sup>14</sup> C, <sup>3</sup> He (box model) | 26-60                    | 0.09                      |

Table 1-2: Summary of available residence time and rate of formation estimates for the Red Sea ( $1\text{Sv} = 10^6 \text{m}^3 \text{s}^{-1}$ )

## 1.6 Exchanges between the Red Sea and Gulf of Aden at the Strait of Bab el Mandeb

As mentioned earlier, the Strait of Bab el Mandeb is about 150 km long and it connects the Red Sea with the Gulf of Aden and the Indian Ocean. There is a strong seasonal variation in the exchange flow through the Strait of Bab el Mandeb (Thompson, 1939), as shown in Figure 1-7 from Smeed (2000).

The three-layer system (Figure 1-7) occurs in the summer (June-September) when the direction of the SSE winds is reversed in the southern region of the Red Sea to NNW winds that blow into the Gulf of Aden. The three layers consist of a surface layer outflow toward the Gulf of Aden (with a shallow depth of roughly 40 m, a warm temperature of  $\sim 29^\circ\text{C}$ , and a high salinity of  $\sim 37.5$  psu) governed by the southern wind reversal and strong upwelling at the entrance of the Red Sea; an inflowing subsurface layer between the depths of 40 m and 80 m (cool,  $\sim 18^\circ\text{C}$ , low salinity  $\sim 36.0$  psu) from the Gulf of Aden due to a reversal of the pressure gradient over the sill (Patzert, 1972a); and a dense deep water layer outflowing from the Red Sea in the region below 180 m (cool,  $\sim 21^\circ\text{C}$ , high salinity  $\sim 40.0$  psu). The two-layer system (Figure 1-7), which occurs in the winter (October-May) in the Strait of Bab el Mandeb, consists of the following: surface layer inflow (with a warm temperature of  $25^\circ\text{C}$  and a low salinity of 36.5 psu) from the Gulf of Aden to the Red Sea, which is driven by strong SSE winds; and deep layer outflow (with a cool temperature of  $23^\circ\text{C}$  and a higher salinity of 40.5 psu) from the Red Sea to the Gulf of Aden as a result of higher water density. These two layers

have the physical characteristics of the Gulf of Aden (surface layer) and the Red Sea (deep layer). It is believed that the main reason for the observed three-layer system during the summer (June-September) at the strait is the upwelling in the Gulf of Aden which is induced by the strong SW monsoon winds (Patzert, 1974b; Smeed, 1997).

Siedler (1969) estimated the annual mean transport of Red Sea water through the Bab el Mandeb Strait (using the Knudsen relations) to be 0.33 Sv. This is about one-third of the annual mean transport of Mediterranean water through the Strait of Gibraltar (Candela, 2001). Furthermore, Patzert (1974a) estimated the maximum outflow of the Red Sea water through the strait to be 0.57 Sv in the winter season, decreasing to 12% of that in early summer and to 6% by the end of summer. The lower-layer exchange flow was shown to vary from an annual average of 0.3 Sv to a maximum of 0.6 Sv in winter (Morcos, 1970; Maillard & Soliman, 1986).

The more recent long-term and comprehensive observations in the Strait of Bab el Mandeb were carried out by Murray and Johns (1997) over 10 months from June 1995 to March 1996, using an ADCP and temperature-salinity chain moorings. It was found that the deep water outflow was still strong in June with a speed of 0.6 m/sec and a volume transport rate of 0.4 Sv. During the summer season (July to mid-September), the speed of deep water outflow decreased to 0.2 m/sec and the volume transport rate to 0.05 Sv. During the winter (November-March), the speed of the lower layer was found to be 0.8–1.0 m s<sup>-1</sup> and that of the upper layer 0.4–0.6 m s<sup>-1</sup>. The maximum exchange was recorded in mid-February, when it was shown to reach 0.7 Sv.

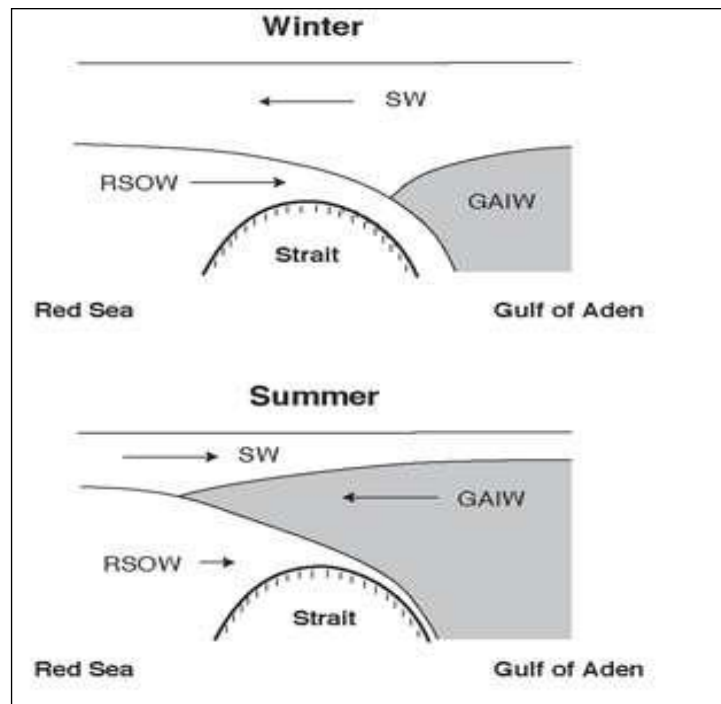


Figure 1-7: Sketch of two circulation patterns in the Strait of Bab el Mandeb during the winter and summer seasons. SW represents the surface water, GAIW represents Gulf of Aden intermediate water and RSOW represents Red Sea outflow water (Smeed, 2000)

## 1.7 Aim of this thesis

The motivation and initial aim of this study is to investigate the potential temperature and salinity variations in Red Sea Deep Water (RSDW) over the years since 1889 and to see whether there are significant trends toward higher salinity and higher temperature against the background of natural seasonal and interannual variability. This aim came as results of observed changes by Woelk and Quadfasel (1996) for the RSDW characteristics (cooling and freshening) in 1982/1983. While the global warming across ocean and seas are evident particularly in the tropics and subtropics such as the Mediterranean Sea. A diagnosis of the circulation of the Red Sea using synoptic hydrographic measurement is utilised together with inverse methods to provide quantification of summer field fluxes (volume, heat and salt) and the southward RSOW export to the Indian Ocean through the Strait of Bab el Mandeb.

# Chapter 2 Dataset

## 2.1 Introduction

The Red Sea is a very poorly surveyed region compared with the neighbouring Mediterranean Sea. According to the literature review given by Morcos (1970), the total number of hydrographic stations occupied in the Red Sea from 1890 to 1968 was only 862 (12- 28°N), with about one-third of them at a depth of less than 50 m. The hydrographic data in the Red Sea are sparse and most of the measurements come from along the main axis of the Red Sea; there are only a few synoptic cruise reports containing a cross section. The earliest recorded measurement of a hydrographic parameter (temperature from a bottle only) in the Red Sea was made in March and April in 1858 by a British cruise of Cyclops. During this cruise 14 profiles were collected in the Indian Ocean, of which 7 profiles (temperature only) were from the Red Sea.

Among the major expeditions exploring the Pacific and Indian Ocean in the nineteenth century, the Russian expedition on board the Vityaz during 1886-1889 passed through the Red Sea and collected only 2 profiles of temperature and salinity in the month of March. An Austrian expedition on board Pola carried out an extensive investigation in the winter season in the northern Red Sea from 25 October 1895 to 2 May 1896 with 143 stations and in the southern Red Sea from 19 September 1897 to 2 March 1898 with 88 stations. In this expedition the accuracy of the instruments was below the modern standards; the thermometers were read to 0.1°C and the salinity was measured by the hydrometer to the nearest 0.1 (psu). (Morcos, 1970). There were two Italian expeditions on board Amiraglio Magnaghi (1923-1924 and 1929), which carried out extensive investigations in the Red Sea and in the Strait of Bab el Mandeb; the former investigated the tides in the Red Sea and the current in the Strait of Bab el

Mandeb and along the axis of the Red Sea. The latter investigated the current in the Gulf of Suez, the central part of the Red Sea and the Strait of Bab el Mandeb in the summer season.

In 1929-1930, the Dutch expedition on board Willebrord Snellius occupied a few stations in the southern part of the main axis of the Red Sea through their navigation to the Indian Ocean. Also in 1933-34, the British John Murray expeditions on board *Mabahiss* occupied a few stations, although most of these were limited to the southern region of the Red Sea. During this cruise observations of the exchange of water in the Strait of Bab el Mandeb were made by Thompson (1939) in September 1933 and May 1934. After a gap of 15 years, several expeditions made some studies while passing through the Red Sea region, such as the Swedish on board *Albatross* in April and May 1948 with 2 profiles; the British on board *Dampier* in July of 1948 with 3 profiles, on board the *Manihine* expedition in 1949, which mostly investigated the Gulf of Aqaba, and on board *Discovery II* in 1950-1951; and two American cruises of *Atlantis* and *Vema* in 1958.

The beginning of the International Indian Ocean Expedition (IIOE) in 1959-1964 with international co-operation to explore the Indian Ocean brought many oceanographic vessels and survey ships through the Red Sea including: *A.I. Voeykov* and *Shoyo Maru* in 1959, *Vityaz* in 1960, *Genie* and *Horizon* in 1962, Commandant Robert Giraud, *Discovery* and *Atlantis II* in 1963, *Meteor* and *Discovery* in 1964, *Atlantis II* and Robert D. Conard in 1965, and *Marlin*, *Antar*, *Ichthiolog* and *Chain* in 1966. Some of these cruises, such as those of *Meteor* and *Discovery*, *Atlantis II* and *Chain*, focused much attention on the exploration of the hot and saline deep water in the Red Sea. Unfortunately, no interest was expressed in the Red Sea region during the IIOE planning stage for exploration of the Indian Ocean because at that time, the Red Sea was better known than the Indian Ocean. Following the IIOE there has been increasing interest in investigating the hot brine region and the exchange with the Indian Ocean in the Strait of Bab el Mandeb. In recent years (2008-2010-2011), there have been large-scale hydrographic surveys in the Red Sea conducted by King Abdullah University in collaboration with the Woods Hole Oceanographic Institution (WHOI) and also by King Abdulaziz University (KAU) in collaboration with the Leibniz Institute of Marine Sciences of the University of Kiel. There are about 1458 hydrographic stations (measuring temperature and salinity) that have been set up since

Vityaz in 1889; about 47% are shallower than 300 m and located at the National Oceanographic Data Center (NODC).

In this chapter the hydrographic data used in the whole thesis, along with their sources, quality control procedure and processing are described.

## 2.2 Hydrographic data

### 2.2.1 Data source

The aim has been to include as far as possible all available historical temperature and salinity profiles for the Red Sea to generate a reliable hydrographic dataset. The data used in this study were retrieved from different sources such as public data centres and direct contact with the principal investigator (PI). There are two main sources for the hydrographic data:

#### 1. Data centres

- a. NODC, Washington, D.C., (<http://www.nodc.noaa.gov/>), which is the largest hydrographic dataset and the main source of available historical data for the Red Sea region (latitude: 14 °N to 27.9 °N; and longitude: 32° E to 43.5° E).

The NODC dataset consists of data from:

- i. High-Resolution Conductivity- Temperature-Depth (CTD) referring to measurement at high frequency vs. depth (pressure). All casts with an interval depth instrument of less than two metres are considered high-resolution CTD. Otherwise the casts are considered low-resolution CTD. Table 2-1 shows the time series of the available CTD profiles in the Red Sea.
- ii. Ocean Station Data (OSD) refers to measurements from bottles with reversing thermometers tripped at depth of interest in water column. The OSD contains bottle data, CTD data, Salinity-Temperature-Depth (STD), some low-resolution expendable XCTDs, some surface only data and plankton taxonomic and biomass measurements. It should be mentioned that only the bottle data from OSD have been used and Table 2-2 shows the available bottle data time series in the Red Sea.

- iii. Profiling Floats (PFL), which are collected from drifting profiling floats such as APEX (Autonomous Profiling Explorer), Profiling Autonomous Lagrangian Circulation Explorer (P-ALACE), PROVOR (a free-drifting hydrographic profiler) and Sounding Oceanographic Lagrangian Observer (SOLO), where the main source of WOD09 is the Argo project (Johnson et al., 2009).
- b. The dataset of the British Oceanographic Data Centre (BODC), which deals with biological, chemical, physical and geophysical data and contains measurements of nearly 22,000 different oceanographic variables. It consists of 68 profiles (temperature and salinity from Argo float no. 2901098) for the Red Sea region.
- c. Scripps Institution of Oceanography: Center for Coastal Studies Data Zoo. This dataset collects historical data from different sources for part of a project studying the Red Sea Model. These data are available on the integrative oceanography division website (<http://zoo.ucsd.edu/redsea/>) which contains CTD and bottle data in two different categories:
  - i. Data centre: NODC and Australian Oceanographic Data Centre (AODC).
  - ii. Scientists' names: Eshel Gidon (Gidon), Catherine Maillard (Maillard) and Detlef Quadfasel (Quadfasel).

Unfortunately, no details of the metadata such as information about their ships' names, nationality, PI and processing of the measurement (such as calibration and quality control applied) are available on the websites.

## **2. Data obtained from PI**

- a. CTD profiles from the Red Sea cruises below obtained personally from Prof. Detlef Quadfasel (Center for Marine and Atmospheric Science, Institute of Oceanography, University of Hamburg):
  - i. R/V Marion Dufresne in October 1982
  - ii. R/V Sagar Kanya in May 1983
  - iii. R/V Meteor (M5\_2) in February 1987
  - iv. R/V Meteor (M5\_5) in July-August 1987

- b. R/V Meteor (M44\_2) in 1999 obtained personally from Dr. Maren Walter (Department of Oceanography, Institute of Environmental Physics, and University of Bremen).
- c. R/V Maurice Ewing from 4 to 19 August 2001. These data were obtained personally from Dr. Sarantis Sofianos (Department of Environmental Physics, University of Athens) and contain 77 profiles of temperature, salinity and oxygen.
- d. CTD and bottle (temperature, salinity and oxygen) profiles were collected during March 2010 on board R/V Aegaeo. On this expedition a comprehensive, large-scale survey was conducted of the hydrographic patterns in the Red Sea especially in the northeast. It had 9 perpendicular transects along the Saudi Arabian coast toward the central ridge of the Red Sea with 110 profiles.

There were a total of 3271 profiles collected from these sources, containing 592 CTD, 2423 bottle and 256 Argo stations (Table 2-3). Figure 2-1 and Figure 2-2 show the distributions of available hydrographic data from different sources for the Red Sea.

| Country       | Ship name                     | Code | Year | No. St.   | St. < 300m | St. ≥ 300m | Month |
|---------------|-------------------------------|------|------|-----------|------------|------------|-------|
| UNITED STATES | MELVILLE                      | MEL  | 1977 | 3         | 0          | 3          | 12    |
| SOVIET UNION  | AKADEMIK VERNADSKIY           | AKV  | 1980 | 9         | 1          | 8          | 6     |
| FRANCE        | MARION DUFRESNE               | MD   | 1982 | 22        | 1          | 21         | 6-10  |
| GREAT BRITAIN | HERALD                        | HER  | 1982 | 2         | 2          | 0          | 2-3   |
| SOVIET UNION  | AKADEMIK ALEKSANDR VINOGRADOV | AAV  | 1985 | 2         | 0          | 2          | 3     |
| SOVIET UNION  | AKADEMIK M.A. LAVRENTYEV      | AML  | 1988 | 8         | 0          | 8          | 12    |
| SOVIET UNION  | IGNAT PAVLYUCHENKOV           | IP   | 1991 | 1         | 1          | 0          | 8     |
| NETHERLANDS   | TYRO                          | TY.1 | 1992 | 6         | 2          | 4          | 5     |
| NETHERLANDS   | TYRO                          | TY.2 | 1993 | 7         | 0          | 7          | 2     |
| GERMANY       | METEOR                        | MET  | 1995 | 16        | 0          | 16         | 2     |
| FRANCE        | BEAUTEMPS-BEAUPRE             | BB.1 | 2008 | 2         | 0          | 2          | 1     |
| FRANCE        | BEAUTEMPS-BEAUPRE             | BB.2 | 2011 | 4         | 0          | 4          | 2-3   |
| <b>total</b>  |                               |      |      | <b>82</b> | <b>7</b>   | <b>75</b>  |       |

Table 2-1: Available CTD data for the Red Sea from the NODC dataset (N1CTD)

| Country       | Ship name                     | Code  | Year | No. St. | St. < 300m | St. ≥ 300m | Month     |
|---------------|-------------------------------|-------|------|---------|------------|------------|-----------|
| SOVIET UNION  | VITYAZ                        | VI1   | 1889 | 2       | 0          | 2          | 3         |
| AUSTRIA       | POLA                          | PO1   | 1895 | 42      | 17         | 25         | 10-11-12  |
| AUSTRIA       | POLA                          | PO2   | 1896 | 42      | 18         | 24         | 1-2-4     |
| AUSTRIA       | POLA                          | PO3   | 1897 | 48      | 22         | 26         | 10        |
| AUSTRIA       | POLA                          | PO4   | 1898 | 27      | 12         | 15         | 2-3       |
| ITALY         | AMMIRAGLIO MAGNAHI            | AM1   | 1923 | 59      | 54         | 5          | 10-12     |
| ITALY         | AMMIRAGLIO MAGNAHI            | AM2   | 1924 | 48      | 38         | 10         | 1-5       |
| NETHERLANDS   | WILLEBROD SNELLIUS            | WS    | 1929 | 3       | 0          | 3          | 4         |
| GREAT BRITAIN | MABAHISS                      | MA1   | 1933 | 3       | 0          | 3          | 9         |
| GREAT BRITAIN | MABAHISS                      | MA2   | 1934 | 1       | 0          | 1          | 5         |
| GREAT BRITAIN | DAMPIER                       | DAM   | 1948 | 3       | 0          | 3          | 7         |
| SWEDEN        | ALBATROSS                     | ALB   | 1948 | 2       | 0          | 2          | 4-5       |
| FRANCE        | UNKNOWN                       | U1    | 1950 | 1       | 0          | 1          | 5         |
| UNITED STATES | ATLANTIS I                    | AT1   | 1958 | 19      | 0          | 19         | 5-6       |
| UNITED STATES | HEMA                          | VEM   | 1958 | 4       | 0          | 4          | 6         |
| EGYPT         | SHOYO MARU                    | SHM   | 1959 | 11      | 0          | 11         | 3         |
| SOVIET UNION  | A.I. VOEYKOV                  | A.I.V | 1959 | 10      | 0          | 10         | 9         |
| SOVIET UNION  | VITYAZ                        | VI2   | 1960 | 11      | 9          | 2          | 4-10      |
| ISRAEL        | GENIE                         | GEN   | 1962 | 17      | 17         | 0          | 3         |
| UNKNOWN       | UNKNOWN                       | U2    | 1962 | 4       | 1          | 3          | 1         |
| UNITED STATES | HORIZON                       | HOR   | 1962 | 9       | 1          | 8          | 9         |
| FRANCE        | COMMANDANT ROBERT GIRAUD      | CRG   | 1963 | 54      | 4          | 50         | 1-2       |
| UNITED STATES | ATLANTIS II                   | AT2.1 | 1963 | 7       | 0          | 7          | 7-8       |
| GREAT BRITAIN | DISCOVERY                     | DIS   | 1964 | 8       | 0          | 8          | 2-3-9     |
| GERMANY       | METEOR                        | MET   | 1964 | 7       | 1          | 6          | 11-12     |
| UNKNOWN       | UNKNOWN                       | U3    | 1964 | 16      | 3          | 13         | 12        |
| SOVIET UNION  | MARLIN                        | MAR.1 | 1965 | 25      | 25         | 0          | 3-6-9     |
| UNKNOWN       | UNKNOWN                       | U4    | 1965 | 108     | 66         | 42         | 1-2-3-4   |
| UNITED STATES | ATLANTIS II                   | AT2.2 | 1965 | 12      | 4          | 8          | 2         |
| UNITED STATES | ROBERT D. CONRAD              | RDC   | 1965 | 4       | 0          | 4          | 7         |
| UNITED STATES | UNKNOWN                       | UU1   | 1966 | 13      | 8          | 5          | 3-5       |
| UNKNOWN       | UNKNOWN                       | U5    | 1966 | 2       | 2          | 0          | 7         |
| SOVIET UNION  | MARLIN                        | MAR.2 | 1966 | 6       | 4          | 2          | 5         |
| CANADA        | ANTAR                         | ANT   | 1966 | 34      | 31         | 3          | 9         |
| SOVIET UNION  | VLADIMIR VOROBYEV             | VV    | 1966 | 10      | 10         | 0          | 8-9-12    |
| SOVIET UNION  | ICHTHIOLOG                    | ICH   | 1966 | 28      | 25         | 3          | 9         |
| UNITED STATES | CHAIN                         | CHA   | 1966 | 19      | 2          | 17         | 10-11     |
| SOVIET UNION  | MYSLITEL                      | MYSL  | 1971 | 33      | 32         | 1          | 8-9       |
| UNKNOWN       | UNKNOWN                       | U6    | 1971 | 118     | 112        | 6          | 4-8-11    |
| SOVIET UNION  | VSEVOLOD BERYEZKIN            | VB    | 1975 | 27      | 1          | 26         | 9         |
| SOVIET UNION  | AKADEMIK KURCHATOV            | AKK   | 1976 | 3       | 0          | 3          | 3-6       |
| UNKNOWN       | UNKNOWN                       | U7    | 1976 | 3       | 1          | 2          | 4-8       |
| UNKNOWN       | UNKNOWN                       | U8    | 1977 | 1       | 0          | 1          | 2         |
| UNITED STATES | MELVILLE                      | MEL   | 1977 | 3       | 0          | 3          | 12        |
| UNKNOWN       | UNKNOWN                       | U9    | 1981 | 11      | 4          | 7          | 5         |
| UNKNOWN       | UNKNOWN                       | U10   | 1981 | 151     | 80         | 71         | 8-9-10-11 |
| UNKNOWN       | UNKNOWN                       | U11   | 1981 | 10      | 0          | 10         | 5         |
| SOVIET UNION  | AKADEMIK ALEKSANDR NESMEYANOV | AAN1  | 1982 | 3       | 0          | 3          | 7         |
| SOVIET UNION  | PROFESSOR KHROMOV             | PK1   | 1983 | 7       | 2          | 5          | 5         |
| SOVIET UNION  | AKADEMIK ALEKSANDR NESMEYANOV | AAN2  | 1983 | 13      | 10         | 3          | 8         |
| SOVIET UNION  | AKADEMIK SHOKALSKIY           | AS    | 1984 | 19      | 2          | 17         | 2         |
| SOVIET UNION  | PROFESSOR KHROMOV             | PK2   | 1984 | 12      | 1          | 11         | 3         |
| SOVIET UNION  | AKADEMIK M.A. LAVRENTYEV      | AML   | 1986 | 1       | 0          | 1          | 6         |
| SOVIET UNION  | PROFESSOR BOGOROV             | PB    | 1990 | 32      | 8          | 24         | 2-3       |
| SOVIET UNION  | IGNAT PAVLYUCHENKOV           | IP    | 1991 | 2       | 2          | 0          | 5-8       |
| INDIA         | UNKNOWN                       | IU1   | 1992 | 6       | 2          | 4          | 5         |
| INDIA         | UNKNOWN                       | IU2   | 1993 | 7       | 0          | 7          | 2         |
| total         |                               |       |      | 1188    | 638        | 550        |           |

Table 2-2: Available bottle data for the Red Sea from the NODC dataset (N10SD)

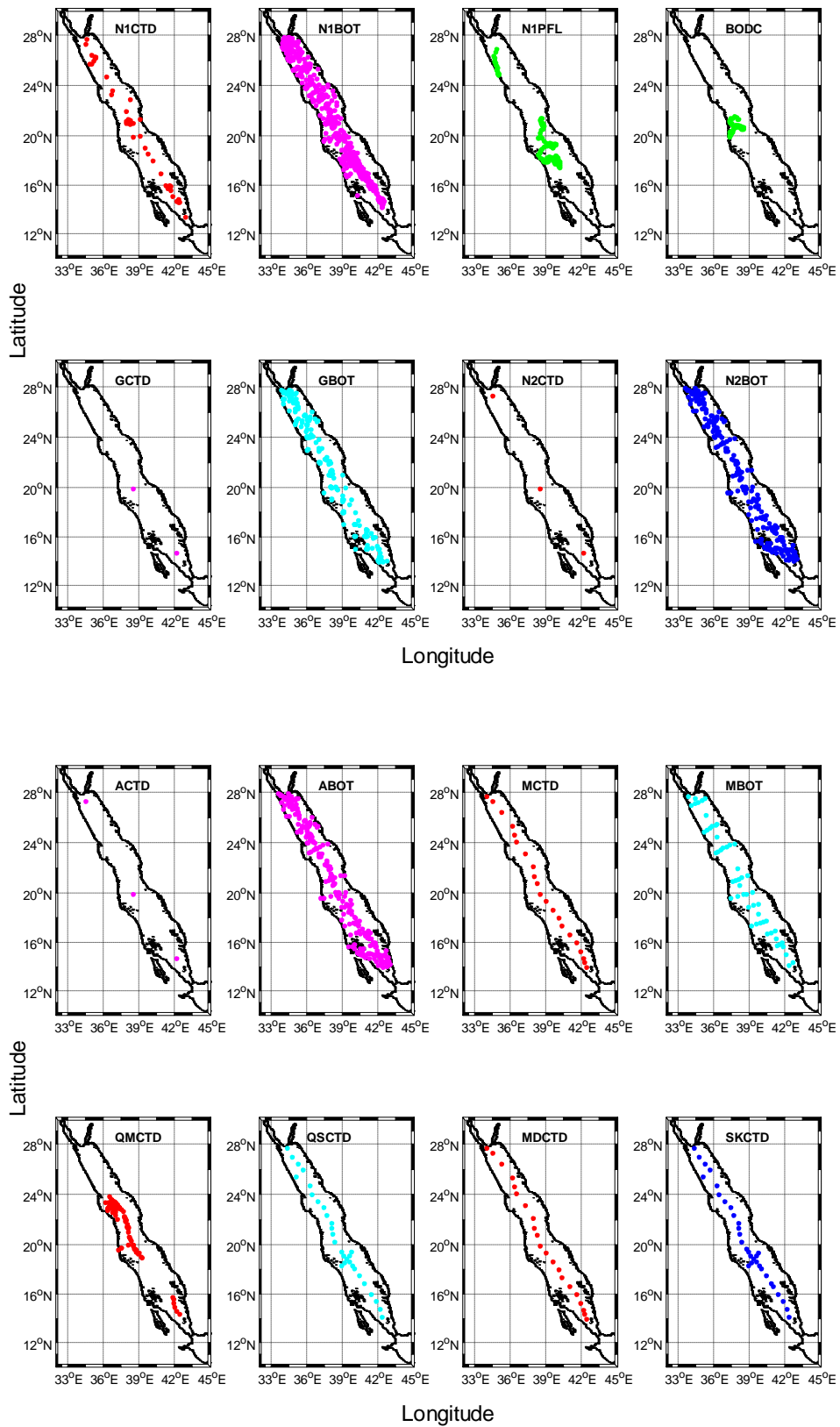


Figure 2-1: Distribution of the hydrographic data for the Red Sea (the codes are explained in Table 2-3)

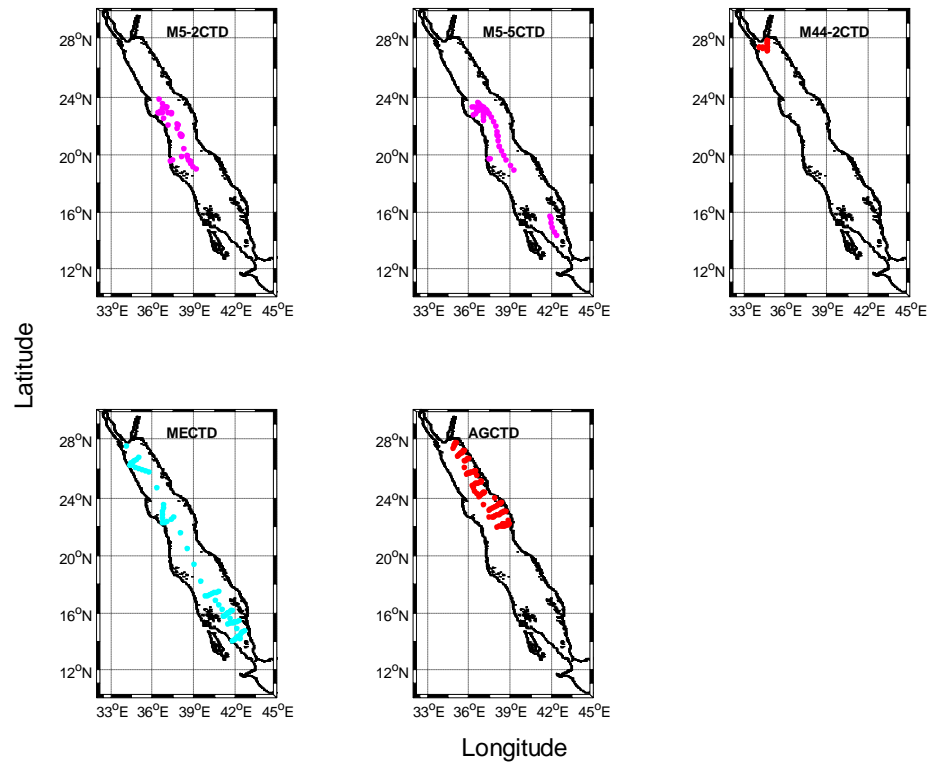


Figure 2-2: Distribution of the hydrographic data for the Red Sea (the codes are explained in Table 2-3)

| Code  | Data Sources                        | No. of Stations |
|---|-------------------------------------|-----------------|
| <b>i. Datasets</b>                            |                                     |                 |
| <b>1. NODC</b>                                |                                     |                 |
| <b>N1CTD</b>                                  | • NODC-CTD                          | 82              |
| <b>N1PFL</b>                                  | • NODC-PFL                          | 188             |
| <b>N1OSD</b>                                  | • NODC-OSD                          | 1188            |
| <b>2. BODC</b>                                |                                     |                 |
| <b>BODC</b>                                   | • Argo float (14/4/2010-15/3/2011)  | 68              |
| <b>3. Scripps Institution of Oceanography</b> |                                     |                 |
| <b>GCTD</b>                                   | • GIDON-CTD                         | 3               |
| <b>GBOT</b>                                   | • GIDON-BOT                         | 367             |
| <b>N2CTD</b>                                  | • NODC-CTD                          | 3               |
| <b>N2OSD</b>                                  | • NODC-OSD                          | 337             |
| <b>ACTD</b>                                   | • AODC-CTD                          | 3               |
| <b>ABOT</b>                                   | • AODC-BOT                          | 367             |
| <b>MCTD</b>                                   | • MAILLARD-CTD                      | 21              |
| <b>MBOT</b>                                   | • MAILLARD-BOT                      | 54              |
| <b>QMCTD</b>                                  | • QUADFASEL-Meteor cruise           | 100             |
| <b>QSCTD</b>                                  | • QUADFASEL-Sagar Kanya cruise      | 31              |
| <b>ii. Principal investigator</b>             |                                     |                 |
| <b>MDCTD</b>                                  | • R/V Marion Dufresne (3-8/10/1982) | 21              |
| <b>SKCTD</b>                                  | • R/V Sagar Kanya (21-30/5/1983)    | 31              |
| <b>M5-2CTD</b>                                | • R/V Meteor (5/2)- (2-27/2/1987)   | 57              |
| <b>M5-5CTD</b>                                | • R/V Meteor (5/5)- (15/7-5/8/1987) | 44              |
| <b>MECTD</b>                                  | • R/V Maurice Ewing (9-18/8/2001)   | 67              |
| <b>M44-2CTD</b>                               | • R/V Meteor (M44_2)- (1999)        | 19              |
| <b>AGCTD</b>                                  | • R/V Aegaeo- CTD (19-29/3-2010)    | 110             |
| <b>AGBOT</b>                                  | • R/V Aegaeo- BOT(19-29/3-2010)     | 110             |
| <b>Total</b>                                  |                                     | 3271            |

Table 2-3: Available data for the Red Sea region from different sources with their codes

## 2.3 Quality control

Dealing with historical data dating back to the end of the nineteenth century means that some vital checks need to be made before the scientific analysis can proceed as historical bottle data provides low vertical resolution results. To ensure high standards of the profile data, quality control (QC) is an important requirement and is necessary to increase our understanding of the ocean environment. In this section the quality analysis procedure for the hydrographic data for the Red Sea needs to follow steps similar to those described by Boyer and Levitus (1994). They established standard QC for oceanographic data (temperature and salinity profiles) at the NODC Ocean Climate Laboratory for their climatological atlases.

### 2.3.1 Preliminary QC

The essential steps for any QC procedure at the observed level of the data are the following.

#### 2.3.1.1 Position check

The first step in the QC is to check the station positions for the Red Sea region. For example, a few profiles have been found with wrong positions located on land in the dataset, as we can see in Figure 2-3. Clearly, these errors have occurred due to wrong entries for the station locations. After this step 82 profiles were removed from GBOT and 7 profiles from the N1OSD data. As can be seen clearly in Figure 2-3, position errors were found in the NODC-OSD and Gidon-BOT data (see Table 2-5).

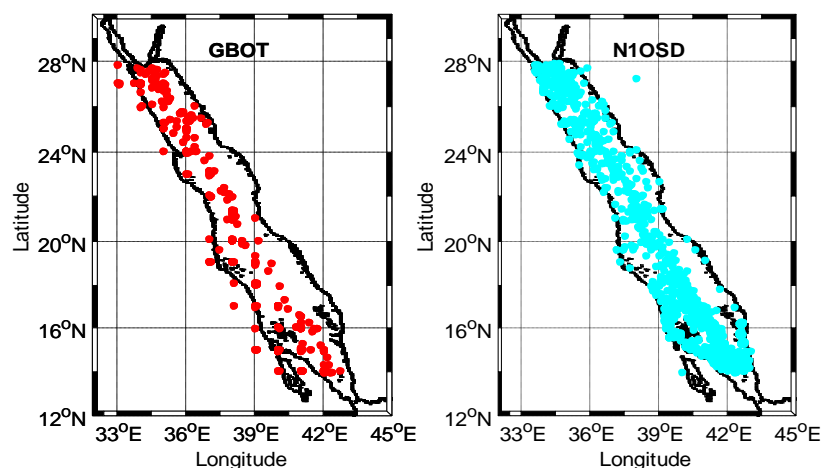


Figure 2-3: Position errors in the hydrographic data from GBOT and N1OSD

#### 2.3.1.2 Duplicate profile check

Since we retrieved the data from multiple sources; it is possible to have the same profiles in more than one dataset. A duplicate profile is a profile containing identical information to another profile, in the same position, and with the same dates as well the data value. Each profile was checked against the other profiles from different data sources. It has been found that the CTD and bottle data from a third source in the data centre (Scripps Institution of Oceanography) in the categories GCTD, N2CTD, ACTD,

GBOT, N2OSD and ABOT have identical information as the first source of N1CTD and N1OSD except for 21 profiles from ABOT. Also, the CTD data in the Maillard and Quadfasel categories are the same as data from R/V Marion Dufresne (3-8/10/1982), Sagar Kanya (21-30/5/1983), R/V Meteor (5/2) - (2-27/2/1987) and R/V Meteor (5/5) - (15/7-5/8/1987). Removing duplicate profiles meant discarding 1192 out of 3271 profiles (see Table 2-5).

#### *2.3.1.3 Depth inversion and depth duplication checks*

Depth inversion occurs in a profile when an observation has a shallower depth than the observation directly preceding it. Duplicate depths occur when a reading has the same depth as the reading before it. In either case, the second observation was eliminated from the data. Each individual profile was checked for depth inversion and duplicate depth. Depth inversions and duplications were found in a few profiles.

#### *2.3.2 Assessing data quality (accuracy)*

As mentioned in Chapter 1, there is a large variability in the thermohaline properties in the upper layers (0-300 m depth) of the Red Sea. Fresh water enters from the Gulf of Aden (as a surface layer in winter and as an intermediate layer in summer) into the Red Sea through the Strait of Bab el Mandeb and mixes with ambient Red Sea water. It can be seen clearly from the  $\theta$ -S diagram (Figure 2-4) that the salinity in intermediate layers increases from the south (lower left) to the north (upper right) of the Red Sea.

Before we applied this QC step to the data, shallower profiles of less than 300 m in depth were discarded due to their high variability and to irregular distribution of the data along the Red Sea. Since we are focusing on the thermohaline properties of the Red Sea deep water ( $\geq 300$  m depth), deep water properties below 300 m have fairly constant temperature and salinity characteristics along the Red Sea basin. The criterion for the range was modified by searching the literature for the Red Sea region; also, this range was chosen from the CTD high-resolution data (1977-2011), excluding the hot pools and the Suez and Aqaba Gulf regions from these processes due to different thermohaline properties. The ranges of the Red Sea deep water properties are 21.5°C for potential temperature and 40.5 psu for salinity data with  $\pm 3$  standard deviations from the mean. Any significant departure from the mean is considered suspicious data.

After that the range was further modified by testing the hydrographic data of the deep water.

Figure 2-5 shows the statistical reference mean and the standard deviation has been applied to the data for potential temperature ( $21.517 \pm 0.089^{\circ}\text{C}$ ), salinity ( $40.553 \pm 0.034$ ) and  $\sigma_{\theta}$  ( $28.582 \pm 0.026$ ) from high-resolution CTD data. The range with the  $\pm 3$  standard deviation checks was calculated for the mean data of the deep water properties below 300 m to the maximum depth for each profile, establishing how many profiles fell outside this range; in these cases the whole profile was discarded from our data. Using the deep water gives a true measure of the errors for the profiles and once this has been done and profiles have been eliminated we can look at 0-2000 m. (i.e. 0-300 m and 300- 2000 m).

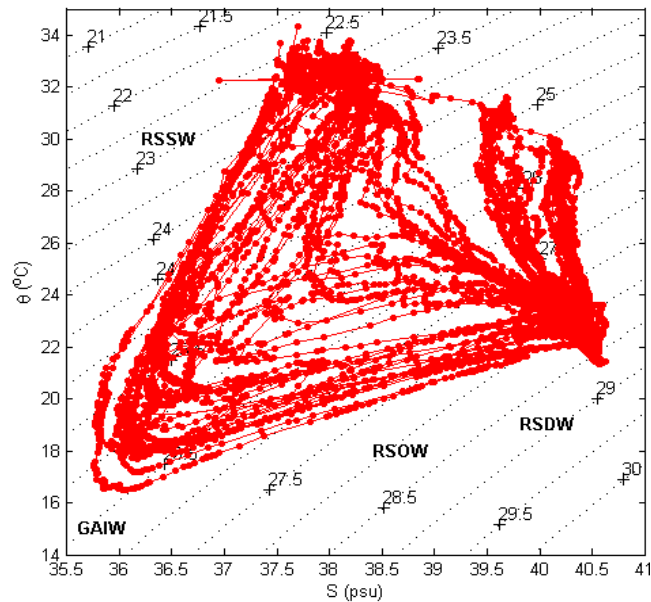


Figure 2-4:  $\theta$ -S diagram for CTD data from the R/V *Maurice Ewing* cruise on August 2001.

Main water masses, Red Sea Surface Water (RSSW), Gulf of Aden Intermediate Water (GAIW), Red Sea Outflow Water (RSOW) and Red Sea Deep Water (RDSW)

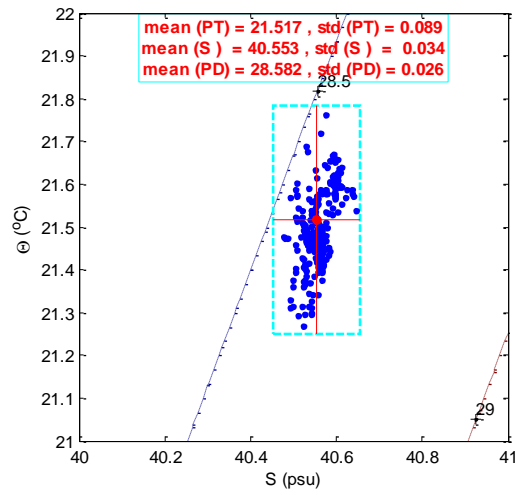


Figure 2-5:  $\theta$ -S diagram for all CTD data. The blue dot represents the mean value of each profile below depth 300 m; a solid red line indicates  $\pm 3$  standard deviations from the mean (red dot) of all profiles. The box indicates the statistical mean and standard deviation for potential temperature (PT), salinity (S) and  $\sigma_{\theta}$  (PD)

An example of suspicious data that were removed from the raw data is shown in Figure 2-6. The removed data were found in groups measured during particular cruises. They are inconsistent with the main data such as the hydrographic profiles from Russian cruises on September 1959 on board R/V A.I. Voeykov and R/V A.A. Nesmeyanov and have a large bias, especially for the salinity data.

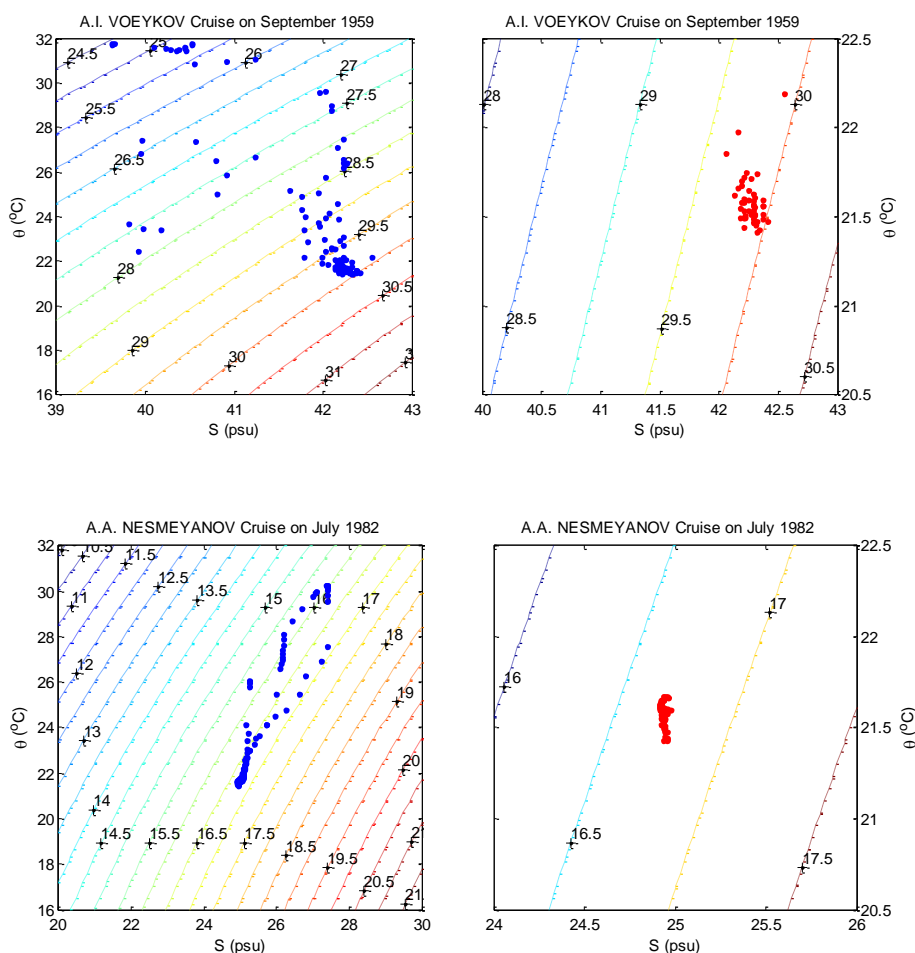


Figure 2-6: Examples of suspicious bottle data from the R/V A.I. Voeykov cruise on September 1959 (upper panel) and the R/V A.A. Nesmeyanov cruise on July 1982 (lower panel) to be removed from our data. The whole profile data (right panel) and data below 300 m depth (left panel)

This step of the QC was applied to each single profile ( $\theta$  and salinity) from different datasets with statistical checks to remove the suspicious data, as described previously. The  $\theta$ -S diagrams in Figure 2-7 show the whole profiles and the mean of each profile below 300 m for all bottle data from the NODC dataset (1889-1993) after the statistical range check step, with a statistical mean of  $21.597 \pm 0.093^\circ\text{C}$ ,  $40.566 \pm 0.046$  (psu) and  $28.570 \pm 0.043$  for potential temperature ( $\theta$ ), salinity and  $\sigma_\theta$

respectively. After this step of the QC about 355 out of 550 profiles were accepted, while 195 profiles were discarded from the NODC bottle data.

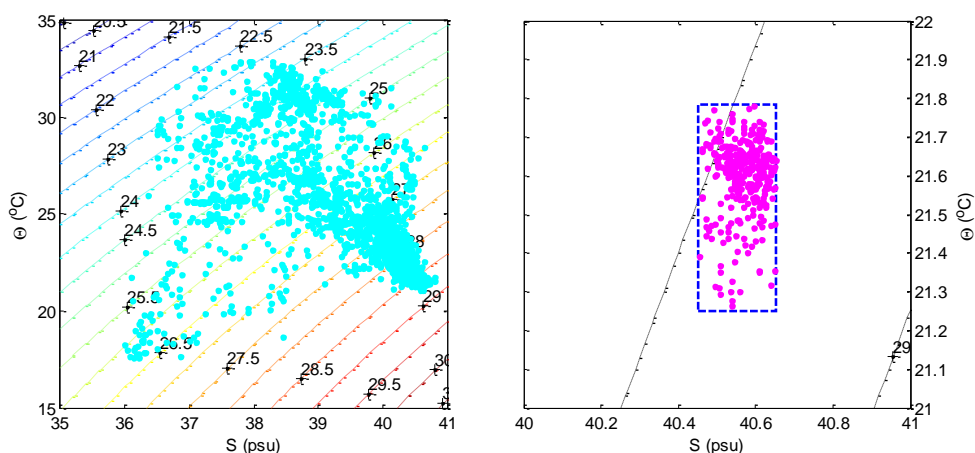


Figure 2-7:  $\theta$ -S diagrams for NIOSD data for the whole profiles (left panel) and deep layer (right panel) after the statistical range check step. The box represents the reference mean with 3 standard deviations from CTD data

The bottle data from the third source in the category of Maillard-BOT data (1904-1921) have 50 profiles with good data if we compare them with CTD data; no profiles were discarded for the statistical range check step. Figure 2-8 illustrates the  $\theta$ -S diagrams for whole profiles and the mean of each profile's data below 300 m from MBOT with a statistical mean of  $21.604 \pm 0.0336$ ,  $40.547 \pm 0.017$  and  $28.553 \pm 0.019$  for the potential temperature, salinity and  $\sigma_\theta$  respectively. In addition, Figure 2-9 shows the  $\theta$ -S diagrams for data from the ABOT source; there are 21 profiles and no discarded data from this source. The statistical value of the mean for potential temperature is  $21.609 \pm 0.042$  °C,  $40.582 \pm 0.014$  (psu) for salinity and  $28.578 \pm 0.018$  for  $\sigma_\theta$ .

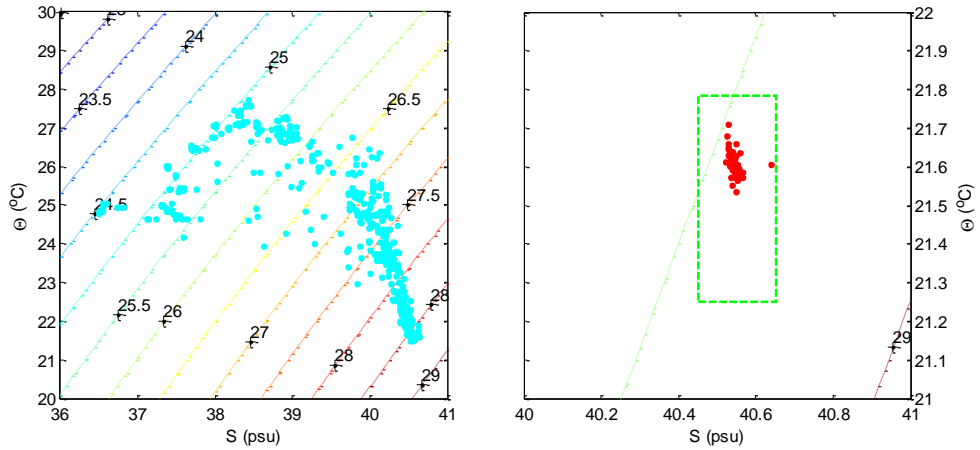


Figure 2-8: As in Figure 2-7 but for MBOT

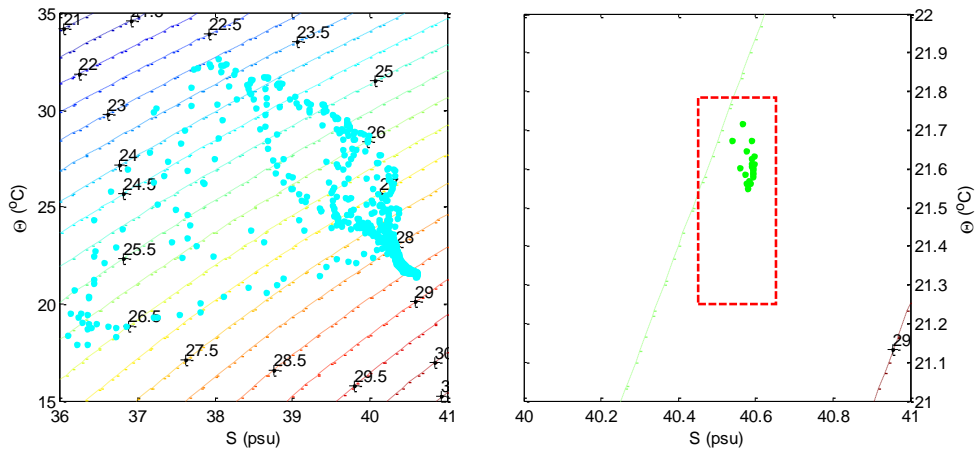


Figure 2-9: As in Figure 2-7 but for ABOT

In this section, the range check was applied to Argo float no. 69008 and no. 69007 from the first dataset source, in the category NODC-PFL (N1PFL). It was found that there is an error in the salinity values from Argo float no. 69008 (2001-2002) for the mean data below 300 m, which can be clearly seen from Figure 2-10. The mean salinity of each profile below 300 m increases with the increasing number of profiles, which can be explained by the biological fouling effect on the conductivity sensor cell (Wong et al., 2003). After the statistical range check was applied, 74 out of 116 profiles were discarded from Argo float no. 69008. However, the data from same Argo float no. 69008 for the years 2000 and 2001 (18 and 20 profiles for T and S respectively) are of good quality when compared with CTD data. The same is true of Argo float no. 69007 for the years 2000 and 2001 (15 and 1 profiles for T and S respectively).

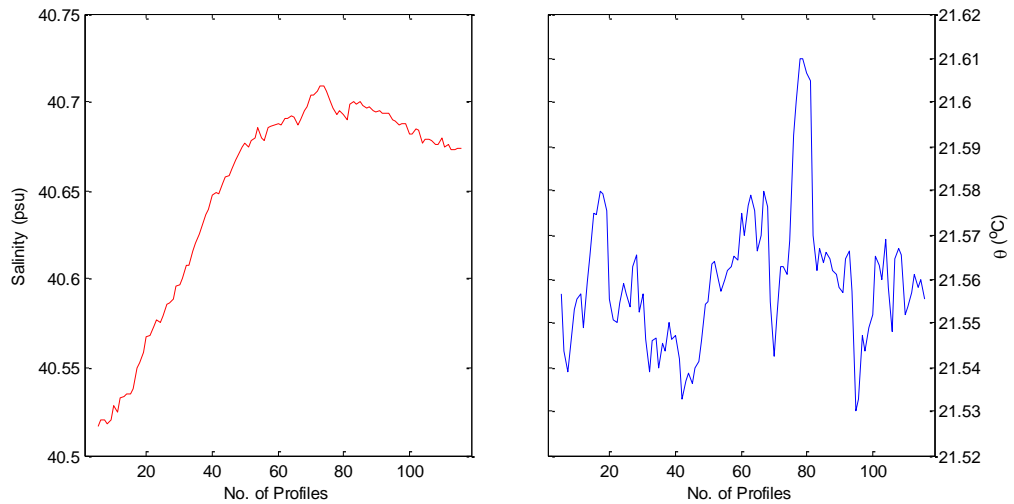


Figure 2-10: Mean salinity and potential temperature below 300 m from Argo float 69008

## 2.4 Comparison to World Ocean Atlas 2009 Database

In this section, a comparison with the mean temperature and salinity below 300 m calculated from the World Ocean Atlas 2009 (WOA09 with a grid resolution of  $0.25^\circ \times 0.25^\circ$ ) climatology is made to evaluate our criteria for choosing the reference for the Red Sea thermohaline properties below 300 m from the high-resolution CTD data. It is also an alternative method to assess the representativeness of the reference selection criteria as the climatology is supposed to represent the long-term mean properties of the ocean. It was found that the reference from the climatology annual mean is similar to the one calculated from CTD with only small differences for the potential temperature ( $21.599 \pm 0.056^\circ\text{C}$ ), salinity ( $40.563 \pm 0.056$ ) and  $\sigma_\theta$  ( $28.567 \pm 0.04$ ). The most reliable explanation for these differences is the climatology data's use of different instruments (CTD, bottle, XBT, and MBT) and the interpolation method as well. Figure 2-11 and Figure 2-12 show the thermohaline properties in the Red Sea region (northern, central and southern regions) from climatology WOA09 for the annual mean and the means of the winter, spring, summer and autumn seasons. There are large spatial and temporal variations for the thermohaline properties in the upper layers ( $< 300$  m depth) compared with the thermohaline properties in the deep water ( $\geq 300$  m depth), except for the summer season (July-September), particularly in terms of the salinity. It is found that the standard deviation of the salinity in the summer season of WOA09 is high with a value of 0.177; this is most likely caused by errors in the measurements from some particular cruises rather than changes in thermohaline properties of the water as was shown in the previous example. However, large errors occur only in the salinity values

for the Red Sea deep water if we compare these with standard deviations for other seasons. Table 2-4 illustrates some of the statistical values of the thermohaline properties for the climatology annual mean and the means of the winter, spring, and summer and autumn seasons.

|               | PT     | STD   | S      | STD   | $\sigma_\theta$ | STD   |
|---------------|--------|-------|--------|-------|-----------------|-------|
| <b>Annual</b> | 21.599 | 0.056 | 40.563 | 0.056 | 28.567          | 0.045 |
| <b>Winter</b> | 21.615 | 0.055 | 40.558 | 0.027 | 28.558          | 0.029 |
| <b>Spring</b> | 21.617 | 0.067 | 40.59  | 0.035 | 28.582          | 0.034 |
| <b>Summer</b> | 21.582 | 0.056 | 40.534 | 0.177 | 28.549          | 0.14  |
| <b>Fall</b>   | 21.580 | 0.064 | 40.569 | 0.024 | 28.577          | 0.03  |

Table 2-4: Statistical values of the thermohaline properties of the Red Sea deep water ( $\geq 300$  m) with their standard deviations for potential temperature (PT), salinity (S) and  $\sigma_\theta$  from climatology data of WOA09

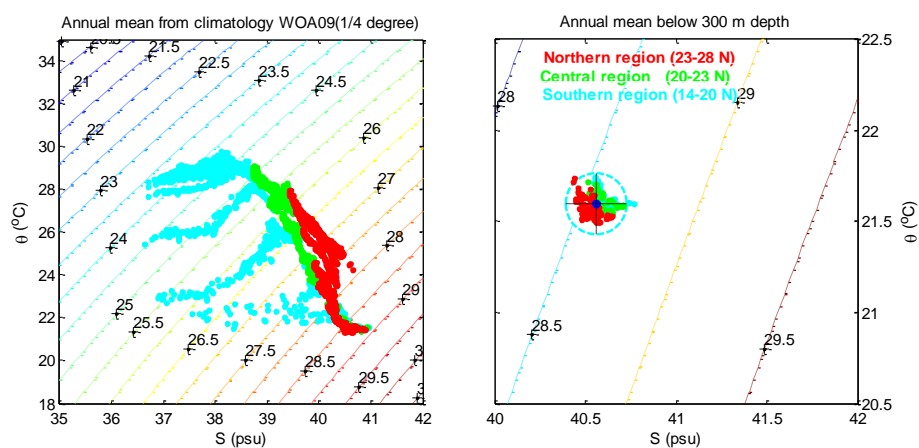


Figure 2-11:  $\theta$ -S diagram for the climatology annual mean of WOD09 for upper layers in the left panel and deep layers in the right panel for three regions of the Red Sea (northern (red), central (green) and southern (cyan)). The circle represents the mean with its three standard deviations from the annual mean of WOD09. The data grid resolution is  $0.25^\circ \times 0.25^\circ$

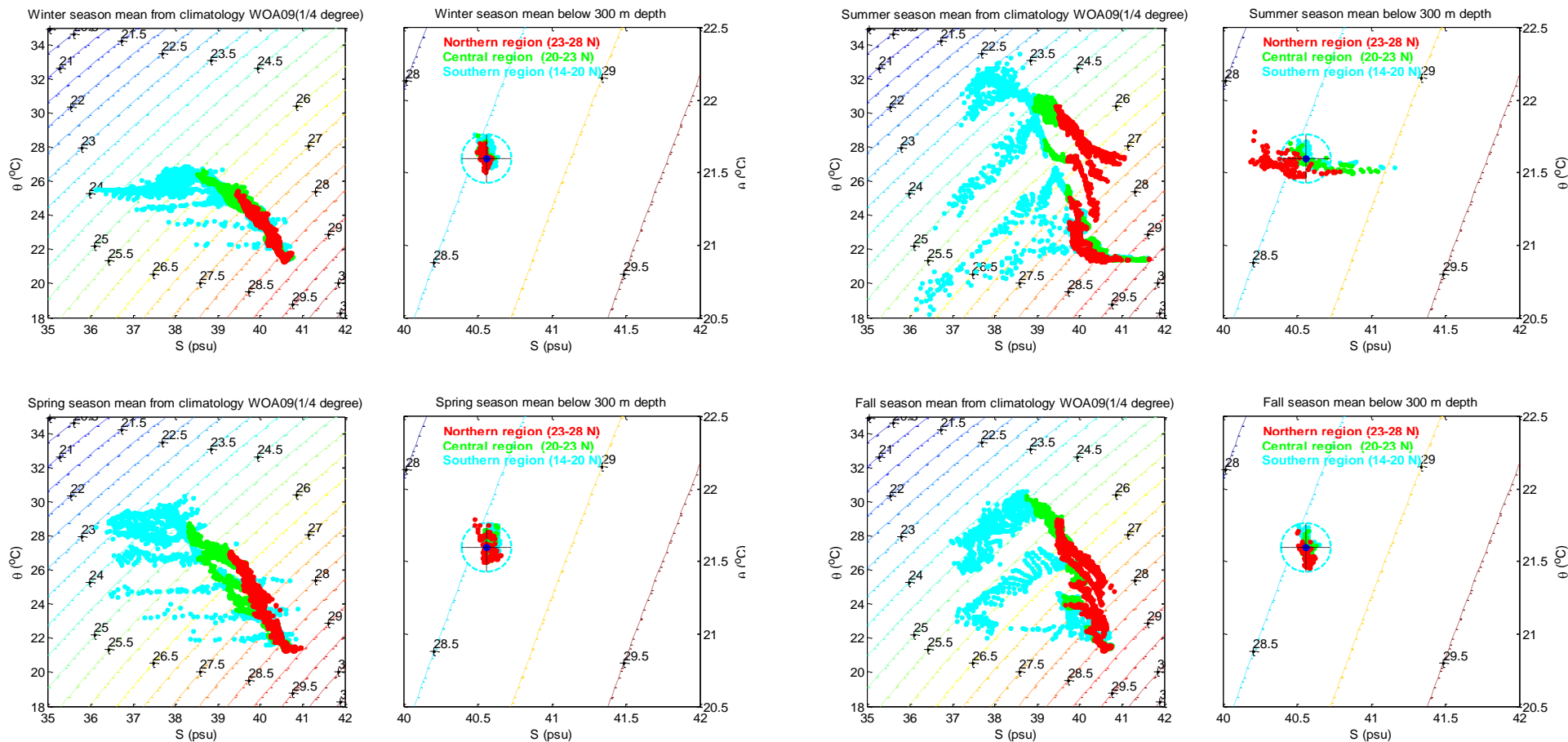


Figure 2-12:  $\theta$ -S diagram for the climatology annual mean and the means of the winter, summer, spring and autumn seasons of WOD09 for upper layers in the left panel and deep layers in the right panel for three regions of the Red Sea (northern (red), central (green) and southern (cyan)). The circle represents the mean with its three standard deviations from the annual mean of WOD09. The data grid resolution is  $0.25^\circ \times 0.25^\circ$

| Code  | Data sources                        | No. of stations | Bad position | Duplicate stations | St.< 300 m | Range check | Accepted stations |
|---|-------------------------------------|-----------------|--------------|--------------------|------------|-------------|-------------------|
| <b>i. Datasets</b>                            |                                     |                 |              |                    |            |             |                   |
| <b>1. NODC</b>                                |                                     |                 |              |                    |            |             |                   |
| N1CTD   | • NODC-CTD                          | 82              | -            | -                  | 7          | -           | 75                |
| N1PFL   | • NODC-PFL                          | 188             | -            | -                  | 60         | 74          | 54                |
| N1OSD   | • NODC-OSD                          | 1188            | 7            | -                  | 631        | 195         | 355               |
| <b>2. BODC</b>                                |                                     |                 |              |                    |            |             |                   |
| BODC  | • Argo float (14/4/2010-15/3/2011)  | 68              | -            | -                  | -          | -           | 68                |
| <b>3. Scripps Institution of Oceanography</b> |                                     |                 |              |                    |            |             |                   |
| GCTD  | • GIDON-CTD                         | 3               | -            | 3                  | -          | -           | -                 |
| GBOT  | • GIDON-BOT                         | 367             | 40           | 327                | -          | -           | -                 |
| N2CTD   | • NODC-CTD                          | 3               | -            | 3                  | -          | -           | -                 |
| N2OSD   | • NODC-OSD                          | 337             | -            | 337                | -          | -           | -                 |
| ACTD  | • AODC-CTD                          | 3               | -            | 3                  | -          | -           | -                 |
| ABOT  | • AODC-BOT                          | 367             | -            | 346                | -          | -           | 21                |
| MCTD  | • MAILLARD-CTD                      | 21              | -            | 21                 | -          | -           | -                 |
| MBOT  | • MAILLARD-BOT                      | 54              | -            | -                  | 4          | -           | 50                |
| QMCTD   | • QUADFASEL-Meteor cruise           | 100             | -            | 100                | -          | -           | -                 |
| QSCTD   | • QUADFASEL-Sagar Kanya cruise      | 31              | -            | -                  | 2          | -           | 29                |
| <b>ii. Principal investigator</b>             |                                     |                 |              |                    |            |             |                   |
| MDCTD   | • R/V Marion Dufresne (3-8/10/1982) | 21              | -            | 21                 | -          | -           | -                 |
| SKCTD   | • R/V Sagar Kanya (21-30/5/1983)    | 31              | -            | 31                 | -          | -           | -                 |
| M5-2CTD                                       | • R/V Meteor (5/2)- (2-27/2/1987)   | 57              | -            | -                  | 10         | -           | 47                |
| M5-5CTD                                       | • R/V Meteor (5/5)- (15/7-5/8/1987) | 44              | -            | -                  | 3          | -           | 41                |
| MECTD   | • R/V Maurice Ewing (9-18/8/2001)   | 67              | -            | -                  | 17         | -           | 50                |
| M44-2CTD                                      | • R/V Meteor (M44_2)- (1999)        | 19              | -            | -                  | 3          | -           | 16                |
| AGCTD   | • R/V Aegaeo- CTD (19-29/3-2010)    | 110             | -            | -                  | 9          | -           | 101               |
| AGBOT   | • R/V Aegaeo- BOT(19-29/3-2010)     | 110             | -            | -                  | 9          | -           | 101               |
| <b>Total</b>                                  |                                     | <b>3271</b>     | <b>47</b>    | <b>1192</b>        | <b>755</b> | <b>269</b>  | <b>1008</b>       |

Table 2-5: Number of profiles discarded and accepted from the hydrographic data of the Red Sea from different sources

## 2.5 Surface heat flux data

The net heat flux on the sea surface is the sum of all its constituents: the radiative components (net shortwave radiation (solar) and net longwave radiation) and the turbulent components (sensible heat and the evaporative transfer of latent heat fluxes):

$$Q_{SW} - Q_{LW} - Q_E - Q_H = Q_N \quad (2.1)$$

where  $Q_N$  is the net heat flux (positive for heat gained by the ocean).  $Q_{SW}$  is the net shortwave radiation  $Q_{LW}$  is longwave radiation,  $Q_H$  is the sensible heat flux and  $Q_E$  is the latent heat flux. Direct measurement of the turbulent heat flux is possible by measuring the turbulent quantities using in situ gust probes on aircraft (low flying) or offshore platforms. But due to the expensive nature of gust-probe measurement and the limitation of its dataset to a few locations, it is only used to calibrate other methods of the heat flux calculation. As result, the most widely applied alternative method to estimate the heat flux is known as the “Bulk Formula Method”. It uses oceanographic and atmospheric variables such as SST, sea level pressure, air temperature near the surface, wind speed, relative humidity, wind speed and cloud cover. These variables are obtained from different sources such as the Voluntary Observing Ship (VOS) programme, moored and drifting buoys, remote sensing and numerical weather prediction model outputs.

The radiative components have been determined over several years by using a wide range of bulk formulae (e.g. (Clark et al., 1974; Bignami et al., 1995; Josey et al., 2003)). The shortwave  $Q_{SW}$  flux requires knowledge of some atmospheric parameters such as cloud cover with sea surface albedo and the local noon solar evaluation. It can be calculated from the following formula (Reed, 1977):

$$Q_{SW} = (1 - \alpha)Q_c(1 - 0.62n + 0.0019\theta_n) \quad (2.2)$$

where  $\alpha$  is the albedo of the sea surface,  $Q_c$  is clear sky solar radiation,  $n$  is the daily mean fractional cloud cover and  $\theta_n$  is local noon solar elevation.

The longwave  $Q_{LW}$  is the difference between upward radiation emitted by the ocean and downward atmospheric radiation reaching the surface; this difference depends on the SST, air temperature and humidity. It can be calculated from several formulae such as the formula of Clark et al. (1974):

$$Q_{LW} = \epsilon\sigma_{SB}T_{sea}^4(0.39 - 0.05e^{1/2})(1 - \lambda n^2) + 4\epsilon\sigma_{SB}T_{sea}^3(T_{sea} - T_{air}) \quad (2.3)$$

where  $\varepsilon$  is the emissivity of the sea surface ( $\varepsilon=0.985$ ),  $\sigma_{SB}$  is the Stefan-Boltzmann constant ( $5.67 \times 10^{-8} \text{ W m}^{-2} \text{ K}^{-4}$ ),  $e$  is the water vapour pressure and  $\lambda$  is the latitude-dependent cloud cover.

The sensible heat ( $Q_H$ ) and latent heat flux ( $Q_E$ ) are generally determined using the following bulk formula (Smith, 1980, 1988):

$$Q_H = \rho C_p C_h u (T_{sea} - T_{air}) \quad (2.4)$$

$$Q_E = \rho L C_e u (q_{sea} - q_{air}) \quad (2.5)$$

where  $\rho$  is the density of the air;  $C_p$ , the specific heat capacity of air at constant pressure;  $C_h$  and  $C_e$  are turbulent exchange coefficients for the sensible and latent heat respectively;  $u$ , the wind speed at 10 m above sea level;  $T_{sea}$ , the SST;  $T_{air}$ , the surface air temperature at 10 m;  $q_{sea}$ , the 98% of the saturation specific humidity at the SST;  $q_{air}$ , the atmospheric specific humidity at 10 m; and  $L$  is the latent heat vaporisation of water. Many researchers have focused on accurately determining values for the exchange coefficient and their variation with the wind speed, height and atmospheric stability by direct flux measurement, particularly through the eddy correlation method. The bulk algorithm for calculation of  $Q_H$  and  $Q_E$  was developed by the Coupled Ocean-Atmosphere Response Experiment (COARE) community from the model of Liu, Katsaros and Businger (Liu et al., 1979) under light wind ( $0-12 \text{ ms}^{-1}$ ) and strongly convective conditions over tropical oceans (Fairall et al., 1996). Since 1996 the COARE algorithm has been published and become one of the most widely used algorithms in the air-sea interaction community. The accuracy of the COARE 3.0 is shown to be within 5% for wind speeds of  $0-10 \text{ ms}^{-1}$  and 10% for wind speeds of between  $10$  and  $20 \text{ ms}^{-1}$ .

Estimates of the zonal ( $\tau_x$ ) and meridional ( $\tau_y$ ) components of the sea surface wind stress are obtained from the following equations:

$$\tau_x = \rho C_D u_x (u_x^2 + u_y^2)^{1/2} \quad (2.6)$$

$$\tau_y = \rho C_D u_y (u_x^2 + u_y^2)^{1/2} \quad (2.7)$$

where  $u_x$  and  $u_y$  are the zonal and meridional 10 m wind speed respectively, and  $C_D$  is the drag coefficient, which depends upon the height of the wind measurement and wave characteristics (wave slope, height and age) (Smith, 1980; Taylor & Yelland, 2001).

### *2.5.1 National Oceanography Centre, Southampton flux dataset*

The atmospheric fields from the National Oceanography Centre, Southampton (NOCS) flux dataset were used to quantify the net heat flux over the Red Sea region. This dataset has been chosen for long time series covering the study region with a resolution spatial grid of  $1^\circ \times 1^\circ$ , which is considered in this study for the surface heat components and net heat flux because it matches the period of high quality data from CTD instrument. Other dataset products such as European Centre for Medium-Range Weather Forecasts ERA40 reanalysis, National Center for Environmental Prediction (NCEP) datasets and Florida State University Fluxes have not been employed for this thesis due to for example the  $2.5^\circ$  resolution being very coarse for a narrow sea such as the Red Sea and it cannot accurately represent the sea only.

The NOCS flux dataset v2.0 by Berry and Kent (2009) is an updated form the formerly NOCS flux dataset v1.1 which refers to the SOC flux climatology (Josey et al., 1999) expanding the period covered and using different methods to grid the data and calculating the heat flux including an uncertainty estimate. The NOCS v2.0 is based on meteorological data from the international Comprehensive Ocean-Atmosphere Data Set (COADS). (Woodruff et al., 1998; Worley et al., 2005) which comprises the data from VOS and moored and drifting buoys. The NOCS flux dataset v2.0 is available for monthly fields for meteorological variables (wind speed, SST, surface air temperature, surface humidity, surface pressure and cloud cover) and surface flux (sensible heat flux, latent heat flux, shortwave radiation and longwave radiation) with their associated uncertainty estimates. The climatological annual mean of each heat flux component averaged for 34 years from NOCS v2.0 data over the Red Sea region (box  $14\text{-}28^\circ\text{N}$ ,  $32\text{-}43.5^\circ\text{E}$ ) is shown in Figure 2-13 where the sign convection is positive for heat gained by sea. The climatology data are currently available for monthly mean resolution fields covering the period from 1973 to 2006 on a  $1^\circ \times 1^\circ$  spatial grid for the NOCS dataset v2.0.

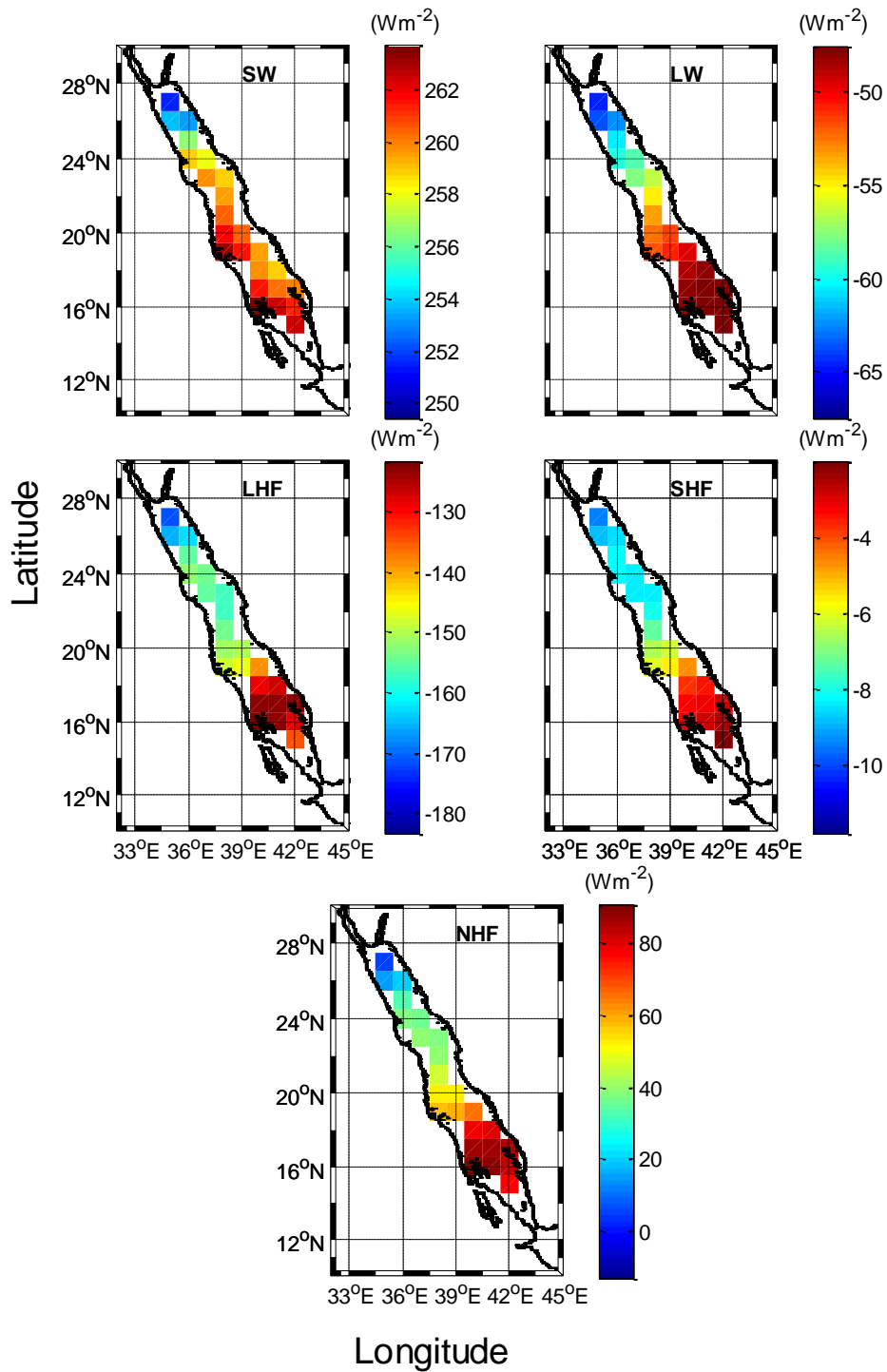


Figure 2-13: Annual NOCS v2.0 climatological mean fields of the different surface heat flux components (shortwave (SW), longwave (LW), latent heat flux (LHF), sensible heat flux (SHF) and net heat flux (NHF)) over the period 1973 to 2006. Positive values indicate heat gained by the sea

The NHF can be calculated from Equation 2.1 over the Red Sea; Figure 2-14 shows the time series of the monthly net heat flux anomaly (seasonal cycle removed) from NOCS v2.0 averaged over the Red Sea (box 14-28°N, 32- 43.5°E). The evaporation can be determined from latent heat  $Q_E$  form the following equation:

$$E = \frac{Q_E}{\rho_w L_e} \quad (2.8)$$

where  $\rho_w$  is density of the sea water,  $L_e$  is the latent heat of vaporisation that can be expressed as  $L_e = (2.501 - 0.00237 \times SST) \times 10^6 \text{ Wm}^{-2}$  and SST is the sea surface temperature. Figure 2-15 shows the time series of the monthly evaporation anomaly (seasonal cycle removed) from NOCS v2.0 averaged over the Red Sea (box 14-28°N, 32-43.5°E). The annual net evaporation rate over the basin from 1973 to 2006 is 1.87 m/year, which fits well with the annual mean evaporation of  $1.75 \pm 0.35 \text{ m y}^{-1}$  provided by Tragou et al. (1999) (see table 1-1).

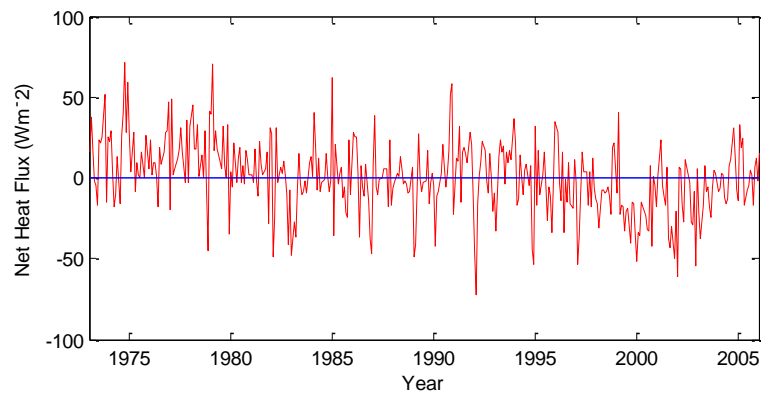


Figure 2-14: Monthly mean of NHF anomalies from NOCS v2.0 over the Red Sea region (for the box 14-28 °N, 32-43.5 °E) from 1973 to 2006

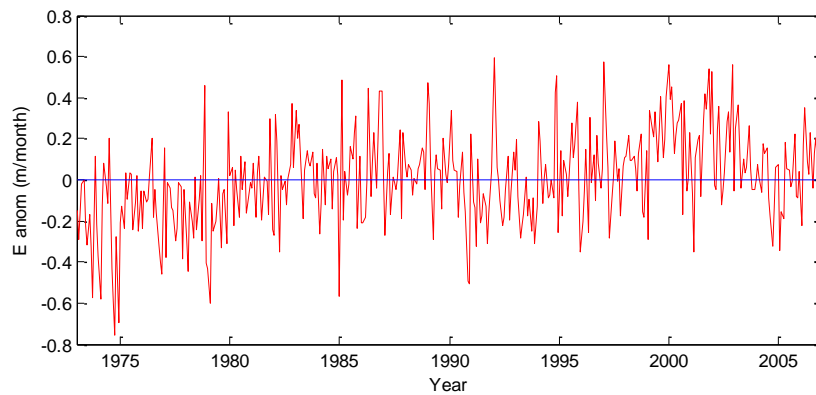


Figure 2-15: Monthly mean of evaporation anomalies from NOCS v2.0 over the Red Sea region (for the box 14-28 °N, 32-43.5 °E) from 1973 to 2006

## 2.5.2 Accuracy of the surface heat flux data

A preliminary comparison was made for the NOCS v2.0 surface heat flux with independent buoy observations from the WHOI mooring by Berry and Kent (2009). They used data gathered over 4 months during the summer of 1991 from the WHOI mooring Marine Light-Mixed Layer experiment in the sub-Arctic North Atlantic Ocean, which had all the components required to estimate the heat budget (radiative and meteorological variables). They compared the daily products with the buoy data to allow close matching with the full deployment period and to account for any gaps in the buoy data. Figure 2-16 shows a comparison of each surface flux component and net heat flux from NOCS v2.0, OAFlux and three analysis products (ERA40, NCEP1 and NCEP2) with WHOI mooring in North Atlantic Ocean (Berry & Kent, 2009). It is found that each component of the NOCS v2.0 surface heat flux is within  $10 \text{ Wm}^{-2}$  and the net heat flux is within  $2 \text{ Wm}^{-2}$  of the buoy values. The uncertainty of the NOCS v2.0 net heat flux estimation is  $4 \text{ Wm}^{-2}$ . However, the net heat flux from the three reanalyses shows biases compared to the buoy values of between  $12$  and  $21 \text{ Wm}^{-2}$ ; the OAFlux has a bias of  $9 \text{ Wm}^{-2}$  from the buoy value. The large bias in OAFlux heat flux compared to the buoy has come from the radiative components (shortwave and longwave), which are satellite-based estimates (Zhang et al., 2004).

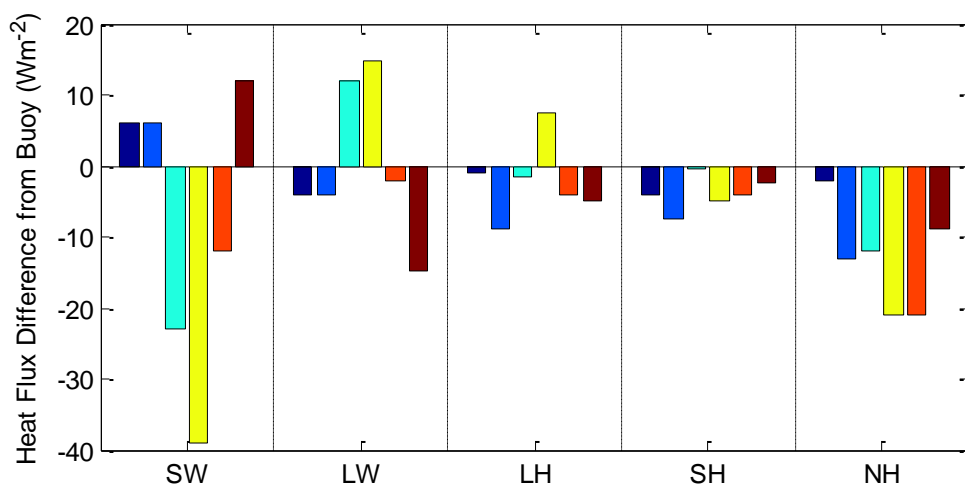


Figure 2-16: Comparison of surface heat flux from the surface mooring Marine Light-Mixed Layer experiment in the sub-Arctic North Atlantic in the summer of 1991. NOCS v2.0 (dark blue), NOCS v2.0 with height adjustment but without bias adjustment (blue), NCEP1 (cyan), NCEP2 (yellow), ERA40 (orange) and OAFlux (brown) (Berry & Kent, 2009)

Moreover, a comparison among NOCS v.2, OAFlux and other products (ERA40, NCEP1 and NCEP2) was made by Berry and Kent (2009) using simple ranking analysis with eleven WHOI moorings. Each of the components of the surface heat flux and net heat flux was ranked against the absolute mean difference from the buoy flux. They found that the NOCS v2.0 surface heat flux was ranked closest to the buoy flux in five out of the eleven WHOI moorings while the other products were ranked closest for either one or two buoy fluxes.

The heat flux components averaged over the Red Sea region from NOCS v2.0 (1973-2006) gives initial calculations:

$$\begin{aligned} Q_{SW} - Q_{LW} - Q_E - Q_H &= Q_N \\ 258 - 54 - 148 - 6 &= 50 \text{ Wm}^{-2} \end{aligned} \quad (2.8)$$

It is clear that there is a significant discrepancy between the net heat gain derived from the NOCS data and expected heat loss of  $7 \text{ Wm}^{-2}$ ,  $8 \pm 2 \text{ Wm}^{-2}$  and  $11 \pm 5 \text{ Wm}^{-2}$  obtained from advective heat flux transported through the Strait of Bab el Mandeb calculated by Patzert (1974b), Tragou et al. (1999) and Sofianos et al. (2002) respectively. The estimates of the longwave flux in the NOCS climatology were obtained using the formula of Clark et al. (1974) which was found to perform well in the mid-latitude North Atlantic (Josey et al., 1997). However, Weller et al. (1998) have shown that the Clark et al. (1974) longwave flux estimates are biased by up to  $20 \text{ Wm}^{-2}$  when evaluating the NOCS data using air-sea interaction data from neighbouring mooring in the Arabian Sea region. The longwave parameterisation developed by Bignami et al. (1995) using data from the western Mediterranean Sea provides a reliable estimate of the longwave flux under clear sky conditions that is similar to Arabian Sea characteristics.

Josey et al. (1997) reveal that the Bignami et al. (1995) formula performed best and most reliably in semi-enclosed seas rather than open ocean conditions, where the other formulae, such as that of Clark et al. (1974), are more appropriate. The basin's annual mean of the longwave flux over the Red Sea obtained from the Bignami et al. (1995) formula is  $-75 \text{ W m}^{-2}$ , which is close to the result using the formula of, considerably stronger than that obtained from using Clark et al. (1974) ( $54 \text{ W m}^{-2}$ ) and as a consequence the basin average is reduced to  $28 \text{ Wm}^{-2}$ . In addition, a further bias in the NOCS climatology estimate referred to the shortwave ( $Q_{SW}$ ) as it was obtained from the Reed (1977) equation, which does not show the effect of the aerosol. This is likely to overestimate the shortwave flux in a region such as the Red Sea, which is

located in a dusty environment due to anthropogenic and mineral aerosol (Tragou et al., 1999).

Tragou et al. (1999) developed an aerosol correction to the Reed (1977) equation by using satellite estimates of the aerosol optical thickness obtained from the advanced very high-resolution radiometer of the National Oceanic and Atmospheric Administration (NOAA) and calibrated them with the differences between high quality ground station measurements and empirical estimates of the shortwave. After applying the Tragou et al. (1999) correction to the NOCS shortwave estimates ( $258 \text{ Wm}^{-2}$ ), a significant adjustment of  $27 \text{ Wm}^{-2}$  was found for the shortwave over the Red Sea, which leads to a reduction of the shortwave flux to  $231 \text{ Wm}^{-2}$ . The mean net heat flux over the basin has reduced to  $2 \text{ Wm}^{-2}$  after combining the correction from the shortwave and longwave. There is a still discrepancy between this value and the value from advective estimates, which is relatively small but still out of the error range.

## 2.6 Conclusion

In this chapter, the quality control process that was applied to our hydrographic data followed similar steps to those described by Boyer and Levitus (1994). They established standard QC for oceanographic data (temperature and salinity profiles) at the NODC Ocean Climate Laboratory for their climatological atlases. The criterion for eliminating profiles from the dataset was  $\pm 3$  standard deviations from the mean reference value of the Red Sea deep water (used as a reference due to high homogeneity), which came from high-resolution CTD data. This reference mean was compared with the WOD09 climatology as an alternative method to assess the representativeness of the reference selection criteria as the climatology is supposed to represent the long-term mean properties of the ocean. The annual mean of the evaporation for the Red Sea ( $1.87 \text{ m y}^{-1}$ ) is similar to the Tragou et al. (1999) estimate of  $1.75 \pm 0.35 \text{ m y}^{-1}$  using Knudsen formulae. The annual mean of heat flux over the Red Sea basin is found to be  $2 \text{ Wm}^{-2}$ .

# **Chapter 3 Decadal changes in the Red Sea Deep Water properties**

## **3.1 Introduction**

The Red Sea is unique among the world's oceans and seas because of the distinctive physical and biochemical processes encountered there. It has remarkable features, such as the highest sea surface salinity in world, and its outflow water through the Strait of Bab el Mendeb is considered one of the most important intermediate water masses (warm and highly saline water) in the Indian Ocean due to its impact on the thermohaline circulation of the Indian Ocean (Plaehn et al., 2002). It has been mapped eastward over 50° E in the northern Indian Ocean to the coast of Sumatra, southward through the Mozambique Channel into the Agulhas Current (Wyrтки, 1971; Shapiro & Meschanov, 1991; Beal et al., 2000) and into the Cape Basin and South Atlantic Ocean (Valentine et al., 1993). However, the formation of the water mass in the northern region of the Red Sea is still obscure and remains a matter of debate and conjecture. Wyrтки (1974) has suggested three different sources for the deep water formation in the Red Sea: the outflows from the Gulf of Suez, the outflows from the Gulf of Aqaba over the sill in the Strait of Tiran and open sea convection in the northern part of the Red Sea south of the Sinai Peninsula.

The main aim of this chapter is to investigate the changes in thermohaline properties of the Red Sea deep water since 1889 to determine whether there is a significant trend toward higher salinity and higher temperature against the background of natural seasonal and interannual variability. It should be noted that no detailed work has addressed the thermohaline variability in the RSDW.

## 3.2 Data and method

The data analysed in this study were obtained from the sources listed in section 2.2; the quality controls applied to them was described in Chapter 2 (section 2.3). This study's area of analysis covers the Red Sea region only (14-27.9°N and 32- 45.5°E): the Suez and Aqaba Gulfs and hot brine regions are excluded from this analysis due to their differing thermohaline properties.

In order to determine the changes in the thermohaline properties of the RSDW for the period between 1889 and 2011, we used a method of analysis similar to that used by Rohling and Bryden (1992) for the Western Mediterranean Deep Water (WMDW). In their study they investigated the thermohaline properties of WMDW at a depth of 2000 m or about 2020 db. Our study investigated the thermohaline properties below 300 m depth using the following method. For each hydrographic profile, the potential temperature and salinity were averaged below 300 m to the maximum depth of that profile. Then the hydrographic profiles were averaged for each cruise and year to obtain one single value. This depth was chosen for RSDW because the distribution of the thermohaline properties (potential temperature and salinity) in the deep layer is almost homogenous at that depth and below as is shown in Figure 3-1. The observation of oxygen distribution in the Red Sea verified the distinction between the intermediate and deep layer water where the oxygen minimum at the intermediate depth (300 m) separates the new intermediate water mass (RSOW) from the older deep water mass (RSDW) (Woelk & Quadfasel, 1996). No vertical interpolation was used in this analysis for long-term trends. The majority of the data comes from the last half of the 20th and first decade of the 21st century, which is most representative of this period as can be seen clearly from Figure 3-2; the density of observations was low at the beginning of the twentieth century. As was mentioned before in section 2.3 our reference mean for the RSDW characteristics came from high-resolution data (CTD) with  $\pm 3$  standard deviations. We will assess whether the analysis method is influenced or not by spatial distribution by dividing the data into several subsets and comparing the results for the whole domain. Regression analysis was used to quantify the changes in the thermohaline properties of the RSDW. Figure 3-2a, b and c show the time series for the hydrographic data in the Red Sea from 1889 to 2011. Most of the historical observations prior to 1980 come from bottle data. Table 3-1 indicates the results of the time series, which are plotted in Figures 3-1 and 3-2.

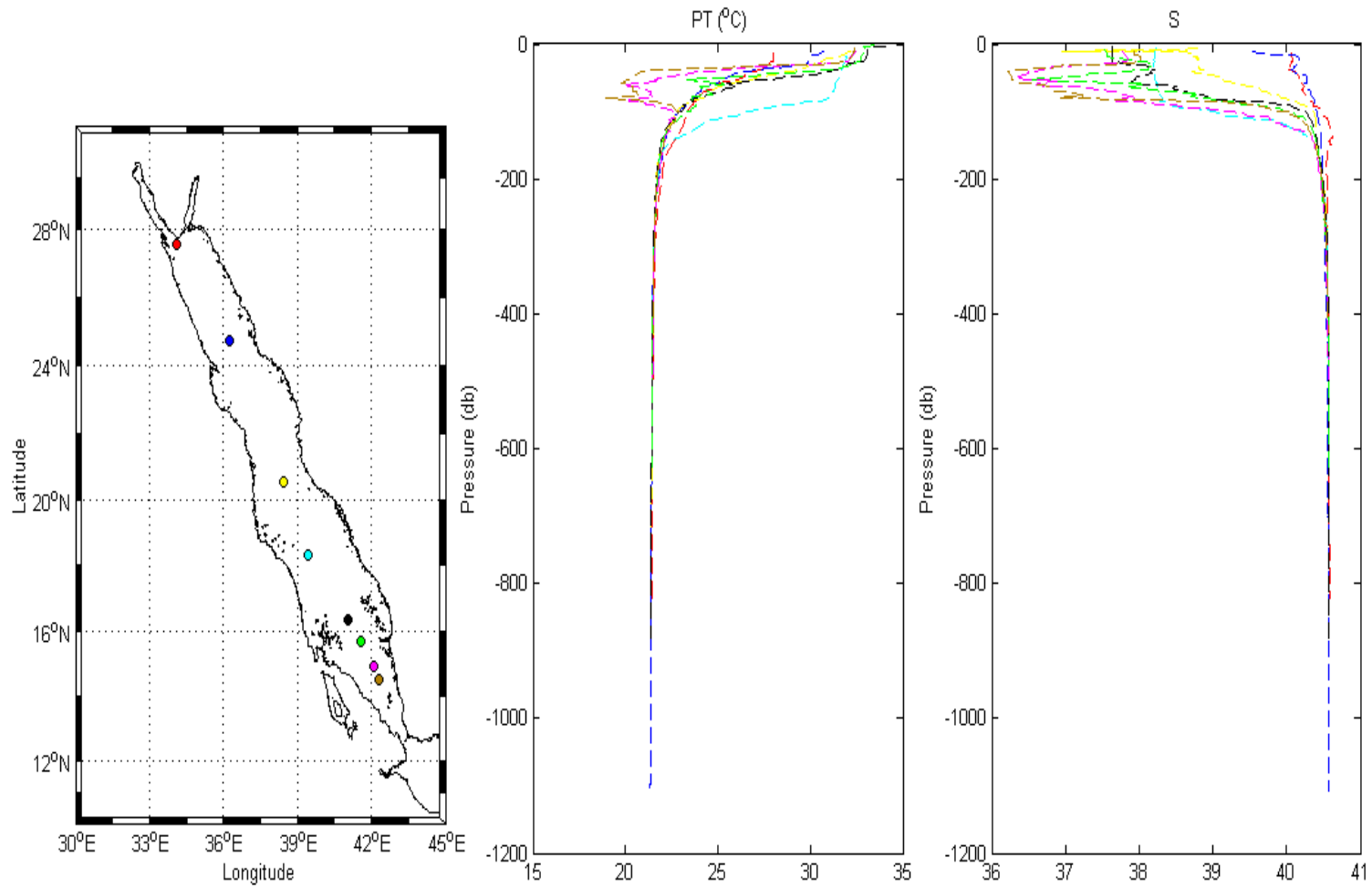


Figure 3-1: Typical profiles along the Red Sea axis for the potential temperature ( $^{\circ}\text{C}$ ) and salinity and their locations based on data from R/V Maurice Ewing during August 2001 (Sofianos & Johns, 2007)

### 3.3 Results

#### 3.3.1 Long-term trends in the variability of the RSDW

The main results of the analysis will be described in this section. As follows from Table 3-1, the results of the RSDW property analysis through the entire dataset (1889-2011) indicate that the potential temperature has decreased by an average of  $2.0 \times 10^{-4} \text{ }^\circ\text{C yr}^{-1}$  and the salinity by  $0.09 \times 10^{-4} \text{ psu yr}^{-1}$ . Also, the potential density of the RSDW appears to have decreased by an average of  $0.0002 \times 10^{-4} \text{ kg m}^{-3} \text{ yr}^{-1}$ . However, these changes in the thermohaline properties of RSDW through the entire dataset are not statistically significant. In Figure 3-2a and b, decreases in the thermohaline properties of the RSDW are not linear but seem to have accelerated since 1950. The dataset was split into two time periods (pre-1950 and post-1950) as shown in Figure 3-3a, b and c to facilitate comparison between the two periods and in accordance with the density of the observations, which showed obvious acceleration in potential temperature and a salinity decrease of RSDW starting in about 1950.

In Figure 3-3a, b and c for the period pre-1950, there is a clear trend showing the potential temperature increasing by an average of  $27 \times 10^{-4} \pm 11 \times 10^{-4} \text{ }^\circ\text{C yr}^{-1}$ . The salinity and potential density of the RSDW appear to decrease for the same period with averages of  $5.7 \times 10^{-4} \pm 3.4 \times 10^{-4} \text{ psu yr}^{-1}$  and  $12 \times 10^{-4} \pm 4.3 \times 10^{-4} \text{ kg m}^{-3} \text{ yr}^{-1}$  respectively. Therefore the pre-1950 data have small changes but indicate statistically significant warming at the 95% confidence level. However, the changes in the salinity (freshening trend) were not statistically significant.

Figure 3-3a, b and c illustrate that the linear regression lines post-1950 have decreased for the potential temperature and salinity of the RSDW by averages of  $35.5 \times 10^{-4} \pm 5.6 \times 10^{-4} \text{ }^\circ\text{C yr}^{-1}$  and  $13.8 \times 10^{-4} \pm 2.8 \times 10^{-4} \text{ psu yr}^{-1}$  respectively. The potential density of RSDW for the same period seems to have decreased by an average of  $0.42 \times 10^{-4} \pm 2.6 \times 10^{-4} \text{ kg m}^{-3}$ . In Figure 3-2a the result suggests that the potential temperature has increased between 1889 and 1950 by as much as  $0.07^\circ\text{C}$  while decreasing between 1950 and 2011 by as much as  $0.12^\circ\text{C}$ . Also, the result in Figure 3-2b suggests that the salinity seems to have decreased between 1889 and 1950 by 0.078 psu, while the decrease between 1950 and 2011 was possibly as much as 0.13 psu.

| <i>Year</i> | $\theta$<br>°C | <i>std</i> | <i>S</i><br>psu | <i>std</i> | $\sigma_\theta$ | <i>std</i> | <i>N</i> | <i>Year</i> | $\theta$<br>°C | <i>std</i> | <i>S</i><br>psu | <i>std</i> | $\sigma_\theta$ | <i>std</i> | <i>N</i> |
|-------------|----------------|------------|-----------------|------------|-----------------|------------|----------|-------------|----------------|------------|-----------------|------------|-----------------|------------|----------|
| 1889        | 21.449         | 0.212      | 40.515          | 0.028      | 28.572          | 0.082      | 2        | 1971        | 21.719         | 0.020      | 40.612          | 0.020      | 28.569          | 0.008      | 3        |
| 1895        | 21.484         | 0.008      | 40.580          | 0.096      | 28.612          | 0.075      | 3        | 1975        | 21.630         | 0.082      | 40.570          | 0.046      | 28.563          | 0.047      | 21       |
| 1896        | 21.355         | 0.103      | 40.554          | 0.042      | 28.629          | 0.019      | 7        | 1976        | 21.653         | 0.008      | 40.582          | 0.012      | 28.566          | 0.006      | 2        |
| 1897        | 21.547         | 0.170      | 40.602          | 0.059      | 28.611          | 0.075      | 10       | 1976        | 21.647         | 0.028      | 40.569          | 0.051      | 28.558          | 0.047      | 2        |
| 1898        | 21.341         | 0.020      | 40.575          | 0.050      | 28.649          | 0.032      | 2        | 1977        | 21.594         | 0.069      | 40.592          | 0.013      | 28.590          | 0.019      | 3        |
| 1904        | 21.619         | 0.041      | 40.541          | 0.016      | 28.544          | 0.024      | 2        | 1977        | 21.619         | 0.000      | 40.518          | 0.000      | 28.526          | 0.000      | 1        |
| 1905        | 21.585         | 0.015      | 40.547          | 0.009      | 28.558          | 0.010      | 6        | 1977        | 21.600         | 0.064      | 40.591          | 0.014      | 28.588          | 0.015      | 3        |
| 1906        | 21.609         | 0.031      | 40.547          | 0.014      | 28.552          | 0.017      | 7        | 1980        | 21.587         | 0.014      | 40.620          | 0.019      | 28.613          | 0.018      | 8        |
| 1915        | 21.615         | 0.064      | 40.547          | 0.012      | 28.550          | 0.027      | 4        | 1981        | 21.637         | 0.036      | 40.611          | 0.008      | 28.592          | 0.014      | 7        |
| 1916        | 21.604         | 0.025      | 40.571          | 0.040      | 28.571          | 0.033      | 5        | 1981        | 21.651         | 0.033      | 40.564          | 0.041      | 28.553          | 0.035      | 66       |
| 1917        | 21.589         | 0.040      | 40.546          | 0.011      | 28.557          | 0.020      | 4        | 1982        | 21.609         | 0.042      | 40.582          | 0.014      | 28.579          | 0.019      | 21       |
| 1918        | 21.609         | 0.045      | 40.542          | 0.010      | 28.548          | 0.020      | 6        | 1982        | 21.596         | 0.048      | 40.587          | 0.015      | 28.586          | 0.022      | 21       |
| 1919        | 21.580         | 0.042      | 40.542          | 0.008      | 28.557          | 0.017      | 5        | 1983        | 21.555         | 0.115      | 40.582          | 0.027      | 28.593          | 0.019      | 29       |
| 1920        | 21.590         | 0.013      | 40.549          | 0.004      | 28.559          | 0.006      | 4        | 1983        | 21.604         | 0.009      | 40.587          | 0.024      | 28.583          | 0.019      | 5        |
| 1921        | 21.605         | 0.031      | 40.539          | 0.007      | 28.546          | 0.012      | 7        | 1984        | 21.415         | 0.033      | 40.469          | 0.021      | 28.547          | 0.007      | 2        |
| 1923        | 21.463         | 0.059      | 40.548          | 0.028      | 28.594          | 0.037      | 3        | 1984        | 21.605         | 0.079      | 40.630          | 0.021      | 28.616          | 0.029      | 5        |
| 1924        | 21.457         | 0.060      | 40.571          | 0.055      | 28.618          | 0.045      | 6        | 1985        | 21.725         | 0.054      | 40.553          | 0.033      | 28.523          | 0.010      | 2        |
| 1929        | 21.475         | 0.016      | 40.573          | 0.031      | 28.610          | 0.028      | 2        | 1986        | 21.431         | 0.000      | 40.598          | 0.000      | 28.641          | 0.000      | 1        |
| 1933        | 21.473         | 0.000      | 40.486          | 0.000      | 28.544          | 0.000      | 1        | 1987        | 21.526         | 0.079      | 40.572          | 0.023      | 28.594          | 0.021      | 47       |
| 1934        | 21.566         | 0.000      | 40.540          | 0.000      | 28.558          | 0.000      | 1        | 1987        | 21.494         | 0.060      | 40.554          | 0.010      | 28.590          | 0.020      | 41       |
| 1948        | 21.653         | 0.000      | 40.565          | 0.000      | 28.553          | 0.000      | 1        | 1988        | 21.553         | 0.032      | 40.506          | 0.006      | 28.536          | 0.011      | 8        |
| 1948        | 21.696         | 0.000      | 40.496          | 0.000      | 28.488          | 0.000      | 1        | 1990        | 21.477         | 0.081      | 40.524          | 0.035      | 28.573          | 0.036      | 19       |
| 1950        | 21.513         | 0.000      | 40.593          | 0.000      | 28.614          | 0.000      | 1        | 1992        | 21.436         | 0.113      | 40.561          | 0.062      | 28.612          | 0.017      | 4        |
| 1958        | 21.566         | 0.040      | 40.593          | 0.026      | 28.599          | 0.023      | 18       | 1992        | 21.471         | 0.086      | 40.556          | 0.060      | 28.598          | 0.021      | 4        |
| 1958        | 21.574         | 0.026      | 40.628          | 0.013      | 28.623          | 0.017      | 4        | 1993        | 21.537         | 0.037      | 40.554          | 0.002      | 28.577          | 0.011      | 7        |
| 1959        | 21.700         | 0.040      | 40.599          | 0.024      | 28.566          | 0.023      | 10       | 1993        | 21.538         | 0.036      | 40.555          | 0.002      | 28.578          | 0.011      | 7        |
| 1960        | 21.565         | 0.000      | 40.562          | 0.000      | 28.575          | 0.000      | 1        | 1995        | 21.343         | 0.053      | 40.527          | 0.025      | 28.612          | 0.018      | 16       |
| 1962        | 21.584         | 0.018      | 40.583          | 0.006      | 28.586          | 0.009      | 8        | 1999        | 21.409         | 0.033      | 40.526          | 0.006      | 28.592          | 0.010      | 16       |
| 1962        | 21.607         | 0.026      | 40.564          | 0.079      | 28.565          | 0.063      | 3        | 2000        | 21.466         | 0.014      | 40.538          | 0.019      | 28.586          | 0.013      | 18       |
| 1963        | 21.602         | 0.053      | 40.637          | 0.014      | 28.622          | 0.026      | 2        | 2000        | 21.417         | 0.026      | 40.509          | 0.010      | 28.577          | 0.015      | 15       |
| 1963        | 21.601         | 0.034      | 40.549          | 0.019      | 28.555          | 0.021      | 50       | 2001        | 21.463         | 0.011      | 40.611          | 0.025      | 28.642          | 0.021      | 20       |
| 1964        | 21.640         | 0.076      | 40.612          | 0.018      | 28.592          | 0.035      | 5        | 2001        | 21.423         | 0.000      | 40.510          | 0.000      | 28.576          | 0.000      | 1        |
| 1964        | 21.603         | 0.023      | 40.584          | 0.027      | 28.582          | 0.024      | 6        | 2001        | 21.455         | 0.042      | 40.560          | 0.010      | 28.605          | 0.018      | 50       |
| 1964        | 21.677         | 0.053      | 40.537          | 0.051      | 28.525          | 0.042      | 12       | 2008        | 21.474         | 0.002      | 40.537          | 0.028      | 28.582          | 0.022      | 2        |
| 1965        | 21.569         | 0.021      | 40.594          | 0.021      | 28.599          | 0.015      | 5        | 2010        | 21.465         | 0.017      | 40.534          | 0.007      | 28.583          | 0.009      | 101      |
| 1965        | 21.570         | 0.007      | 40.636          | 0.011      | 28.630          | 0.009      | 3        | 2010        | 21.476         | 0.018      | 40.533          | 0.008      | 28.579          | 0.011      | 101      |
| 1965        | 21.651         | 0.048      | 40.548          | 0.055      | 28.540          | 0.047      | 34       | 2010        | 21.501         | 0.008      | 40.495          | 0.026      | 28.542          | 0.020      | 53       |
| 1966        | 21.667         | 0.049      | 40.548          | 0.059      | 28.536          | 0.059      | 2        | 2011        | 21.525         | 0.035      | 40.487          | 0.008      | 28.530          | 0.016      | 15       |
| 1966        | 21.607         | 0.026      | 40.632          | 0.021      | 28.617          | 0.009      | 3        | 2011        | 21.471         | 0.009      | 40.487          | 0.013      | 28.545          | 0.013      | 4        |
| 1966        | 21.739         | 0.000      | 40.505          | 0.000      | 28.482          | 0.000      | 1        |             |                |            |                 |            |                 |            |          |

Table 3-1: Potential temperature ( $\theta$ ), salinity (*S*) and potential density ( $\sigma_\theta$ ) in the RSDW below 300 m depth. The results represent averages per cruise per year; *N* indicates the number of the observations on which the averages were based

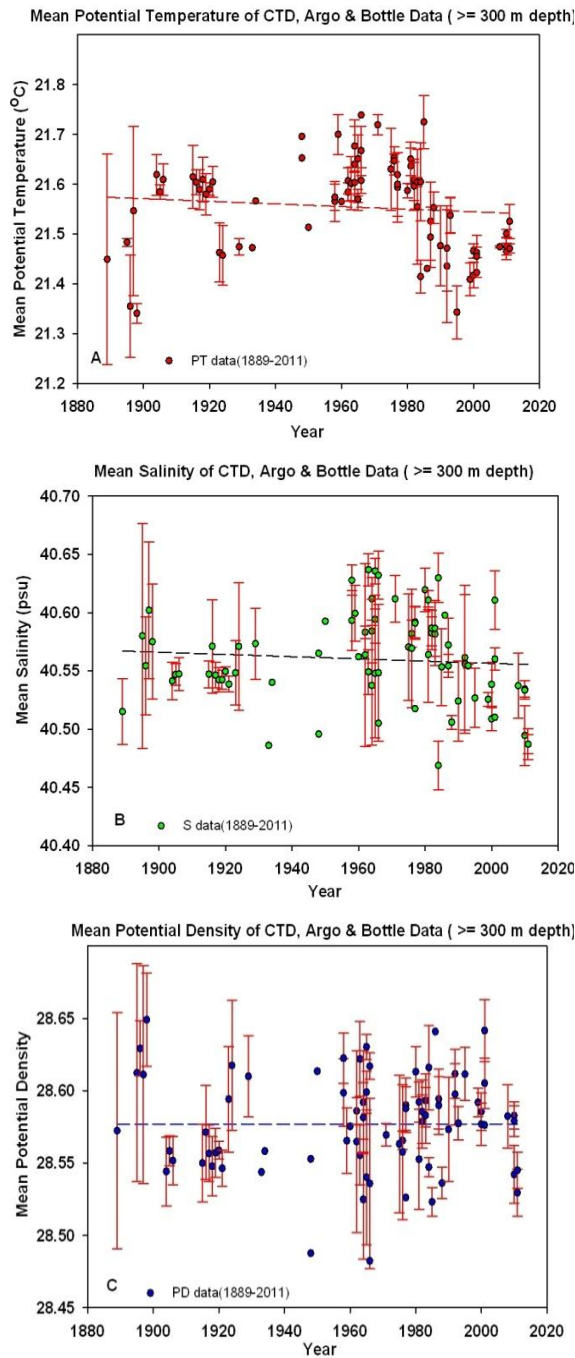


Figure 3-2: a, b and c: Properties of RSDW at a depth of 300 m to a maximum depth of each profile for the area between latitude 14 and 27.9° N. Each point represents an average per profile per cruise per year with its standard deviation

a) Potential temperature  $\theta$ , the dashed red line is the linear regression for the entire dataset.

$$\theta = -2.6 \times 10^{-4} (\text{year}-1900) + 21.571.$$

b) Salinity  $S$ , the dashed black line is the linear regression for the entire data set.

$$S = -0.09 \times 10^{-4} (\text{year}-1900) + 40.566.$$

c) Potential density  $\sigma_\theta$ , the dashed blue line is the linear regression for the entire data set.  $\sigma_\theta = -0.0002 \times 10^{-4} (\text{year}-1900) + 28.$

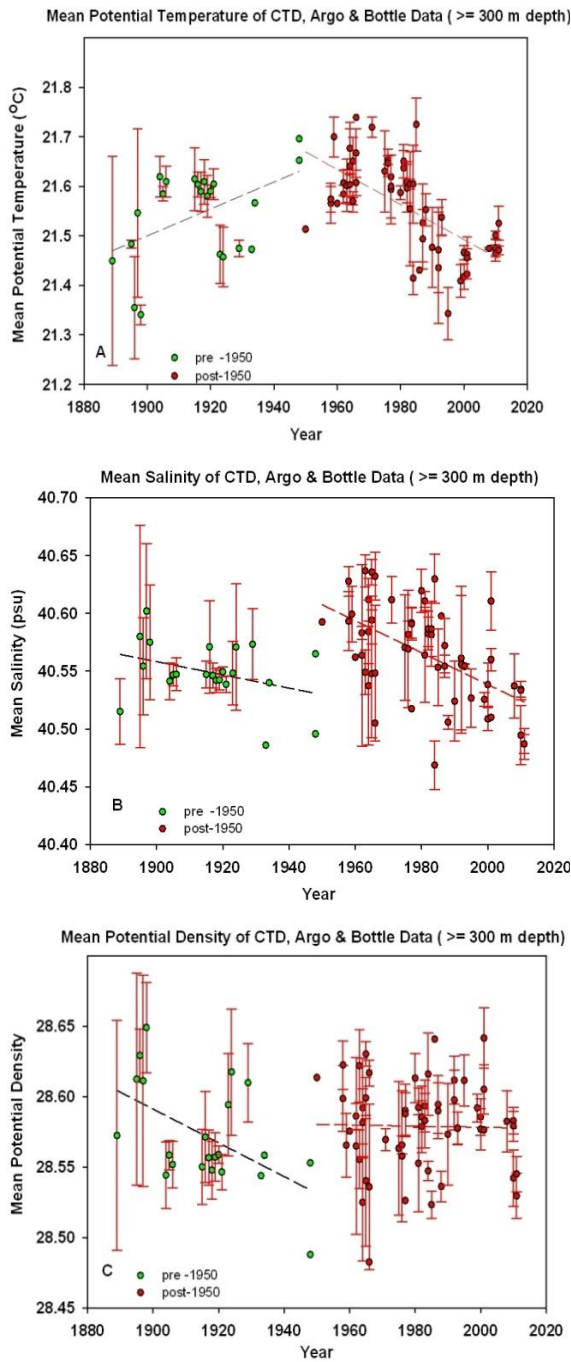


Figure 3-3: a, b and c: Properties of RSDW at a depth of 300 m to a maximum depth of each profile for the area between latitude 14 and 27.885° N. Each point represents an average per profile per cruise per year with its standard deviation

a) Potential temperature  $\theta$ , the dashed black line is the linear regression for the data pre-1950.  $\theta = 27 \times 10^{-4} (\text{year} - 1900) + 21.50$ ; the dashed red line is the linear regression for data post-1950.  $\theta = -35.5 \times 10^{-4} (\text{year} - 1900) + 21.847$ .

b) Salinity  $S$ , the dashed black line is the linear regression for the data pre-1950.  $S = -5.7 \times 10^{-4} (\text{year} - 1900) + 40.558$ ; the red dashed line is the linear regression for the data post-1950.  $S = -13.8 \times 10^{-4} (\text{year} - 1900) + 40.676$ .

c) Potential density  $\sigma_{\theta}$ , the dashed black line is the linear regression for the data pre-1950.  $\sigma_{\theta} = -12 \times 10^{-4} (\text{year} - 1900) + 28.591$ ; the red dashed line is linear regression for data post-1950.  $\sigma_{\theta} = -0.42 \times 10^{-4} (\text{year} - 1900) + 28.582$

### 3.3.2 Influence of the spatial variability

In order to assess the spatial coherence of the changes in thermohaline properties as described in the previous section, the differences among five sections along the Red Sea basin (Figure 3-4) are analysed following the method of Parrilla et al. (2002) and Veñez-belchi et al.(2010). The five sections differ in the details, in terms of, for example, sampling, seasons and station spacing. The 1962 (September) section consisted of 8 bottle stations with an average station separation of 226.55 km; the 1963 (January-February) section consisted of 18 Nansen bottle stations with different sampling depths and an average station separation of 97.82 km; the 1982 (October) section consisted of 21 CTD stations with an average station separation of 89.28 km; the 1983 (May) section consisted of 24 CTD stations with an average station separation of 72.65 km; and the 2001 (August) section consisted of 24 CTD stations with an average station separation of 92.09 km. Each section was interpolated onto two-dimensional grid points along the Red Sea axis. The potential temperature and salinity data were interpolated vertically onto 22 standard depths (from surface to 1400 m) and then linearly interpolated onto the 0.5° meridional (latitude) interval grid.

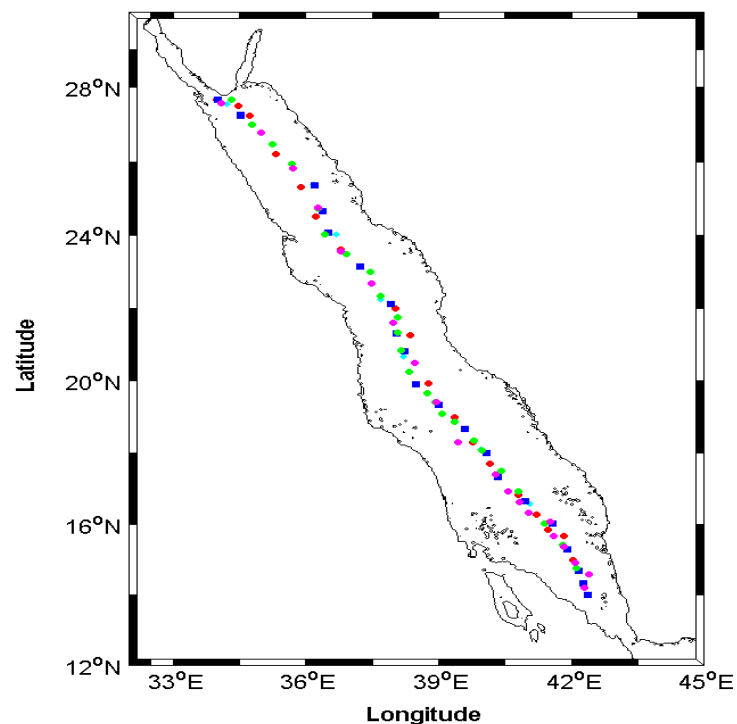


Figure 3-4: Location of the hydrographic sections along the Red Sea axis

1962 (cyan diamond), 1963 (red circle), 1982 (blue square), 1983 (green circle) and 2001 (magenta circle)

### *a. Short timescale differences*

It should be emphasised that the salinity and temperature in the cruises of 1962 and 1963 were measured by water samples compared to other sections in terms of data accuracy. We look at the short time scale especially for available winter time data like 1962/1963 and 1982/1983 to see if there are any signs of deep convection that occurred in previous winter seasons. The potential temperature differences for 1963-1962 (Figure 3-5a) indicate that there were negative differences in a very thin layer at the surface (~50 m depth) along the Red Sea basin. These negative differences could be the result of seasonal variability because the measurements were made in September for 1962 and during January-February for 1963. Below the cool layer and at a depth of 300 m there are positive differences (warming) except for some cooling at the upper layer between latitude ~25°N and ~20°N. In the southern part of Red Sea (south of 22°N) there is a cooler layer between 300 and 600 m above a warmer layer. There is also a warm layer in the deep water column at a depth of 300 m between latitude 20°N and 25°N. On the other hand the salinity differences for 1963-1962 (Figure 3-5b) indicate an overall freshening of the upper 300 m except at the southern end of the Red Sea, where a thin subsurface layer of ~50 m and a thin surface layer at latitude ~25°N are warming. At the depth below 300 m there was freshening of the entire basin except at 300-450 m depth in the southern Red Sea centered on latitude ~17°N. The thermohaline property average for the deep layer below 300 m was  $-0.004 \pm 0.022^{\circ}\text{C}$  for potential temperature and  $-0.020 \pm 0.029$  psu for salinity.

Potential temperature differences for 1983-1982 (Figure 3-5c) show cooling in the upper layers due to seasonal variability (the measurements were taken in May 1983 and October 1982) that extends to the whole water column in the north of the Red Sea (north of latitude ~22°N). There is also a warm layer between the surface and less than 100 m depth at the southern end of the Red Sea basin. Deeper than 300 m, there is substantial meridional variability in the middle of the Red Sea basin around latitude 21°N, and a warm layer extends from ~300 m down to the bottom, while there is a cold layer (300 m - bottom) north of latitude 22°N and south of latitude 19°N. The salinity differences (Figure 3-5d) present a meridional distribution similar to that of the potential temperature differences, except for the subsurface layer and the top of the deep layer in the north of the Red Sea; this also applies at a deep layer below 300 m around latitude 19°N and south of the Red Sea. The potential temperature average for the deep layer (below 300 m) of the Red Sea is  $-0.057 \pm 0.094^{\circ}\text{C}$  and  $-0.010 \pm 0.027$

psu for the salinity. It should be noted that the thermohaline property differences for the deep layer ( $\geq 300$  m depth) of the Red Sea are statistically not significant over the short term.

### *b. Long timescale differences*

For 1982-1963 potential temperature differences (Figure 3-6a), the surface layer down to about 50 m has warmed along the entire basin. Below this layer down to 300 m depth the differences are negative. This cooling reaches  $\sim 400$  m depth in the northern Red Sea (north of latitude  $20^\circ\text{N}$ ). Warmer water appears below a depth of 400 m along the basin down to 1000 m with an average of  $0.041 \pm 0.027^\circ\text{C}$ . The salinity differences for 1982-1963 (Figure 3-5b) are positive in the upper layer from the surface down to 300 m at latitudes between  $16^\circ\text{N}$  and  $\sim 23^\circ\text{N}$ , while there are negative values from the surface down to  $\sim 200$  m at latitudes between  $23^\circ\text{N}$  and  $26^\circ\text{N}$ . The most important features are the basin-wide positive trend below  $\sim 400$  m except some small spots with negative differences. The average of the thermohaline properties for the deep layer below 300 m is  $0.036 \pm 0.027^\circ\text{C}$  and  $0.030 \pm 0.015$  psu for potential temperature and salinity respectively.

For the potential temperature differences between 1983 and 2001 (Figure 3-6c), the surface layer is warmer along the Red Sea basin between 0 and  $\sim 200$  m (due to seasonal variability in the upper layer when the measurements were done during August 2001 and May 1983), except for some negative differences at a depth of 100 m in the middle basin around  $\sim 21^\circ\text{N}$ . There is a large area of cooling (with an average of  $-0.19 \pm 0.09^\circ\text{C}$ ) below a depth of 300 m through the entire basin deepening to the bottom, except for some warming (with an average of  $-0.031 \pm 0.010^\circ\text{C}$ ) found in the northern part of the Red Sea ( $\geq 26^\circ\text{N}$  latitude). The salinity differences (Figure 3-6 d) show a very thin layer ( $\sim 50$  m in thickness) with positive differences along the basin except for small positive differences in the middle of the basin at  $\sim 21^\circ\text{N}$  latitude. Below that depth, there are negative differences in the bottom in the southern part of the Red Sea, while there is a core of positive differences below the surface layer that extends to a depth of 600 m in the middle of the basin between latitudes  $21^\circ\text{N}$  and  $24^\circ\text{N}$ . In the northern part of the Red Sea ( $\geq 24^\circ\text{N}$  latitude), there are positive differences that extend from a depth of  $\sim 300$  m to the bottom. The average of the potential temperature and salinity for the deep layer (below 300 m) of the Red Sea are  $-0.204 \pm 0.11^\circ\text{C}$  and  $-0.007 \pm 0.027$  psu respectively.

The 2001-1962 differences (Figure 3-7a and b) for potential temperature and salinity present a similar meridional distribution except near the surface. The water below a depth of 300 m is mostly fresher and cooler along the entire section. This fresher and cooler water reaches the bottom of the basin with an interruption around 1000 m in the northern part of the Red Sea ( $\geq 26^{\circ}\text{N}$ ). The averages of RSDW (below depth of 300 m) properties are  $-0.250 \pm 0.029^{\circ}\text{C}$  for the potential temperature and  $-0.018 \pm 0.008$  psu for salinity.

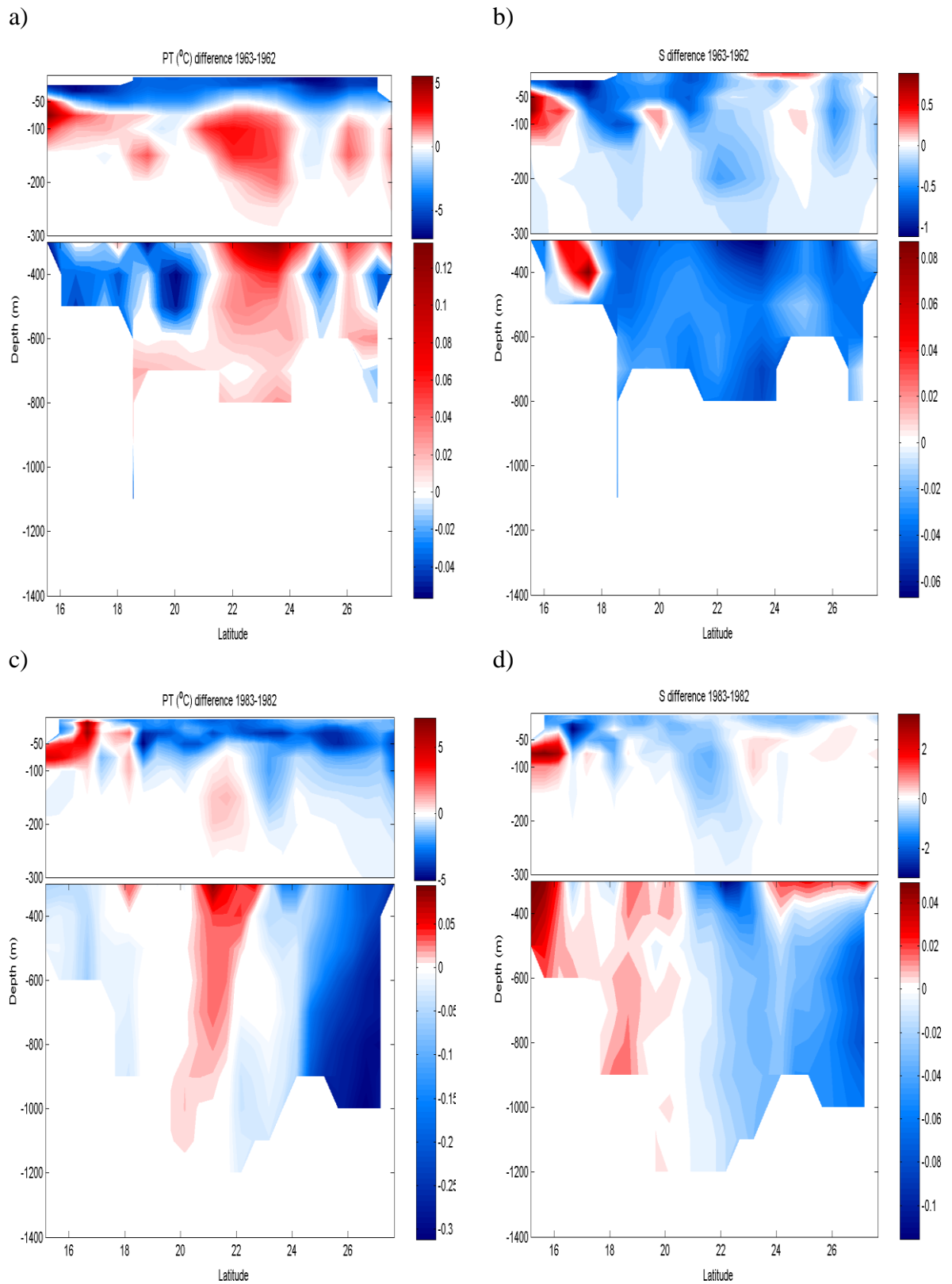


Figure 3-5: Differences of the thermohaline properties along the Red Sea basin: a, potential temperature differences in 1963-1962; b, salinity differences in 1963-1962; c, potential temperature differences in 1983-1982; d, salinity differences in 1983-1982

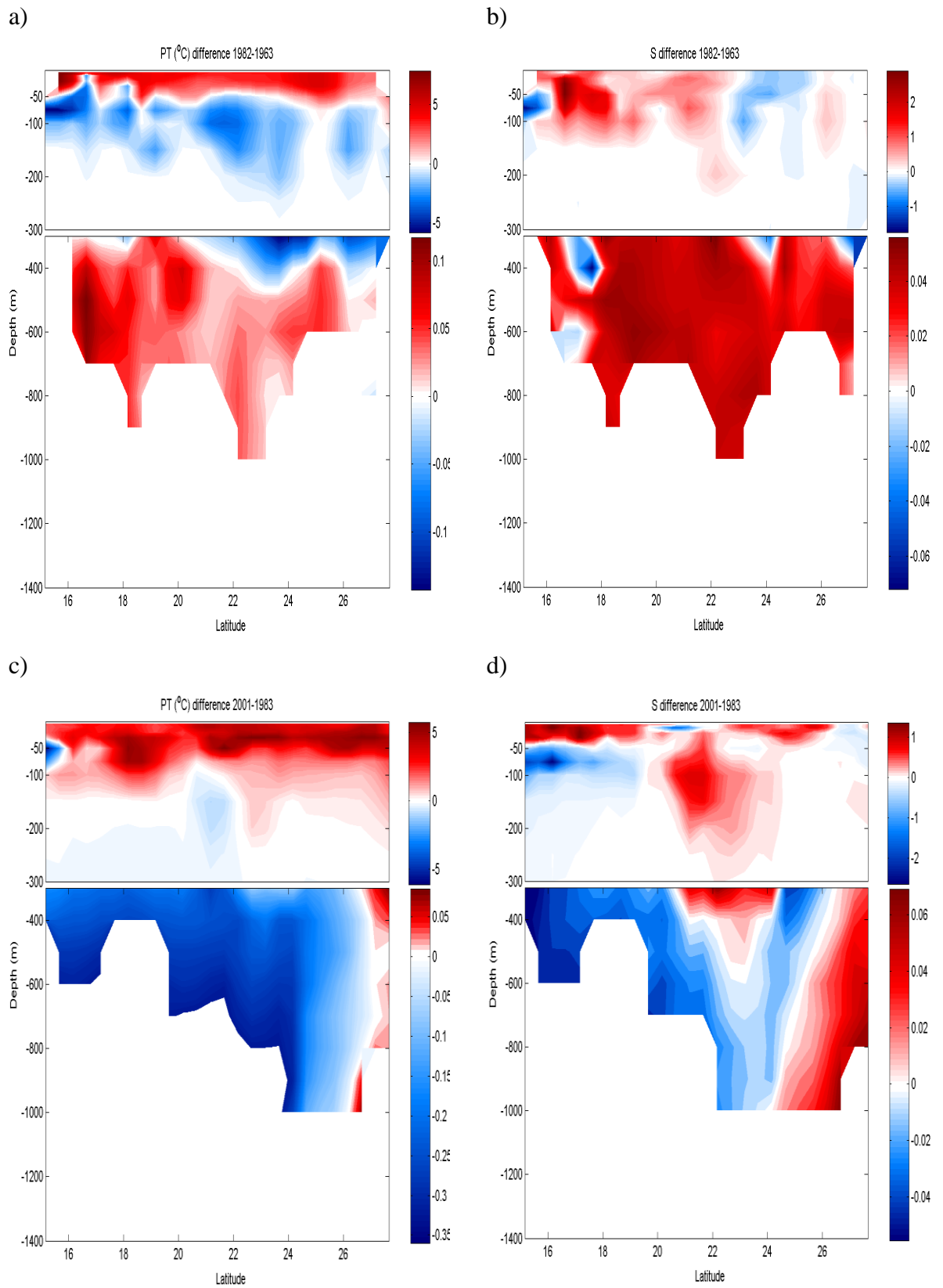


Figure 3-6: As in Figure 3-5 but for a, potential temperature differences in 1982-1963; b, salinity differences in 1982-1963; c, potential temperature differences in 2001-1983; d, salinity differences in 2001-1983

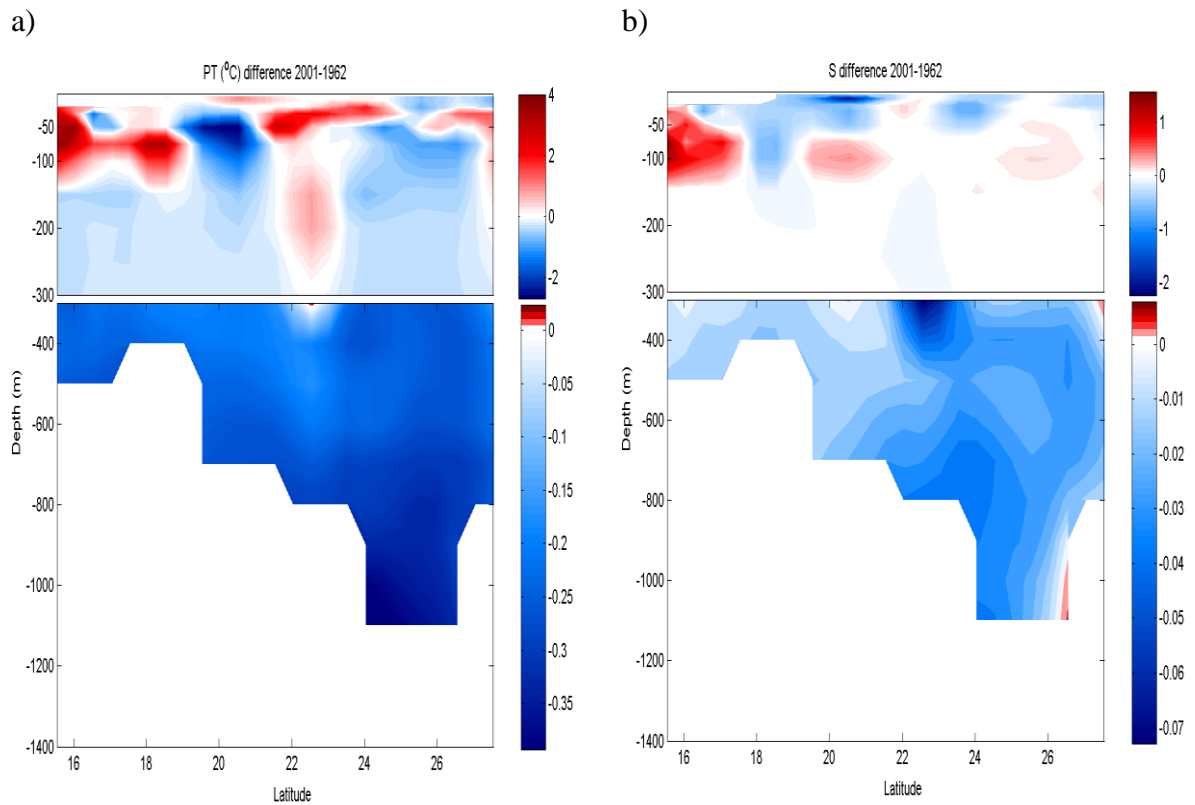


Figure 3-7: As in Figures 3-5 but for a, potential temperature differences in 2001-1962; b, salinity differences in 2001-1962

### c. Meridional average changes

The average of potential temperature and salinity was taken at each standard depth with the standard deviation to determine the mean differences at each standard level. In Figures 3-8, 9 and 10 the meridional average potential temperature and salinity plus/minus the standard deviation for the thermohaline differences for the short timescales 1963-1962 and 1983-1982 and for the long timescales 1982-1963, 2001-1983 and 2001-1962 were plotted from the surface down to 300 m (upper panel) and from 300 m to the bottom (lower panel). The meridional average along the Red Sea axis indicates warming (cooling) and salinification (freshening) in the upper layers as a result of different sampling times within the annual cycle. On the basis of Figure 3-8a and c for short timescales there is cooling for 1963-1962 differences above 50 m in depth; there is warming occurring below that depth down to a depth of 400 m. There is cooling between 400 and 500 m with values around  $-0.005^{\circ}\text{C}$ . There is a continuous warming between 500 m and 900 m; below that there is cooling with a value ranging from  $-0.010^{\circ}\text{C}$  to  $-0.036^{\circ}\text{C}$ . In contrast, the potential temperature differences in 1983-1982 show that cooling occurred throughout the water column. The maximum decrease

in the potential temperature for RSDW was  $-0.094^{\circ}\text{C}$  at a depth of 1000 m. For Figure 3-8b and d the salinity differences for 1963-1962 indicate that the whole water column appears to freshen from the surface down to a depth of 1200 m with a maximum value of  $-0.033$  at a depth of 1100 m. On the other hand, the salinity differences for 1983-1982 indicate that there is saltier water found between 50 and 100 m, and below that fresher water with a maximum value of  $-0.023$  at a depth of 1000 m.

The differences of 1982-1963 (Figure 3-9a and b) show warming for the upper 50 m layer and below that cooling down to a depth of 300 m. Below 300 m, there is warming occurring with a peak value of  $0.042$  at a depth of 500 m. In contrast, the whole water column appears more saline with a peak value of  $0.039$  at a depth of 900 m.

For the long period, from 1983 to 2001 (Figure 3-9c and d), there is warming in the upper layers down to a depth of 200 m; below that, the potential temperature decreases with maximum cooling of  $-0.22^{\circ}\text{C}$  found at a depth of 600 m. While the salinity in the upper layer increases, there is freshening between depths of 300 and 700 m with a peak value of  $-0.014$ ; below that the salinity increases down to 1100 m.

From 1962 to 2001, the meridional averaged potential temperatures decrease from a depth of around 150 m to a depth of 1100 m (Figure 3-10a). The maximum cooling occurs at a depth of 1100 m and reaches as high as  $0.37^{\circ}\text{C}$  over 39 years or  $0.009^{\circ}\text{C yr}^{-1}$ . The analysis of the salinity differences shows that there is freshening for the water column from 200 m down to 1100 m with maximum freshening occurring at a depth of 800 m, which reaches  $0.027$  psu over 39 years or  $0.0007$  psu  $\text{yr}^{-1}$  (Figure 3-10b).

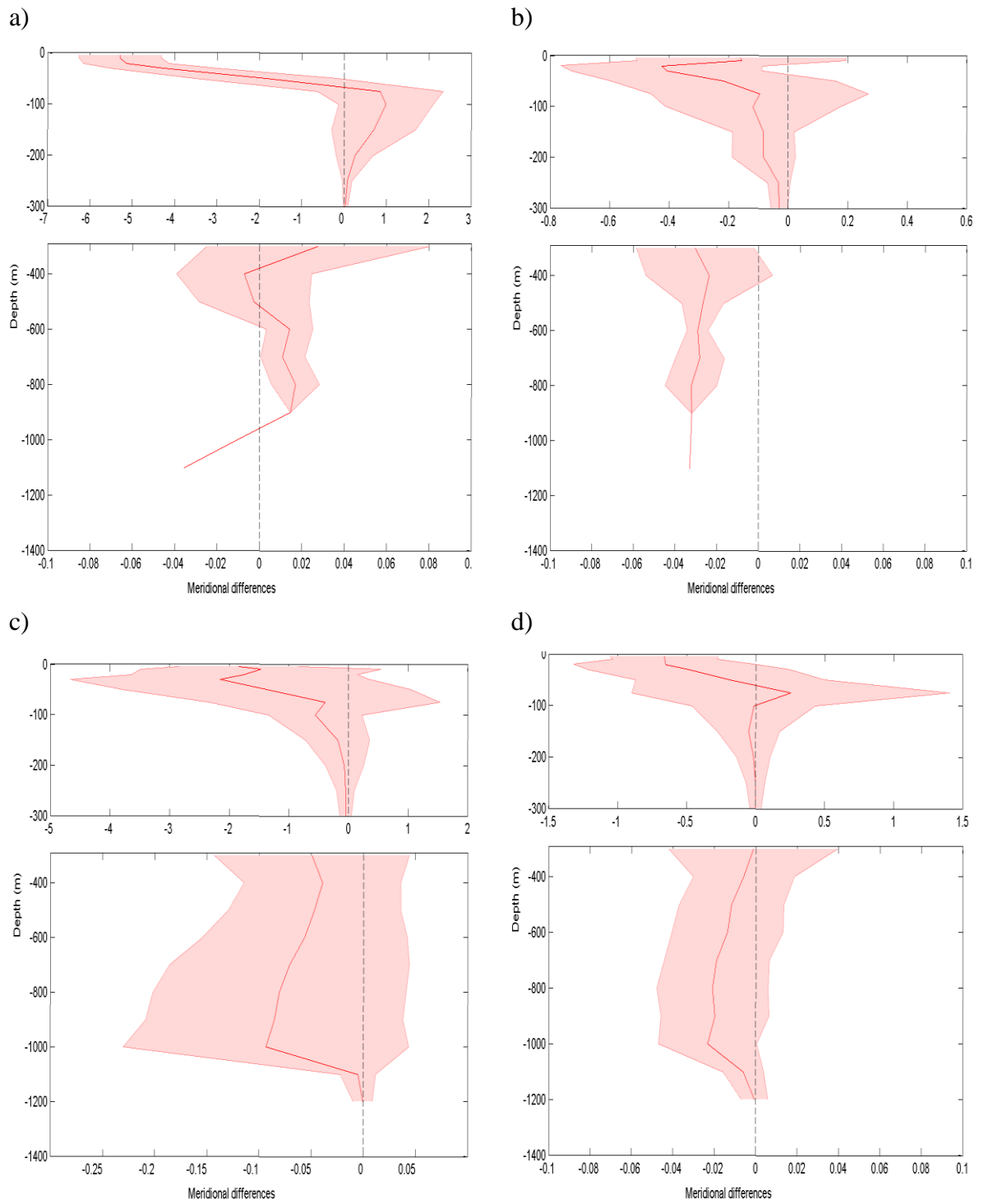


Figure 3-8: Vertical meridional averaged thermohaline properties differences plotted plus/minus one standard deviation for a, potential temperature differences in 1963-1962; b, salinity differences in 1963-1962; c, potential temperature differences in 1983-1982; d, salinity differences in 1983-1982 along the Red Sea basin. Note that the x-axis scales are different

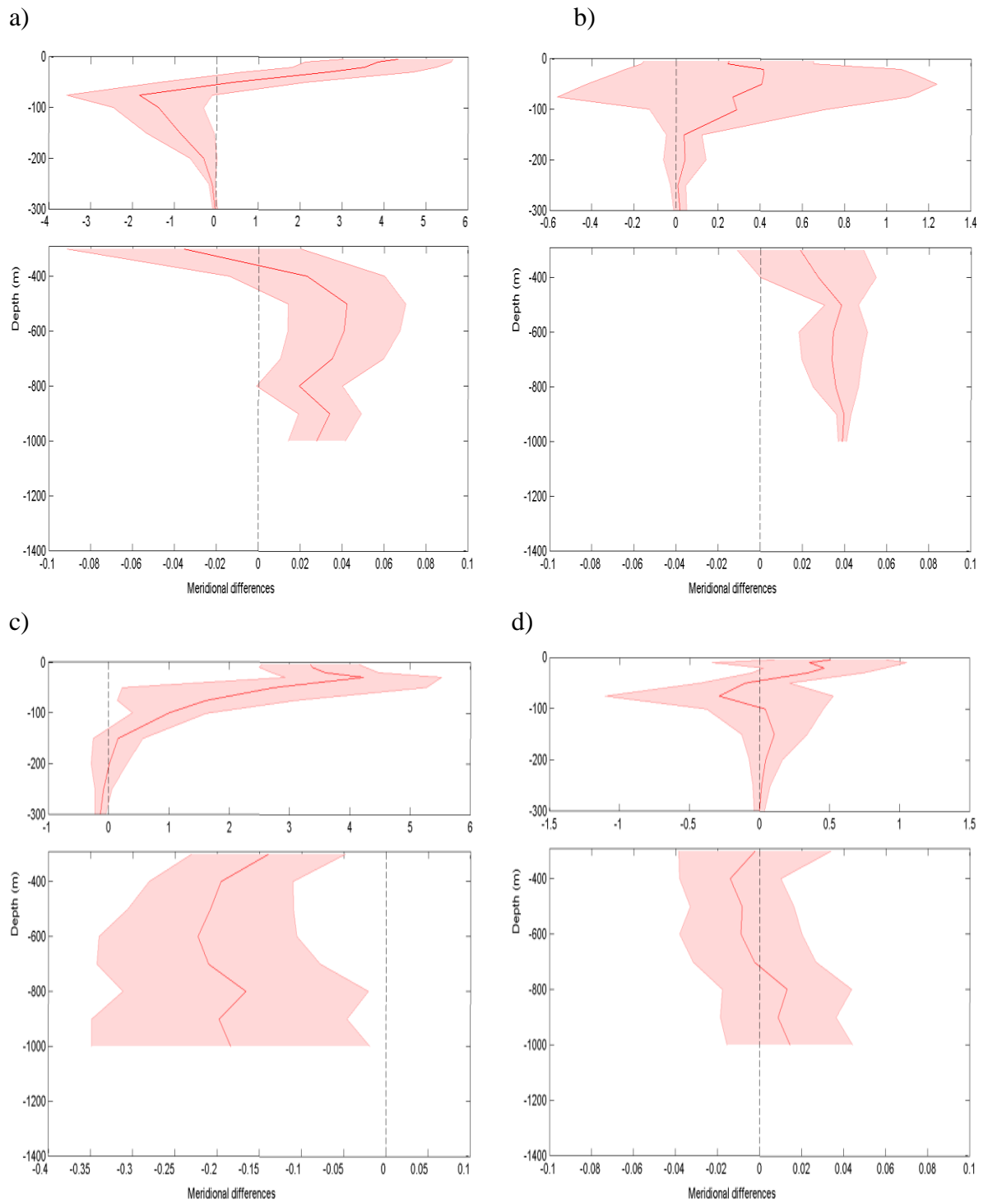


Figure 3-9: Vertical meridional averaged thermohaline properties differences plotted plus/minus one standard deviation for a, potential temperature differences in 1982-1963; b, salinity differences in 1982-1963; c, potential temperature differences in 2001-1983; d, salinity differences in 2001-1983 along the Red Sea basin. Note that the x-axis scales are different

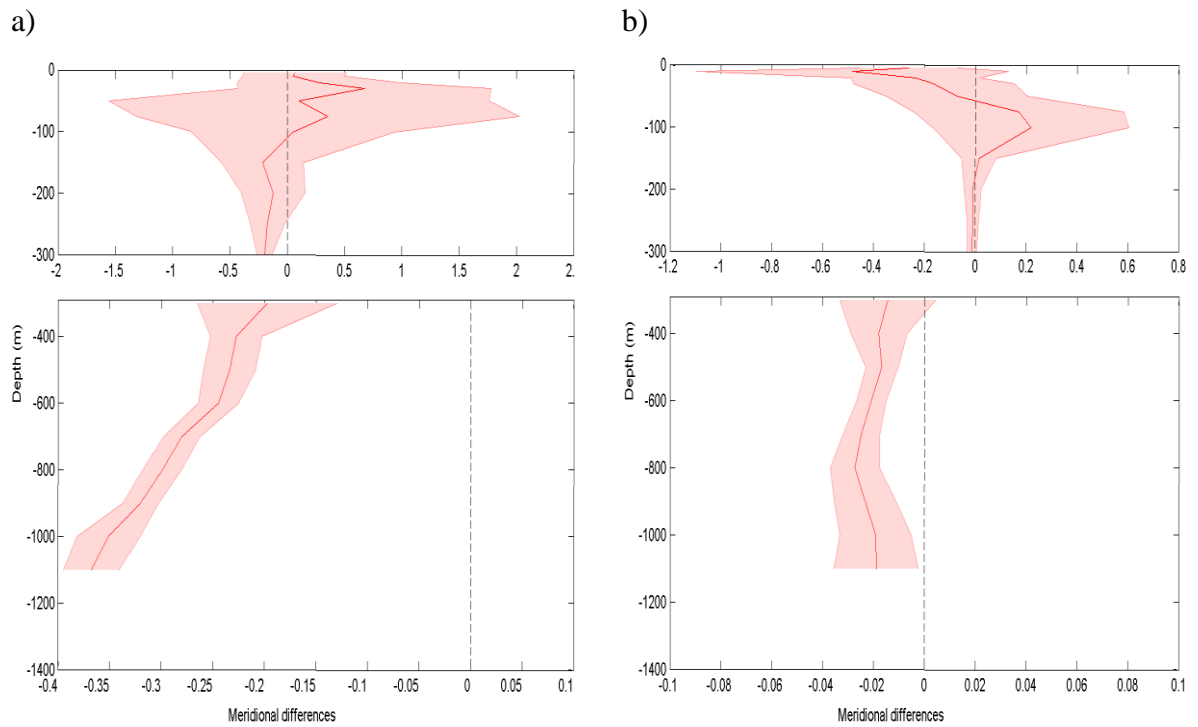


Figure 3-10: Vertical meridional averaged thermohaline properties differences plotted plus/minus one standard deviation for a, potential temperature differences in 2001-1962; b, salinity differences in 2001-1962 along the Red Sea basin. Note that the x-axis scales are different

### 3.4 Air-Sea interaction in the Red Sea

To find a possible connection between the changes observed in the RSDW properties and climate variability over the Red Sea, we analysed air-sea exchange data for the whole Red Sea and in the formation sources of the deep water, namely the Gulf of Suez, Gulf of Aqaba and the northern part of the Red Sea as proposed by Wyrтки (1974). This was also a result of the lack of continuous time series of hydrographic data, especially winter data in the formation regions to explain that cooling and freshening found in the Red Sea deep water. The triggering and the intensity of convection are connected to air-sea interaction events by cooling and evaporation in the formation areas of the deep.

These data are available from the National Oceanography Centre, Southampton in the form of the Surface Flux Dataset v2.0 (1973-2006) with a grid resolution of  $1^\circ \times 1^\circ$ , consisting of meteorological parameters (latent heat, sensible heat, short and longwave radiation). From these the net heat flux and rate of evaporation can be

calculated for the Red Sea and the three regions with one grid point for the Suez and Aqaba Gulfs and two grid points for the northern part of the Red Sea (26°N-28°N).

The net heat flux, sea surface temperature and evaporation in different years were compared with the observed changes in the RSDW properties, and the values of the monthly mean anomalies for these parameters over the whole winter season in the Red Sea and the other three regions are shown in Figures 3-11, 12 and 13. The averages of the net heat flux and evaporation were taken for six months (October-March) and (November-April) for SST. The surface net heat flux is shifted by one month compared to the SST because the cooling of the sea surface is a reaction to the fluxes (Woelk & Quadfasel, 1996).

The results (Figure 3-11a, b, c, and d) indicate that the mean net heat flux anomalies for the winter seasons (October-March) over the whole Red Sea region and other three source formation regions are consistent, decreasing by an average of  $-0.99 \pm 0.25 \text{ Wm}^{-2}$ ,  $-1.12 \pm 0.49 \text{ Wm}^{-2}$ ,  $-1.75 \pm 0.49 \text{ Wm}^{-2}$  and  $-1.58 \pm 0.47 \text{ Wm}^{-2}$  for the Red Sea, the northern part of the Red Sea, and the Gulfs of Suez and Aqaba respectively. The analyses show that the net heat flux over the four regions has a statistically significant cooling tendency at a confidence level of more than 95%.

The changes in the SST for the winter season (November-April) show an increase in the Red Sea and the Gulfs of Suez and Aqaba by an average of  $6.9 \times 10^{-3} \pm 6.2 \times 10^{-3} \text{ } ^\circ\text{C}$ ,  $7.2 \times 10^{-3} \pm 0.12 \text{ } ^\circ\text{C}$  and  $5.6 \times 10^{-3} \pm 0.011 \text{ } ^\circ\text{C}$  respectively. However, these changes appear to show a decrease in the northern part of the Red Sea by an average of  $-0.33 \times 10^{-3} \pm 8.5 \times 10^{-3} \text{ } ^\circ\text{C}$  (Figure 3-12a, b and c). These changes in the SST are very small and statistically not significant.

Furthermore, Figure 3-13a, b, c and d show that the evaporation is consistently increasing by an average of  $0.010 \pm 0.002 \text{ m yr}^{-1}$ ,  $0.012 \pm 0.004 \text{ m yr}^{-1}$ ,  $0.020 \pm 0.005 \text{ m yr}^{-1}$  and  $0.018 \pm 0.005 \text{ m yr}^{-1}$  for the Red Sea, the northern part of the Red Sea, and the Gulfs of Suez and of Aqaba respectively. These increases in the evaporation are statistically significant at a confidence level of more than 95%.

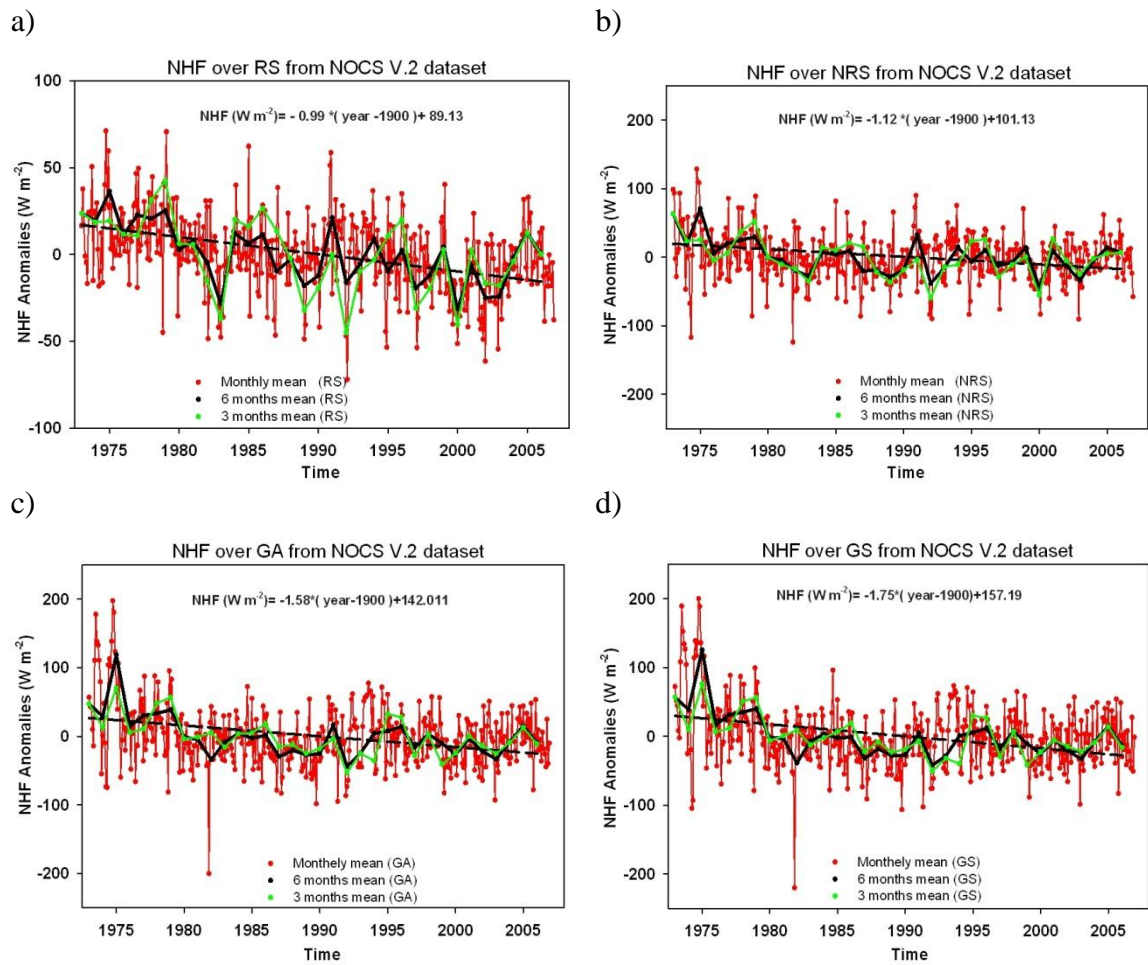


Figure 3-11: Monthly net heat flux anomalies over a, the Red Sea (RS); b, the northern Red Sea (NRS); c, the Gulf of Suez (GS) and d, the Gulf of Aqaba (GA) derived from the NOCS v2.0 dataset with a six month running mean represented by solid black with a regression line and a three month running mean by a solid green line (+ gained, - loss)

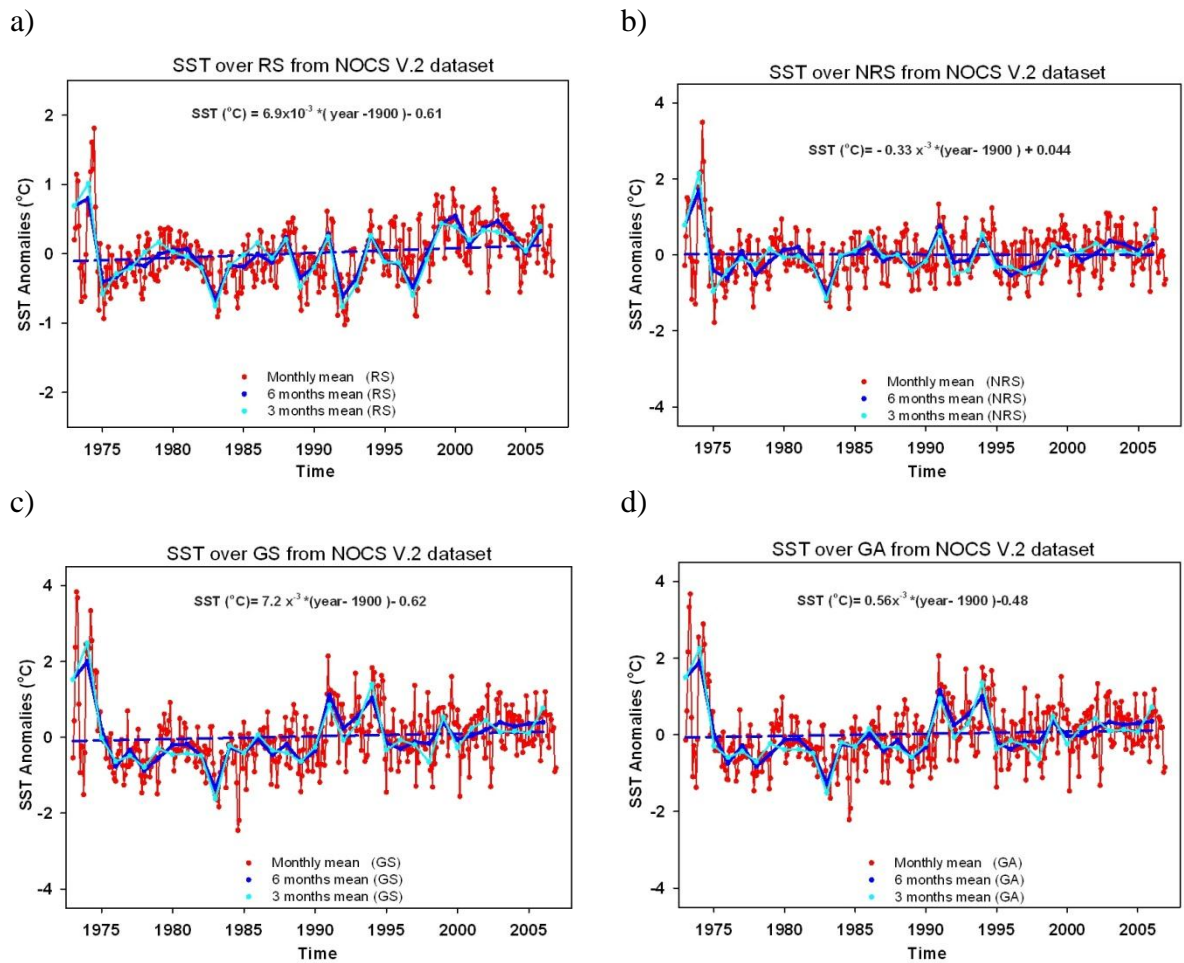


Figure 3-12: Monthly sea surface temperature anomalies over a, the Red Sea (RS); b, the northern Red Sea (NRS); c, the Gulf of Suez (GS); and d, the Gulf of Aqaba (GA) derived from the NOCS v2.0 dataset with a six month running mean represented by solid blue with a regression line and a three month running mean represented by a solid cyan line

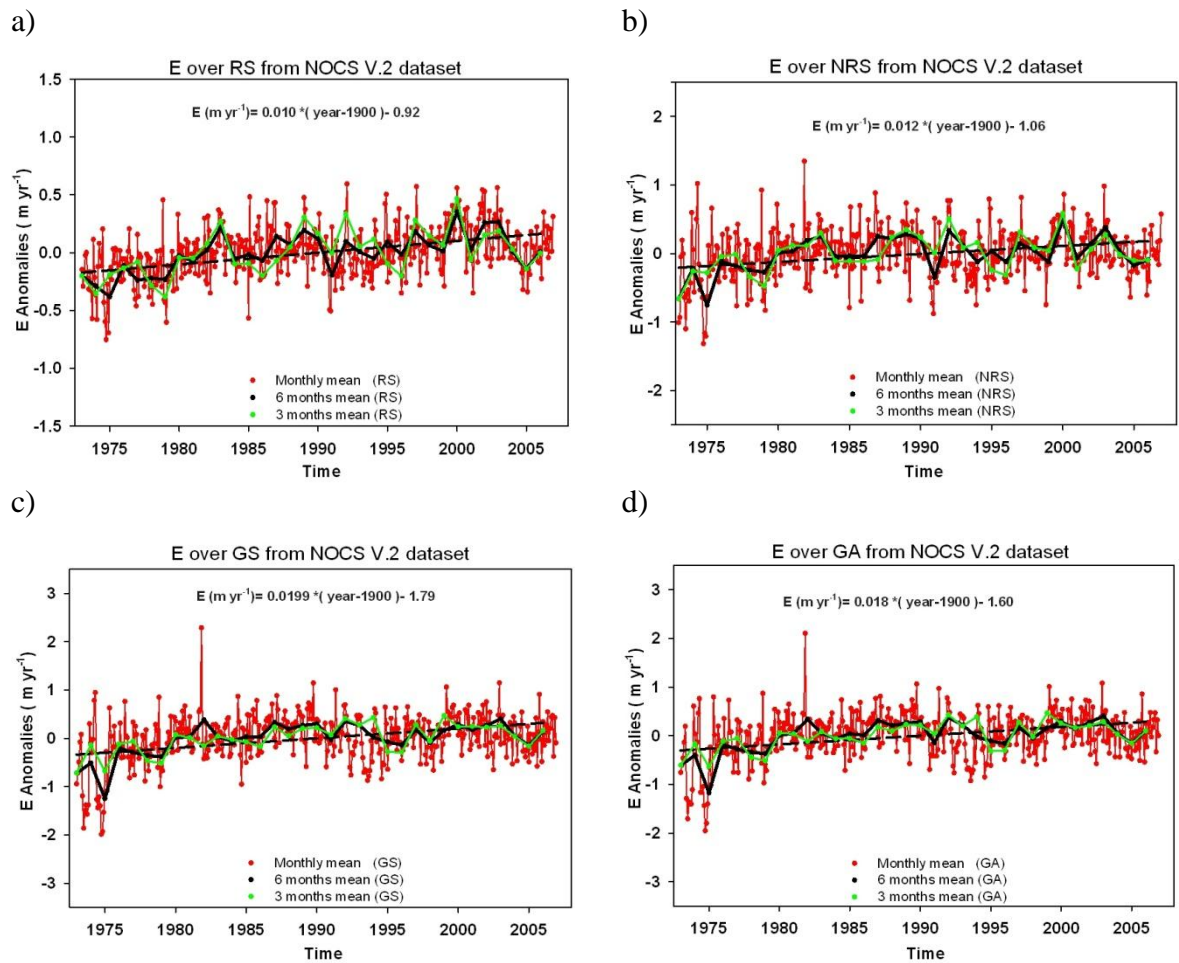


Figure 3-13: Monthly evaporation anomalies over a, the Red Sea (RS); b, the northern Red Sea (NRS); c, the Gulf of Suez (GS) and d, the Gulf of Aqaba (GA) derived from the NOCS v2.0 dataset with a six month running mean represented by solid black with a regression line and a three month running mean represented by a solid green line

### 3.5 Discussion and conclusion

The long-term variability of the RSDW thermohaline properties were investigated based on hydrographic data stretching back to 1889. Our analysis of the historical hydrographic data indicates that there is cooling of deep water with an average of  $-2.5 \times 10^{-4} \text{ }^\circ\text{C yr}^{-1}$  and freshening with an average of  $-0.09 \times 10^{-4} \text{ psu yr}^{-1}$  through the entire dataset from 1889 to 2011. Furthermore, the analysis shows a decreasing potential density trend with an average of  $-0.0002 \times 10^{-4} \text{ kg m}^{-3} \text{ yr}^{-1}$ . However, these changes in the thermohaline properties of RSDW were not statistically significant.

After the splitting of the data into two groups to facilitate the comparison between them according to the density of the observations, the analysis indicates that there is warming ( $27 \times 10^{-4} \pm 11 \times 10^{-4} \text{ }^\circ\text{C yr}^{-1}$ ) and freshening ( $5.7 \times 10^{-4} \pm 3.4 \times 10^{-4} \text{ psu yr}^{-1}$ ) in the RSDW for the period of time between 1889 and 1950 (pre-1950). In contrast, for the period of time between 1950 and 2011 (post-1950), there is cooling and freshening in the RSDW by an average of  $35.5 \times 10^{-4} \pm 5.6 \times 10^{-4} \text{ }^\circ\text{C yr}^{-1}$  and  $13.8 \times 10^{-4} \pm 2.8 \times 10^{-4} \text{ psu yr}^{-1}$  respectively. This cooling and freshening signal (post-1950) is statistically significant with a confidence level of more than 95%. While, the warming and freshening signal for the period of time (pre-1950) is only significant at a confidence level of more than 95% for the warming trend.

According to the dataset used in this study, the potential temperature differences in the RSDW between 1950 and 2011 amount to about  $0.12^\circ\text{C}$ . Furthermore, the salinity differences for the same period are found to be as much as 0.13 psu. Remarkably, the changes in the potential temperature and salinity in the RSDW are correlated with  $r=0.4$ , which suggests that long-term potential temperature and salinity changes in the RSDW are density-compensated. This is supported by the evidence for no significant trend in the long-term RSDW potential density.

Our analysis of thermohaline properties of RSDW from the hydrographic sections along the Red Sea axis between 1962 and 2001 reveals a mean cooling of  $0.25 \pm 0.028^\circ\text{C}$  and freshening of  $0.018 \pm 0.008 \text{ psu}$  occurring in the RSDW properties over the four decades (Figures 3-7 and 3-10).

| Time      | $\theta$ ( $^{\circ}\text{C}$ )            | S   | NHF ( $\text{Wm}^{-2}$ ) |                   |                   |                   |
|-----------|--|---|--------------------------|-------------------|-------------------|-------------------|
|           |  |   | RS                       | NRS               | GS                | GA                |
| 1889-2011 | $-2.5 \times 10^{-4} \pm 3 \times 10^{-4}$ | $-0.09 \times 10^{-4} \pm 1 \times 10^{-4}$ | -                        | -                 | -                 | -                 |
| 1889-1950 | $27 \times 10^{-4} \pm 10 \times 10^{-4}$  | $-6 \times 10^{-4} \pm 3 \times 10^{-4}$    | -                        | -                 | -                 | -                 |
| 1950-2011 | $-35 \times 10^{-4} \pm 6 \times 10^{-4}$  | $-13 \times 10^{-4} \pm 2 \times 10^{-4}$   | -                        | -                 | -                 | -                 |
| 1973-2006 | -  | -   | $-0.99 \pm 0.25$         | $-1.12 \pm 0.49$  | $-1.75 \pm 0.49$  | $-1.58 \pm 0.47$  |
| 1975-2001 | $-90 \times 10^{-4} \pm 10 \times 10^{-4}$ | $-17 \times 10^{-4} \pm 7 \times 10^{-4}$   | $-1.25 \pm 0.34$         | $-1.21 \pm 0.57$  | $-2.06 \pm 0.72$  | $-1.92 \pm 0.70$  |
|           |  |   | E ( $\text{myr}^{-1}$ )  |                   |                   |                   |
|           |  |   | RS                       | NRS               | GS                | GA                |
| 1889-2011 | $-2.5 \times 10^{-4} \pm 3 \times 10^{-4}$ | $-0.09 \times 10^{-4} \pm 1 \times 10^{-4}$ | -                        | -                 | -                 | -                 |
| 1889-1950 | $27 \times 10^{-4} \pm 10 \times 10^{-4}$  | $-6 \times 10^{-4} \pm 3 \times 10^{-4}$    | -                        | -                 | -                 | -                 |
| 1950-2011 | $-35 \times 10^{-4} \pm 6 \times 10^{-4}$  | $-13 \times 10^{-4} \pm 2 \times 10^{-4}$   | -                        | -                 | -                 | -                 |
| 1973-2006 | -  | -   | $0.010 \pm 0.002$        | $0.012 \pm 0.004$ | $0.020 \pm 0.005$ | $0.018 \pm 0.005$ |
| 1975-2001 | $-90 \times 10^{-4} \pm 10 \times 10^{-4}$ | $-17 \times 10^{-4} \pm 7 \times 10^{-4}$   | $0.013 \pm 0.003$        | $0.013 \pm 0.006$ | $0.022 \pm 0.007$ | $0.020 \pm 0.007$ |

Table 3-2: Results are presented for the potential temperature ( $\theta$ ) and salinity (S) for the RSDW (300-1000) and Net heat fluxes and evaporation anomalies over the Red Sea (RS) and the sources region: Northern of the Red Sea (NRS), Gulf of Suez (GS) and Gulf of Aqaba (GA); the linear trend and the standard error are also presented

To distinguish between the spatial variability and basin-wide changes in the thermohaline properties of the RSDW, the basin was subdivided into seven geographical regions with grids of  $2^{\circ}$  latitude intervals and using the available high-resolution CTD data from 1977 to 2011. The method that was applied to obtain Figures 3-2 and 3-3 was used again. The results are shown in Table 3-3 and plotted in Figure 3-15a, b and c. The results indicate that there is consistent cooling and freshening in all the seven regions over the time period between 1977 and 2011 (Figure 3-15a and b). The possible changes in the potential density decrease can be concluded from Figure 3-14c except for regions of  $20-22^{\circ}\text{N}$  and  $24-26^{\circ}\text{N}$ . This supports the results we obtained regarding long-scale cooling and freshening that occurred in the previous analysis, which implies that the changes are most likely caused by changes in the conditions of formations.

The surface net heat flux and evaporation were calculated in the three formation source areas from the available atmospheric data in order to investigate a possible connection between changes observed in the RSDW properties and climate variability over the Red Sea (see Table 3-2). We find that the cooling and freshening in the

thermohaline properties of RSDW could indeed have resulted from the increase in bottom water formation in the Gulf of Suez in winter, leading to a strong plume entraining with warm and fresh near-surface water from the northern Red Sea. This is the primary mechanism for the observed cooling and freshening occurred in the winter of 1982/1983 observed by Woelk and Quadfasel (1996). Their hypothesis that is during the winter season the increase in the evaporation (buoyancy loss) leads to convection that reaches the bottom of the northern part of Gulf of Suez. During the deep convection, the cold and saline water flows southward to the mouth of the Gulf of Suez and then sink down the continental slope in a series of plumes (Figure 3-14).

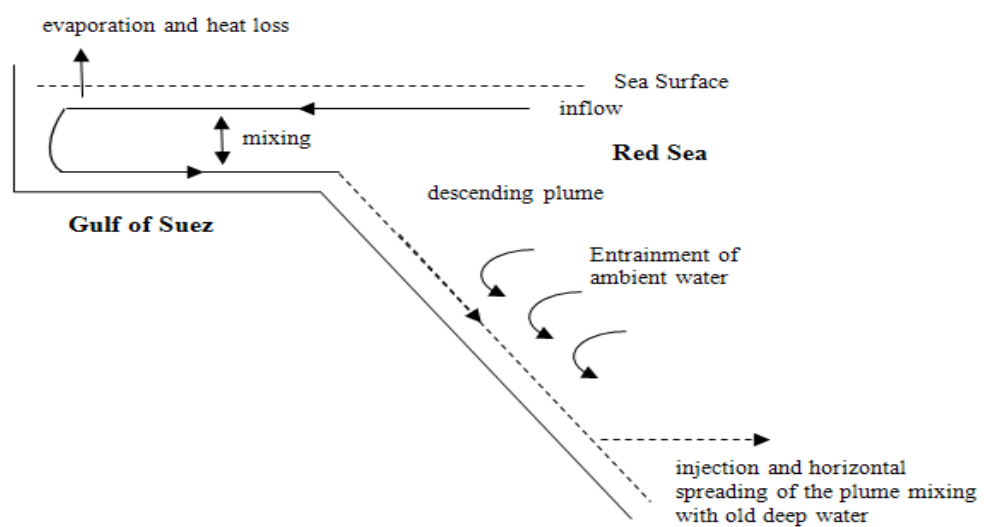


Figure 3-14: Schematic of the processes important for the deep water formation in the northern of the Red Sea according to (Woelk & Quadfasel, 1996)

A comparison of the results of the net heat fluxes showed good accordance with the long-term changes in the potential temperature and salinity in the RSDW for the Red Sea, Gulf of Suez, Gulf of Aqaba and northern part of the Red Sea. The net heat flux results show consistent decreasing by an average of  $-0.99 \pm 0.25 \text{ Wm}^{-2}$ ,  $-1.12 \pm 0.49 \text{ Wm}^{-2}$ ,  $-1.75 \pm 0.49 \text{ Wm}^{-2}$  and  $-1.58 \pm 0.47 \text{ Wm}^{-2}$  for the Red Sea, the northern part of the Red Sea, and the Gulfs of Suez and Aqaba respectively (Table 3-2). There is a strong correlation found for the net heat losses (wintertime) over the three main formation sources with correlation reaching 0.9, which is statistically significant at a 99% level.

Furthermore, the significant trend in evaporation anomalies in the formation regions supports the hypothesis about changes in the RSDW resulting from the deep convection in the Gulf Suez and other possible contributory factors (Wyrтки, 1974;

Cember, 1988; Woelk & Quadfasel, 1996). In conclusion, this is clear evidence for large-scale significant cooling and freshening occurring in the RSDW properties over the last six decades (1950-2011) and linked to the interannual variations of the atmospheric forcing.

Comparison of our findings with a sub-region such as the Western Mediterranean Deep Water indicates that the trends of the potential temperature and salinity are of opposite sign to the warming and salinification trends in the WMDW. These trends in WMDW have been attributed to anthropogenic greenhouse warming (Bethoux et al., 1990), to decreasing precipitation trends over the region since the 1940s (Bethoux et al., 1998; Krahnemann & Schott, 1998) and to anthropogenic reduction of the freshwater flux inflow (Rohling & Bryden, 1992).

| <b><u>14-16</u></b> |          |                            |          |                                   | <b><u>16-18</u></b> |          |                            |          |                                   |
|---------------------|----------|----------------------------|----------|-----------------------------------|---------------------|----------|----------------------------|----------|-----------------------------------|
| <b>Year</b>         | <b>T</b> | <b><math>\theta</math></b> | <b>S</b> | <b><math>\sigma_\theta</math></b> | <b>Year</b>         | <b>T</b> | <b><math>\theta</math></b> | <b>S</b> | <b><math>\sigma_\theta</math></b> |
| 1977                | 21.755   | 21.665                     | 40.593   | 28.570                            | 1980                | 21.685   | 21.592                     | 40.618   | 28.611                            |
| 1980                | 21.659   | 21.572                     | 40.639   | 28.632                            | 1982                | 21.777   | 21.615                     | 40.597   | 28.588                            |
| 1982                | 21.776   | 21.676                     | 40.578   | 28.556                            | 1983                | 21.734   | 21.624                     | 40.603   | 28.590                            |
| 1983                | 21.741   | 21.649                     | 40.607   | 28.586                            | 1993                | 21.620   | 21.512                     | 40.556   | 28.586                            |
| 1987                | 21.709   | 21.594                     | 40.556   | 28.563                            | 2001                | 21.562   | 21.441                     | 40.564   | 28.612                            |
| 1992                | 21.621   | 21.545                     | 40.607   | 28.616                            | 2011                | 21.620   | 21.477                     | 40.476   | 28.535                            |
| 1993                | 21.618   | 21.557                     | 40.553   | 28.571                            | <b><u>20-22</u></b> |          |                            |          |                                   |
| 1995                | 21.500   | 21.369                     | 40.539   | 28.614                            | 1980                | 21.663   | 21.578                     | 40.638   | 28.629                            |
| 2001                | 21.584   | 21.500                     | 40.556   | 28.589                            | 1982                | 21.785   | 21.568                     | 40.596   | 28.601                            |
| 2011                | 21.679   | 21.474                     | 40.486   | 28.544                            | 1983                | 21.764   | 21.596                     | 40.591   | 28.589                            |
| <b><u>18-20</u></b> |          |                            |          |                                   | 1987                | 21.647   | 21.472                     | 40.559   | 28.600                            |
| 1977                | 21.801   | 21.599                     | 40.604   | 28.598                            | 1987                | 21.656   | 21.467                     | 40.556   | 28.598                            |
| 1980                | 21.673   | 21.577                     | 40.628   | 28.623                            | 1988                | 21.687   | 21.553                     | 40.506   | 28.536                            |
| 1982                | 21.776   | 21.584                     | 40.595   | 28.596                            | 1992                | 21.638   | 21.393                     | 40.506   | 28.582                            |
| 1983                | 21.741   | 21.618                     | 40.599   | 28.589                            | 1995                | 21.597   | 21.512                     | 40.574   | 28.600                            |
| 1985                | 21.840   | 21.763                     | 40.577   | 28.530                            | 2001                | 21.572   | 21.430                     | 40.564   | 28.616                            |
| 1987                | 21.687   | 21.569                     | 40.590   | 28.595                            | 2008                | 21.604   | 21.473                     | 40.557   | 28.598                            |
| 1987                | 21.675   | 21.468                     | 40.560   | 28.601                            | <b><u>24-26</u></b> |          |                            |          |                                   |
| 2001                | 21.594   | 21.432                     | 40.561   | 28.613                            | 1982                | 21.747   | 21.568                     | 40.586   | 28.593                            |
| 2011                | 21.612   | 21.475                     | 40.480   | 28.539                            | 1983                | 21.583   | 21.444                     | 40.557   | 28.606                            |
| <b><u>22-24</u></b> |          |                            |          |                                   | 1985                | 21.760   | 21.687                     | 40.530   | 28.516                            |
| 1980                | 21.687   | 21.605                     | 40.593   | 28.588                            | 1995                | 21.481   | 21.330                     | 40.530   | 28.618                            |
| 1982                | 21.793   | 21.562                     | 40.593   | 28.600                            | 2001                | 21.548   | 21.414                     | 40.560   | 28.617                            |
| 1983                | 21.719   | 21.567                     | 40.558   | 28.572                            | 2010                | 21.603   | 21.470                     | 40.538   | 28.585                            |
| 1987                | 21.625   | 21.501                     | 40.557   | 28.590                            | <b><u>26-28</u></b> |          |                            |          |                                   |
| 1987                | 21.639   | 21.487                     | 40.552   | 28.590                            | 1977                | 21.674   | 21.537                     | 40.576   | 28.594                            |
| 1992                | 21.564   | 21.403                     | 40.503   | 28.577                            | 1982                | 21.703   | 21.586                     | 40.569   | 28.575                            |
| 1995                | 21.563   | 21.343                     | 40.556   | 28.634                            | 1983                | 21.430   | 21.292                     | 40.528   | 28.627                            |
| 2001                | 21.572   | 21.454                     | 40.550   | 28.598                            | 1995                | 21.477   | 21.327                     | 40.511   | 28.604                            |
| 2010                | 21.588   | 21.476                     | 40.530   | 28.577                            | 1999                | 21.532   | 21.409                     | 40.526   | 28.592                            |
| 2011                | 21.665   | 21.457                     | 40.506   | 28.563                            | 2001                | 21.568   | 21.451                     | 40.568   | 28.612                            |
|                     |          |                            |          |                                   | 2008                | 21.584   | 21.476                     | 40.517   | 28.567                            |
|                     |          |                            |          |                                   | 2010                | 21.594   | 21.483                     | 40.532   | 28.576                            |

Table 3-3: Potential temperature ( $\theta$ ), salinity (S) and potential density ( $\sigma_\theta$ ) in the Red Sea deep water below 300 m depth; results represent averages per cruise per year

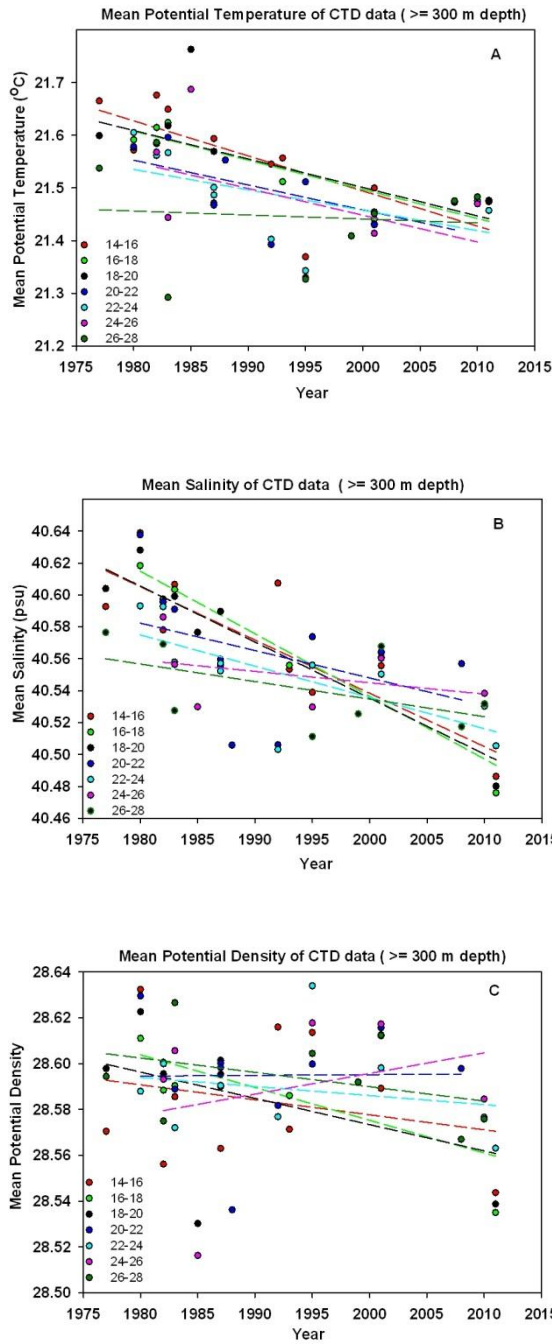


Figure 3-15: a, b and c: Properties of the RSDW for different sub-regions in the Red Sea from CTD data

a) Potential temperature ( $\theta$ )

$$\theta (14-16) = - 6.7 \times 10^{-3} (\text{year}-1900) + 22.160$$

$$\theta (16-18) = - 5.5 \times 10^{-3} (\text{year}-1900) + 22.049$$

$$\theta (18-20) = - 5.4 \times 10^{-3} (\text{year}-1900) + 22.041$$

$$\theta (20-22) = - 4.7 \times 10^{-3} (\text{year}-1900) + 21.931$$

$$\theta (22-24) = - 3.9 \times 10^{-3} (\text{year}-1900) + 21.845$$

$$\theta (24-26) = - 5.1 \times 10^{-3} (\text{year}-1900) + 21.956$$

$$\theta (26-28) = - 0.8 \times 10^{-3} (\text{year}-1900) + 21.516$$

b) Salinity (S)

$$S (14-16) = -3.3 \times 10^{-3} (\text{year}-1900) + 40.873$$

$$S (16-18) = -3.9 \times 10^{-3} (\text{year}-1900) + 40.929$$

$$S (18-20) = -3.5 \times 10^{-3} (\text{year}-1900) + 40.887$$

$$S (20-22) = -1.7 \times 10^{-3} (\text{year}-1900) + 40.720$$

$$S (22-24) = -1.9 \times 10^{-3} (\text{year}-1900) + 40.732$$

$$S (24-26) = -0.71 \times 10^{-3} (\text{year}-1900) + 40.616$$

$$S (26-28) = -1.1 \times 10^{-3} (\text{year}-1900) + 40.645$$

c) Potential density ( $\sigma_\theta$ )

$$\sigma_\theta (14-16) = -0.65 \times 10^{-3} (\text{year}-1900) + 28.643$$

$$\sigma_\theta (16-18) = -1.4 \times 10^{-3} (\text{year}-1900) + 28.718$$

$$\sigma_\theta (18-20) = -1.2 \times 10^{-3} (\text{year}-1900) + 28.688$$

$$\sigma_\theta (20-22) = 0.003 \times 10^{-3} (\text{year}-1900) + 28.592$$

$$\sigma_\theta (22-24) = -0.04 \times 10^{-3} (\text{year}-1900) + 28.626$$

$$\sigma_\theta (24-26) = 0.09 \times 10^{-3} (\text{year}-1900) + 28.506$$

$$\sigma_\theta (26-28) = -0.06 \times 10^{-3} (\text{year}-1900) + 28.652$$

# Chapter 4 Heat and salt storage in the Red Sea

## 4.1 Introduction

Heat and salt storage in the upper layers of the ocean plays an important role in the dynamics of the atmosphere-ocean system. The salt storage in the ocean mainly depends on fresh water fluxes defined as evaporation-precipitation. The heat storage capacity of the world ocean is much higher than that of the atmosphere by more than three orders of magnitude. Therefore the oceans play an important role in global heat content variation of Earth's climate system (Levitus et al., 2005; Lyman et al., 2006). During the second half of the twentieth century, the analysis of large volumes of data on the world's oceans revealed that they have stored approximately 93% of the heat absorbed by Earth's system because of global warming (Levitus et al., 2012).

The heat and salt storage in the upper layers may be subjected to considerable variations in space and time. For example, large amounts of the heat are gained in the ocean during the summer season and released back to the atmosphere in the winter season, thus affecting the climate of neighbouring areas.

The annual cycle of heat storage for the world oceans and seas has been described by several authors such as Bryan and Schroeder (2005), Bathen (1999), Merle (2003), Levitus (1984), Maiyza (1993), Ivchenko et al. (2010), Anotonov et al. (2004) and Kamel and Eid (2005). A number of studies such as Levitus (1986) have also described the annual cycle of salt storage in the world's oceans and seas.

The objective of this chapter is to quantify the temporal variation (time series) of heat and salt storage in the upper layers ( $\leq 300\text{m}$ ) and deep layers ( $\geq 300\text{m}$ ) of the

Red Sea's water. The focus of this work resulted from the lack of literature for this kind of study on the Red Sea.

## 4.2 Data and method

The data used in this study are retrieved from the sources mentioned in Chapter 2. It should be mentioned that only CTD, bottle and Argo data from 1977 to 2011 have been used in this part of the study. The potential temperature and salinity data were interpolated vertically onto 18 standard depth levels: 0, 10, 20, 30, 50, 75, 100, 150, 200, 250, 300, 400, 500, 600, 700, 800, 900 and 1,000 m.

## 4.3 Heat and salt storage of the Red Sea Water

Typically, heat and salt storage calculations came from the depth integration of the potential temperature and salinity in the water column. Therefore, the direct way to calculate heat storage (HS) and salt storage (SS) at any point is defined as (Levitus, 1984, 1986, 1987)

$$HS = \int_{-h}^0 \rho C_p \theta dz \quad (4.1)$$

$$SS = \int_{-h}^0 \rho CS dz \quad (4.2)$$

Heat ( $Jm^{-2}$ ) storage and salt ( $kg m^{-2}$ ) storage have been estimated using the following finite-difference approximation (Maiyza, 1993):

$$HS = \frac{1}{8} \sum_{i=1}^{i=N} (\rho_i + \rho_{i+1})(C_{p_i} + C_{p_{i+1}})(\theta_i + \theta_{i+1})(z_{i+1} - z_i) \quad (4.3)$$

$$SS = \frac{1}{8} \sum_{i=1}^{i=N} (\rho_i + \rho_{i+1})(C_i + C_{i+1})(S_i + S_{i+1})(z_{i+1} - z_i) \quad (4.4)$$

The variations of the specific heat and density of sea water are sufficiently small and vary so insignificantly that they can be used as constant values. However, the  $C_p$  and  $\rho$  have been calculated at each standard depth level, where:

$C_{p_i}$ = specific heat capacity ( $J kg^{-1} ^\circ C^{-1}$ ),

$\rho_i$ = water density ( $kg m^{-3}$ ),

$\theta_i$ = potential temperature ( $^{\circ}\text{C}$ ),

$S_i$ = salinity of sea water,

$C_i$ = constant conversion factor (1 kg/1000 gm),

$z_i$ = level depth of water column and subscript  $i$  refers to  $i$  th level, and

$\Delta z = z_{i+1} - z_i$  ;  $z = 0$ , when  $i = 1$  and  $z = -h$  when  $i = N$ .

Heat and salt storage was calculated at each station by vertical integration (4.1 and 4.2) from the surface through all the standard depths to a specific depth and then averaged per year and per cruise to produce one single value, regardless of the season and the area of the observation. For example, if we have three stations in 1977 in different locations in the Red Sea, heat and salt storage was calculated at each station from surface to specific depths and then averaged per year and per cruise to get one single average value for heat or salt. The assumption is valid for the deep layer (300-1000) and the results are not sensitive to this assumption as we discuss in the quality control section (section 2.3.2). However, we look at the upper layers at different depth intervals just to see how the signals of heat and salt storage react over the time series.

This dataset was divided into two groups:

**Upper layers:** In order to study the changes in heat and salt storage over time in the upper layers of the Red Sea (from the surface to 300 m depth), four depth levels were chosen with depth intervals:  $z = 0-100$ ,  $100-200$ ,  $200-300$  and  $0-300$  m. A total of 520 stations were analysed. Figure 4-1a shows the distribution of temperature and salinity profiles throughout the completed period analysed for the selected depth levels  $0-100$ ,  $100-200$ ,  $200-300$  and  $0-300$  m for upper layers  $\leq 300$  m in the RSW.

**Deep layers:** Here the changes in heat and salt storage were investigated in the deep layers (between 300 and 1000 m depth). Therefore, the integration of temperature and salinity is assumed to be representative of heat and salt storage in the entire deep water column ( $z=300-1000$  m depth). The consideration for this depth was based on availability of maximum depth in the majority of the dataset. As previously mentioned, the thermohaline properties of the Red Sea deep water below 300 m depth are almost homogenous. A total of 209 stations were analysed in this section. Figure 4-1b shows the distribution of the temperature and salinity profiles throughout the completed period analysed for selected depth levels within deep layers of 300-1000 m depth in the RSW. Clearly, the data used for the deep layer analysis was located along the central axis of the Red Sea as result of the Red Sea topography.

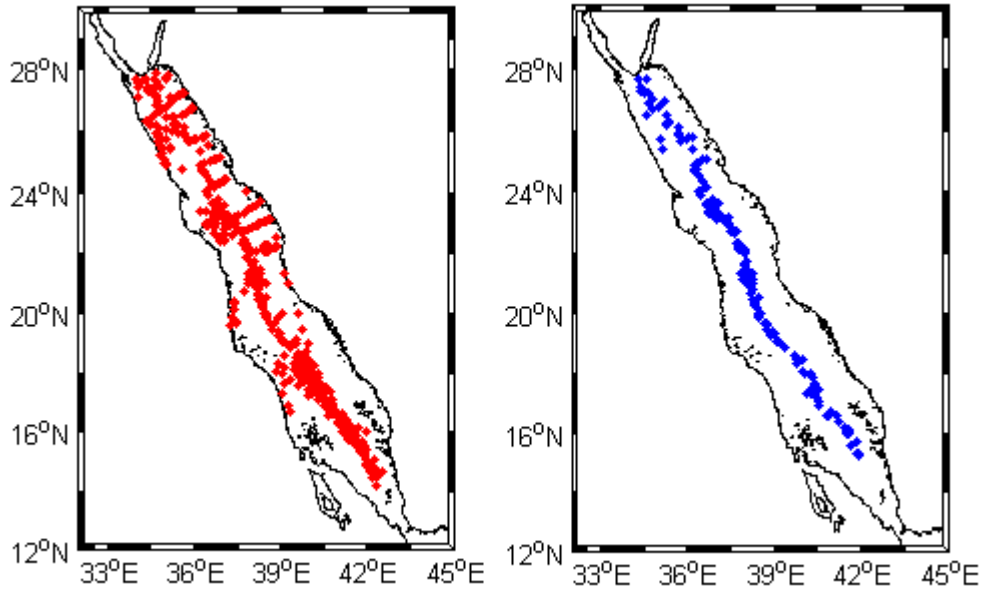


Figure 4-1: Distribution of the stations used for a) upper layers (0-300m) (left) and b) deep layers (300-1000m) (right) in the Red Sea

## 4.4 Results

### 4.4.1 Heat and salt storage variability in the upper layers

The Red Sea water column has been decomposed in 3 layers of 100 m thickness, from the surface to a depth of 300 m for the upper layers (0-300m). Linear trends for the heat and salt storage time series at each layer were estimated using linear regression by means of the least squares method. The slope of the regression represents a trend or mean rate of annual change. The time series of heat and salt storage is shown in Figures 4-2 and 4-3, and resulting trends (Equations 4.3 and 4.2) are presented in Table 4-1.

The variability of the heat storage in the upper 100 m layer includes the Red Sea's surface and the Gulf of Aden's water masses (Figure 4-2a), and shows large variation compared to the other layer in terms of the magnitude due to the interaction of air-sea processes, which gained more heat than other layers. The heat storage varies in the upper 100 m layer from a minimum of  $8.70 \pm 0.11 \times 10^9 \text{ Jm}^{-2}$  in 1984 to a maximum of  $10.80 \pm 0.34 \times 10^9 \text{ Jm}^{-2}$  in 2000. These magnitudes are less than the climatology values between  $9.13 \times 10^9 \text{ Jm}^{-2}$  and  $11.79 \times 10^9 \text{ Jm}^{-2}$  estimated by Kamel and Eid (2005).

The variability of the heat storage shows that there is a negative trend (cooling) over time with an average of  $0.6 \pm 9.4 \times 10^6 \text{ Jm}^{-2} \text{ yr}^{-1}$  (0-100 m). However, the layer

(100-200 m) beneath it shows the opposite sign with a positive trend (warming) for heat storage by an average of  $5.4 \pm 2.5 \times 10^6 \text{ Jm}^{-2} \text{ yr}^{-1}$ . In the layer at 200-300 m the slope of the regression line indicates that there is a negative trend (cooling) by an average of  $0.4 \pm 0.6 \times 10^6 \text{ Jm}^{-2} \text{ yr}^{-1}$ .

|  | Period    | Linear trend (yr <sup>-1</sup> ) | SE   |
|--|-----------|----------------------------------|------|
| Heat Storage (*10 <sup>6</sup> J m <sup>-2</sup> ) |           |                                  |      |
| 0 -100 m   | 1977-2011 | -0.6                             | 9.4  |
| 100-200 m  | 1977-2011 | 5.4                              | 2.5  |
| 200-300 m  | 1977-2011 | -0.4                             | 0.6  |
| 0 -300 m   | 1977-2011 | 3.7                              | 10.7 |
| 300-1000 m   | 1977-2011 | -13                              | 3    |
| Salt Storage ( kg m <sup>-2</sup> )                |           |                                  |      |
| 0 -100 m   | 1977-2011 | 0.95                             | 0.95 |
| 100-200 m  | 1977-2011 | -0.08                            | 0.15 |
| 200-300 m  | 1977-2011 | -0.14                            | 0.08 |
| 0 -300 m   | 1977-2011 | 0.77                             | 0.89 |
| 300-1000 m   | 1977-2011 | -1                               | 0.5  |

Table 4-1: Results are presented for the heat (\*10<sup>6</sup> J m<sup>-2</sup>) and salt (kg m<sup>-2</sup>) storage for upper (0-300m) and deep layers (300-1000); the linear trend and the standard error are also presented

The trend of heat storage is positive (warming) for the 0-300 m layer as a whole water column for the upper layers by an average of  $3.7 \pm 10.1 \times 10^6 \text{ Jm}^{-2} \text{ yr}^{-1}$ . The magnitude of the heat storage in the whole 0-300 m layer varies in range between  $26.31 \pm 0.10 \times 10^9 \text{ Jm}^{-2}$  in 1984 and  $28.92 \pm 0.19 \times 10^9 \text{ Jm}^{-2}$  in 1989, which are lower than the climatology values of  $26.98 \times 10^9 \text{ Jm}^{-2}$  and  $29.92 \times 10^9 \text{ Jm}^{-2}$  for this layer (Kamel & Eid, 2005). It should be noted that all these calculated trends are not statistically significant except for the 100-200 m layer, which has a statistically significant trend at a confidence level of 95 %.

Salt storage in the upper 100 m layer during the period between 1977 and 2011 (Figure 4-3a) indicates that there is an increased trend (salinification) by an average of  $0.95 \pm 0.95 \text{ kg m}^{-2} \text{ yr}^{-1}$  while the linear trend in the layer beneath it (100-200 m) shows a decreased trend (freshening) for salt storage by an average of  $0.08 \pm 0.15 \text{ kg m}^{-2} \text{ yr}^{-1}$ . The magnitudes of the salt storage in the upper 100m vary from  $3.70 \pm 0.04 \times 10^3 \text{ kg m}^{-2}$  in 1995 to  $3.93 \pm 0.005 \times 10^3 \text{ kg m}^{-2}$  in 2000, which are less than the climatology magnitude values of  $3.81 \times 10^3 \text{ kg m}^{-2}$  and  $4.17 \times 10^3 \text{ kg m}^{-2}$  estimated by Kamel and Eid (2005).

For the 200-300 m layer, the slope of the regression line indicates that there is a negative trend (freshening) by an average of  $0.14 \pm 0.08 \text{ kg m}^{-2} \text{ yr}^{-1}$ .

The slope of the regression lines for upper layers of 0-300 m as a whole water column indicate that there is an increased trend (salinification) for salt storage by an average of  $0.77 \pm 0.89 \text{ kg m}^{-2} \text{ yr}^{-1}$ . The magnitude of the salt storage in this layer varies between  $12.04 \pm 0.04 \times 10^3 \text{ kg m}^{-2}$  and  $12.25 \pm 0.04 \times 10^3 \text{ kg m}^{-2}$ , which are lower than the climatology values between  $12.06 \times 10^3 \text{ kg m}^{-2}$  and  $12.59 \times 10^3 \text{ kg m}^{-2}$  estimated by Kamel and Eid (2005). It should be noted that all these trends calculated for these layers are not statistically significant at the 95% level.

The heat and salt storage in the whole water column (0-300 m) shows positive (warming and salinification) trends for the period between 1977 and 2011 but these are statistically not significant at the level of 95%. It must be mentioned that the data in Figure 4-1a and b are for different seasons and different locations. Therefore it is likely that seasonal variations in the distribution of data points severely affected our ability to detect long period trends in the seasonally varying water above 300 m depth (Figure 3-1).

#### *4.4.2 Heat and salt storage variability in the deep layers*

A similar analysis was done for heat and salt storage in the deep layers from a depth of 300 m to 1000 m (Figure 4-4a and b). Over the long term (1977-2011), the deep layers of between 300 and 1000 m in depth show a clear decreasing trend in both heat and salt storage over time (Figure 4-4a and b). Generally there is a close match between the signals of cooling and freshening occurring in the Red Sea deep layers. The correlation between the heat and salt storage reaches 0.4 but it is not statistically significant at 95% level.

The heat and salt storage in the RSDW has decreased by averages of  $-13 \pm 3 \times 10^6 \text{ Jm}^{-2} \text{ yr}^{-1}$  and  $-1 \pm 0.5 \text{ kg m}^{-2} \text{ yr}^{-1}$  respectively. Both of these trends have statistically significant negative trends with a confidence level of more than 95%. The results indicate that a general decrease of heat and salt storage (Figure 4-4a and b),  $-0.53 \times 10^9 \text{ J m}^{-2}$  and  $-0.04 \times 10^3 \text{ kg m}^{-2}$  respectively, occurs over the Red Sea deep layers (300-1000 m) for the period between 1977 and 2011.

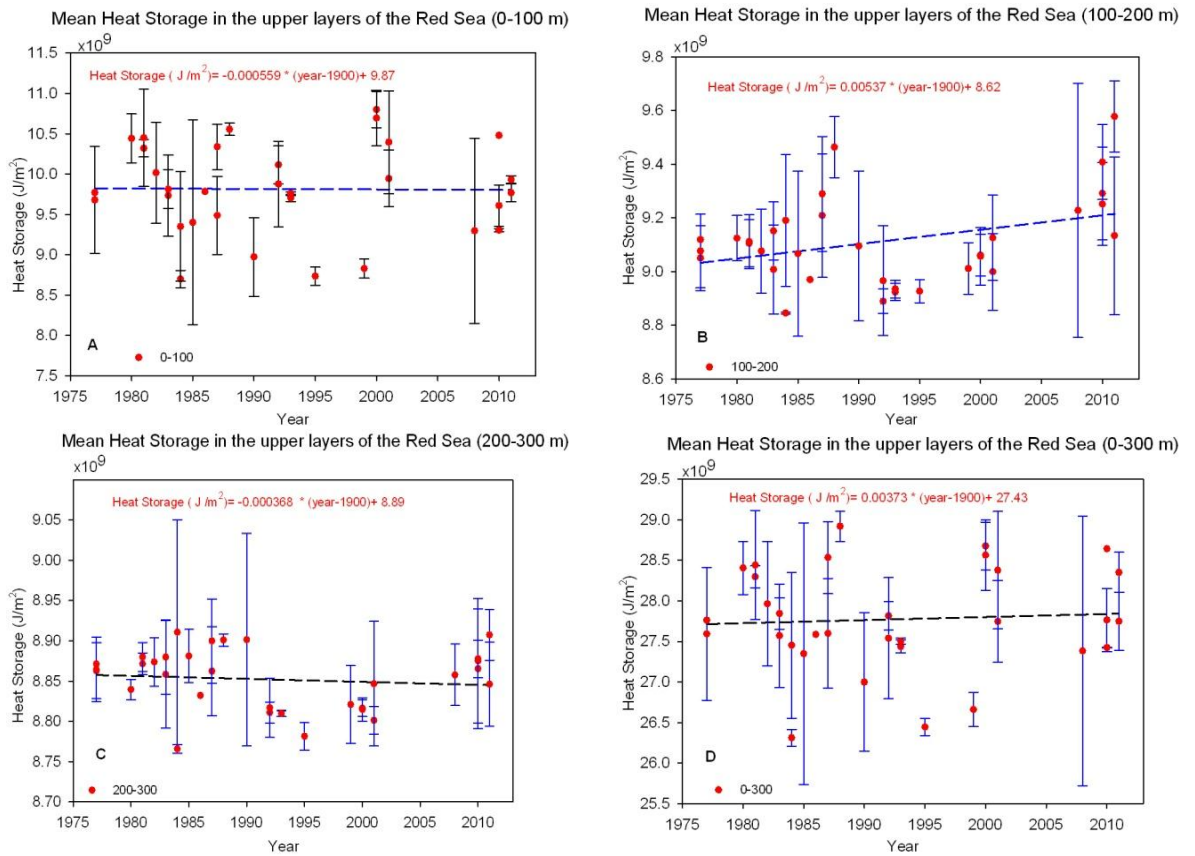


Figure 4-2: Mean heat storage ( $Jm^{-2}$ ) in the upper layers in each 100 m layer from the surface to 300 m depth in the Red Sea. Vertical bars represent one standard deviation and the dashed lines represent a linear regression. Note that the y-axis scales are different

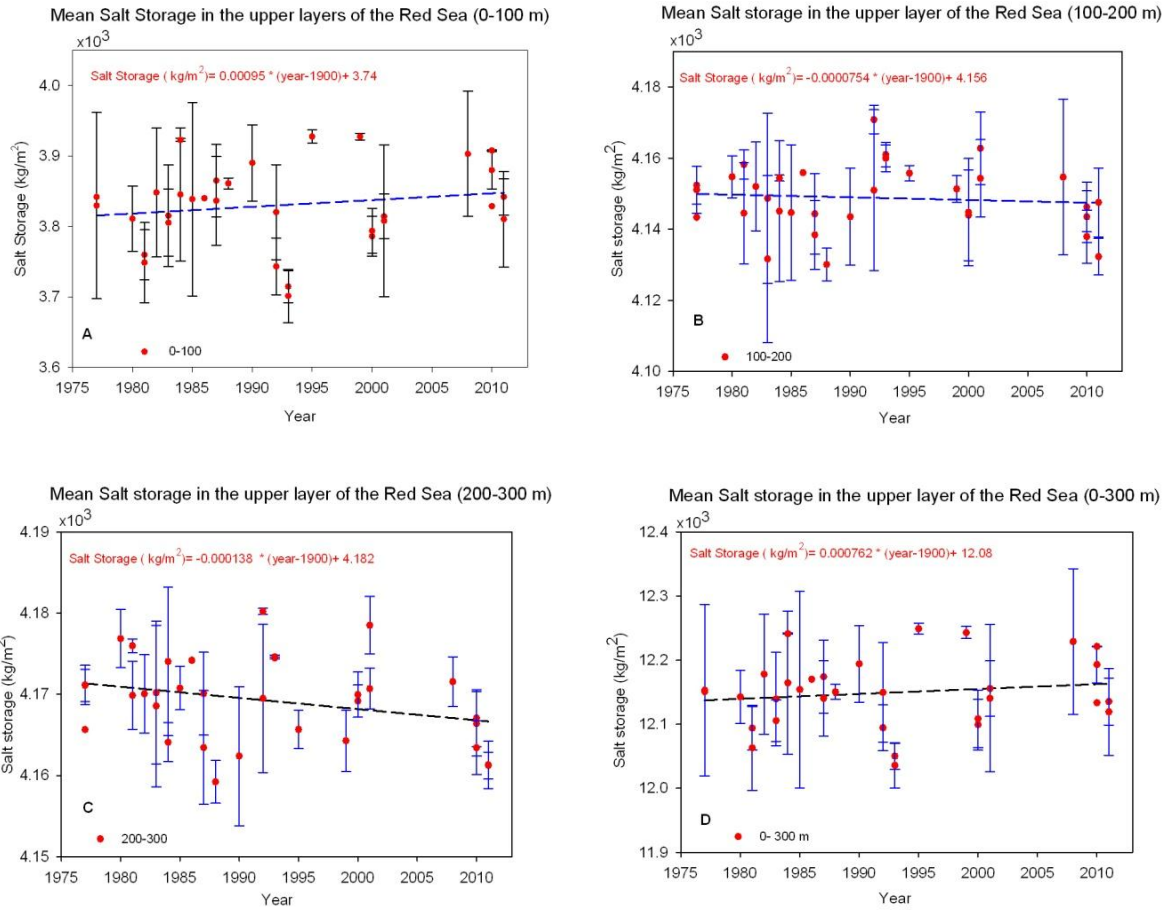


Figure 4-3: Mean salt storage ( $\text{kg/m}^2$ ) in the upper layers in each 100 m layer from the surface to 300 m depth in the Red Sea. Vertical bars represent one standard deviation and the dashed lines represent a linear regression. Note that the y-axis scales are different

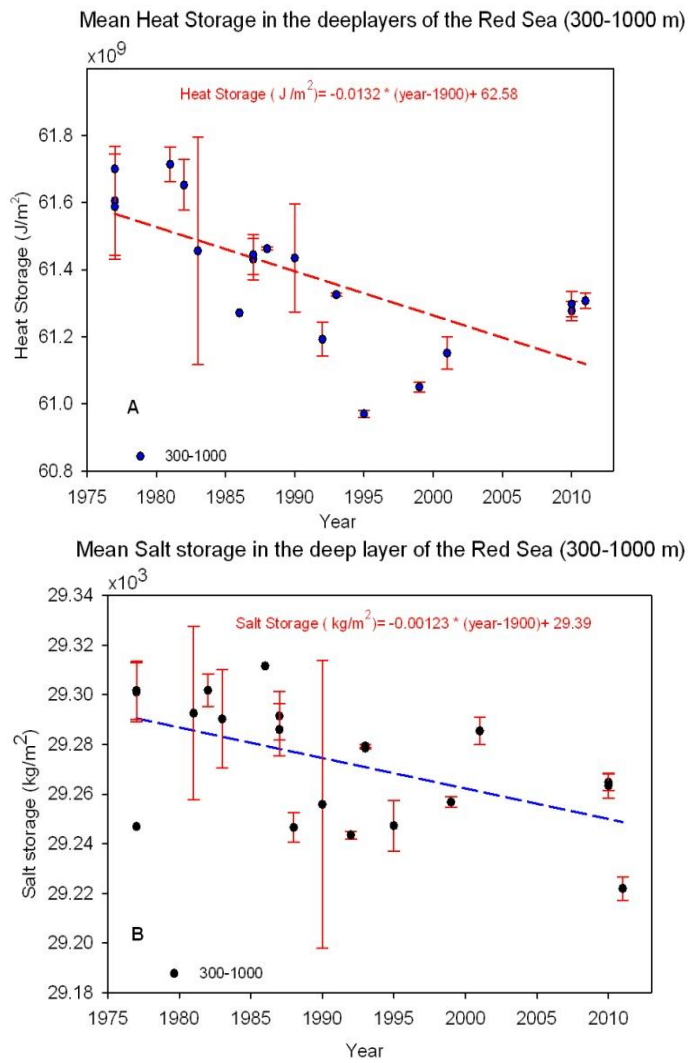


Figure 4-4: Linear regression for the properties of RSDW from 300 m to 1000 m depth for (a) heat storage ( $\text{J/m}^2$ ) and (b) salt storage ( $\text{kg/m}^2$ ). Vertical bars represent one standard deviation and the dashed lines represent a linear regression

## 4.5 Discussion and conclusion

Heat and salt storage variability in the upper (0-300 m) and deep (300-1000 m) layers of the Red Sea is investigated using hydrographic data from different surveys which were irregularly distributed in time and space between 1977 and 2011. Linear regression analysis was used to quantify heat and salt storage changes that have occurred the periods. The analysis indicates that there are warming and salinification for the upper layer (0-300 m) of the Red Sea for the overall period (1977-2011) but these trends are not statistically significant. However, our results indicate that there are significant signals of cooling and freshening in the deep layers (300-1000 m) for the last three decades. This agrees with our findings showing a statistically significant decrease in the potential temperature and salinity in the Red Sea deep layers (below 300 m) between 1950 and 2011.

Heat storage in the deep layers of the RSDW is equivalent to a heat loss of  $-0.41 \pm 0.095 \text{ Wm}^{-2}$ . In the upper layers of 0-300 m, this change is equivalent to a heat gain of  $0.11 \pm 3.2 \text{ Wm}^{-2}$ . Salt storage in the deep layers in the RSDW decreased with an average of  $-1.23 \pm 0.46 \text{ Kg m}^{-2} \text{ yr}^{-1}$ .

There are major differences between the calculated trends for upper (0-300 m) and deep (300-1000 m) layers; the estimated trends for the two sets of layers show opposing signals. Nevertheless, none of the changes calculated (heat and salt storage) in each layer for the upper layers were significant, except for heat storage in the second layer (100- 200 m). The variability of heat and salt storage is not synchronised in either time or space as result of different control mechanisms for the variability. The variability of heat storage in the upper water column is due to the interaction of air-sea processes, in particular heat gained due to solar radiation and losses due to latent heat flux, sensible heat flux and longwave radiation. Salt storage in the water column is controlled by evaporation and precipitation and the divergence of the salt within the water column (SHI et al., 2003). It is not possible to detect from these datasets whether or not long-term changes in heat and salt storage for the upper Red Sea layers are due to irregular temporal and spatial distribution of stations and whether a lack of observational data in the Red Sea restricted our ability to establish spatial and temporal patterns in interannual variability of potential temperature and salinity in the upper layers.

Kamel and Eid (2005) investigated seasonal changes in the heat and salt storage in the upper 300 m of the Red Sea by subdividing the Red Sea basin into four regions

using historical data obtained from the World Ocean Atlas 1998. They found that the heat storage in the upper layers (0-300 m) increases southward of the Red Sea with the maximum value for the heat storage found at latitudes between 17°N and 20°N. The salt storage decreases from north to south and the maximum value is found in the extreme north of the Red Sea. These patterns reflect the distribution of the temperature and salinity over the Red Sea. As mentioned in Chapter 1 (section 1.4, Figure 1-3, middle panel), the salinity at the surface and subsurface increases from south to the north of the Red Sea (Vercelli, 1927). Grasshoff (1969) attributed these increases to two main factors: evaporation and the mixing of the surface water with the more saline deep water through turbulence. Conversely, the sea surface temperature increases from the north towards the maximum in the southern area of the Red Sea (zone of maximum temperature) and then decreases towards Perim Island at the entrance of the Strait of Bab el Mandeb (Figure 1-3, upper panel). Buchan (1895) found that the temperature in the subsurface layers (at 100 m) increases from 18.3°C in the north to 23.9°C in the south of the Red Sea.

The heat and salt storage of the deep water supports our finding for long cooling and freshening trends in relation to the potential temperature and salinity (1950-2011). RSDW is formed through three possible contributions: outflow from the Gulf of Aqaba, outflow from the Gulf of Suez and open convection in the northern Red Sea (Wyrki, 1974; Cember, 1988). It has been shown that deep layer cooling and freshening was an effect of plume convection from the Gulf of Suez under the winter conditions of 1982/1983 (Woelk & Quadfasel, 1996). They linked the triggering and the intensity of the convection to the atmospheric forcing, such as cooling and evaporation over the Gulf of Suez (as the main source for RSDW formation) during the winter of 1982/83 as shown in Figure 3-14. However, the winter time-integrated NOCS heat fluxes anomalies indicate that the cooling and net evaporation increase over the three source regions for deep water formation and not just over the Gulf of Suez (Figures 3-11 and 3-13 and Table 4-2). The cooling signal and the net evaporation over three sources region are very well correlated to each other.

The net heat flux and net evaporation time series over the northern Red Sea, Gulf of Suez and Gulf of Aqaba show that the winters of 1986/1987, 1988/1989, 1989/1990, 1991/1992 and 1999/2000 were also periods of potentially high renewal of the deep water in the northern Red Sea. The long trend of cooling and freshening observed in the Red Sea deep water is linked to the convection which occurs irregularly rather than

constantly during wintertime in the source regions for the RSDW formation. It should be noticed that the winter 1991/1992 stands out as having extreme forcing with NHF anomalies of the order -41.68, -44.04 and -38.40  $\text{Wm}^{-2}$  for the Gulf of Suez, the Gulf of Aqaba and northern of the Red Sea respectively. Raitsos et al. (2013) noted that the winter of 1992-93 had the coldest signal in the SST during 1985-2007 over the Red Sea region. Also, it is interesting to note that when the cooling signal notably increased in several winter times are occasions when the Southern Oscillation Index (SOI) is low, i.e., to El Nino years (see Wallace et al., 1998 for SOI record). This influence of the Pacific pressure system has been detected by Villwock (1994) in the equatorial part of the Indian Ocean.

More recently, Papadopoulos et al. (2013) has explored the atmospheric forcing of the winter air-sea heat fluxes over the northern Red Sea during 1985-2011, they report that an extreme heat loss (sum of latent and sensible heat flux lower than  $-400 \text{Wm}^{-2}$ ) is observed over the northern Red Sea when anticyclonic conditions prevail over the Mediterranean Sea region to eastern Asia. A distinct large scale sea level pressure (SLP) pattern affects the wind regime over the northern Red Sea; this transfers dry and cold air from higher latitudes and generates a steep SLP gradient, producing strong winds. As sequence of that enhances the rate of evaporation over the three sources formation region which can leads to extreme heat loss at the sea surface.

Papadopoulos et al. (2013) show that the temporal distribution of the extreme events is in accordance with the negative latent and sensible heat loss trend as the number of strong heat loss increases with time.

The heat exchange between the Red Sea and the Gulf of Aden through the strait of Bab el Mandeb by advection suggests that the annual exchange is small and plays little part in the seasonal change in the total heat content (Patzert, 1972b). The annual net heat exchange by advection through the strait of Bab el Mandeb is  $-7$ ,  $-8 \pm 2$  and  $-11 \pm 5 \text{Wm}^{-2}$  (Patzert, 1974b; Tragou et al., 1999; Sofianos et al., 2002). However, our result from the inverse model indicate that there is heat loss by advection of  $-23.5 \pm 5 \text{Wm}^{-2}$  ( $\sim -10.6 \text{TW}$ ); however, this applies to August only and does not represent the annual mean of the heat exchange through the strait of Bab el Mandeb. If we compare the heat storage changes during 1977-2011 in the RSDW with advected heat through the strait of Bab el Mandeb, it is found that the changes in heat storage with magnitude of  $-0.04 \times 10^{10} \text{W}$  represent less than 1% of the advected heat (with magnitude of  $-1.06 \times 10^{13} \text{W}$ ).

In order to determine quantitatively the equivalent of the heat and salt storage changes that occurred in the RSDW to surface fluxes, we used the time series shown in Figures 3-11 and 3-12 for net heat flux and evaporation and Figure 4-4 for heat and salt storage. A calculation has been made for similar periods (1977-2001) as can be seen in Table 4-2 and using following equation

$$\frac{\Delta C_{i+1} - \Delta C_i}{\Delta t} = W m^{-2} \quad (4.3)$$

Where  $\Delta C$  refers to the changes of the heat and salt storage in RSDW respectively;  $i$  refers to specific time. These changes for specific time can be calculated from the regression equation for the periods between 1977 and 2001

$$HS = -0.026 \times 10^9 (\text{year} - 1900) + 63.68 \quad (4.4)$$

$$SS = -0.0012 \times 10^3 (\text{year} - 1900) + 29.39 \quad (4.5)$$

Using the equations (4.3) to (4.5) for the time series (1977-2001) for both data, it is found that the observed changes in the heat storage in the RSDW is equivalent to  $-1.19 \text{ Wm}^{-2}$  which has the same order of magnitude, for the net heat flux over the Red Sea and the three sources regions; the northern of the Red Sea, the Gulf of Suez and the Gulf of Aqaba. For the salinity calculation if we assume that there is an addition of fresh water volume by  $\Delta V$  each year, then the density does not change.

The initial volume of the beginning of the year is equal to  $V$  and the final volume at the end of the year will be equal to  $V + \Delta V$ . The initial salinity is equal to  $S_o$  and the final salinity will be equal to  $S_f$ . The initial salt =  $V \times S_o \times \rho$  gm of salt. Salt =  $(V \times S_o \times \rho) / 1000$  kg of salt

The final salt =  $((V + \Delta V) \times (S_o + \Delta S) \times \rho) / 1000$  kg of salt.

The mass of the salt cannot change. The initial salt will be equal to the final salt

$$(V \times S_o) = (V + \Delta V) \times (S_o + \Delta S)$$

$$(V \times S_o) = (V + S_o + \Delta V \times S_o + \Delta S \times V + \Delta S \times \Delta V)$$

$$0 = (\Delta V \times S_o + \Delta S \times V + \Delta S \times \Delta V) \text{ ignoring last (1)}$$

$$\Delta V = (\Delta S \times V) / S_o$$

$V = Ah$  assume  $h$  changes but the area does not change

$$\Delta h = (\Delta S \times h) / S_o$$

$h = 700 \text{ m}$ ,  $S_o = 40.0$ ,  $\Delta S = 7.010^{-4}$ . These value comes from figures 3-10b

$$\Delta h = (\Delta S \times h) / S_o = 0.01225 \text{ m/year}$$

Fresh water added =  $0.01225 \text{ m/year}$

Now let us check the size of the ignored term in (1)

$$0 = (\Delta h \times S_o + \Delta S \times h + \Delta S \times \Delta h)$$

$$0 = (0.01 \times 40 + 7.010^{-4} \times 700 + 7.010^{-4} \times 0.01)$$

$$= 0.4 + 0.49 + 0.10^{-5}$$

The last term is very small compared with the other terms. However, the calculations show that the salt is not consistent with evaporation changes.

The flushing time calculated from the inverse box model is 69 years for the deep Red Sea water below 300 m which is in the agreement with the timescale estimated from previous studies in the literature. However, the signal of cooling and freshening that has occurred in the RSDW is linked to winter convection such event during 1982/83 by Woelk and Quadfasel (1996).

| Time      | HS<br>( $10^6 \text{ J m}^{-2}$ ) | SS<br>( $\text{kg m}^{-2}$ ) | NHF ( $\text{Wm}^{-2}$ ) |                   |                   |                   |
|-----------|-----------------------------------|------------------------------|--------------------------|-------------------|-------------------|-------------------|
|           |                                   |                              | RS                       | NRS               | GS                | GA                |
| 1973-2006 | -                                 | -                            | $-0.99 \pm 0.25$         | $-1.12 \pm 0.49$  | $-1.75 \pm 0.49$  | $-1.58 \pm 0.47$  |
| 1977-2001 | $-26 \pm 4$                       | $-1 \pm 0.7$                 | $-1.09 \pm 0.38$         | $-0.70 \pm 0.57$  | $-1.07 \pm 0.57$  | $-1.00 \pm 0.57$  |
| 1977-2011 | $-13 \pm 3$                       | $-1 \pm 0.5$                 | -                        | -                 | -                 | -                 |
|           |                                   |                              | E ( $\text{myr}^{-1}$ )  |                   |                   |                   |
|           |                                   |                              | RS                       | NRS               | GS                | GA                |
| 1973-2006 | -                                 | -                            | $0.010 \pm 0.002$        | $0.012 \pm 0.004$ | $0.020 \pm 0.005$ | $0.018 \pm 0.005$ |
| 1977-2001 | $-26 \pm 4$                       | $-1 \pm 0.7$                 | $0.011 \pm 0.004$        | $0.007 \pm 0.006$ | $0.012 \pm 0.006$ | $0.011 \pm 0.006$ |
| 1977-2011 | $-13 \pm 3$                       | $-1 \pm 0.5$                 | -                        | -                 | -                 | -                 |

Table 4-2: Results are presented for the heat ( $*10^6 \text{ J m}^{-2}$ ) and salt ( $\text{kg m}^{-2}$ ) storage for the RSDW (300-1000) and Net heat fluxes ( $\text{Wm}^{-2}$ ) and evaporation ( $\text{myr}^{-1}$ ) anomalies over the Red Sea (RS) and the sources region: Northern of the Red Sea (NRS), Gulf of Suez (GS) and Gulf of Aqaba (GA); the linear trend and the standard error are also presented

# Chapter 5 Box inverse model

## 5.1 Introduction

One of the objectives of this thesis is to diagnose the circulation of the Red Sea such as the southward export of the RSOW into the Gulf of Aden through the Strait of Bab el Mandeb. The main technique used in this study is box inverse modelling in order to quantify the summer field fluxes (volume, heat and salt fluxes) in the Red Sea.

In this chapter a short review of the inverse modelling method used in oceanography is presented together with the basic machinery of the inverse box model. Ocean circulation has been determined by oceanographers using inverse methods for more than three decades. All inverse methods contain a combination of observation and dynamical information to estimate unknown features of ocean circulation. A box inverse model is very useful in combined equations describing the conservation properties of the flow with hydrographic data sections. The inverse methods have been applied to ocean circulation problems by Wunsch (1978), who used the box inverse model to determine the geostrophic transport in North Atlantic (estimate of absolute velocity from thermal wind and unknown reference level velocity). The Wunsch formulation of the inverse problem has become known as the method for the inverse box model. Since then, the inverse box model has become commonly used to estimate ocean circulation and transports using hydrographic data (McIntosh & Rintoul, 1997; Ganachaud, 2003a)

The inverse models have been used on a large scale using data from the World Ocean Circulation Experiment to determine mass, heat and freshwater transports (Ganachaud & Wunsch, 2003; Ganachaud, 2003b; Lumpkin & Speer, 2007). It has also been used for regional studies by Naveira Garabato et al. (2003) in the Scotia Sea, McDonagh and King (2005) in the South Atlantic and Fraile-Nuez et al. (2008) in the

Bay of Biscay. However, the accuracy of a box inverse model applied to real data is highly sensitive to design of the model and quality of the data (McIntosh & Rintoul, 1997; Jullion, 2008). The rest of the chapter will introduce the theory of the box inverse model and its strength and weaknesses.

## 5.2 The theory of the box inverse model

### 5.2.1 Basic inverse model

To describe how the box inverse model works, a simple example using a basic inverse model is presented and the inverse model constructed step by step. Let us assume a volume of ocean bounded by a pair of hydrographic sections and land in the horizontal, and divided vertically into isopycnal layers as shown in Figure 5-1.

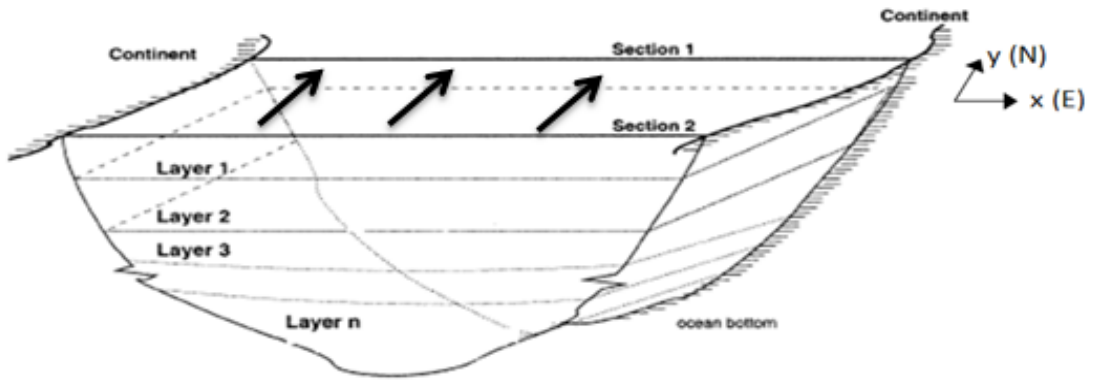


Figure 5-1: Inverse model structure reproduced from Ganachaud and Wunsch (2003). The volume of the ocean is closed by two hydrographic sections (S1 and S2) and land boundaries

We assumed the mean circulation to be steady, hydrostatic and in geostrophic balance

$$\frac{\partial p}{\partial z} = -g\rho \quad (5.1) \quad f u = -\frac{1}{\rho} \frac{\partial p}{\partial y}, \quad f v = \frac{1}{\rho} \frac{\partial p}{\partial x} \quad (5.2)$$

where  $f$  is the coriolis parameter ( $f = 2\Omega \sin \varphi$ ,  $\Omega$  is the angular speed of the rotation rate of Earth ( $7.29 \times 10^{-5} \text{ s}^{-1}$ ) and  $\varphi$  is the geographic latitude),  $u$  and  $v$  are the horizontal components of velocity ( $\text{m s}^{-1}$ ) in the  $x$  and  $y$  direction respectively,  $\rho$  is the density of sea water ( $\text{kg m}^{-3}$ ),  $g$  is the acceleration of gravity ( $\text{m s}^{-2}$ ) and  $p$  is pressure (Pa).

The geostrophic approximation in Equations 5.1 and 5.2 can be written in the form of the thermal wind relation

$$f \frac{\partial u}{\partial z} = \frac{g}{\rho} \frac{\partial \rho}{\partial y} \quad (5.3)$$

$$f \frac{\partial v}{\partial z} = \frac{-g}{\rho} \frac{\partial \rho}{\partial x} \quad (5.4)$$

which defines the vertical velocity shear ( $\partial u/\partial z$  and  $\partial v/\partial z$ ). In our example the velocity will be estimated as being normal for the section and the sections being only zonal (Figure 5-1). From the thermal wind equation, the geostrophic velocity is calculated only in the northward direction ( $u=0$ ) and integrating Equation 5.4 in the vertical from the surface to the depth of the reference level to obtain:

$$v(x, z) = \underbrace{\frac{-g}{\rho f} \int_{z_0}^z \frac{\partial \rho}{\partial x} dz}_{\text{baroclinic component}} + \underbrace{b(x, z_0)}_{\text{barotropic component}} = v_R(x, z) + b(x) \quad (5.5)$$

The first term of the right hand side of Equation 5.5 is relative velocity,  $v_R(x, z)$ , which can be determined from observation of temperature and salinity,  $z_0$  is the depth of the reference level and  $z$  is the sea surface. The second term is the unknown reference velocity at  $z_0$ ,  $b$  is the constant of integration,  $v(x, z)$  is the absolute velocity and  $x$  and  $z$  are the horizontal and vertical coordinates respectively.

We can assume the volume and other tracers (heat, salt and chemicals) are conserved (continuity equation) due to the closed volume. The equation may be written as

$$\nabla \cdot \rho(\vec{U}) = 0 \quad (5.6)$$

$$(\vec{U} \cdot \nabla) \rho C = \frac{\partial}{\partial z} \left( \kappa_v \frac{\partial(\rho C)}{\partial z} \right) + \nabla_H^2 \kappa_H(\rho C) + Q \quad (5.7)$$

where  $\vec{U}$  is the three-dimensional velocity vector ( $u, v, w$ ),  $C$  is the tracer concentration per unit mass,  $Q$  is a possible source and  $\kappa_v$  and  $\kappa_H$  are vertical and horizontal eddy diffusivities respectively.  $\nabla_H = \partial/\partial x + \partial/\partial y$ , the horizontal gradient operator. The horizontal diffusion ( $\kappa_H$ ) is not included in model because its inclusion is difficult and the results uncertain.

Using Equation 5.6 and integrating Equation 5.7 over a layer of the box in our example (Figure 5-1) which is bounded horizontally by two sections and land and vertically between selected isopycnal surfaces gives:

$$\left[ \int_W^E \int_{z(\rho_1)}^{z(\rho_2)} v \rho C dz dx \right]_{S_1}^{S_2} = \left[ \int_W^E \int_N^S \left( \kappa_v \frac{\partial(\rho C)}{\partial z} - w \rho C \right) dx dy \right]_{z(\rho_1)}^{z(\rho_2)} + Q \quad (5.8)$$

If  $u$  vanishes because there is no net flux across the boundaries section 1 (S1) and section 2 (S2) then using equation (5.5) we obtain:

$$\left[ \int_W^E \int_{z(\rho_1)}^{z(\rho_2)} (v_R + b_x) \rho C dz dx \right]_{S_1}^{S_2} = \left[ \int_W^E \int_N^S \left( \kappa_v \frac{\partial(\rho C)}{\partial z} - w \rho C \right) dx dy \right]_{z(\rho_1)}^{z(\rho_2)} + Q \quad (5.9)$$

The left hand side is the horizontal transport and can be calculated from the geostrophic velocity across the two sections. The first part of the right hand side is the diffusivity and the second part is vertical advection transport, which can be neglected for now because the vertical exchange between layers defined isopycnally is very small (McIntosh & Rintoul, 1997). So if Equation 5.7 is converted into its numerical form it becomes

$$\sum_{i=1}^n \sum_{j=1}^m D_{ij} L_i (v_{ij} + b_{ij}) \delta_i \rho_{ij} C_{ij} = 0 \quad (5.10)$$

where  $i = 1 \dots n$  is the number of station pairs,  $j = 1 \dots m$  is the number of layers in the box,  $L_i$  is the distance between stations,  $\delta_i \pm 1$  is the unit depending on the transport into or out of the box and  $D_{ij}$  is the thickness of the layers for each station pair. These conservation constraints cannot be satisfied exactly with real data due to incomplete physics in the geostrophic model and existence of noise in every layer. The system can be written as single matrix form as

$$\mathbf{Ax} + \mathbf{n} = \mathbf{b} \quad (5.11)$$

where  $\mathbf{A}$  ( $m \times n$ ) is a matrix with a conservation equation for each station pair and layer, where the elements of matrix  $\mathbf{A}$  consist of station pair layers multiplied by the areas of property concentration and layer interface areas multiplied by mean interfacial property concentration.  $\mathbf{n}$  ( $m \times 1$ ) is an error of each equation,  $\mathbf{x}$  ( $1 \times n$ ) contains the unknown reference velocity  $b_i$  at each station pair and unknown interfacial 'fluxes' for mass, heat and salt anomalies ( $w_m$ ,  $w_h$  and  $w_s$  respectively) and  $\mathbf{b}$  is residual transport resulting from the relative velocity (i.e. the value to which the system is constrained). There are many methods in the literature to solve such system (Wunsch, 1996). Here the inverse problem was solved using Singular Value Decomposition (SVD). This technique allows the researcher to control which information is used in the

solution by choosing the rank of the solution. The SVD transforms any arbitrary matrix into two orthogonal matrices U and V and a usually non-square diagonal matrix  $\Lambda$

$$A = U\Lambda V^T \quad 5.12)$$

The SVD solution seeks least squares fit to simultaneously minimise the size of the solution  $\mathbf{x}$  and the size of the residuals  $(\mathbf{Ax} - \mathbf{b})$ . The SVD solution is the simplest solution in the sense that it introduces the minimum correction to the initial model required to satisfy the constraints (McIntosh & Rintoul, 1997)

### 5.2.2 Weighting and uncertainties

As mentioned before, all the data used and theoretical assumptions are subject to uncertainties and approximation that lead to errors. To solve Equation 5.11, it needs to be weighted to account for these uncertainties. An *a priori* estimate of equations and unknown uncertainties should be introduced to guide the model to a realistic solution. In order to account for the uncertainties in the conservation equations and reference velocity (unknowns), both of the equations (rows) and the unknowns (columns) should be weighted to their *a priori* uncertainties.

The row weighting is the inverse of the square root of the *a priori* equation covariance matrix, which is usually taken to be diagonal in the absence of an *a priori* estimate  $W_r$  (Wunsch, 1996). The column weighting is the square root of the *a priori* solution error covariance matrix, which is also taken to be a diagonal as  $W_c$  for the same reason (McIntosh & Rintoul, 1997), with the size of the diagonal elements chosen to reflect the relative magnitude of the elements of  $\mathbf{x}$ . Determination of the proper weighting for both rows and columns of the matrix is essential in order to achieve good results for the inversion and more experiments are needed to test the sensitivity of the results to the choice of weighting. So the row and column weighting becomes

$$W_r = \begin{pmatrix} 1 & \dots & 0 \\ \frac{1}{\sqrt{\varepsilon_r}} & \dots & \vdots \\ \vdots & \ddots & \vdots \\ 0 & \dots & \frac{1}{\sqrt{\varepsilon_r}} \end{pmatrix} \quad W_c = \begin{pmatrix} 1 & \dots & 0 \\ \frac{1}{\sqrt{\varepsilon_c}} & \dots & \vdots \\ \vdots & \ddots & \vdots \\ 0 & \dots & \frac{1}{\sqrt{\varepsilon_c}} \end{pmatrix}$$

where  $\varepsilon_r$  is a priori uncertainty of the conservation equations and  $\varepsilon_c$  is a priori uncertainty of the reference velocities. Errors may arise from different sources, for example inaccuracy in the data used for the thermal wind equation due to errors in the temperature and salinity measurements or position, error in wind stress when calculating Ekman transport and error from extrapolating for the depth below the deepest common level between the hydrographic station pairs (McIntosh & Rintoul, 1997). These errors must not be neglected as they can have a significant impact on the model results.

Ganachaud (2003a) used the Global Circulation Models (GCM) to assess the different source of errors and their importance and he found that the errors are larger in the upper ocean than in the deep ocean due to the baroclinic variability. Following, his results, uncertainties in the deep layers volume conservation should be reduced compared to the uncertainties in the upper layer and in the full-depth equation. In addition, the weights of the layer model should be normalized by its area in order to take into account the difference of the area between the layers.

The uncertainties in the reference velocities can be determined by using direct velocity measurement for example such as current meters or LADCP. The variability of the a priori reference velocity magnitude was evaluated by Ganachaud (2003b) using GCM as lying between 0.5 and 1 cm s<sup>-1</sup> and he suggested using the deep reference level in order to minimise the error in the deep transport that might occur due to an artificially high velocity at the bottom. These general rules can be used as guidance when there is a lack of information on the variability in transport and the reference velocity.

The weighted system of equations is solved by SVD (Wunsch, 1996; McIntosh & Rintoul, 1997). Using the row weighting matrix  $W_r$  (M x M) and column weighting matrix  $W_c$  (N x N)

$$A' x' = b' \quad (5.13)$$

where

$$A' = W_r A W_c, \quad x' = W_c^{-1}x \text{ and } b' = W_r b \quad (5.14)$$

The weighted system of equation solved using SVD (Wunsch, 1996) such that

$$A' = U \Lambda V^T \quad (5.15)$$

and the solution was recovered by

$$x' = U^T \Lambda^{-1} V b' \text{ or } x = W_c U^T \Lambda^{-1} V W_r b \quad (5.16)$$

The *a posteriori* uncertainty can be calculated from the square root of the diagonal component of the error covariance matrix  $\mathbf{P}_{xx}$  following the method of Wunsch (1996) which is estimated using Gauss-Markov formalism

$$\mathbf{P}_{XX} = \mathbf{R}_{XX} - \mathbf{R}_{XX} \mathbf{A}^T (\mathbf{A} \mathbf{R}_{XX} \mathbf{A}^T + \mathbf{R}_{nn})^{-1} \mathbf{A} \mathbf{R}_{XX} \quad (5.17)$$

where  $\mathbf{R}_{XX}$  is the square root of the column weight and  $\mathbf{R}_{nn}$  is the square root of the row weights.

### 5.2.3 Diapycnal mixing

The basic inverse model can be improved by including other important physical processes such as interfacial fluxes which represent the diapycnal mixing in the model. Diapycnal mixing in the interiors of the ocean refers to the entire water column beneath the sea surface. There are two different methods to parameterise the diapycnal fluxes in the inversion. In the first method, the convergence and divergence of the lateral transport give a vertical velocity ( $w$ ) (Ganachaud & Wunsch, 2000) but this velocity is not diapycnal as it will move isopycnally. However, since the mean circulation is assumed to be in a steady state, the vertical upward advection must be balanced by a downward diffusion,  $\frac{\partial C}{\partial z} w = \frac{\partial}{\partial z} \left( \kappa_c \frac{\partial C}{\partial z} \right)$ .  $\frac{\partial C}{\partial z}$  is the vertical gradient of the property concentration  $C$ ,  $w$  is diapycnal velocity and  $\kappa_c$  is the diffusion coefficient. The second method which is used in this study is a combination of the vertical velocities and the mixing into effective diapycnal velocity  $w^*$ , which represents the advection ( $w$ ) and diffusion ( $\kappa_c \frac{\partial C}{\partial z}$ ) components. The diapycnal velocity ( $w^*$ ) has the same dimension as velocity but is not equal to the vertical velocity  $w$  except when considering volume because the effective velocity is the advective velocity but for heat and salinity it has contributions from both advection and diffusion. The volume diapycnal flux can be estimated by multiplying the velocity ( $w^*$ ) by the area of the layer interface and the other properties' heat and salinity diapycnal flux can be estimated by multiplying the velocity ( $w^*$ ) by the area of the layer interface and mean property concentration. The diapycnal mixing is expressed in the inverse model as

$$\left[ \int_W^E \int_S^N \left( \kappa_v \frac{\partial(\rho C)}{\partial z} - w \rho C \right) dx dy \right]_{z(\rho_1)}^{z(\rho_2)} = [A \rho C \omega_c^*]_{z(\rho_2)} - [A \rho C \omega_c^*]_{z(\rho_1)} \quad (5.18)$$

where  $A$  is the area of the layer interface and  $\omega_c^*$  is the effective diapycnal velocity for a given tracer  $c$ . The diapycnal fluxes are weighted by the square root of the uncertainties ( $\sigma$ ) and divided by the area of the layer interface  $W = \sqrt{\frac{\sigma}{\text{area}}}$  in order to account for the variation.

#### 5.2.4 Ekman volume transport

The Ekman transport over the chosen box is estimated using the wind stress of the Scatterometer Climatology of Ocean Winds (SCOW). It is estimated from the 8-yr record (September 1999-August 2007) of wind measurements by the NASA Quick Scatterometer (QuikSCAT) (Risien & Chelton, 2008). The wind stress fields projected onto the stations will be used to estimate the cross section Ekman fluxes from the equation

$$T^{\text{Ek}} = \frac{-\tau^x \Delta x}{\rho f} \quad (5.21)$$

where  $T^{\text{Ek}}$  is the Ekman volume transport (Sv),  $\tau^x$  is wind stress along the section ( $\text{Nm}^{-2}$ ),  $\Delta x$  is the distance between stations (m),  $f$  is the coriolis parameter ( $f = 2\Omega \sin \varphi$ ,  $\Omega$  is the rotation rate of Earth and  $\varphi$  the latitude) and  $\rho$  is the sea water density ( $\text{kg m}^{-3}$ ).

The Ekman transport estimate will combine with other property measurement to calculate the properties' fluxes. Hence, Ekman transport affects the lateral transport each tracer by

$$T_j^{\text{Ek}} = C_j \rho v_j^{\text{Ek}} \quad (5.22)$$

where  $v_j^{\text{Ek}}$  is Ekman transport velocity in layer  $j$  and  $C_j$  tracer in layer  $j$  (Jullion, 2008)

#### 5.2.5 Final inversion form

The final form for the basic inverse box model may be written as the following:

$$\sum_{i=1}^n \sum_{j=1}^m [D_{ij} L_i (v_{ij} + b_{ij}) \delta_i \rho_{ij} C_{ij} + \rho C^{\text{Ek}} v^{\text{Ek}} h_{\text{Ek}}] - [A \rho C \omega_c]_{\text{bot}}^{\text{top}} = 0 \quad (5.23)$$

### 5.3 Conclusion

This chapter's focus was on the technique that will be used to diagnose the circulation in the Red Sea. The theory of the box inverse model was described by using a basic inverse model and improved by including other important physical processes such as diapycnal mixing and Ekman transport. The box inverse model is very useful technique; for example, it resolves fluxes at the boundaries so that the inflow and outflow of the RSW can be diagnosed. In the next chapter the application of this model in the southern Red Sea region and the initial solution will be described.

# **Chapter 6 Hydrographic characteristics of the southern Red Sea**

## **6.1 Introduction**

This chapter is split into two main parts. The first part presents a description of the hydrography of each section used to construct our box in the southern Red Sea. The second part presents the thermohaline properties of the different water masses present in the southern Red Sea region. The data used in this thesis for the inverse box model was collected on board the R/V Maurice Ewing during the period from 4 August to 19 August 2001 (Sofianos & Johns, 2007). It encompassed 77 hydrographic stations distributed along the Red Sea as shown in the dataset chapter (Chapter 3).

## **6.2 Section description**

Traditionally, the inverse box is built using hydrographic data from coast to coast sections in order to capture the flow between the two land boundaries. Two synoptic transects at the southern end of the Red Sea were used to build the box with a total of 16 stations. Section C consists of 7 stations with an average station separation of 18.43 km and section F consists of 9 stations with an average station separation of ~14.7 km. Figure 6-1 shows the two transects used to build our inverse box model and other sections (D and E) used to study the thermohaline properties of the southern Red Sea are shown.

### 6.2.1 Bathymetry of the southern Red Sea region

As mentioned before the Red Sea is a rift valley formed by the separation of Arabian and African plates. It has a very complex topography with very wide continental shelves on the both sides (Arabian and African) and the deepest trench is located on the central axis with a maximum recorded depth of 2920 m, which extends from about 14°N to 28°N. The bathymetry of the box rises from a depth of 1216 m (section C) to depth of 528 (section F) at the main axis of the basin.

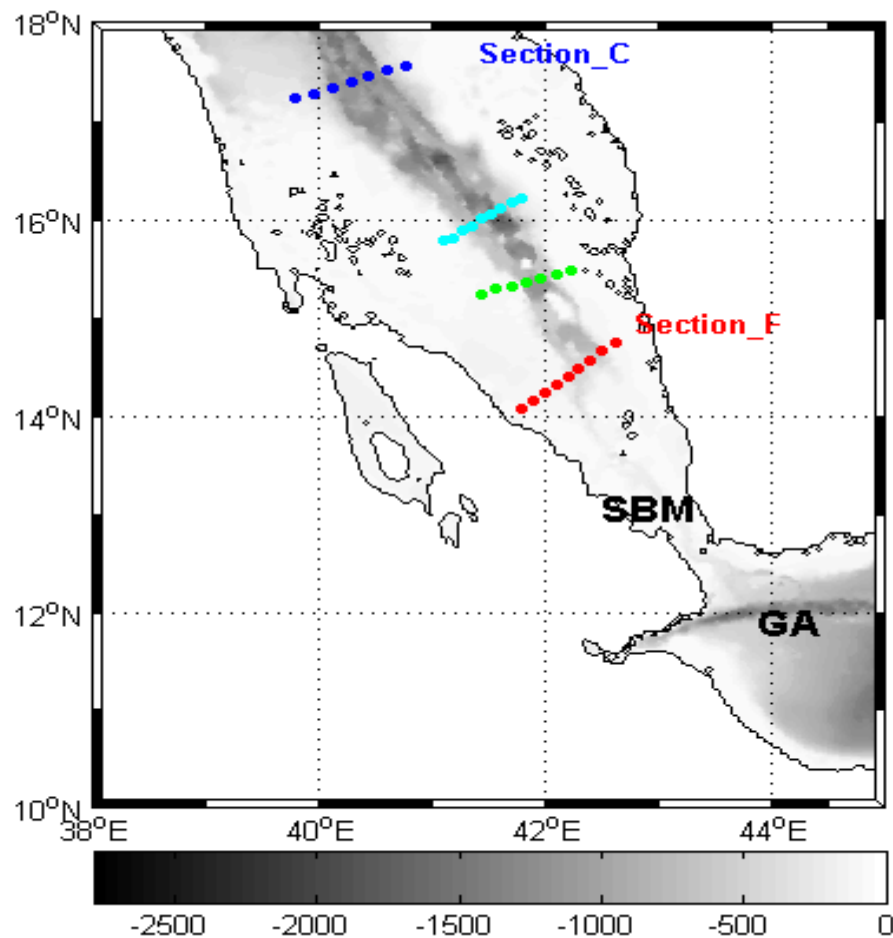


Figure 6-1: Bathymetry of the southern Red Sea (Smith & Sandwell, 1997). The two transects used to construct the box (in blue and red) and the other sections used to study the thermohaline properties of the southern of the Red Sea (section D in cyan and E in green). SBM: Strait of Bab el Mandeb and GA: Gulf of Aden

### 6.2.2 Hydrographic properties

In this part, the vertical distribution of temperature and salinity of two zonal transects will be described following Sofianos and Johns (2007). The potential temperature, salinity, potential density and dissolved oxygen in each section of our box are shown in Figures 6-2 to 5. Cross section F is located in the southern part of the Red Sea region at latitude  $\sim 14^{\circ}\text{N}$ , approximately 70 km from the Strait of Bab el Mandeb (Figure 6-1). The distribution of the potential temperature in the surface layers is uniform with small differences between the east and west of the section and the mixed layer extends to less than  $\sim 20$  m with the western side warmer than the eastern side. The structure of the thermohaline characteristics shows that the RSSW (warm and saline) is flowing southward to the Strait of Bab el Mandeb overlying the GAIW, which is intensified on the eastern side (right) in a thin layer of  $\sim 20$  m. The GAIW is fresher and colder flowing northward into the Red Sea on the eastern side (right) with a thickness layer of  $\sim 50$  m. The minimum thermohaline properties for GAIW are found on the eastern side of the section with  $18.03^{\circ}\text{C}$  and 36.06 psu for temperature and salinity respectively. The RSOW (warm and saline) is overlying the RSDW and below that the GAIW layer, which is flowing southward on the western side (left) with a thicker layer than on the eastern side. The RSOW has high dissolved oxygen values on both sides of the section with the maximum core at  $\sim 115$  m depth. This high dissolved oxygen layer lies between the two minimum oxygen layers of GAIW and RSDW, where it is thick on the western side.

Section C is located at latitude  $\sim 17^{\circ}\text{N}$ , approximately 400 km from the Strait of Bab el Mandeb region. The water mass characteristics show that the GAIW signal can be detected near the eastern and the central parts of the section with a very thin layer at  $\sim 60$  m depth. Compared to section F it can be seen that the GAIW becomes thinner in this section and its potential temperature and salinity characteristics change as a result of strong mixing with ambient water with the minimum salinity of the section at 37.80 psu. Below the GAIW layer, the distribution of the dissolved oxygen shows that the RSOW with its maximum signal ( $\sim 112 \mu\text{mol/kg}$ ) is found between 100 and 150 m depth toward the west of the section and is thicker on the western side, reaching a depth of 200 m. The RSOW has thermohaline properties similar to RSDW's salinity and potential temperature. There is minimum dissolved oxygen at a depth of around 400 m, as was observed by Sofianos and Johns (2007) in the southern part of the Red Sea in the summer of 2001. This is related to the old RSDW as they recirculated to the north

part of the basin. They also observed a high dissolved oxygen concentration in the bottom of the northern part at latitude  $27^{\circ}\text{N}$ , which indicates new deep waters formed during the past winter. While the RSDW moves southward through the basin, the dissolved oxygen concentration is depleted.

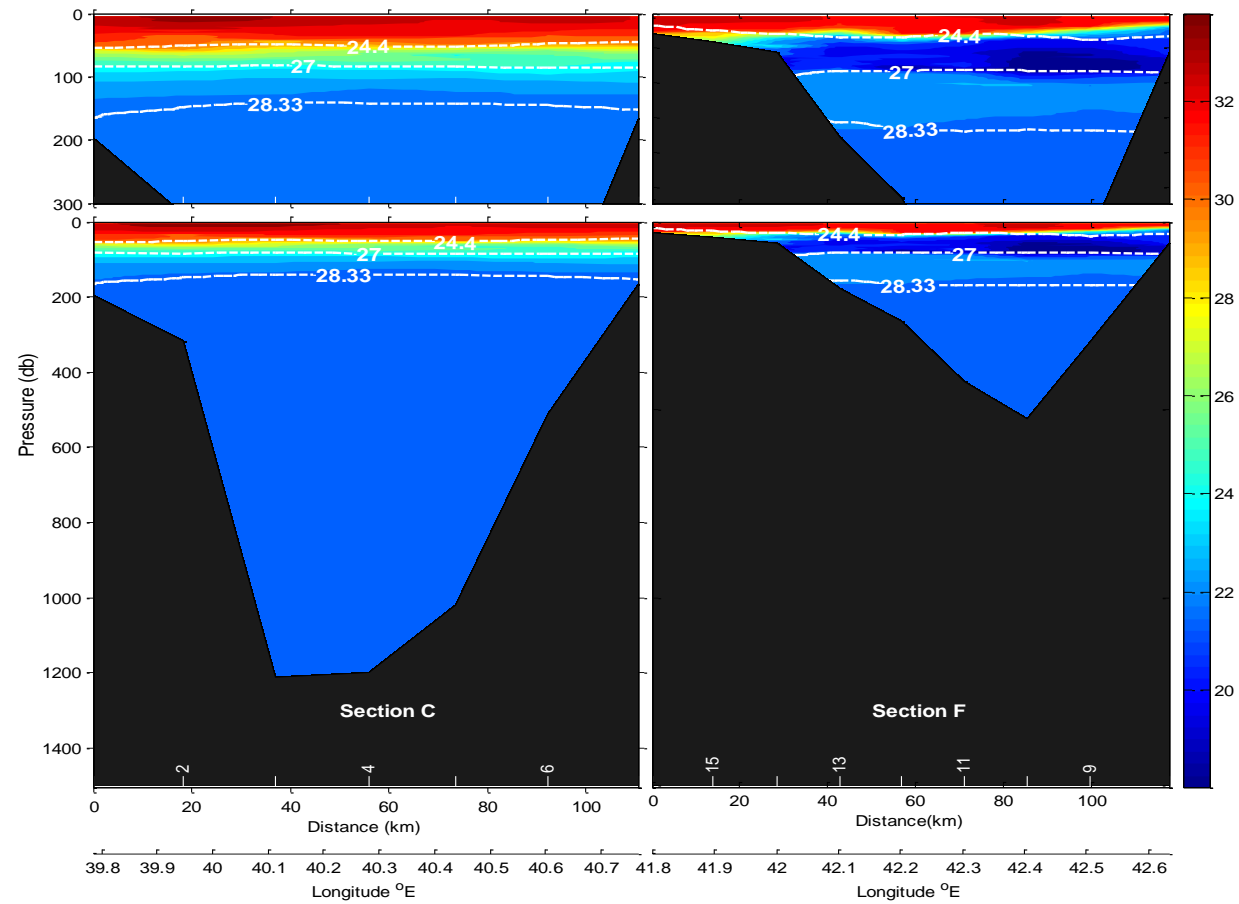


Figure 6-2: Vertical distribution of potential temperature along the rim of the box in the southern Red Sea. Upper panel: upper 300 m. Lower panel: whole profile from the surface to the bottom. The station numbers are shown in white along the lower axis and the white lines represent the boundaries of the water mass.

Longitudes are shown over the two zonal transects

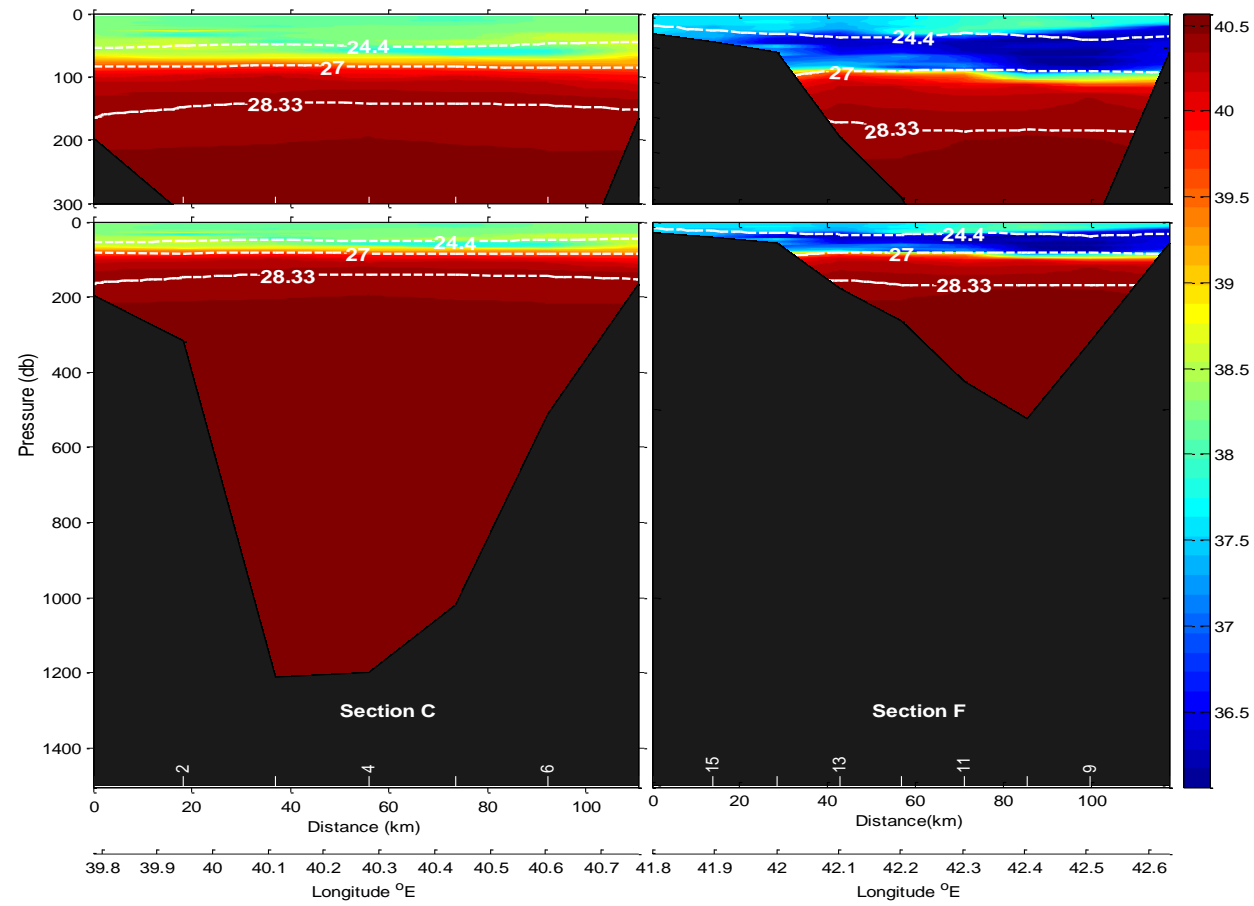


Figure 6-3: Vertical distribution of salinity along the rim of the box in the southern Red Sea. Upper panel: upper 300 m. Lower panel: whole profile from the surface to the bottom. The station numbers are shown in white along the lower axis and the white lines represent the boundaries of the water mass. Longitudes are shown over the two zonal transects

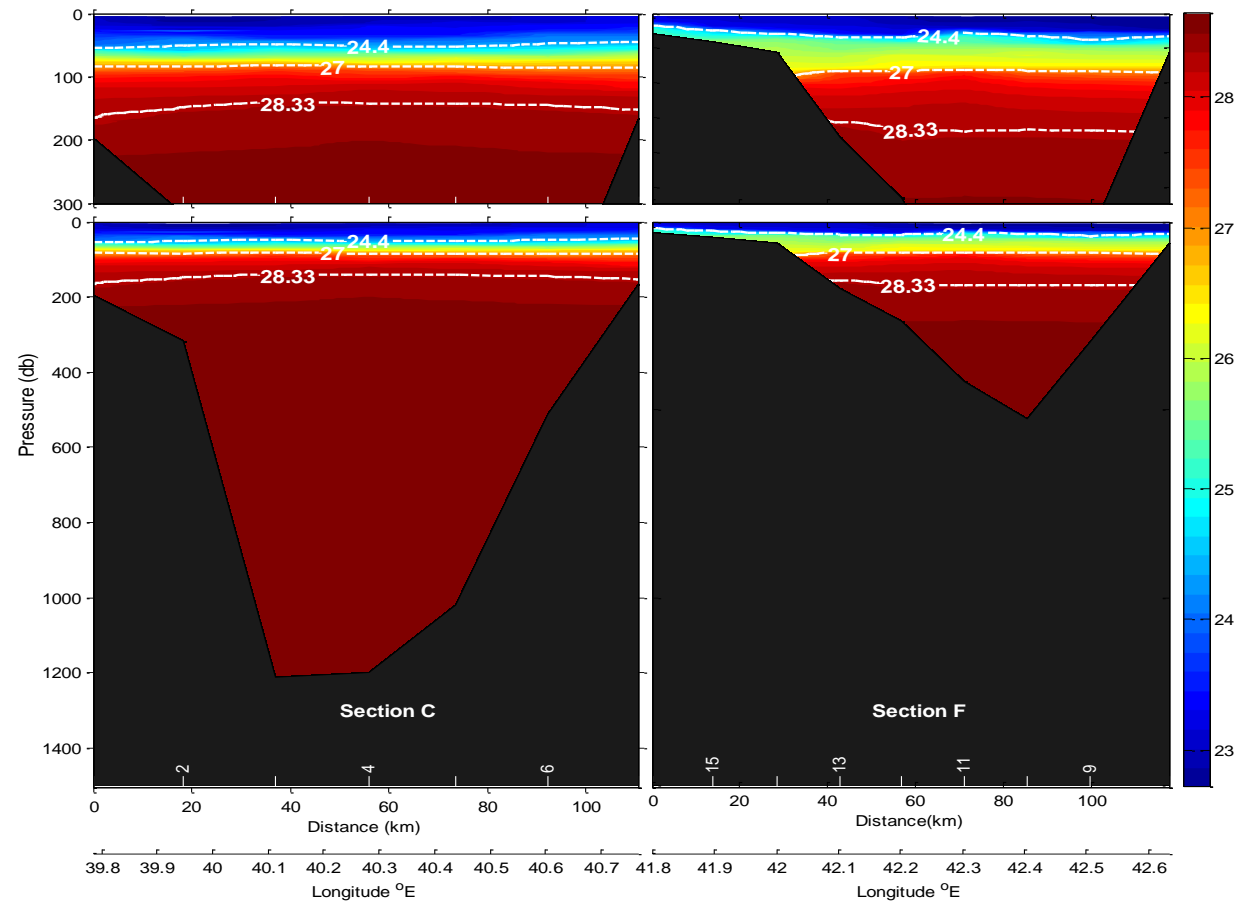


Figure 6-4: Vertical distribution of potential density along the rim of the box in the southern Red Sea. Upper panel: upper 300 m. Lower panel: whole profile from the surface to the bottom. The station numbers are shown in white along the lower axis and the white lines represent the boundaries of the water mass. Longitudes are shown over the two zonal transects

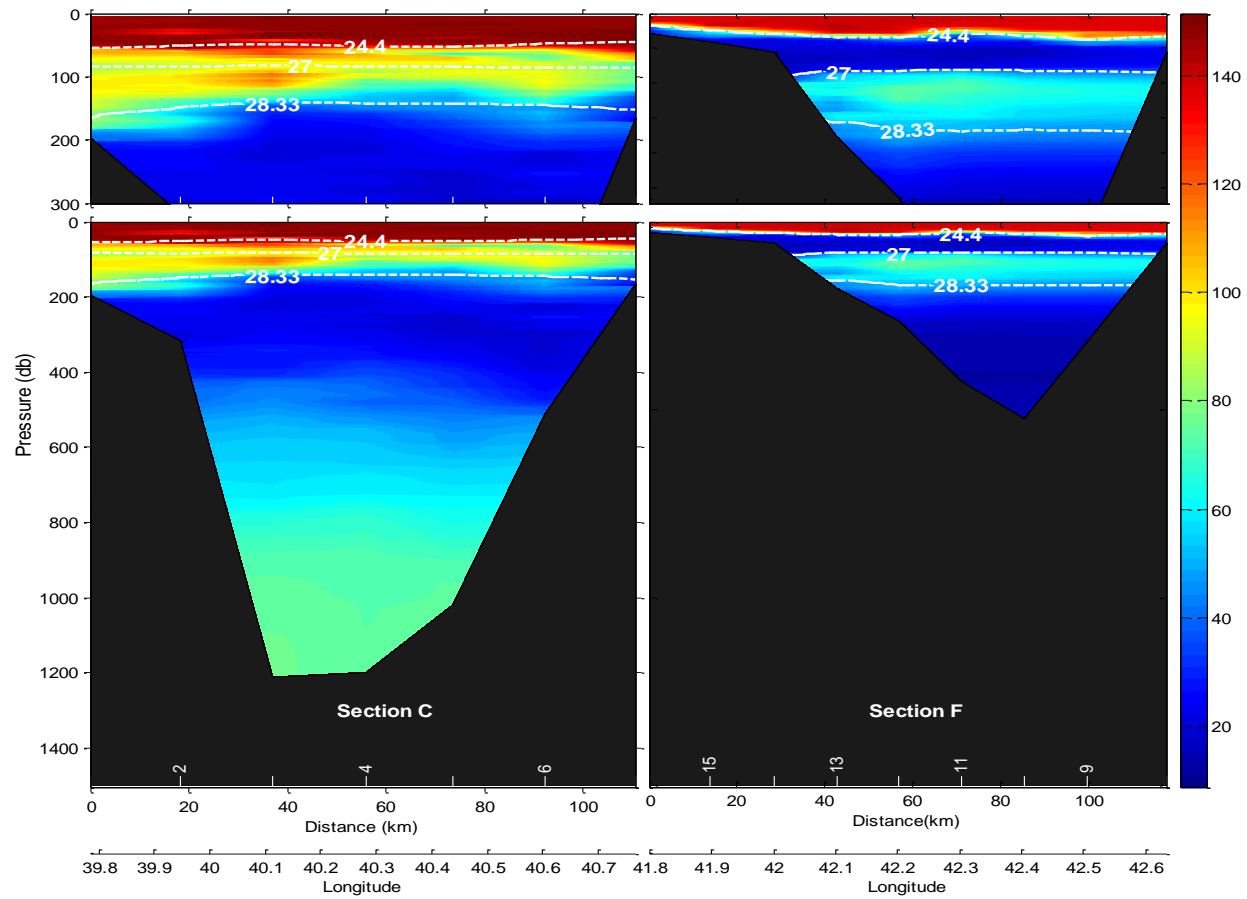


Figure 6-5: Vertical distribution of dissolved oxygen concentration along the rim of the box in the southern Red Sea. Upper panel: upper 300 m. Lower panel: whole profile from the surface to the bottom. The station numbers are shown in white along the lower axis and the white lines represent the boundaries of the water mass. Longitudes are shown over the two zonal transects

### 6.2.3 Water masses

To describe the circulation in any particular region it is important to define the water masses present by identifying their thermohaline properties. Figure 6-6 shows the  $\theta$ -S diagram of the box (two transects) indicating the water masses present in the southern Red Sea region.

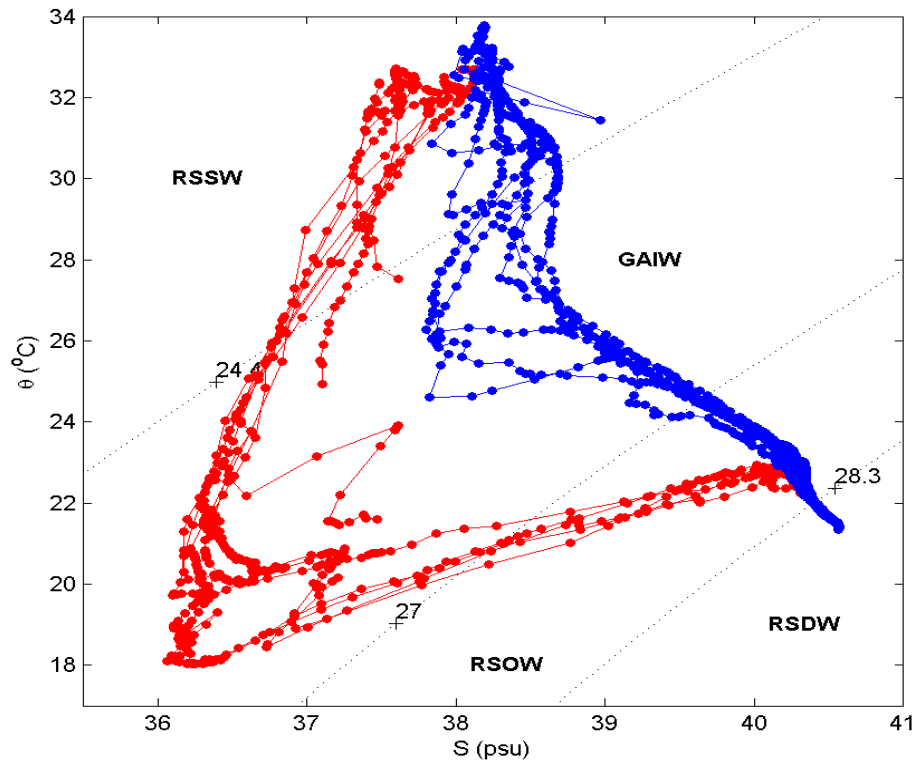


Figure 6-6:  $\theta$ -S diagrams of sections C (blue lines) and F (red lines) in the southern region of the Red Sea.  $\sigma_{\theta}$  boundaries of the main water masses (dotted lines). The main water masses are labelled

The surface layer of the two transects C and F is characterised by warm and saline RSSW mass outflowing southward toward the Strait of Bab el Mandeb which is intensified toward the eastern side of the Red Sea with a thickness of less than 30 m. In its pathway southward the RSSW is affected by the surface circulation features in the southern region and mixed with the layer beneath it. Its characteristics change rapidly as can be seen from  $\theta$ -S diagram for layer  $\sigma_{\theta} < 24.4$ . The surface temperature and salinity are reduced to  $\sim 31^{\circ}\text{C}$  and to 37.5 psu respectively when it reaches section F. Below the RSSW layer, there is a fresh and cool water mass GAIW inflowing northward overlying RSOW and its potential temperature and salinity change rapidly

with the latitude. Over the box from section F to section C there are increases in both potential temperature and salinity due to mixing with RSSW and RSOW. When it reaches section C its temperature is increased from  $\sim 18^{\circ}\text{C}$  to  $\sim 25^{\circ}\text{C}$  and its salinity from  $\sim 36$  to  $39$  psu. Underlying the GAIW, there are two water masses RSOW and RSDW in which can be seen dissolved oxygen (Figure 6-5). The RSOW marked by salinity close to  $40$  psu flows southward at a depth of  $\sim 80$ - $180$  m with a potential density ranging from  $27$ - $28.33$   $\sigma_{\theta}$  (Figure 6-6). The thermohaline characteristics of the RSOW decrease as it flows southward and this can be attributed to mixing with the GAIW. The RSDW is the densest water mass located below a density range of  $\sigma_{\theta} > 28.33$  and its mean potential temperature, salinity and dissolved oxygen are  $\sim 21.50^{\circ}\text{C}$ ,  $40.55$  psu and  $39.81$   $\mu\text{mol/kg}$  respectively (Figures 6-2 to 5).

Based on the water mass properties in the box we can define the boundaries by using the potential density for each water mass as defined in Table 6-1 and Figure 6-6.

| <b>Water mass</b> | <b>Layer boundaries</b>        |
|-------------------|--------------------------------|
| RSSW              | $\sigma_{\theta} < 24.4$       |
| GAIW              | $24.4 < \sigma_{\theta} < 27$  |
| RSOW              | $27 < \sigma_{\theta} < 28.33$ |
| RSDW              | $\sigma_{\theta} > 28.33$      |

Table 6-1:  $\sigma_{\theta}$  boundaries of the main water mass used in the entire thesis

### 6.3 Thermohaline properties of the southern Red Sea region

This section deals with inspection of the thermohaline properties in the southern region of the Red Sea to allow us to track the presence of the four water masses in the box. Sofianos and Johns (2007) have described the water masses observed along the Red Sea region in summer 2001 but without showing the modifications happening to these water masses. A total of 37 stations over the box have been chosen to describe the thermohaline properties. The  $\theta$ -S properties show all the profiles over the box, roughly follow a south-north orientation and illustrate the variability of the surface water decreasing southward to the Strait of Bab el Mandeb (Figure 6-7). Conversely, the  $\theta$ -S of the subsurface layers (GAIW) shows a large variability in thermohaline properties that increase as it flows northward. The differences of the thermohaline properties in the upper layers are not obvious but if we look at the two deeper water masses, the thermohaline variability is very small.

### 6.3.1 Surface layers (RSSW, surface-24.4 $\sigma_\theta$ )

The August  $\theta$ -S diagrams (Figure 6-7, left panel) show the evolution of the upper layer from section C (northern boundary of the box) to section F (southern boundary of the box). In all cross sections (C, D, E and F), the RSSW flows southward as it is affected by the northwesterly wind which is dominant in the summer season in the southern region of the Red Sea. The potential temperature and salinity in the surface layer (upper 10 m) following the southward direction (figure not shown) decrease from  $\sim 33.49^\circ\text{C}$  to  $32.70^\circ\text{C}$  for potential temperature and from  $\sim 38.30$  to  $37.59$  psu for salinity in section C ( $\sim 17.4^\circ\text{N}$ ) and section F ( $\sim 14.4^\circ\text{N}$ ) respectively. In section C, the RSSW shows variability of the thermohaline properties along the section (west-east) where the western side is warmer than eastern side. The RSSW flows southward through section C to both boundaries, where it is intensified in the western side of the section (stations 30-32) as shown in Figure 6-8. The RSSW is defined in section C by relative salinity maximum ( $S = 38.97$ ,  $T = 33.78^\circ\text{C}$  at station 31) at  $\sigma_\theta < 24.4$ . As the RSSW flows southward, the surface flow pathways are intensified towards the eastern coast, as can be seen from Figure 6-9, when across section D (located  $\sim 300$  km from the Strait of Bab el Mandeb) with a return northward flow in the western side of the section (stations 40-42). The maximum salinity of RSSW is found in section D at the eastern side with maximum  $S = 38.41$  psu and  $T = 33.18^\circ\text{C}$ . The returned flow might be attributed to the cyclonic rotation as described by Sofianos and Johns (2003), which is centred between  $15^\circ\text{N}$  and  $16^\circ\text{N}$  on the western side of the basin.

Tracing the flow of RSSW in section E, which is located  $\sim 213$  km from the Strait of Bab el Mandeb (Figure 6-10), shows that the flow is concentrated on the eastern side (stations 54-56) of the section with anticyclonic northward flow on the western side. As the RSSW layer reaches the south of the box (section F), the flow is concentrated on the eastern and western sides of the section by eddies (according to the geostrophic circulation shown in Figure A-5 (appendix A) for section F).

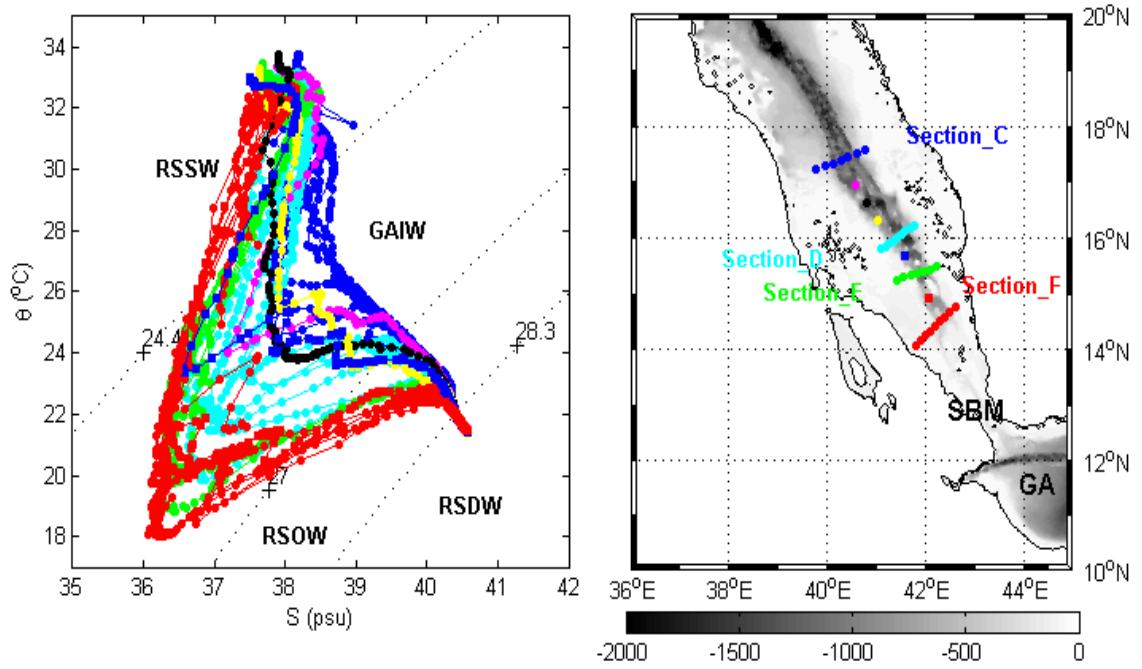


Figure 6-7:  $\theta$ -S diagrams of all the profiles over the box (C, D, E and F) in the southern Red Sea (left panel) and their corresponding stations are shown (right panel).  $\sigma_{\theta}$  boundaries of the main water masses (dotted lines). SBM: Strait of Bab el Mandeb and GA: Gulf of Aden

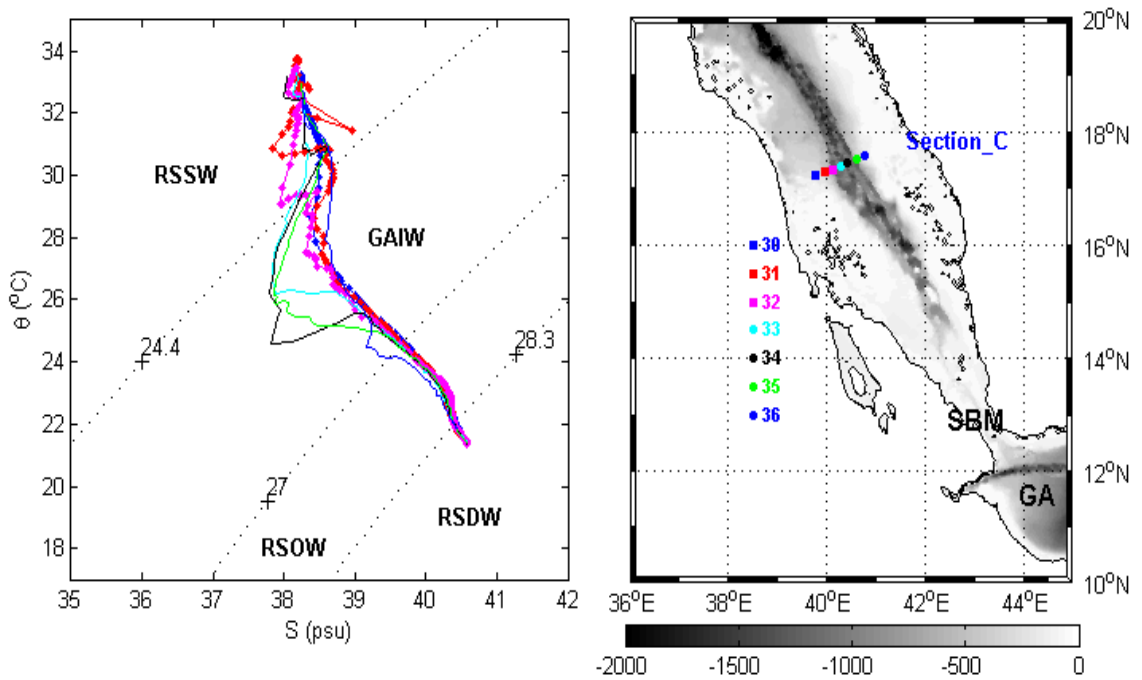


Figure 6-8:  $\theta$ -S diagrams of main water masses found in section C (left panel) and their corresponding stations are shown (right panel)

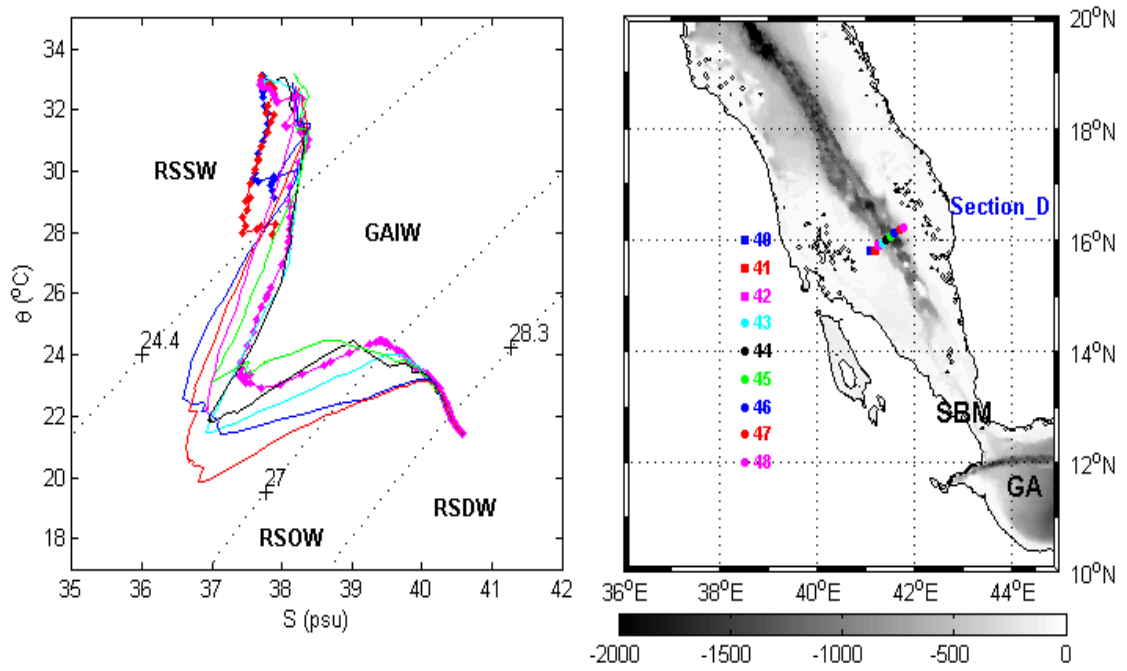


Figure 6-9:  $\theta$ -S diagrams of main water masses found in section D (left panel) and their corresponding stations are shown (right panel)

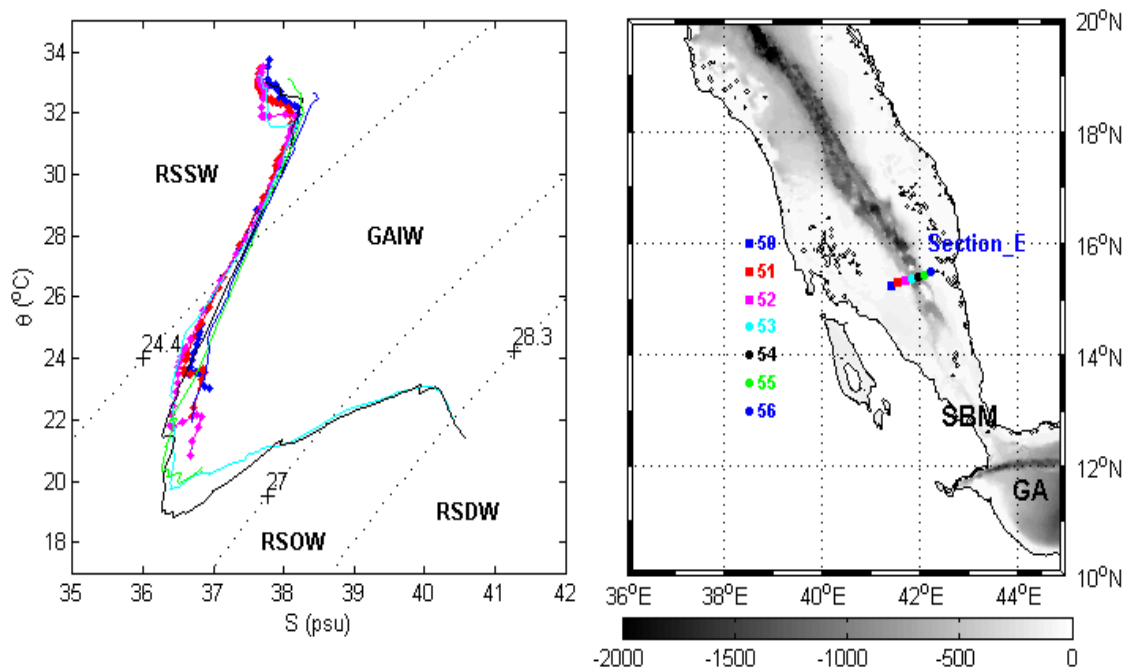


Figure 6-10:  $\theta$ -S diagrams of main water masses found in section E (left panel) and their corresponding stations are shown (right panel)

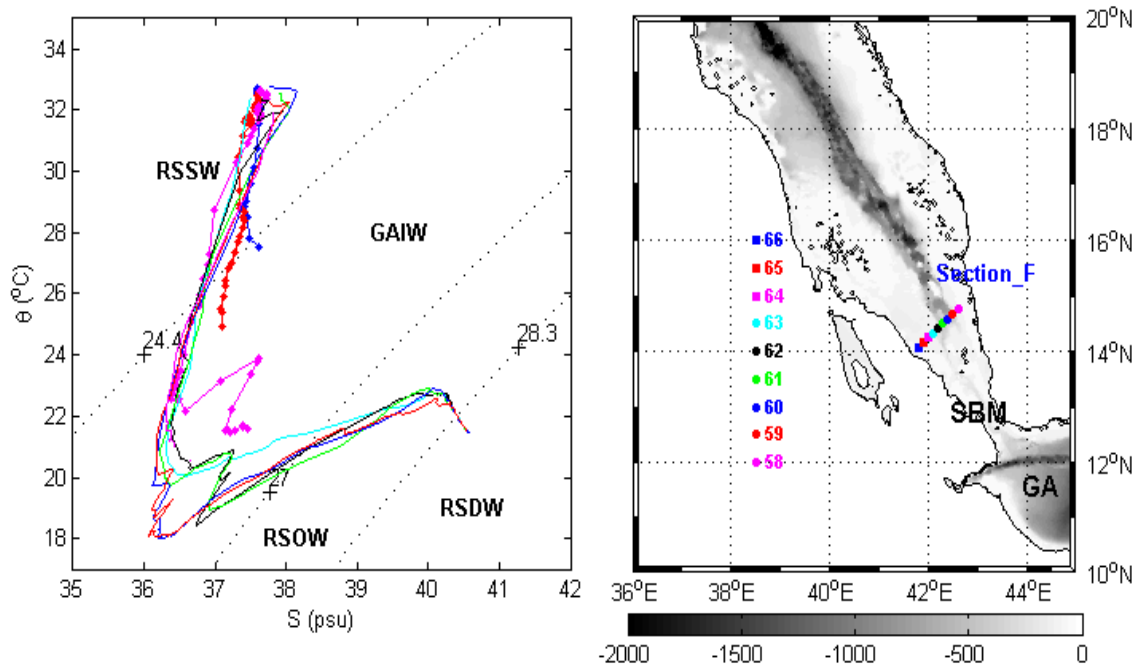


Figure 6-11:  $\theta$ -S diagrams of main water masses found in section F (left panel) and their corresponding stations are shown (right panel)

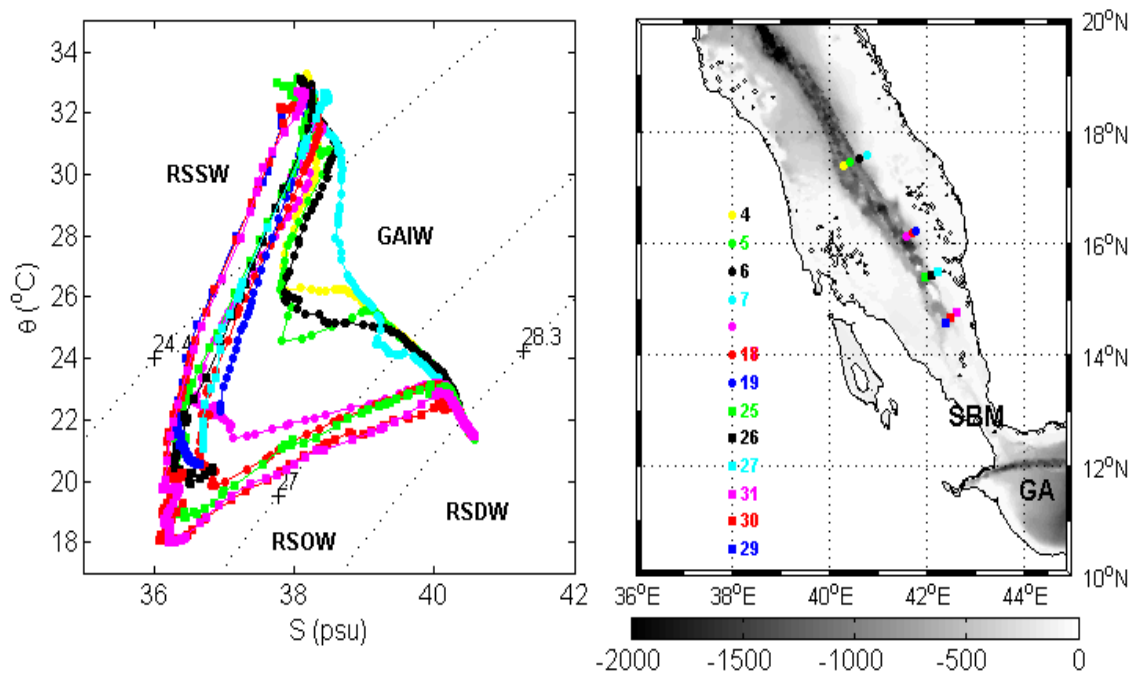


Figure 6-12:  $\theta$ -S diagrams of main water masses found along the eastern side of the basin (left panel) and their corresponding stations are shown (right panel)

### 6.3.2 Intermediate layers (GAIW, 24.4- 27 $\sigma_\theta$ )

In the south of the box (section F) where the GAIW is flowing to the Red Sea through the Strait of Bab el Mandeb, there is cool and fresh water mass across this section on the eastern side. The core of this layer lies in the potential density range 24.4-27  $\sigma_\theta$  and has values of 18.04°C, 36.05 psu 8.8  $\mu\text{mol/kg}$  (stations 59-60) for temperature, salinity and dissolved oxygen concentration respectively (Figure 6-11). If we look at along the section from west to east, the temperature and salinity increase towards the western side (from stations 61 to 64), which could be attributed to the strong mixing with overlying RSSW (warm and saline) and underlying layer RSOW (warm and saline) by eddies. The core of the GAIW is found in the central part of section E (station 54) as it flows northward (Figure A-4 in appendix A). This core has values of 18.82°C and 36.26 psu for temperature and salinity respectively. The salinity and temperature minimum for the GAIW layer has increased by 0.14 °C and 0.24 psu respectively from section F to section E (about 100 km northward). The GAIW across section D on the eastern side and the core of this layer found at station 47 show a minimum of 19.86°C and 36.58 psu for temperature and salinity respectively. The thermohaline variability for this layer can be seen from Figure 6-9 for section D to increase towards the western side. North of this section, the flow of GAIW across section C (northern box boundaries) on the eastern side with a minimum of 24.15°C for temperature and 37.80 psu for salinity is located at station 34 (Figure 6-8). The GAIW can be traced on the eastern side of the basin as shown in Figure 6-12 from the southern boundary towards the northern boundary of the box.

### 6.3.3 Deep layers (RSOW, 27-28.33 $\sigma_\theta$ and RSDW, $\sigma_\theta > 28.33$ )

The RSOW is located between GAIW and RSDW and is characterised by high dissolved oxygen that is formed during the winter in the northern part of the Red Sea (Sofianos & Johns, 2003). This layer flows south of the basin and flows out at the Strait of Bab el Mandeb. The RSOW has a potential density range between  $\sigma_\theta = 27$  and  $\sigma_\theta = 28.33$  as can be seen in Figure 6-7. The RSOW flows southward and across section C on the western side as shown in Figure 6-8 (stations 30-32); Figure 6-5 (station 3) illustrates dissolved oxygen concentration with its core located between 100 and 150 m depth. The signal of the dissolved oxygen concentration decreases slightly towards the middle of the section with a return flow towards the north at eastern side (station 33-36

in Figure 6-8). It can also be seen from geostrophic velocity at this section in Figure A-2 (appendix A). Following the pathway of the RSOW as it flows southward, the width of the basin becomes smaller at section D and the structure of the RSOW layer become more complicated. Figure 6-9 shows the RSOW is concentrated at the western side of section (station 40-45) and there are changes in temperature and salinity characteristics (cooler and fresher) toward the eastern side that attributed to the mixing with overlying GAIW layer. There is a cyclonic northward flow for RSOW along the eastern side of the section as shown in Figure A-3 (appendix A). The RSOW across section E (Figure 6-10, stations 53-54) which is concentrated on western side, the core of this layer has  $T = 22.44$  °C,  $S = 40.34$  psu and  $O = 82.49$   $\mu\text{mol/kg}$  at  $\sim 122$  m depth (figure not shown). Figure 6-5 (left panel) shows the dissolved oxygen concentration structure at section F, where the core of RSOW is intensified at western side of the section (station 61-63, Figure 6-11) and has a maximum signal of  $76.9$   $\mu\text{mol/kg}$  at  $\sim 105$  m depth.

## 6.4 Conclusion

In this chapter, the hydrographic setting of the southern of the Red Sea is described using data from R/V Maurice Ewing during the period from 4 August to 19 August 2001 (Sofianos & Johns, 2007). The study of the thermohaline properties of the water masses present in the box has shown the presence of the four water masses involved in the summer circulation of the Red Sea. The circulation in the southern Red Sea is summarised in the map in Figure 6-13. RSSW flows southward and is intensified on the eastern side of the basin and its temperature and salinity characteristics change rapidly with the latitude as it is mixed with the underlying layer (GAIW) (Sofianos & Johns, 2007). Similarly, the RSOW flows southward into the Strait of Bab el Mandeb and its temperature and salinity characteristics decrease as it flows southwards and there is a cyclonic recirculation flow toward the north. Conversely, the GAIW flows northward with concentration along the eastern coast of the basin. Its thermohaline properties change rapidly with the latitude and its thickness is greatly reduced northward from section F toward section C. RSDW generally flows southward and it is characterised by low dissolved oxygen concentration but its thermohaline properties are similar to those of the RSOW.

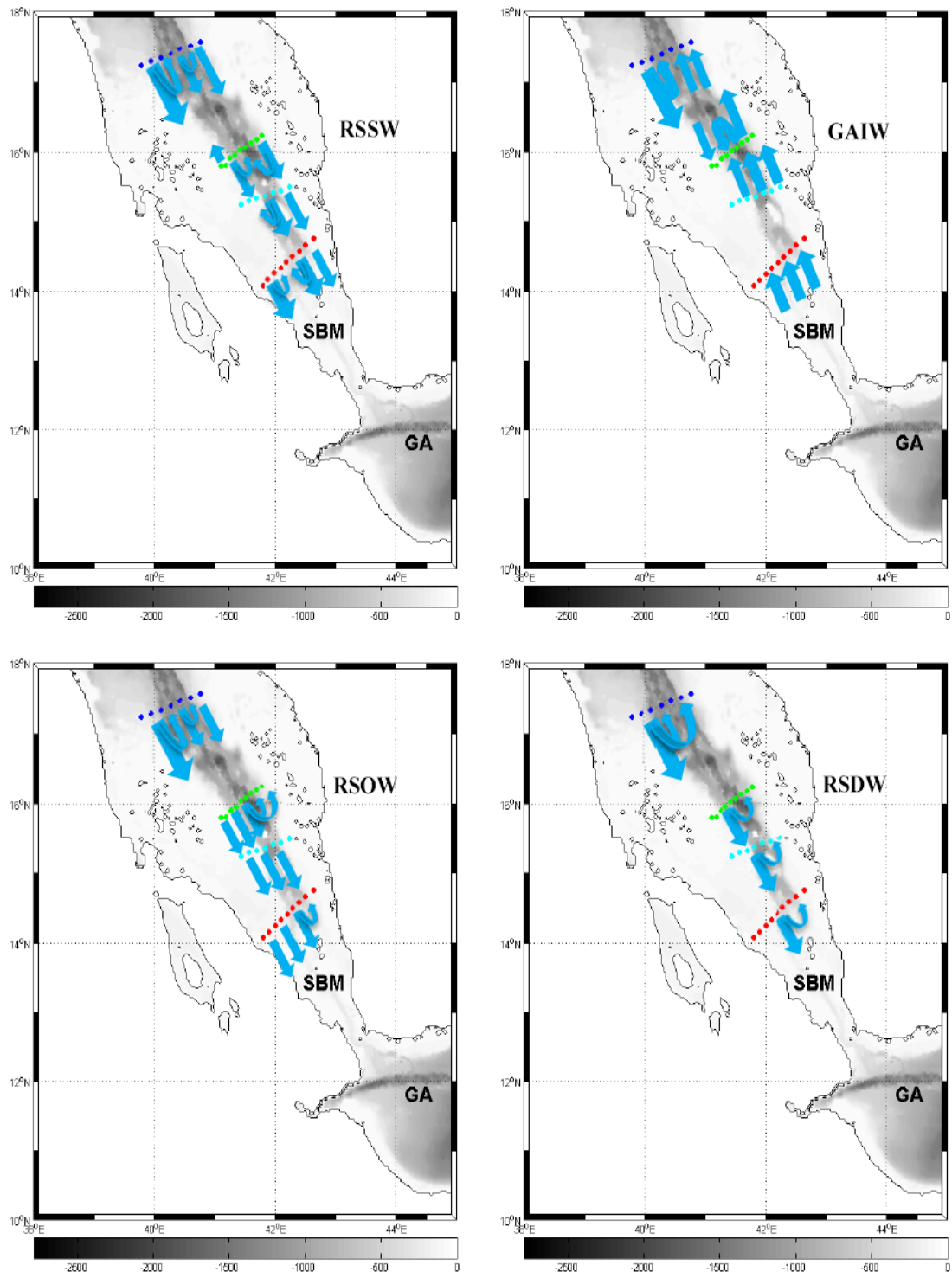


Figure 6-13: Circulation scheme for the southern Red Sea based on results from the geostrophic circulation. The major water masses (see Table 6-1). RSSW for Red Sea Water mass, GAIW for Gulf of Aden Water mass, RSOW for Red Sea Outflow Water mass and RSDW for Red Sea Water mass. SBM represents the Strait of Bab el Mandeb region and GA the Gulf of Aden region. The dots indicate the hydrographic data from R/V Maurice Ewing (2001) for section C (blue), section D (green), section E (cyan) and section F (red)

# Chapter 7 Setup of the standard inverse box model

## 7.1 Introduction

This chapter presents the *a priori* estimate of the circulation in the inverse box model. It gives a description of the setup of the inversion model in the southern region of the Red Sea, including the choice of the initial geostrophic velocity field, the choice of the reference level and reference velocities and the implementation of the other unknowns in the model, such as interior diapycnal mixing and Ekman transport.

## 7.2 Setup of the standard inverse box model

In this thesis, the software used to run the inverse box model is DOBOX (Morgan, 1995) written in MATLAB, which has been used in several studies (Naveira Garabato et al., 2003; Jullion et al., 2010; Palmer et al., 2011; Tsubouchi et al., 2012). A closed box of 16 stations in the southern Red Sea was considered (Figure 7-1) and divided vertically into 4 layers defined by a potential density surface. These layer divisions were based on the hydrographic characteristics of the Red Sea water masses: RSSW, GAIW, RSOW and RSDW (as described in section 6.2.2). A neutral density variable,  $\gamma_n$  (a function of salinity, temperature, pressure, latitude and longitude), was not used in the model because it has not yet been defined for the Red Sea region. The potential density and the neutral density are similar in the upper ocean and the latter can be used for the whole water column to avoid using different potential density references at different depths (Hernández-Guerra et al., 2005). However, in this study the potential density has been used because the Red Sea is shallow.

Full-depth and layer conservation of mass, heat and salt were required in the model, which gives a total of 15 equations (4 layer equations and one full-depth equation for each tracer). Increasing the number of the layers in the model does not give a better result because it would increase the condition number of the matrix (McIntosh & Rintoul, 1997). The conservation equation is enforced within specified uncertainties to determine two types of unknowns:

- The depth-independent adjustment (the reference velocity) to the relative velocity at each station pair (14 unknowns, one for each station pair).
- A diapycnal velocity  $\omega^*$  in the ocean interior (where the ‘interior’ refers to the entire water column below the surface including the mixed layer) for each of the 3 layer interfaces for volume, salinity and potential temperature (9 unknowns).

The results of the system equation can be presented in a 15 by 23 (unknown) matrix and is solved by using singular value decomposition. The following sections give details of how the system is initialised.

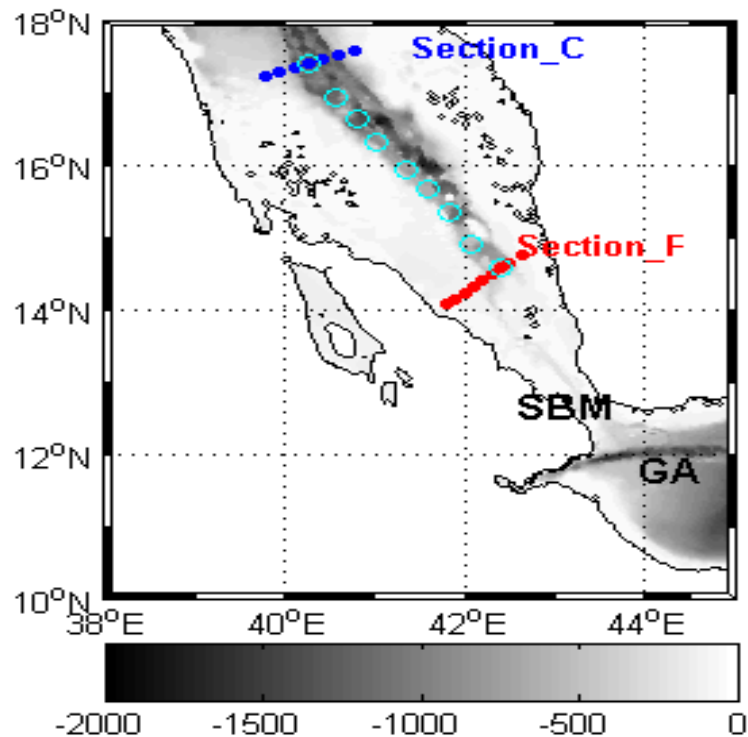


Figure 7-1: Two transects used to build the box (blue circles (section C) and red circles (section F)) and the axis station used to calculate the property mean in the layer of each interface (cyan circles). SBM: Strait of Bab el Mandeb, GA: Gulf of Aden

| <b>Layer</b> | <b>Water mass</b> | <b>Layer boundaries</b>      |
|--------------|-------------------|------------------------------|
| 1            | RSSW              | $\sigma_\theta < 24.4$       |
| 2            | GAIW              | $24.4 < \sigma_\theta < 27$  |
| 3            | RSOW              | $27 < \sigma_\theta < 28.33$ |
| 4            | RSDW              | $\sigma_\theta > 28.33$      |

Table 7-1: Layers used in the model defined by the  $\sigma_\theta$  surface (potential density minus 1000 kg m<sup>-3</sup> in reference to the surface)

### 7.3 Conservation constraints

The constraints were applied to conserve volume, salinity and potential temperature in the box within each layer individually. Also, the standard model solution requires the conservation of the volume, salinity and the potential temperature flux over the full depth of the water column. These constraints are summarised in Table 7-2. The conservation equations for salinity and potential temperature were written in term of property anomalies, obtained by subtracting the mean property value along the rim of the box. The aim of using these anomalies was to improve the condition of the system by reducing the dependence of the property equation on the volume (mass) equations (McIntosh & Rintoul, 1997; Ganachaud, 1999). A further four constraints are included for the full depth for the volume and salinity at each section as follows: 0.015 Sv and 0.095 Sv for sections C and F respectively.

| Constraint Description |                       | Transection |
|------------------------|-----------------------|-------------|
| Full- Depth            | Volume                | Section C   |
| Full- Depth            | Salinity              | Section C   |
| Full- Depth            | Potential temperature | Section C   |
| Full- Depth            | Volume                | Section F   |
| Full- Depth            | Salinity              | Section F   |
| Full- Depth            | Potential temperature | Section F   |
| Individual layers 1-4  | Volume                | Section C   |
| Individual layers 1-4  | Salinity              | Section C   |
| Individual layers 1-4  | Potential temperature | Section C   |
| Individual layers 1-4  | Volume                | Section F   |
| Individual layers 1-4  | Salinity              | Section F   |
| Individual layers 1-4  | Potential temperature | Section F   |

Table 7-2: Constraints applied to the inverse box model (standard solution). Each constraint represents a conservation equation for the flux (volume, salinity or temperature) constrained to zero

## 7.4 Initial geostrophic velocity field

The initial estimate of the geostrophic velocity is the one of most basic and fundamental parts of the inversion model and can be calculated from hydrographic data using the thermal wind equation (Equation 5.4). To obtain a successful inversion, the a priori estimate of the geostrophic velocity needs to be carefully constructed using all available information.

### 7.4.1 *A priori reference level and reference velocity*

The geostrophic velocity in each section of the box can be calculated with the traditional method by using the thermal wind equation (Equation 6). The classical technique is to use a level of no motion defining the velocity to be zero at some depth as suggested by water mass boundaries or absence of the velocity shear. There is also an alternative method involving direct velocity measurement (e.g. current meters). Employing the traditional method to reference geostrophic velocities based upon the water mass distributions does not always accurately represent the velocity field (Donohue et al., 2000), since the density structure alone is insufficient to fully describe the circulation. A lack of initial information about the velocity in the deep water and

direct current measurement data for the Red Sea are the major limitations of the method. Therefore, the initial geostrophic velocity was assumed to be zero at the bottom in Equation 5.5.

#### 7.4.2 Bottom triangle

The Bottom triangles can be defined at the station pair as the area between the bottom of the shallower station and the bottom of the deeper station. There is not enough information in the bottom triangle to calculate the geostrophic velocity using the dynamic method. The velocity in the bottom triangle can be neglected or extrapolated from the velocity at the Deepest Common Level (DCL). However, neglecting the transport in the bottom triangles can introduce significant error into the transport calculation, which depends on the slope of the topography and the distance between the stations (Friedrichs, 1993). There are several methods to calculate the transport in the bottom triangle. For example:

- The first method is to assume that the velocity in the bottom triangle does not change by reproducing the velocity at the DCL of the station pairs throughout the bottom triangle (constant velocity).
- The second method is to extrapolate the velocity shear just above the DCL into the bottom triangle and modulate it using the ratio of the Brunt-Vaisala frequencies at the depth of extrapolation and at the DCL. Zemba (1991) in his model assumes that the slope of the isopycnal surface and the separation between the station pairs are constant in the bottom triangle calculation. The way to conserve the velocity shear at the DCL is by measuring the vertical density gradient at the DCL. This can be written mathematically as follows:

$$\partial\rho = \frac{\partial\rho}{\partial x}\partial x + \frac{\partial\rho}{\partial z}\partial z \quad (7.1)$$

$$0 = \frac{\partial\rho}{\partial x}\partial x + \frac{\partial\rho}{\partial z}\partial z \quad (7.2)$$

$$\frac{\partial\rho}{\partial x}\partial x = -\frac{\partial\rho}{\partial z}\partial z \quad (7.3)$$

$$\frac{\partial\rho}{\partial x} = -\frac{\partial\rho}{\partial z}\frac{\partial z}{\partial x} \Big|_{\rho} \quad (7.4)$$

$$\frac{\partial \rho}{\partial x}(p) \cong -\frac{\partial \rho}{\partial z}(p) \frac{\partial z}{\partial x}(\text{DCL}) = -\frac{\frac{\partial \rho}{\partial z}(p) \frac{\partial \rho}{\partial x}(\text{DCL})}{\frac{\partial \rho}{\partial z}(\text{DCL})} \quad (7.5)$$

from the thermal wind equation

$$v_{i,j} - v_{i-1,j} = \frac{g}{f\rho_0} \frac{\partial \rho}{\partial x} \Delta h = \frac{g}{f\rho_0} \frac{\partial \rho}{\partial x} (h_{i,j+1} - h_{i,j}) \quad (7.6)$$

where  $v$  is the geostrophic velocity,  $i$  is the layer and  $j$  is new column between the paired stations.  $\rho_0$  is the average density of sea water and  $h$  is the thickness of each layer.  $f$  is the coriolis parameter ( $f = 2\Omega \sin \varphi$ ,  $\Omega$  is the rotation rate of Earth and  $\varphi$ , the latitude) and  $g$  is the acceleration of gravity.

Substituting  $\frac{\partial \rho}{\partial x}$  in equation 7.5 leads to:

$$v_{i,j} - v_{i-1,j} = \frac{g}{f\rho_0} \frac{\frac{\partial \rho}{\partial z}(p)_{i,j+1} \frac{\partial \rho}{\partial x}(\text{DCL})_{i,j+1}}{\frac{\partial \rho}{\partial z}(\text{DCL})_{i,j}} (h_{i,j+1} - h_{i,j}) \quad (7.7)$$

The second method has been used in this study and the velocity shear at the DCL extrapolated through the bottom triangle area of each station pair. The first method could not be used in the large bottom triangle area between stations pairs due to the large uncertainty arising from that (see Figure 7-2). The effects of including or excluding the bottom triangle in the inversion will be investigated in Chapter 8.

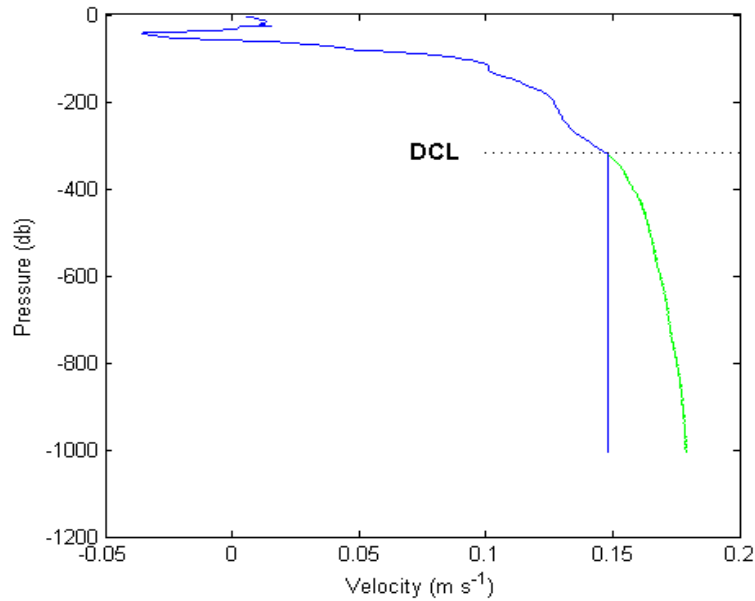


Figure 7-2: Comparison of the velocity profiles from the two methods showing that they differ only below DCL. The two computation methods are constant velocity (blue) and shear scaled by the vertical density gradient (green)

### 7.4.3 Initial geostrophic velocity and transport field

The geostrophic velocity and volume transport across each transect can be calculated by using the reference velocity that is described in section 7.4.1. It will guide the model in order to determine the best solution to choose from the infinity of solutions available (Figures 7.2 and 7.3). As can be seen in Figure 7.3, the geostrophic velocities are high with flow across section C (southwards, into the box) at the surface on both sides except for some northward flow (out of the box) in the middle of the section.

The geostrophic field clearly shows the inflow of RSSW (both sides), RSOW (western side) and RSDW (western side) with outflow of GAIW on the eastern side of section C. The maximum geostrophic velocities are found at the surface layers and can reach values higher than  $0.4 \text{ ms}^{-1}$ . The geostrophic field shows a strong flow in the upper layers and a weak flow or outflow in the deep layers. The circulation across section C (the northern edge of the box) can be seen as meridional inflows from the north and outflows in section F (the southern edge of the box). The volume transport across the northern box edge (section C) is 0.16 Sv and at the southern edge (section F) is 0.24 Sv. The initial volume transport across the edge of the box at each layer is

shown in Table 7-3. The volume transport indicates that the initial imbalance occurs primarily within waters with  $\sigma_\theta < 24.4$  in section C and within  $24.4 < \sigma_\theta < 27$  in section F. Figure 7-5 shows the initial residual of volume, potential temperature anomaly and salinity anomaly in individual model layers. The net initial imbalances are for volume in excess of 0.393 Sv, a potential temperature anomaly of 1.242°C Sv and a salinity deficit anomaly of 1.167 Sv. So the cumulative volume transport was not conserved along the rim of the box and a positive imbalance of 0.393 Sv was found.

| <b>Layer</b> | <b>Water mass</b> | <b>Layer boundaries</b>      | <b>Section C</b> | <b>Section F</b> | <b>Whole box</b> |
|--------------|-------------------|------------------------------|------------------|------------------|------------------|
| 1            | RSSW              | $\sigma_\theta < 24.4$       | 0.134            | -0.112           | 0.022            |
| 2            | GAIW              | $24.4 < \sigma_\theta < 27$  | -0.003           | 0.427            | 0.424            |
| 3            | RSOW              | $27 < \sigma_\theta < 28.33$ | 0.051            | -0.074           | -0.024           |
| 4            | RSDW              | $\sigma_\theta > 28.33$      | -0.024           | -0.005           | -0.029           |
| 1-4          | -                 | Full Depth                   | 0.157            | 0.236            | 0.393            |

Table 7-3: Initial volume transports (Sv) for each section (C and F) and for each layer (in each section and along the rim of the box). The sign convection (+) is into the box and (-) is out of the box

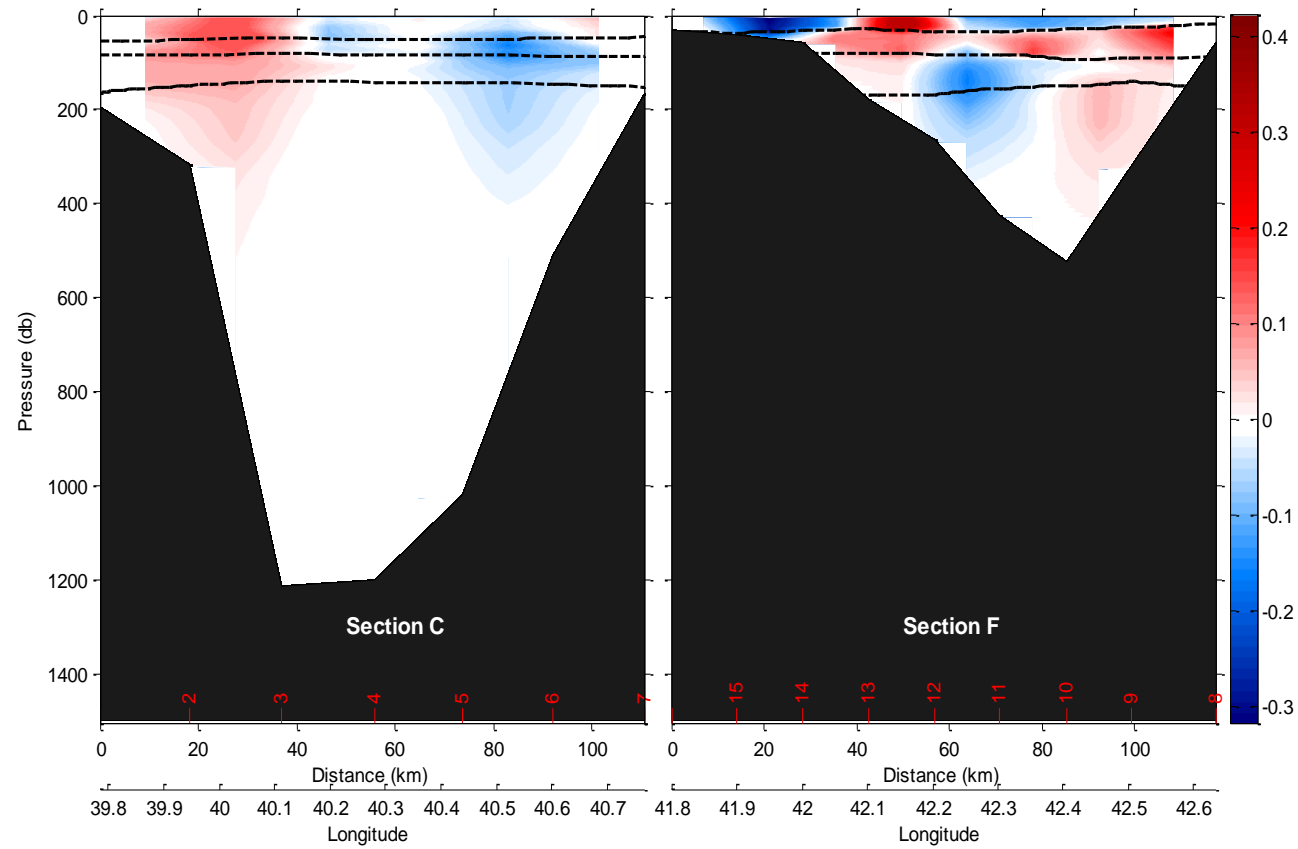


Figure 7-3: *A priori* geostrophic velocity along the rim of the box with water mass boundaries (the black dashed lines). Positive velocities are directed into the box. Stations are shown in red along the x-axis. Longitudes are also shown

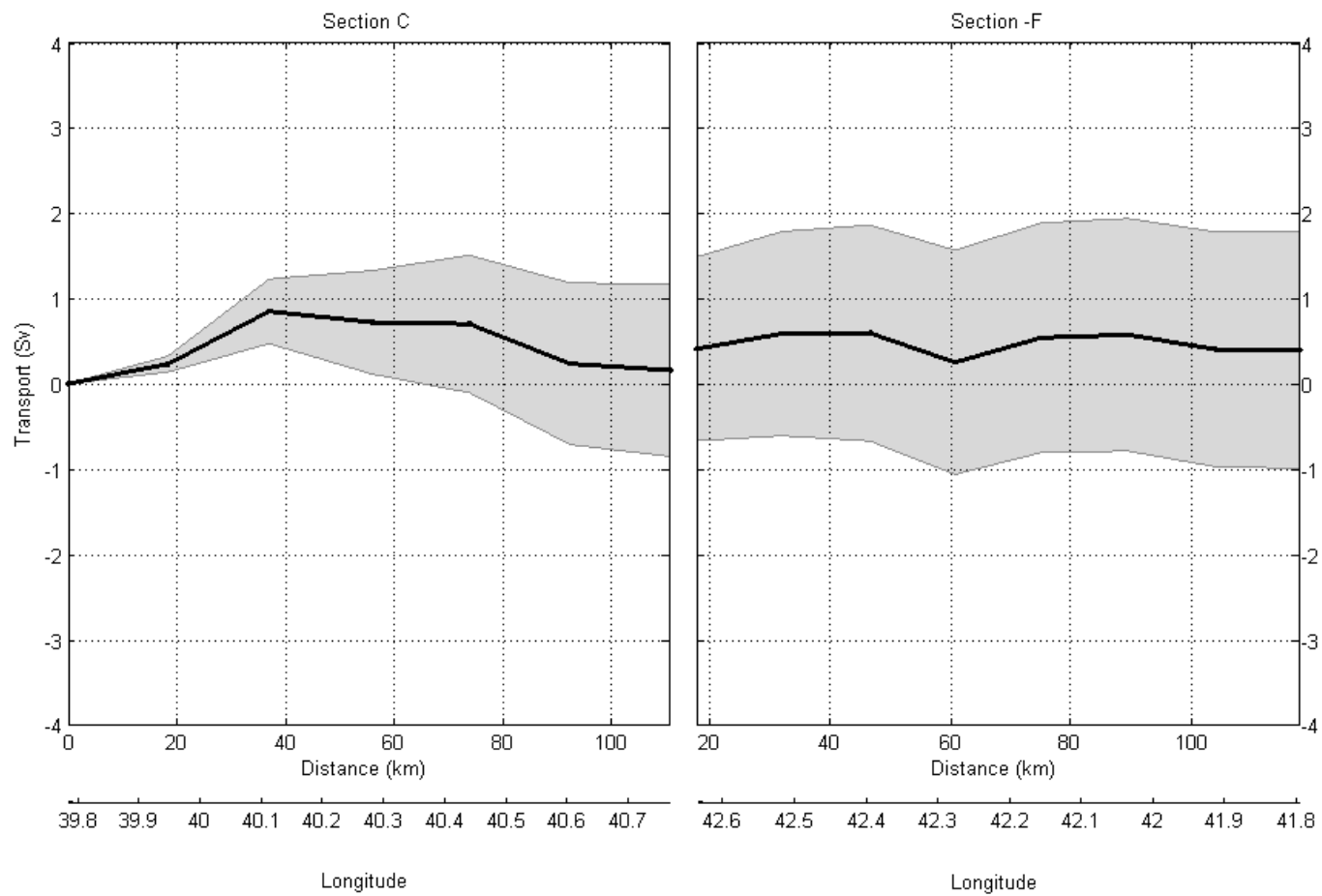


Figure 7-4: *A priori* cumulative volume transport along the rim of the box with *a priori* cumulative uncertainties (shaded area). Longitudes are also shown

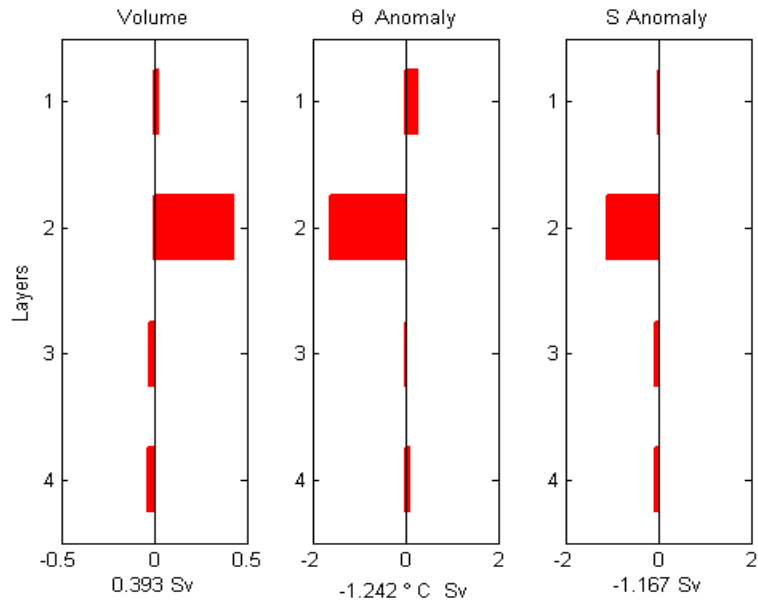


Figure 7-5: Initial residual of the volume, potential temperature ( $\theta$ ) anomaly and salinity anomaly in individual model layers. The full-depth residual and units are indicated beneath each graph

#### 7.4.4 Choice of *a priori* uncertainties

The *a priori* estimate is a vital step to be introduced into the inverse box model and needs to be weighted according to the uncertainties. Uncertainties for conservation equations and reference velocities need to be introduced as explained in section 5.2.2. The model equations (volume) are weighted by the inverse of the *a priori* estimates of their uncertainties. For the property equations other than volume, the uncertainties are estimated as double the product of the *a priori* uncertainties in volume conservation and the mean or standard deviation (whichever is largest) of property variations within the relevant layer (Naveira Garabato et al., 2003; Jullion et al., 2010). This choice between the mean and standard deviation is motivated by the presence of a very small standard deviation resulting from the large weight given to that layer. This ad hoc best guess was proposed by Ganachaud et al. (2000) where the factor of 2 accounts for possible correlation between the section-average and mesoscale components of the noise in the property conservation equations. In order to reach the best estimate of the *a priori* uncertainties number of inversions have been run to assess the model's behaviour following Ganachaud (2003a). However, in the present case assume lower uncertainty in the upper layers than in the deep water and that gives a realistic estimate

of transport. The selected *a priori* uncertainties that were used in the model for the volume conservation are listed in Table 7.4.

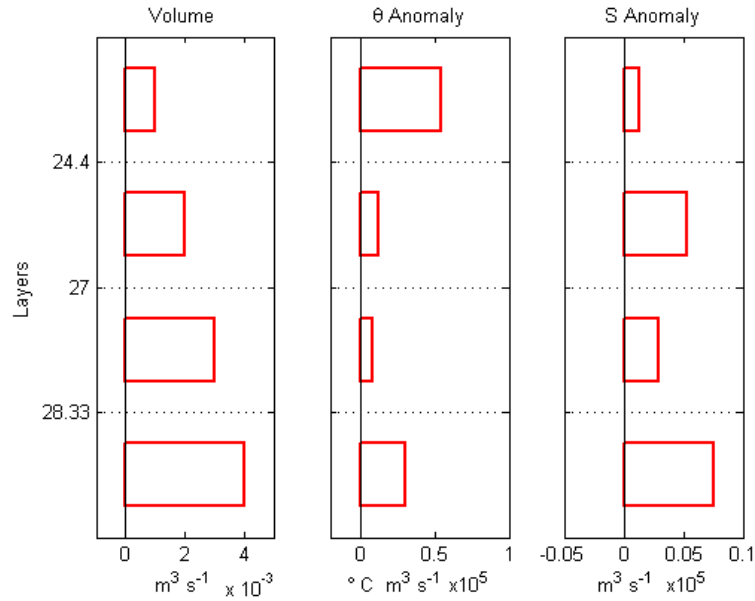


Figure 7-6: *A priori* volume, potential temperature and salinity anomaly uncertainties

| Model layer | Uncertainty (Sv) | Potential temperature anomaly ( $\theta$ , $^\circ\text{C}$ ) | Salinity anomaly |
|-------------|------------------|---|------------------|
| 1           | 0.001            | $7.35 \pm 0.06$   | $-1.13 \pm 0.33$ |
| 2           | 0.002            | $-1.17 \pm 2.56$  | $-1.63 \pm 0.63$ |
| 3           | 0.003            | $-1.69 \pm 0.20$  | $0.99 \pm 0.16$  |
| 4           | 0.004            | $-2.78 \pm 0.06$  | $1.38 \pm 0.03$  |
| Full depth  | 0.001            | $-1.79 \pm 1.46$  | $0.89 \pm 1.17$  |

Table 7-4: *A priori* errors in the volume conservation equations for model layers and the layer mean and standard deviation of potential temperature ( $\theta$ ) and salinity anomalies

The reference velocities are weighted by the square root of their uncertainties. The preliminary uncertainties assigned to the unknowns are  $0.01 \text{ m s}^{-1}$  for the reference velocities for stations pairs over the open sea (in the middle of the section) and  $0.02 \text{ m s}^{-1}$  over the shallow water close to the Arabian and African sides (at each section boundary), these differences being due to the high velocity expected at the shallower station pair. Moreover, the sensitivity tests for the *a priori* uncertainties for the reference velocities will show that increasing the uncertainties does not affect the solution significantly (see section 8.3.5). The uncertainties used to weight the reference velocities at each station pair are summarised in Table 7.5.

| Station Pair                       | Section C           |                     |                     | Section F           |                     |
|------------------------------------|---------------------|---------------------|---------------------|---------------------|---------------------|
|                                    | 1:2                 | 3:6                 | 7:8                 | 9:12                | 13:14               |
| Uncertainties (m s <sup>-1</sup> ) | 2 X10 <sup>-2</sup> | 1 X10 <sup>-2</sup> | 2 X10 <sup>-2</sup> | 1 X10 <sup>-2</sup> | 2 X10 <sup>-2</sup> |

Table 7-5: Uncertainties for reference velocities for each station pair

## 7.5 Other unknowns parameters

In this section the implementation of other unknowns used in the inverse box model will be described in detail.

### 7.5.1 Diapycnal mixing

As mentioned earlier in section 5.2.3, the interior diapycnal mixing between the layers at each interface is parameterised by following McIntosh and Rintoul (1997). For the volume, the diapycnal velocity needs to be multiplied by the area of the layer interface and for the other properties (temperature and salinity) by the area of the layer interface and the mean property concentration along the layer interface in the box. The area and the mean property concentration (temperature and salinity anomalies) were extracted from hydrographic data (CTD data from R/V Maurice Ewing, August 2001) at each layer interface in the box. The *a priori* estimate of the unknown diapycnal velocity is initialised to zero with *a priori* uncertainty of  $10^{-5}$  m s<sup>-1</sup>, near the upper end of the range observed for deep ocean mixing rates (Munk & Wunsch, 1998). This condition for the diapycnal mixing is usually used in the inverse box model (McIntosh & Rintoul, 1997; Sloyan & Rintoul, 2000) due to the lack of data for the mixing in the ocean. McIntosh and Rintoul (1997) show that the inclusion of the diapycnal velocities is crucial to obtaining satisfying results. The sensitivity test for including or excluding diapycnal mixing and different initial uncertainties used for this condition will be described in section 8.3.4.

| Layer interface ( $\sigma_\theta$ ) | Area ( $\text{m}^2$ ) |
|-------------------------------------|-----------------------|
| 24.4                                | $4.56 \times 10^{10}$ |
| 27                                  | $3.87 \times 10^{10}$ |
| 28.33                               | $3.87 \times 10^{10}$ |

Table 7-6: The initial solution for the model layer interfaces derived from CTD data and then included in the inversion. The area is the total area of each potential density ( $\sigma_\theta$ ) interface over the whole box

### 7.5.2 Ekman transport

The wind stress of the SCOW has high spatial resolution ( $0.25^\circ$  degree) in the wind fields compared with other climatological datasets. It estimated from the 8-yr record (September 1999-August 2007) of wind measurements by QuikSCAT, (Risien & Chelton, 2008). In the literature there are many methods used to calculate the Ekman transport in the inverse model. For example, Ekman transport can be calculated for each station pair and included in the inversion as an extra unknown (Naveira Garabato et al., 2003; Hernández-Guerra et al., 2005; Fraile-Nuez et al., 2008). The direction of the surface wind over the Red Sea is stressed along the main axis of the Sea due to the existence of the high mountain located along the Arabian and African coasts (Figure 7.1). The wind stress over our box is dominated by a weak northwesterly wind during the SW monsoon (June-September). The average climatology wind stress magnitude for August is shown in Figure 7.1. The Ekman transport has been calculated across each section from climatological wind stress fields (section 5.2.5) over the box area. Table 7.7 summarises the Ekman volume transport for each transect and over the whole box in the southern area of the Red Sea. These values give a net divergence over this region (as enclosed by the inverse box) of  $-0.004$  Sv for the volume transport. So the Ekman transport in the box is negligible compared to the total transport of the upper layers.

| <b>Volume Transports<br/>(Sv)</b> |                     |
|-----------------------------------|---------------------|
| Section C                         | $-0.0188 \pm 0.001$ |
| Section F                         | $0.0147 \pm 0.001$  |
| The whole box                     | $-0.004 \pm 0.003$  |

Table 7-7: Ekman volume transport (Sv) calculated from SCOW August average climatology.

For the whole box, positive transport indicates a convergence over the box

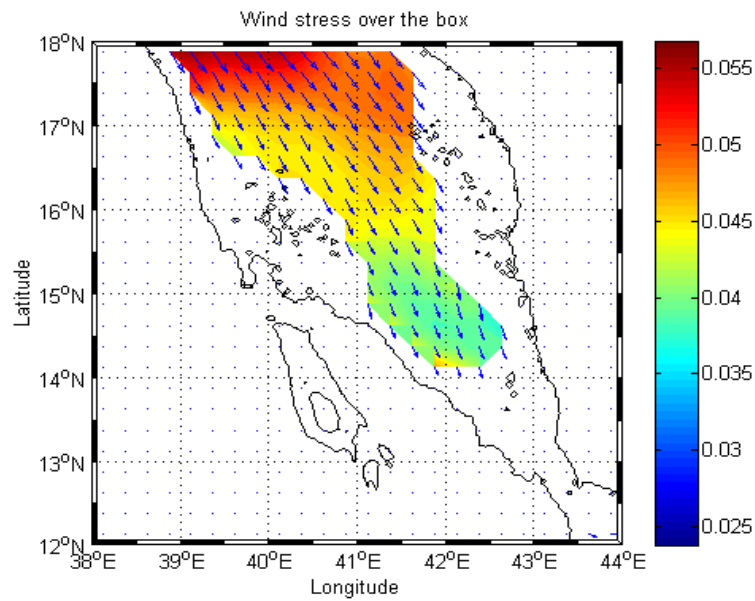


Figure 7-7: Climatology mean of the wind stress magnitude for August over the box in the southern region of the Red Sea. Wind stress ( $\text{Nm}^{-2}$ ) is shown by colour and wind direction by vectors

## 7.6 Conclusion

This chapter has described the inverse box model setup and constraints (volume, potential temperature and salinity) that apply in the inverse box mode. The geostrophic velocity and transport were calculated along the rim of the box from the available hydrographic data. In addition, the data extracted from CTD data from R/V Maurice Ewing (August 2001) along the box at each layer interface were used to provide information about the interior of the box. The choices of *a priori* estimates of the reference level and the velocities with their uncertainties were made using available data (hydrographic data). A lack of initial information on the velocity of the deep water and direct current measurement data for the Red Sea is the major limitation of this method. The bottom triangles between the station pairs were included in the model by extrapolating velocity shear at the DCL through the bottom triangle. The cumulative volume transport was not conserved and a positive imbalance of 0.39 Sv was found. Building the initial solution for the inverse box model is a crucial step and several tests were made to include possible components in the model. These sensitivity tests will be described in the following chapter.

# Chapter 8 The standard model and solution

## 8.1 Introduction

A box inverse model is applied to the initial state of the circulation as described in Chapter 7. The inverse model is set up as an underdetermined problem system since there are fewer conservation equations than unknowns. The SVD method seeks a solution from infinite solutions for the system and to choose the appropriate one of these an extensive analysis of the sensitivity of the model is required for its parameters. The selected solution is truncated to balance the requirement for the theoretical constraints (conservation equations) to be satisfied while introducing small noise into the solution. There is no certain process for determining the selected solution, and this choice is always subject to discussion as it is selected from the infinity of possible solutions.

The inverse box model solution is based on the hypothesis that volume, heat and salinity are conserved within their *a priori* uncertainties. However, as the solution of the inversion is based on hydrographic data, a snapshot of the circulation in the southern Red Sea region, the solution needs to be robust so that the changes in the parameters will not significantly change the solution. In addition the *a priori* uncertainties play an important part in the inversion as they will produce good results if adequately weighted (McIntosh & Rintoul, 1997).

In order to assess the model's stability, a set of number of sensitivity tests were performed to assess the robustness of the model in relation to its parameters and all the results of those tests will be discussed in this chapter.

The first part of this chapter looks at the selection of the appropriate solution, compares that with the *a priori* estimate and verifies that the constraints are satisfied with one *a posteriori* error (as calculated from Equation 5.16 in Chapter 5). The second part goes on to discuss the sensitivity of the final configuration of the model to changes in the model variables.

## 8.2 Standard inverse box model

### 8.2.1 Choice of the solution degree

The row- and column-weighted system of equations is solved by using a truncated SVD (Wunsch, 1996). The rank of the solution (5 out of 14) is considered. In order to choose the appropriate rank many experiments were run to test all ranks using the final configuration of the model. Figure 8-1 indicates the full depth for the volume residual at different ranks, showing how the solution reacts with different ranks as compared to the residual from the initial solution. The first low solution rank (rank 1) has an unacceptably large residual, showing that the solution of the inversion has not changed much from the initial solution. On the other hand, the high solution ranks (greater than 7) have very low residuals, indicating that almost all equations are satisfied. However, increasing the number of the solution rank while reducing the residual's size also adds considerable noise to the model. As shown in Figure 8-1 the inverse solutions are quite similar between ranks 2 and 4, with a residual of 0.15 Sv. In addition, the solution from rank 6 could be used to obtain a similar result as that from rank 5. In order to choose the correct solution rank for the standard model, the solutions for each rank were analysed and tested. Therefore, in this thesis the preferred solution rank was selected such that the equation residuals are indistinguishable from zero, within one *a posteriori* standard deviation, and perturbations to the initial estimates of the unknowns (*a posteriori*) remain within one *a priori* standard deviation (Figure 8-2, Figure 8-3 and Figure 8-4). These considerations lead to the selection of rank 5 as the preferred solution for the standard model. The sensitivity test for choice of rank will be discussed in section 8.3.1.

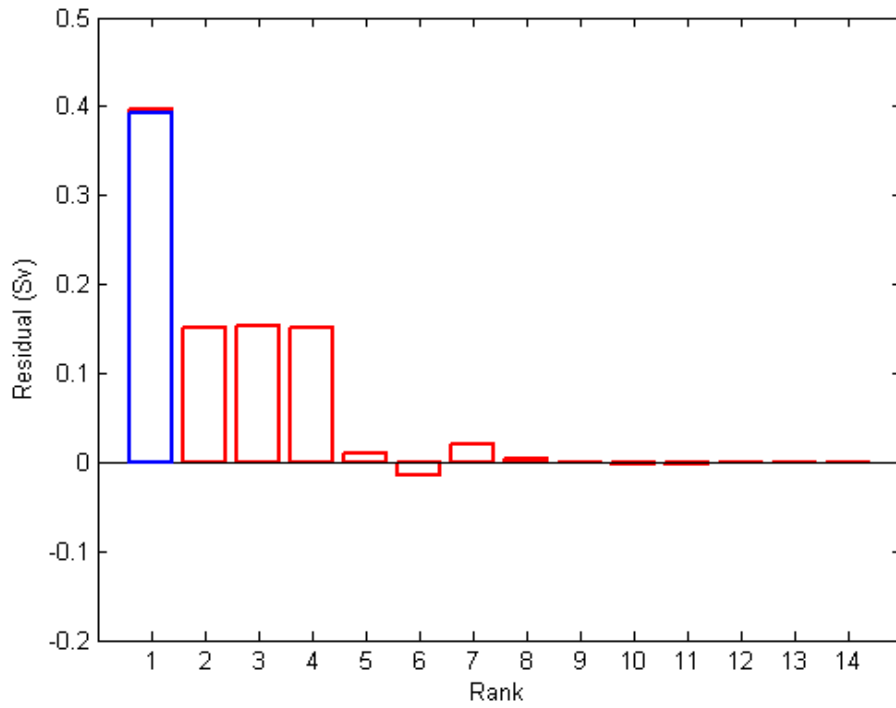


Figure 8-1: Full-depth volume residual as a function of the rank solution (red) and the full-depth volume residual for the initial solution (blue)

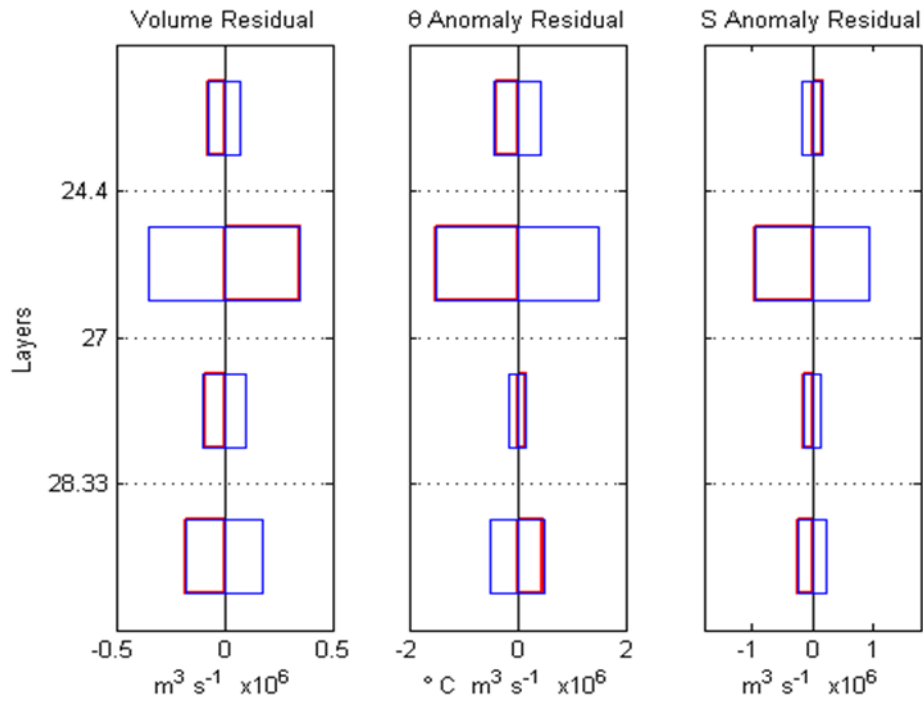


Figure 8-2: Standard solution residual of volume, potential temperature ( $\theta$ ) anomaly, and salinity (S) anomaly in individual layers (red). One *a posteriori* standard deviation uncertainty (blue)

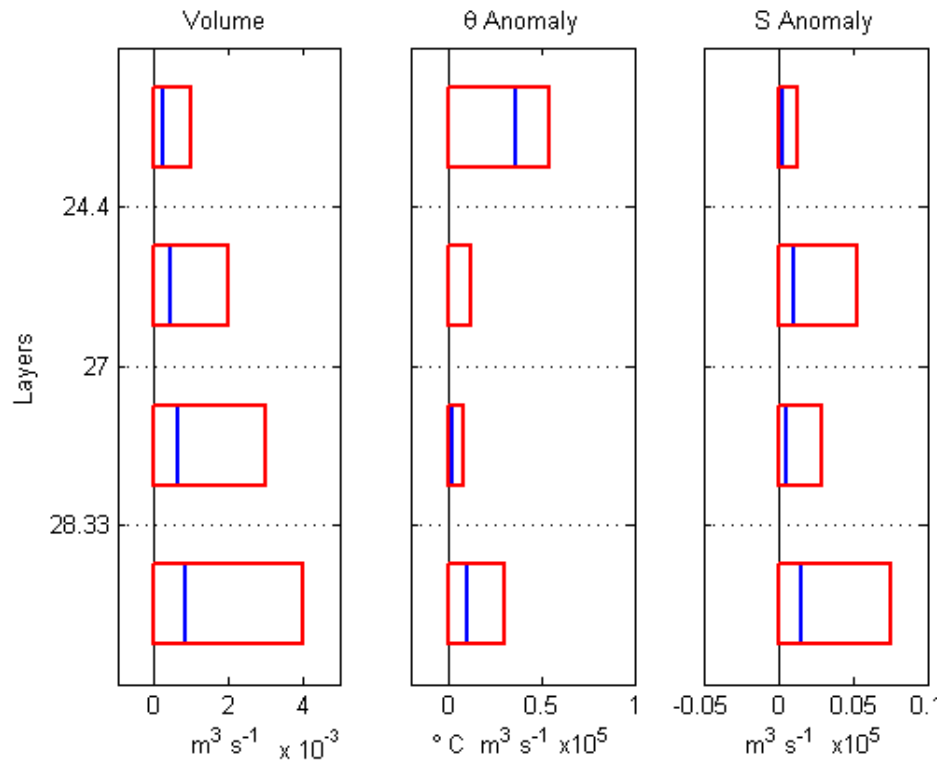


Figure 8-3: Comparison between the *a priori* standard deviation (red) and the *a posteriori* standard deviation (blue) for the volume, potential temperature anomaly and salinity anomaly

### 8.2.2 Description of the model solution

The velocities with a priori uncertainty for the reference level as a function of the station pairs, and as determined by the inversion, are shown in Figure 8-4 (lower panel). As we can see from Figure 8-4, the inversion makes large changes to the initial reference velocity (which is assumed to be 0 in the model). These changes came as a result of the inversion trying to reduce the imbalance that occurred in the initial full-depth volume transport (Figure 7-4, previous chapter). Thus changes in the reference velocity along the rim of the box vary between  $-0.029 \text{ cm s}^{-1}$  and  $7.12 \text{ cm s}^{-1}$ . The largest changes in the reference level velocities are found at the western boundary of the section F (the right of Figure 8-4) ( $7.12 \text{ cm s}^{-1}$ ) and this may be related to the large uncertainty associated with section F due to the GAIW inflow. If we look at the western part of section F (the right of Figure 8-4), there is a large change in the reference velocities (station pairs 13 to 14) due to the fast outflow of the current from the Red Sea at the subsurface layer which is subjected to the higher variability of the thermohaline properties (Figure 8-5, lower panel). The changes in the reference velocity in section C vary between  $-0.029 \text{ cm s}^{-1}$  and  $1.77 \text{ cm s}^{-1}$  with the largest

changes occurring at both the western ( $1.77 \text{ cm s}^{-1}$ ) and eastern ( $0.58 \text{ cm s}^{-1}$ ) boundaries of section C. In the rest of section C the changes in the initial reference velocity are less than  $\sim 2.41 \text{ mm s}^{-1}$ .

The gain of the information ratio,  $\frac{\sigma_s - \sigma_0}{\sigma_0}$  (where  $\sigma_s$  is the *a posteriori* standard deviation and  $\sigma_0$  the *a priori* standard deviation), can be used to explore the reduction of the uncertainty as compared to the *a priori* uncertainty. The upper panel in Figure 8-3 indicates that the amount of information gained is small, less than 3% in section F and less than 5% higher in section C (except for station pairs 2-4), reflecting the low *a priori* uncertainty that was introduced into the inverse model in section C. As is shown in Figure 8-3, the errors in the individual layers are reduced only slightly by the inversion that might be due to the rank chosen (5 out of 14).

As mentioned in the previous section (8.2.1), in order for the solution to be satisfactory, the residuals are required to be within one *a posteriori* uncertainty and that condition is well satisfied as shown in Figure 8-2. The largest residual is found in the subsurface inflowing GAIW layer, where the baroclinic transports are greatest. This is to be expected because section F is very close to the Strait of Bab el Mandeb region (0.42 Sv from the initial solution). The modification made by inversion to the lateral transport on the full-depth volume transport in section C is  $\sim 0.16 \text{ Sv}$  (Figure 8-5) while most of the changes in the full-volume depth transport occur in section F.

In the selected solution, the volume residual is reduced to 0.01 Sv (0.39 Sv was the residual of the initial solution), showing that the inversion satisfies conservation constraints well in terms of volume (Figure 8-5, middle panel). The conservation constraints for RSSW and RSOW water masses are the least satisfying with magnitude of -0.07 Sv and -0.09 Sv for their volume imbalance, respectively.

The inversion makes little changes to the *a priori* estimates by reducing the inflow of RSSW, RSOW and RSDW in section C, and of the GAIW in section F (into the box), whereas the outflow increases in section F (out of the box). The volume transports in each of the model sections and layers are summarised in Table 8-1. The volume transports within these layers are illustrated in Figure 8-6.

In order to reach the solution that was described previously, several inversion tests were run to assess the inversion behaviour and in the next section the sensitivity tests for the main parts of the selected solution are presented.

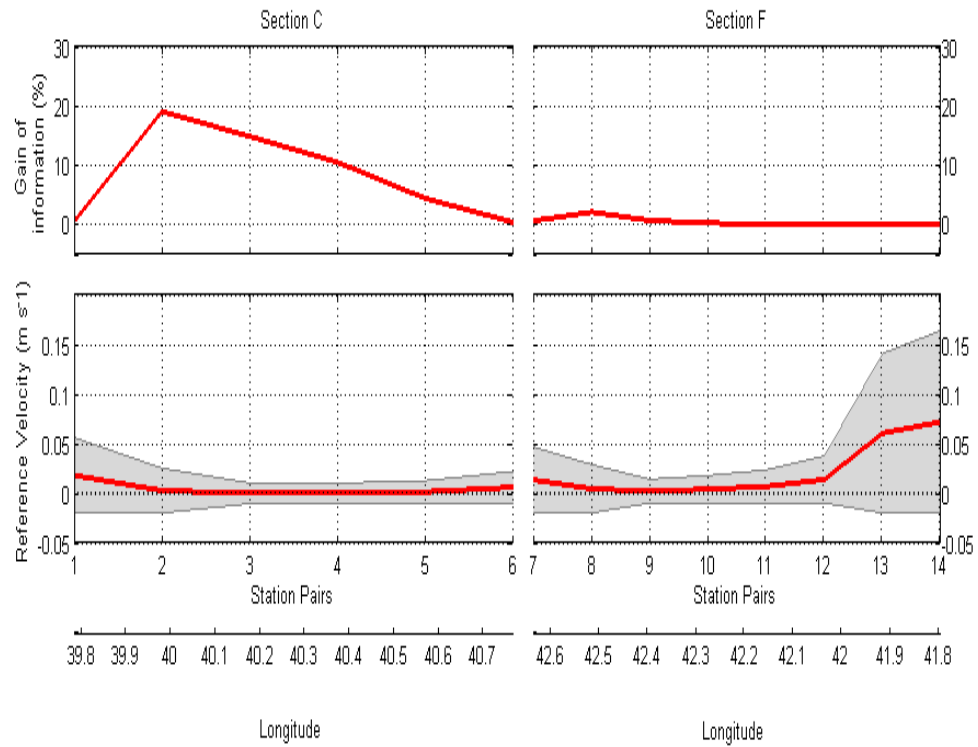


Figure 8-4: Upper panel: Gain of information ( $(\sigma_s - \sigma_0) / \sigma_0$ ) with  $\sigma_s$  the a posteriori standard deviation and  $\sigma_0$  the a priori standard deviation. Lower panel: Reference velocity after the inversion for each station pair. One a priori standard deviation is shown in the shaded area

| Layer | Water mass | Layer boundaries             | Section C |       | Section F |       | Whole box |       |
|-------|------------|------------------------------|-----------|-------|-----------|-------|-----------|-------|
|       |            |                              | Initial   | Final | Initial   | Final | Initial   | Final |
| 1     | RSSW       | $\sigma_\theta < 24.4$       | 0.13      | 0.11  | -0.11     | -0.18 | -0.02     | -0.07 |
| 2     | GAIW       | $24.4 < \sigma_\theta < 27$  | -0.00     | -0.02 | 0.43      | 0.37  | 0.42      | 0.35  |
| 3     | RSOW       | $27 < \sigma_\theta < 28.33$ | 0.05      | 0.02  | -0.07     | -0.11 | -0.02     | -0.09 |
| 4     | RSDW       | $\sigma_\theta > 28.33$      | -0.02     | -0.11 | -0.01     | -0.06 | -0.03     | -0.18 |
| 1-4   | -          | Full depth                   | 0.16      | 0.00  | 0.24      | 0.02  | 0.39      | 0.01  |

Table 8-1: Volume transports (Sv) for each section (C and F) along the rim of the box and for each layer (the initial and final solutions of the inversion). The sign convection (+) is into the box and (-) is out of the box

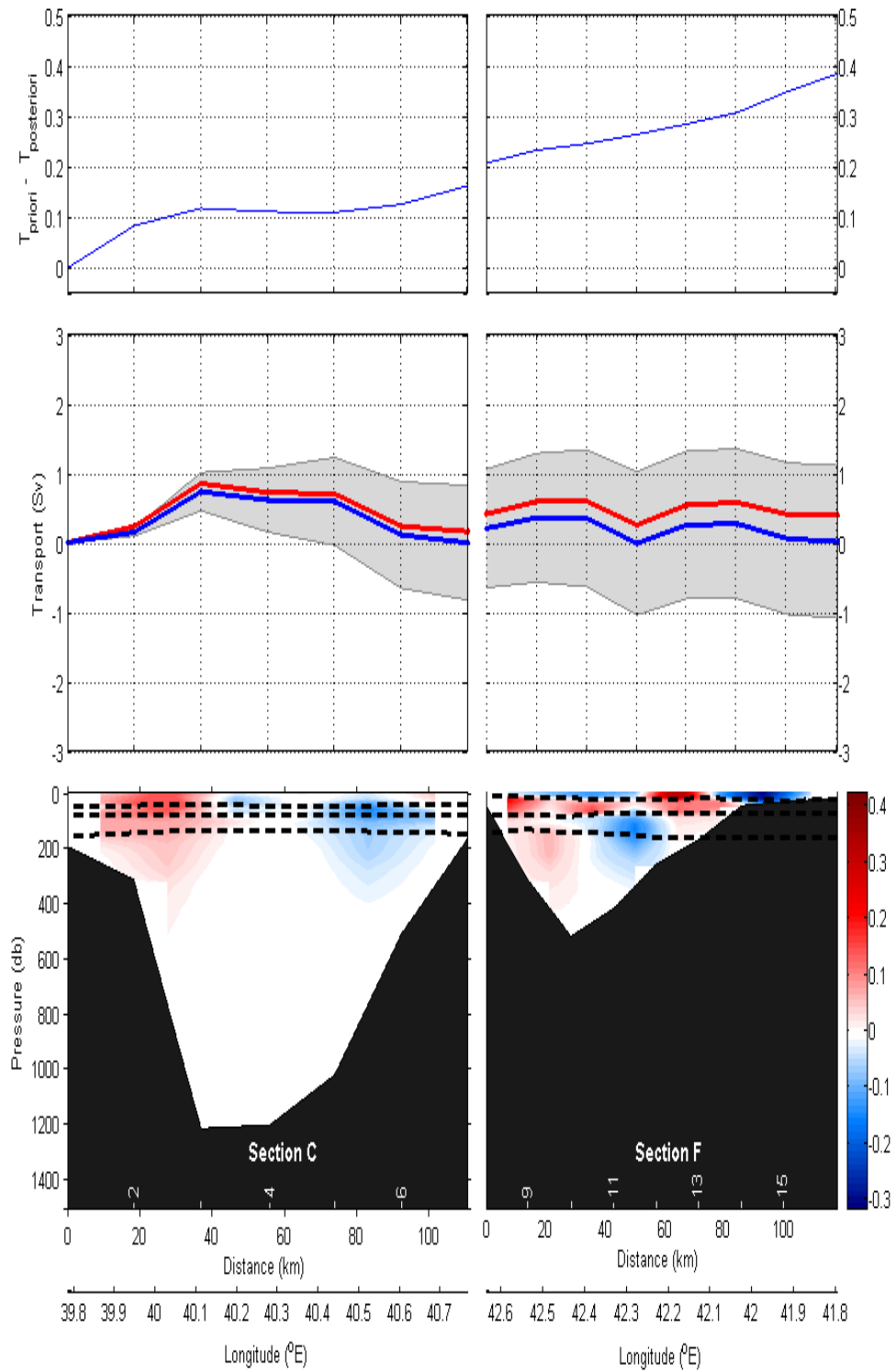


Figure 8-5: Upper panel: differences between the *a priori* and the *a posteriori* full-depth cumulative volume transport (Sv) along the rim of the box. Middle panel: comparison between the *a priori* (red) and the *a posteriori* (blue) full-depth cumulative volume transport (Sv) along the rim of the box. The shaded area gives accumulated *a posteriori* uncertainty in the full-depth transport. Lower panel: geostrophic velocities ( $\text{m s}^{-1}$ ) diagnosed by the inverse box model. The sign convection (+) is directed into the box and (-) is directed out of the box

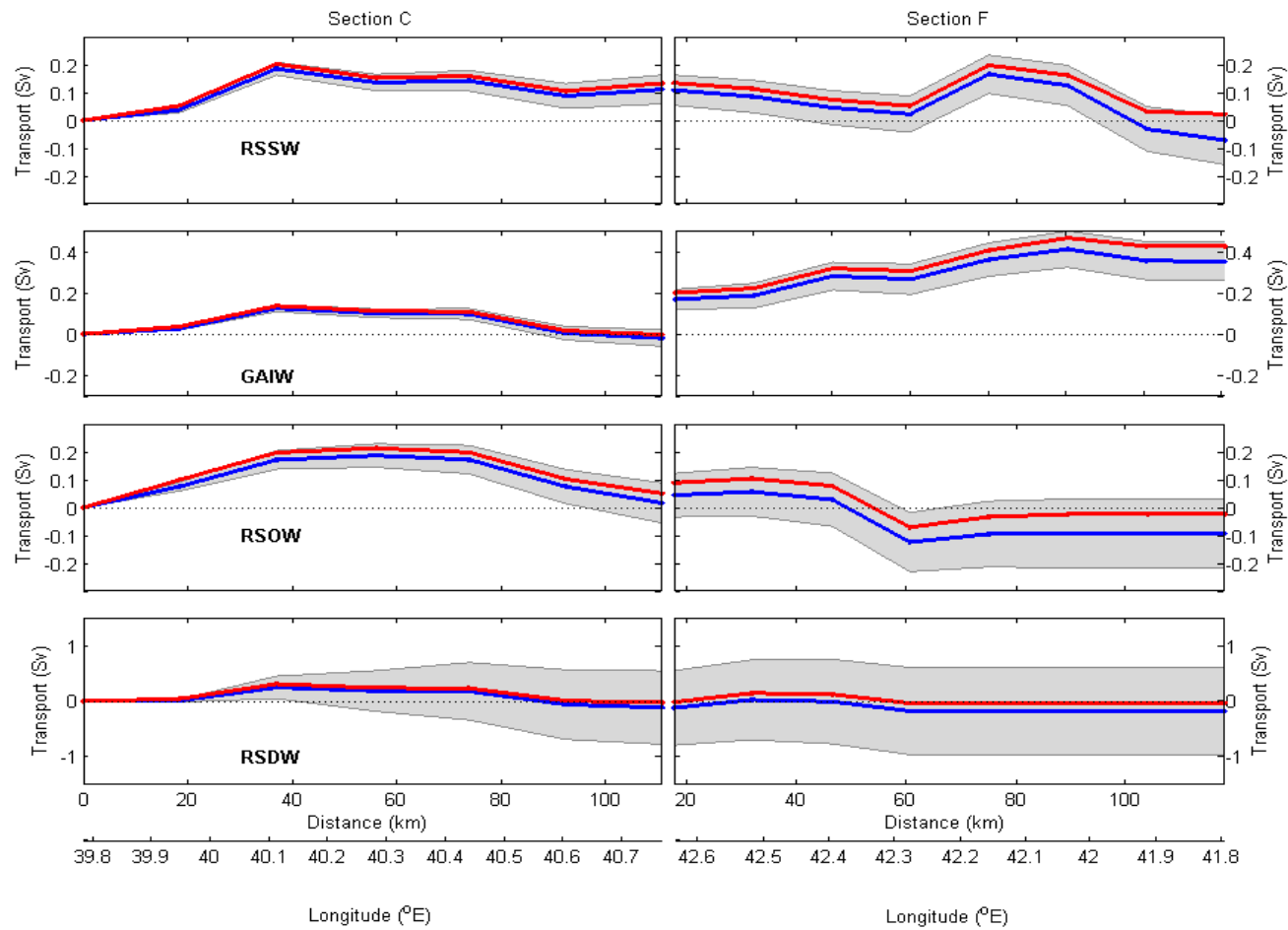


Figure 8-6: *A posteriori* solution (blue) and *a priori* solution (red) cumulative volume transport (Sv) for each water mass RSSW, GAIW, RSOW and RSDW in each section. The shaded area represents *a posteriori* cumulative uncertainties

### 8.3 Inverse box model sensitivity

The sensitivity of the inversion model to the changes in its parameters can be investigated by running a number of different models that each vary from the standard model (which is the preferred solution rank 5) by one factor, as explained in the previous section. The sensitivity of the standard model was examined by allowing each of its parameters to vary within a prescribed range. Several experiments were run to illustrate the importance of the various characteristics and their effects on the net fluxes were observed.

#### 8.3.1 *Choice of the rank*

As mentioned in section 8.2.1 the rank of the selected solution was chosen to be such that the model residuals are required to be zero, within one standard deviation of the error estimate. Here, to illustrate the effect of the choice of rank on the selected solution, the results are compared with ranks of 3, 4, 8, 10 and 14 respectively. Table 8-2 shows the comparison of different solution residuals with different ranks for the volume transport fluxes. Figure 8-7 shows a comparison of different ranks with the selected solution and the initial solution. At the higher ranks of 8, 10 and 14, the solutions have smaller residuals than the selected solution, with unreasonable circulation that had increased the fluxes across each section. In particular, the magnitudes of the inflow of RSDW across section C are increased to 0.82, 0.81 and 0.57 Sv (as compared to 0.25 Sv with the selected solution and 0.31 Sv with the initial solution) for ranks 8, 10 and 14 respectively. Also, the magnitudes of the outflow of RSDW across section F are increased to 0.61, 0.61 and 0.51 Sv for the same ranks, respectively (as compared to 0.21 Sv with the selected solution, and 0.18 Sv with the initial solution).

The lower rank solutions of 2 and 4 give higher residuals than the selected solution as is shown in Table 8-2, and they also give higher fluxes across individual sections. The solutions from the lower ranks are quite close to the initial solution that came from the velocity field (as described in section 7.4) since the adjustments made by the inversion are small.

| Volume fluxes (Sv) | Selected          | Rank 2 | Rank 4 | Rank 8 | Rank 10 | Rank 14 |
|--------------------|-------------------|--------|--------|--------|---------|---------|
|                    | solution (rank 5) |        |        |        |         |         |
| RSSW               | -0.07             | 0.01   | 0.01   | -0.03  | -0.03   | 0.02    |
| GAIW               | 0.35              | 0.40   | 0.40   | 0.13   | 0.13    | 0.04    |
| RSOW               | -0.09             | -0.05  | -0.05  | -0.19  | -0.18   | -0.20   |
| RSDW               | --0.18            | -0.21  | -0.21  | 0.08   | 0.08    | 0.13    |
| Full depth         | 0.01              | 0.15   | 0.15   | 0.00   | 0.00    | 0.00    |

Table 8-2: Volume transport estimates (Sv) for the southern Red Sea for the selected solution and the alternative models, run with different ranks

### 8.3.2 Sensitivity to the number of constraints

A number of experiments were run with the model with different constraints applied. If the number of the constraints in the inversion model is reduced, this is a good test for assessing the robustness of the model, as fewer equations give fewer degrees of freedom for the model to adjust. Figure 8-8 shows how the model solution reacts when the number of constraints varies. When the volume constraint is only applied to the inverse model, the full-depth cumulative transport for volume conservation is quite similar to that from the selected solution (with conservation of volume, temperature and salinity). Most of the changes between the two experiments occurred in the RSDW in both sections (C and F) while the solution did not vary in the shallower water masses when the number of constraints varied. The residual of the experiment with the volume only is reasonably satisfied with a magnitude of 0.002 Sv at an equivalent rank as compared with 0.01 Sv for the selected solution (Figure 8-8). These changes in the solution at the deep layer might be explained by a dominance of the barotropic components in the deep layers, whereas the baroclinic velocities of geostrophic velocities dominate in the upper layers (Jullion, 2008). The adjustment made by the inversion on the barotropic velocities at the reference level will affect the deep layers much more than the upper layers. When more constraints are added (volume + salinity conservation) to the model, the solution varies quite significantly from the selected solution with a residual of 0.23 Sv at the equivalent rank. The inverse box model is quite robust to the set of constraints. However, this suggests that at least three constraints including volume constraint provide satisfactory constraints for the inverse solution.

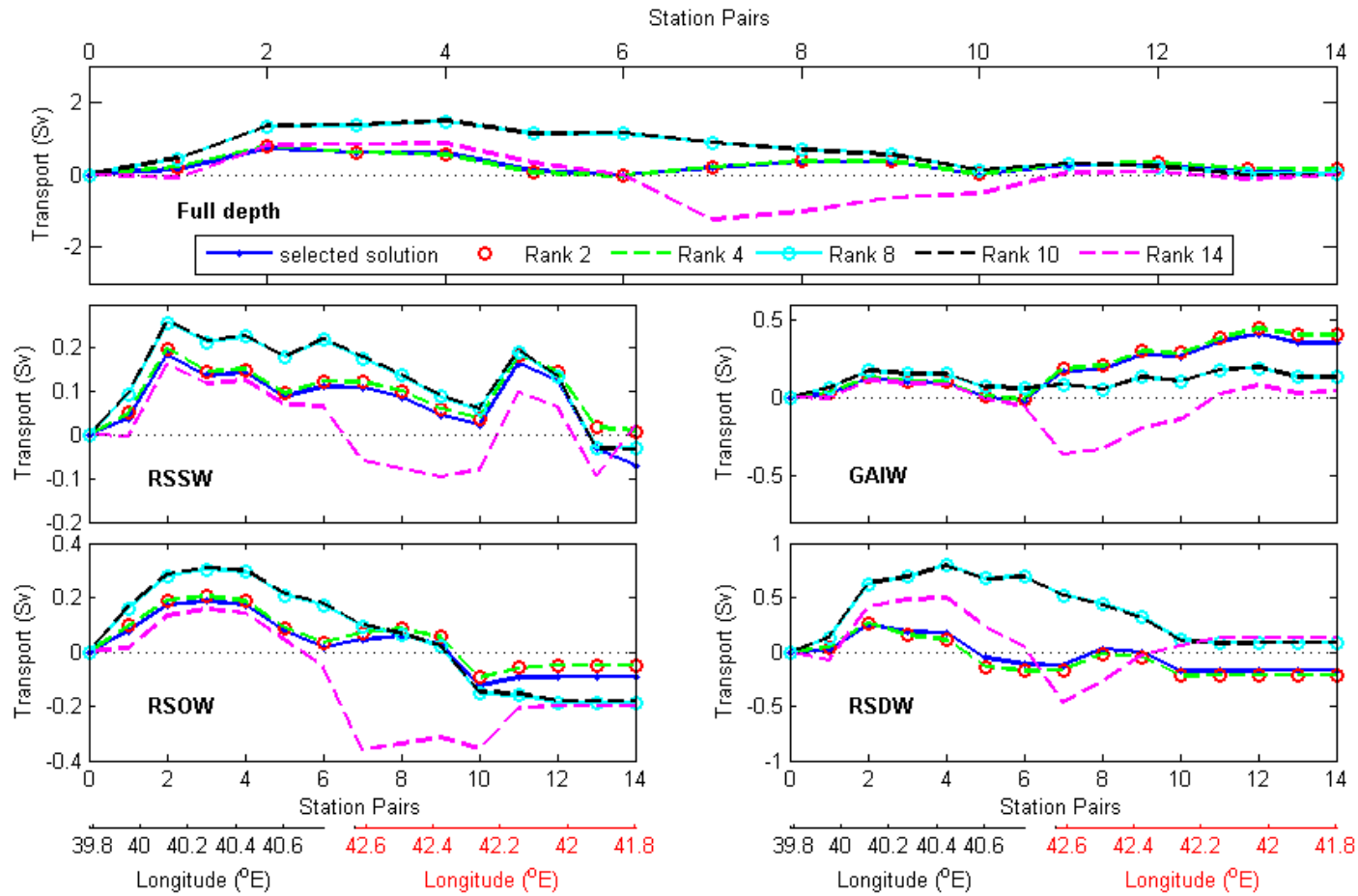


Figure 8-7: Cumulative volume transport (Sv) along the rim of the box for simulation with the different ranks 2, 4, 8, 10 and 14 (red circle, green dashed line, cyan circle, black dashed line and magenta dashed line) and for the selected solution (blue)

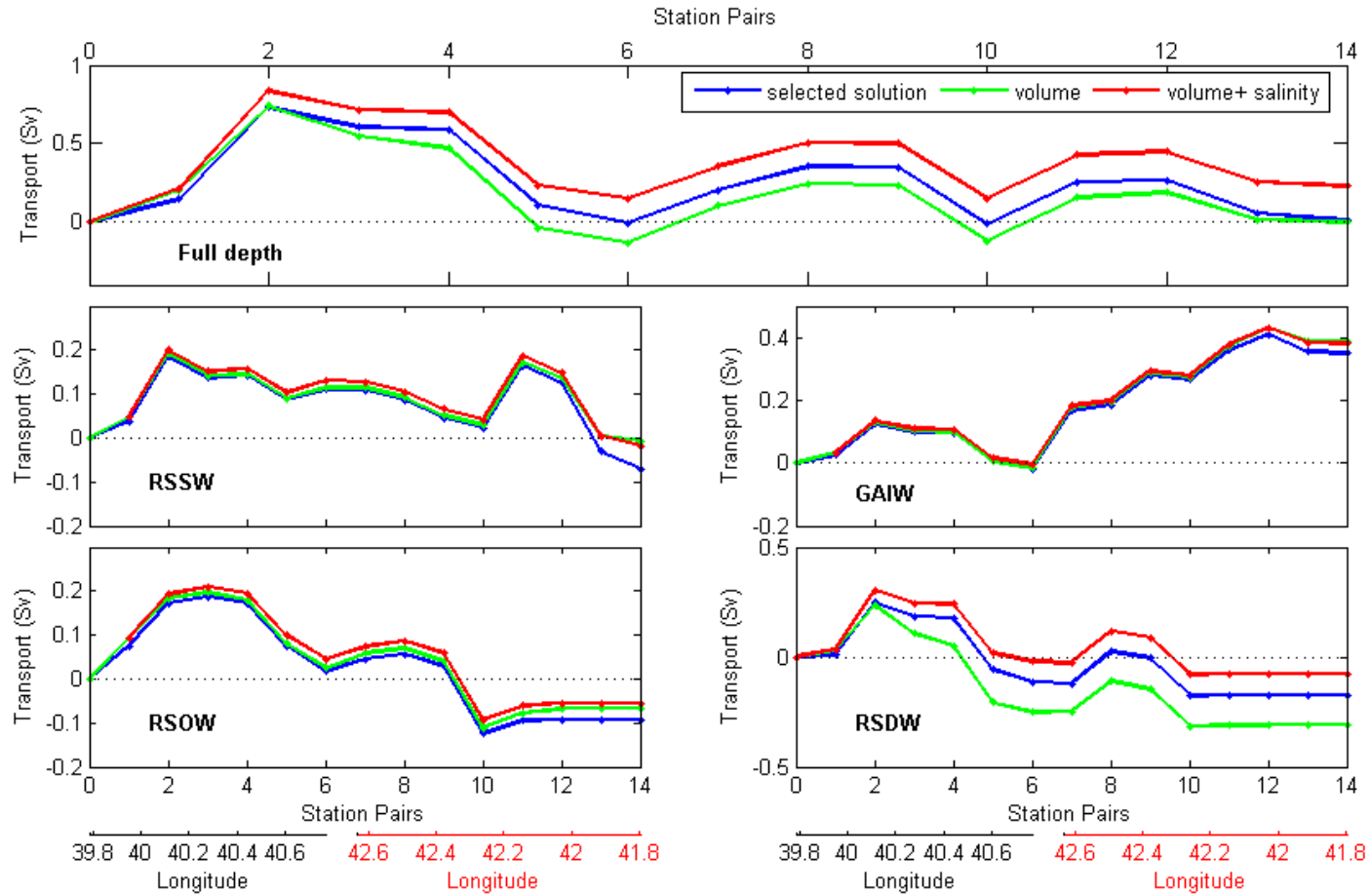


Figure 8-8: Cumulative transport (Sv) along the rim of the box for volume conservation only (green), for volume and salinity conservation (red) and for the selected solution (blue)

### 8.3.3 Sensitivity to *a priori* errors on the constraints

As described before (see section 7.4.4), the *a priori* estimate for the inverse model needs to be weighted according to the uncertainties. A number of models were used to modify the weighting of the conservation equations (volume, salinity and potential temperature). Since the residuals in the conservation equations are acceptable in the inversion, the weighting of these residuals becomes very important. For example, if the system is solved without row weighting at rank 5 (the same as the selected solution rank) the solution has significant differences, with a larger magnitude for the residual of 0.20 Sv, as compared to the selected solution (0.01 Sv), and increased fluxes across the individual sections. In particular, the magnitudes of the RSSW inflow are increased to 0.25 and 0.15 Sv in sections C and F respectively; also, the GAIW inflows are increased to 0.14 and 0.48 in sections C and F respectively. Table 8-3 shows the comparison of the selected solution and the initial solution (pre-inversion) with different simulations, without row and column weighting. Figure 8-9 shows a comparison of the full-depth and individual layer cumulative volume transport for the selected solution and initial solution with alternative model runs. Without column weight the solution at rank 5 shows large differences from the selected solution particularly, in the magnitude of residuals with higher fluxes across the individual sections for RSOW and RSDW. Without row and column weighting, this simulation shows significant differences from the selected solution and initial solution; in particular, the magnitudes of the inflow and outflow for all water masses (RSSW, GAIW, RSOW and RSDW) are increased.

In order to investigate how the model reacts if the relative weights are modified for individual layers, an experiment was run with all the *a priori* uncertainty set to be equal (0.2 Sv) in the volume layer (Figure 8-10). The residual of this experiment (0.13 Sv) for full-depth volume transport is significantly changed by less than 0.12 Sv as compared to the residual of the selected solution (0.01 Sv). Also, the solution of the inverse model is significantly changed for the individual layer transport in the RSDW layer (~0.16 Sv) and RSOW (~0.06 Sv) but not in the upper layers of RSSW and GAIW (less than ~0.009 Sv).

| Layers     | Initial solution |       |       | Selected solution |       |       | No RW |       |       | No CW |       |       | NO RW-CW |       |       |
|------------|------------------|-------|-------|-------------------|-------|-------|-------|-------|-------|-------|-------|-------|----------|-------|-------|
|            | C                | F     | box   | C                 | F     | box   | C     | F     | box   | C     | F     | box   | C        | F     | box   |
| RSSW       | 0.13             | -0.11 | 0.02  | 0.11              | -0.18 | -0.07 | 0.15  | -0.11 | 0.03  | 0.13  | -0.12 | 0.01  | 0.18     | -0.21 | -0.03 |
| GAIW       | -0.00            | 0.43  | 0.42  | -0.02             | 0.37  | 0.35  | 0.01  | 0.35  | 0.35  | -0.02 | 0.08  | 0.06  | 0.01     | 0.06  | 0.06  |
| RSOW       | 0.05             | -0.07 | -0.02 | 0.02              | -0.11 | -0.09 | 0.07  | -0.15 | -0.08 | 0.05  | -0.20 | -0.16 | 0.13     | -0.14 | -0.02 |
| RSDW       | -0.02            | -0.01 | -0.03 | -0.11             | -0.06 | -0.18 | 0.07  | -0.18 | -0.11 | -0.44 | 0.54  | 0.10  | 0.12     | -0.15 | -0.02 |
| Full-depth | 0.16             | 0.24  | 0.39  | -0.00             | 0.02  | 0.01  | 0.30  | -0.10 | 0.20  | -0.29 | 0.30  | 0.01  | 0.44     | -0.45 | -0.01 |

Table 8-3: Volume transport (Sv) estimates for the initial solution, selected solution, alternative model runs (no row weight (RW), no column weight (CW) and no row-column weight (RW-CW) included in the selected solution)

#### 8.3.4 Sensitivity to the number of layers

According to McIntosh and Rintoul (1997), increasing or decreasing the number of layers that are used in the inversion should not affect the inverse box model if it is well designed. In order to investigate the sensitivity of the solution to its number of layers, one simulation was performed with 6 layers (Figure 8-11). The full-depth cumulative volume transport is fairly similar to that of the selected solution when the number of layers in the model was increased with a residual of 0.04 Sv at the equivalent rank (as compared to 0.01 Sv for the selected solution). The most noticeable differences between the selected solution and this simulation are seen in the different water masses, with very small differences due to differences in the repartition of the layers between the water masses. These small differences (less than 0.007 Sv) were not significant between the selected solution and this simulation except in RSSW (0.016 Sv) and GAIW (0.01 Sv).

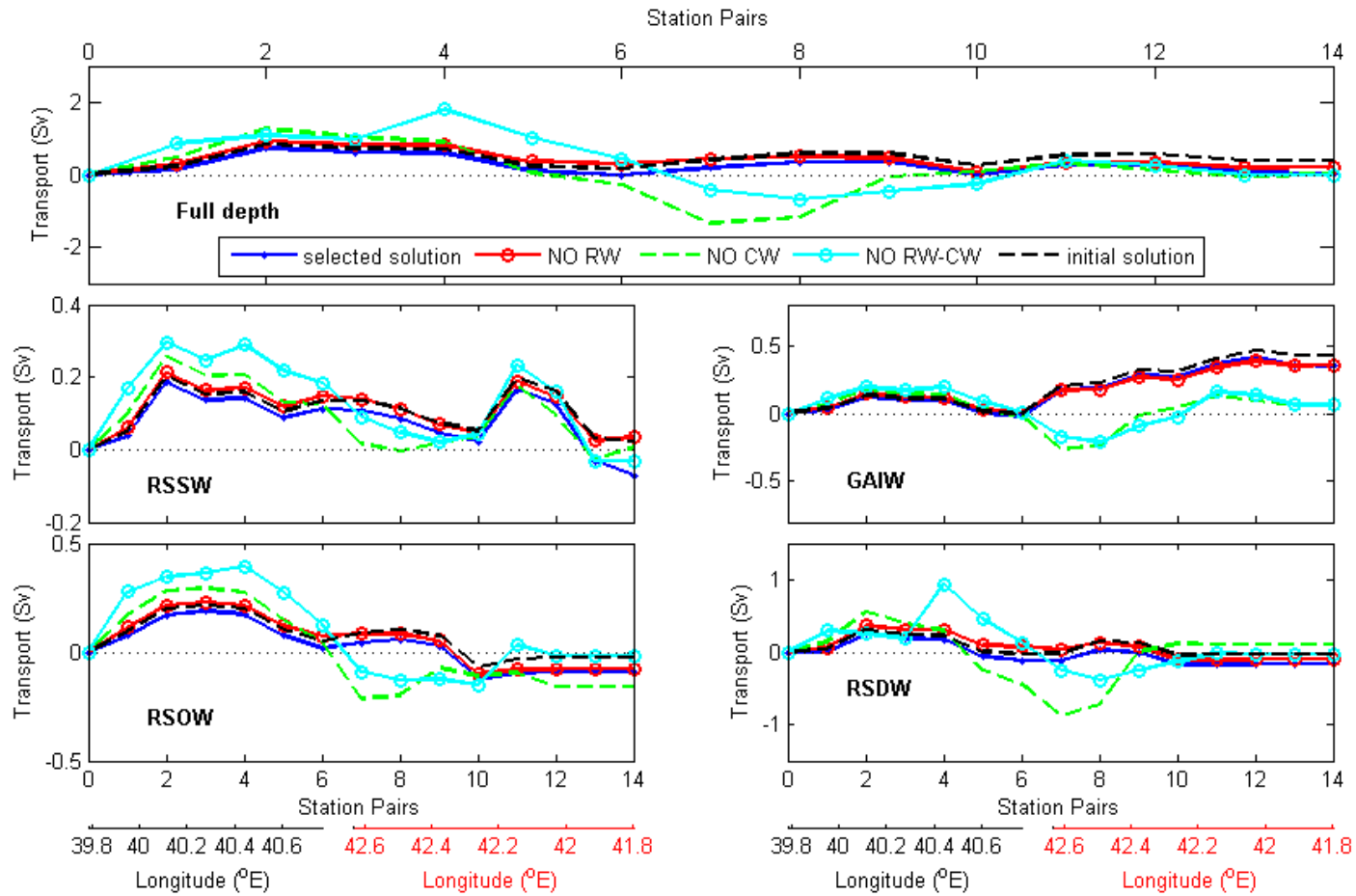


Figure 8-9: Cumulative volume transport (Sv) along the rim of the box when weighting is not included, for row weighting (RW, red line), column weighting (CW, green dashed line), row and column weighting (cyan line) for the selected solution (blue line) and for the initial solution (black dashed line)

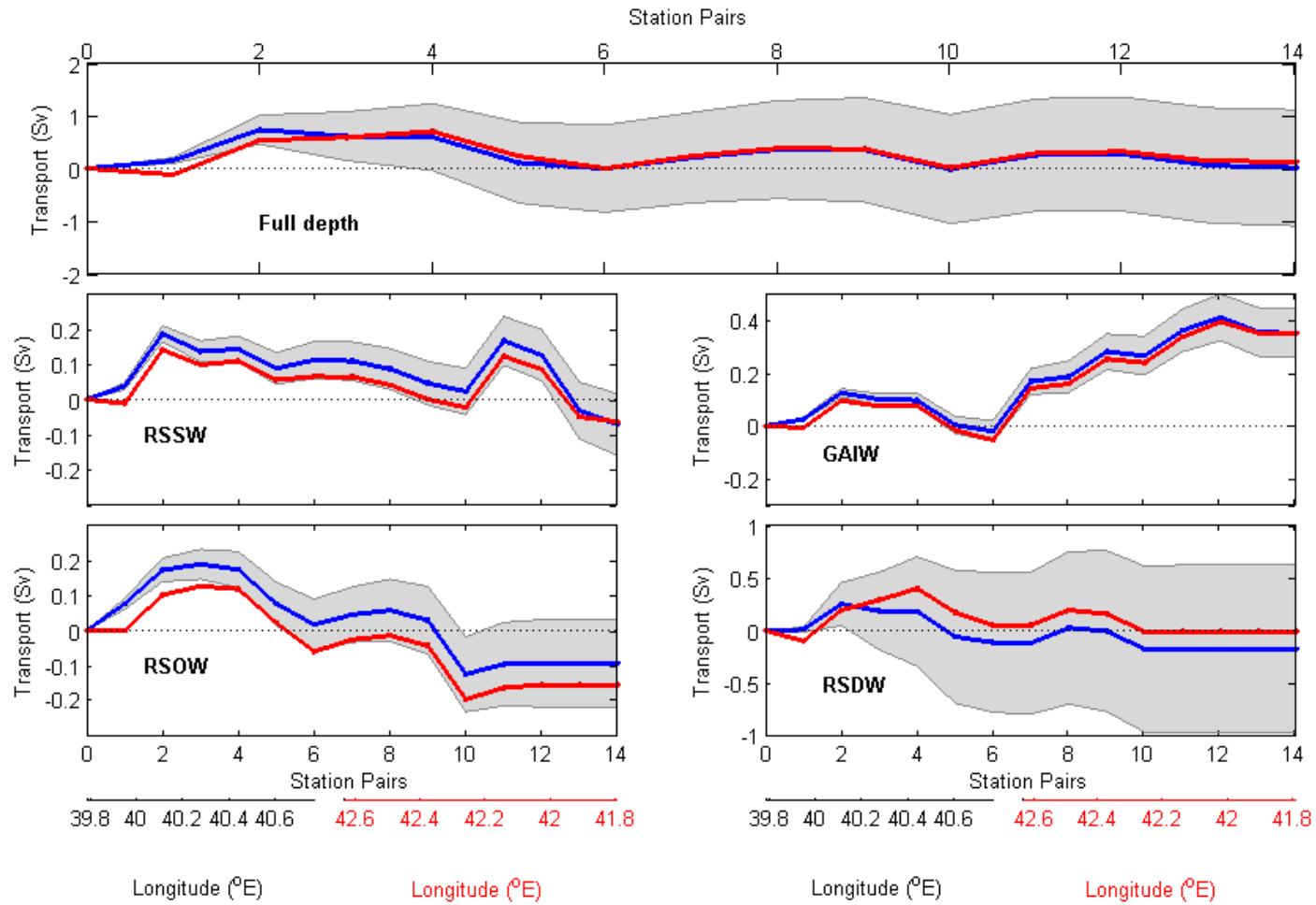


Figure 8-10: Cumulative transport (Sv) along the rim of the box when the *a priori* uncertainties about the volume conservation are constant (0.2 Sv) (red) and for the selected solution (blue). The *a posteriori* cumulative error is shown in the grey shaded area

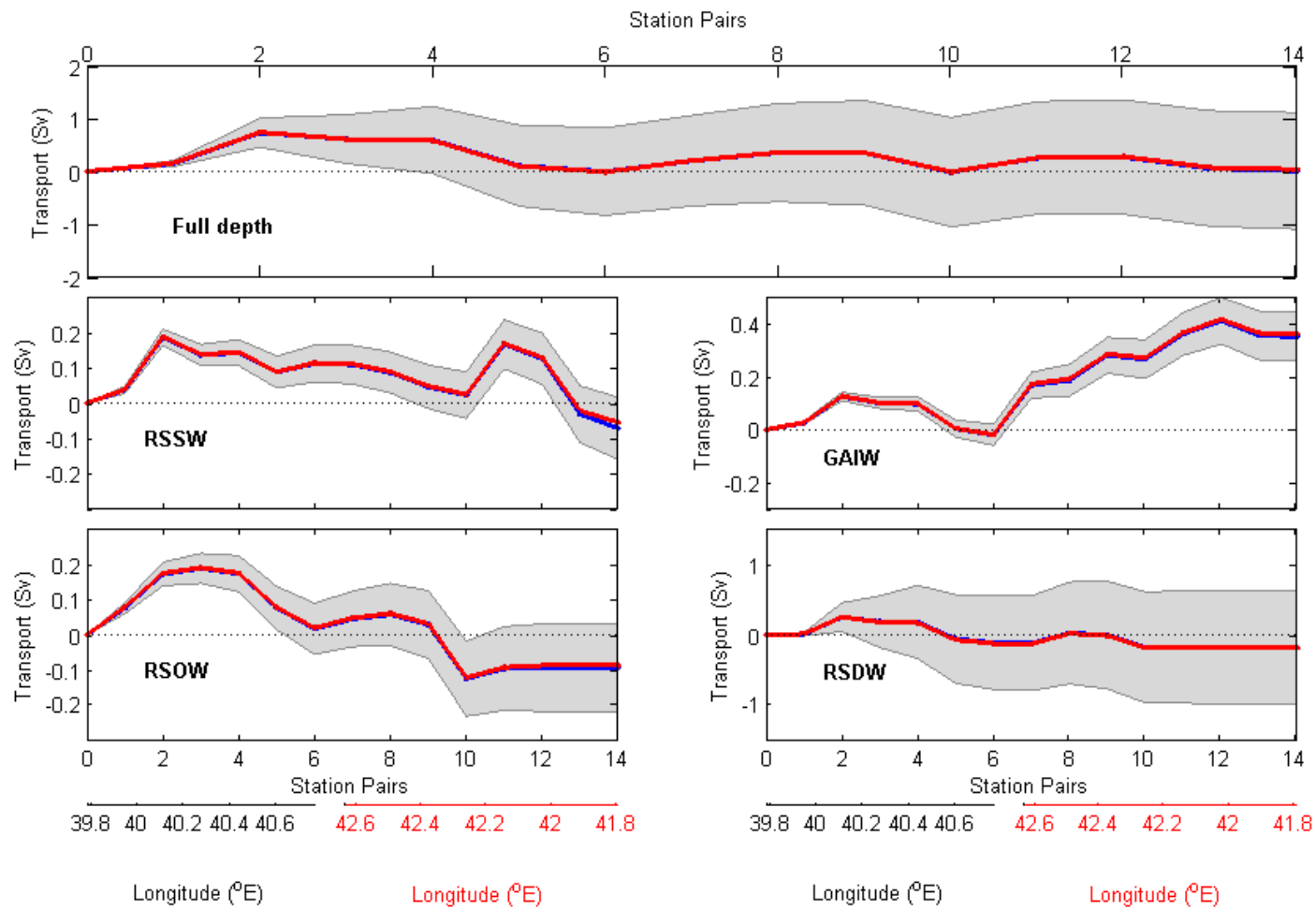


Figure 8-11: Cumulative volume transport (Sv) along the rim of the box when the number of the layers is increased to 6 (red) and for the selected solution (blue).  
The *a posteriori* cumulative error is shown in the grey shaded area

### 8.3.5 Sensitivity to inclusion of diapycnal velocities

The diapycnal velocities are an important part of the inversion as they provide information on the interfacial fluxes which are hard to measure. Figure 8-12 shows that inclusion of the interfacial fluxes is crucial to reproducing the lateral transport in the box. As we can see from Figure 8-12, the selected solution without including the diapycnal velocities gives very large differences in the cumulative transport of all water masses. Also, the fluxes across individual sections are unrealistically low as compared with the selected solution. Following McIntosh and Rintoul (1997), the inclusion of the diapycnal fluxes is necessary for the inversion model to be physically consistent, and must be significant in the box.

The *a priori* uncertainty of the diapycnal velocities is chosen as  $10^{-5} \text{ ms}^{-1}$  for the selected solution near the upper end of the observed ocean mixing rates. Also, the *a priori* uncertainty is tested by varying the *a priori* uncertainties for the diapycnal velocity. One simulation was run by increasing the *a priori* uncertainty of the diapycnal velocity to be equal to  $10^{-3} \text{ ms}^{-1}$  (Figure 8-13). The cumulative volume transport in the box was changed significantly from that of the selected solution, with most changes occurring in RSDW ( $\sim 0.15 \text{ Sv}$ ).

### 8.3.6 Sensitivity to choice of the initial velocities

In order to assess the robustness of the solution to changes in the reference velocities, the *a priori* uncertainties in the reference velocities were modified. One simulation was performed with the *a priori* reference velocities set to be  $0.04 \text{ ms}^{-1}$ , as compared to the *a priori* uncertainties that had been applied in the selected solution (see section 7.4.4). Figure 8-14 shows the comparison between the two experiments, with the differences in the accumulative volume transport in each layer varying with a large residual. The most noticeable differences from the selected solution occur in section F, except for the RSDW in section C. This might be explained by the large changes made to the initial reference velocities in the selected solution, as described in section 8.2.2 (Figure 8-4).

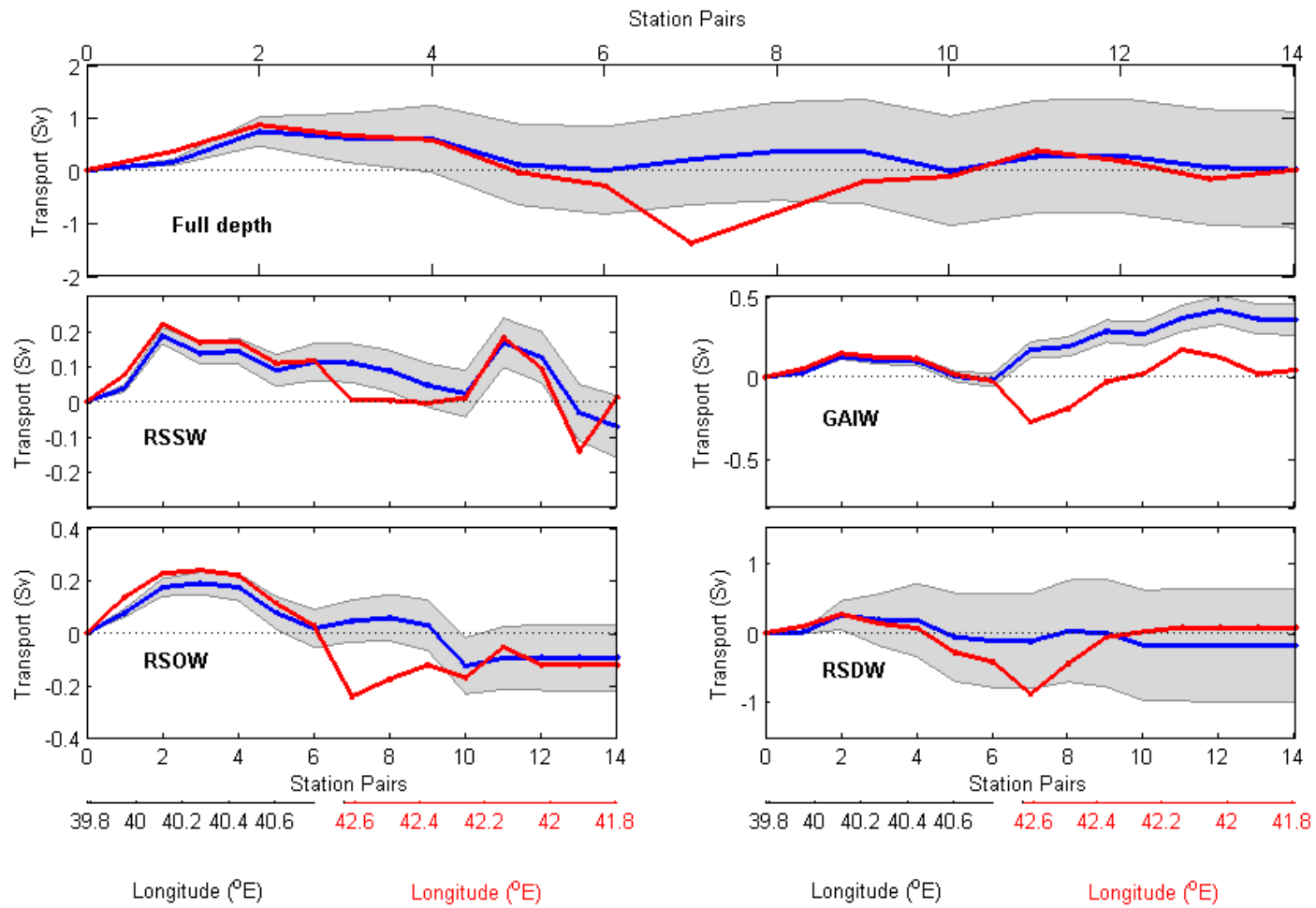


Figure 8-12: Cumulative volume transport (Sv) along the rim of the box when the diapycnal velocities are not included (red) and for the selected solution (blue).  
The *a posteriori* cumulative error is shown in the grey shaded area

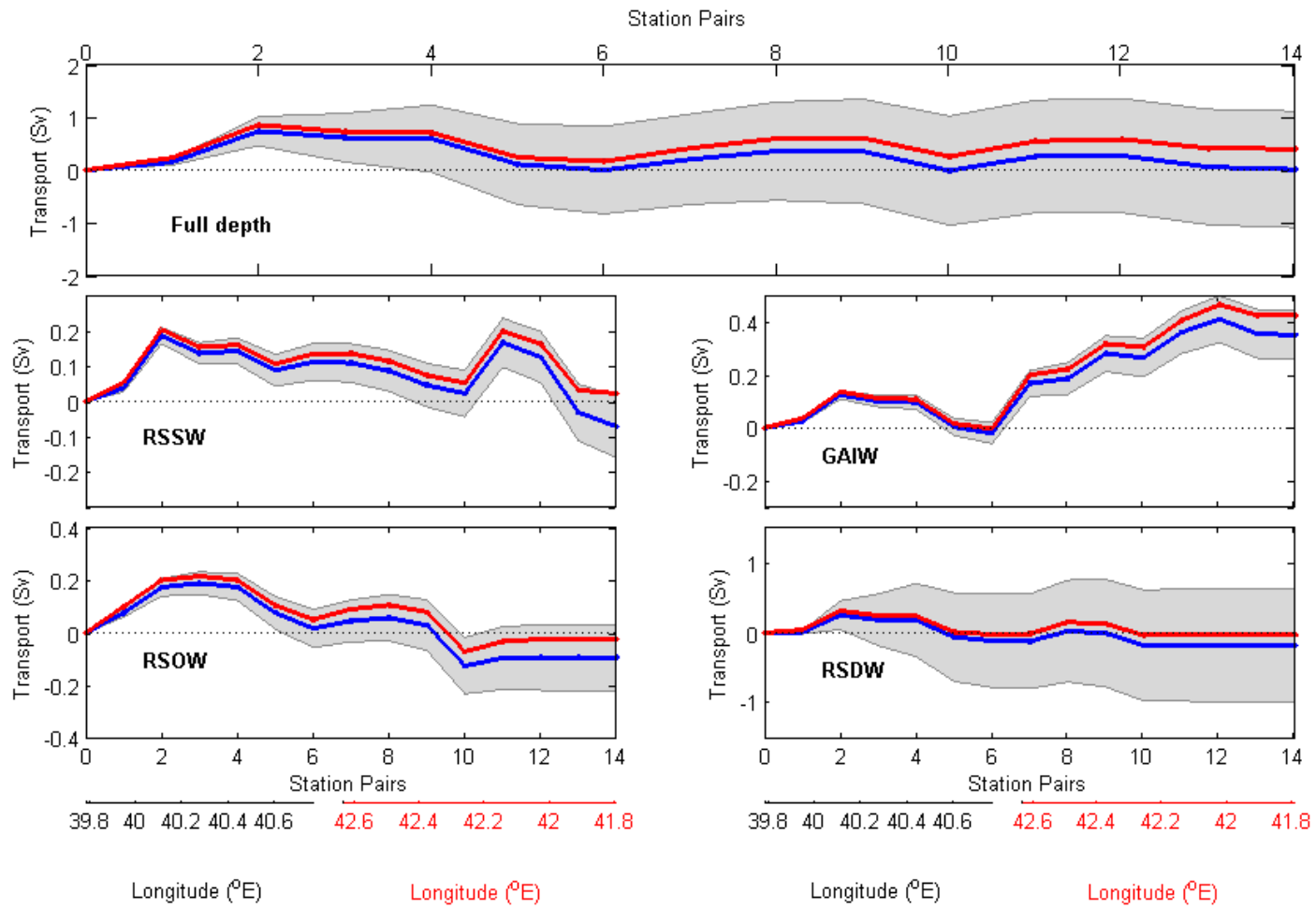


Figure 8-13: Cumulative volume transport (Sv) along the rim of the box when the *a priori* uncertainties for diapycnal velocity are increased ( $10^{-3}$ ) (red) and for the selected solution (blue). The *a posteriori* cumulative error is shown in the grey shaded area

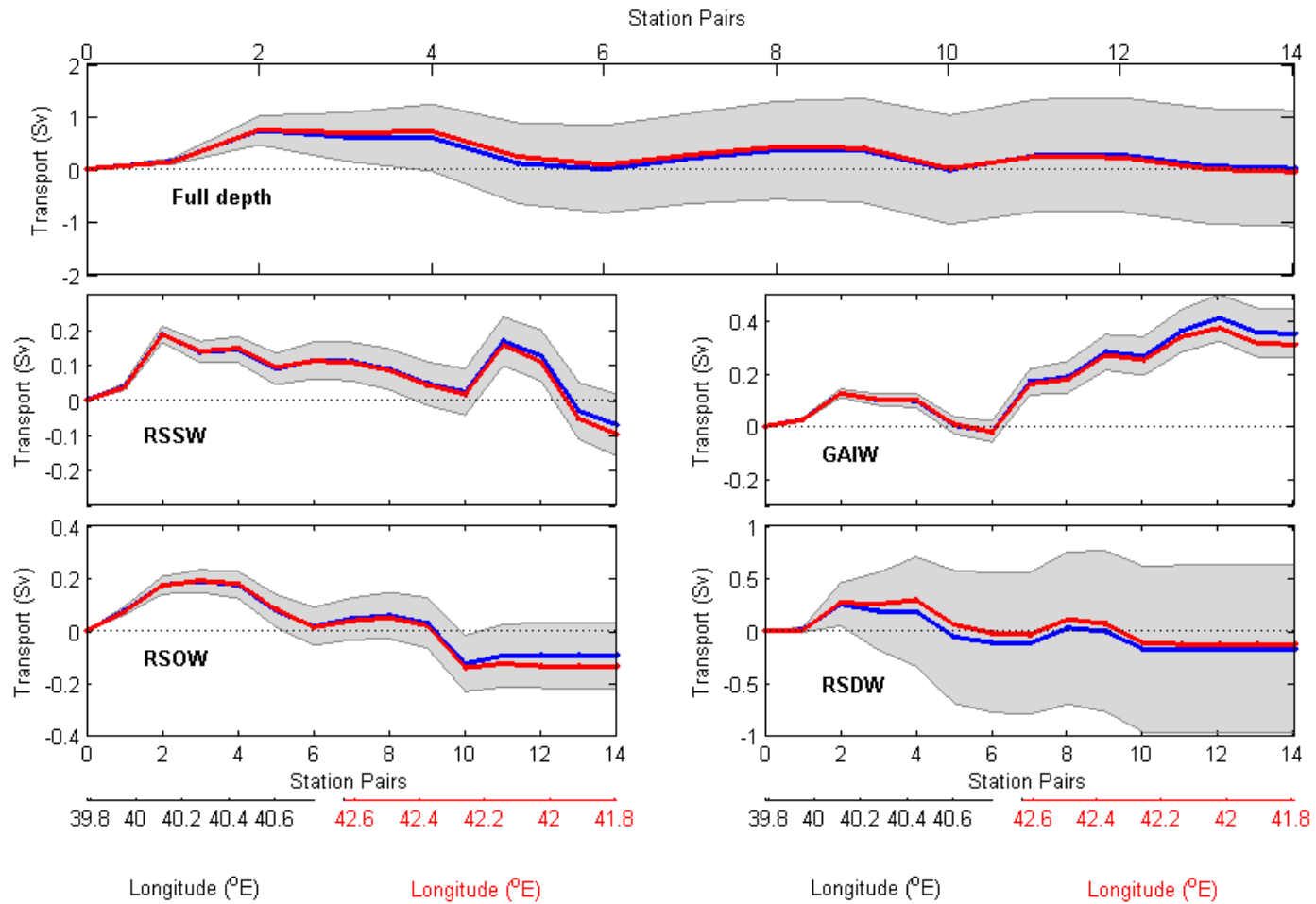


Figure 8-14: Cumulative volume transport (Sv) along the rim of the box when the *a priori* uncertainties for reference velocity are constant at  $0.04 \text{ ms}^{-1}$  (red) and for the selected solution (blue). The *a posteriori* cumulative error is shown in the grey shaded area

### 8.3.7 *Sensitivity to the bottom triangle*

A number of methods have been used to estimate the transport in the bottom triangle, below the deepest common level (Wunsch, 1996; Ganachaud, 1999). However, the method used in this thesis extrapolates the velocity shear at the DCL through the bottom triangle to the maximum depth of the station pairs, as described in Chapter 7. In order to assess the influence of excluding the bottom triangles from the selected solution, a simulation was run without the bottom triangles, as shown in Figure 8-15. The full-depth cumulative volume transport was not significantly influenced by excluding the bottom triangle from the selected solution, and the differences in the residual transport were less than 0.008 Sv. However, the most noticeable differences occurred in section F in the RSDW and GAIW water masses. The difference in the GAIW water mass comes almost entirely from the station pairs 7 to 14 in section F.

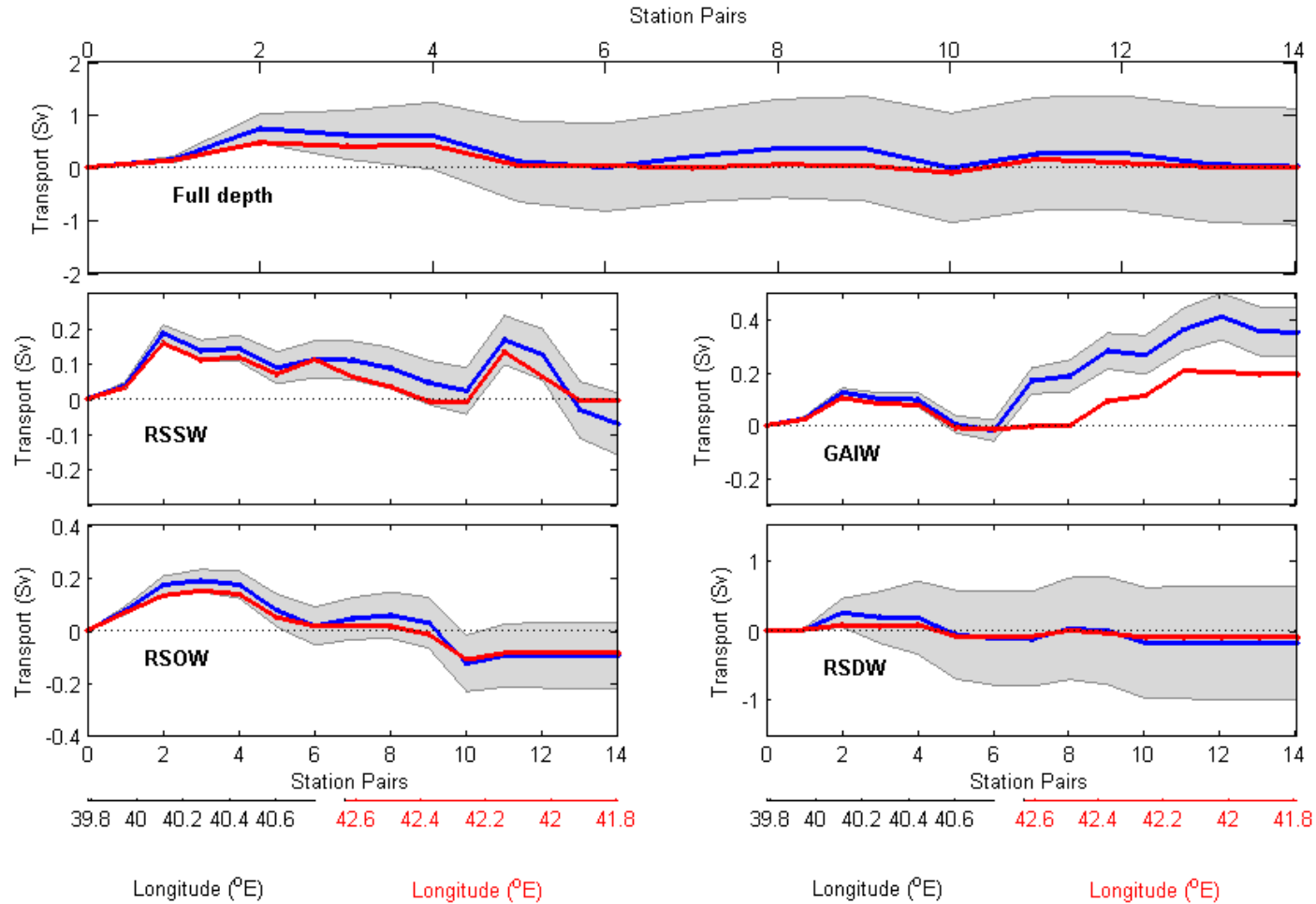


Figure 8-15: Cumulative volume transport (Sv) along the rim of the box when the bottom triangles are not included (red) and for the selected solution (blue). The *a posteriori* cumulative error is shown in the grey shaded area

## 8.4 Conclusion

This chapter was dedicated to describing how the inverse box model is correctly built and to showing that changes in its configuration do not change the solution structure. The inversion makes little change to the *a priori* estimate of the solution (pre-inversion) and the conservation constraints are satisfied. Several sensitivity tests were done in order to evaluate the robustness of the selected solution to modifications in its parameters. All these tests were comparable with the selected solution. The largest differences occurred when the equation uncertainties were modified and when the diapycnal mixing in the interfacial water mass was not included in the model. It is necessary to show that the inversion is very sensitive to these components if good results are to be obtained. However, the modifications in the various parameters as in all the different experiments stayed within the *a posteriori* error of the selected model, indicating that the solution is robust to these changes.

Building the inverse box model requires careful study of the *a priori* uncertainties in the conservation equations (volume, salinity and potential temperature anomaly) because this is the key to the inversion. As a result of lack of data (direct velocity observations) from the southern Red Sea region, the inversion used a large number of different *a priori* uncertainties for the volume conservation equation and for reference velocity in reaching a good solution. In this thesis the preferred solution was selected such that the equation residuals are required to be zero, within one *a posteriori* standard deviation; also, the solution was required to be within one standard deviation of the *a priori* error estimate. As mentioned before, there is no definitive method for determining the selected solution, and the method used here is likely to advance the way of evaluating uncertainties regarding transport that will help reduce the *a posteriori* errors arising from the inversion. In the next chapter, the focus will be on the interpretation of the results from the selected solution in physical terms, in order to contribute to a better understanding of the circulation in the southern the Red Sea.

# Chapter 9 Circulation in the southern Red Sea region

## 9.1 Introduction

In this chapter, the selected solution of the inverse box model will be described and interpreted in physical terms to contribute to a better understanding of the circulation in the southern Red Sea region and of the exchanges with the Gulf of Aden. It should be mentioned that the data used to build our inverse box were collected during August of 2001 when three-layer circulation was present. It is believed that the reversal of winds to northwesterly winds in the summer over the southern Red Sea region led to a three-layer flow pattern in the Strait of Bab el Mandeb with a thin surface layer outflow, an intermediate inflow and deep water outflow (Neumann & McGill, 1961; Patzert, 1974a). In this chapter, the geostrophic velocity field over the box is described and the summer circulation in the southern Red Sea is also discussed.

## 9.2 Geostrophic velocity field

Figure 9-1 shows the structure of the geostrophic velocity field over the box in the southern Red Sea region. In section C, there is an inflowing current (into the box, directed southward) over the whole water column on the western boundary of the section (station pairs 1 and 2) with a maximum magnitude of  $0.22 \text{ m s}^{-1}$  in the surface layer. The inflowing water in the western side of section C reaches down to the relatively shallow bottom (station pairs 1 and 2). There is also an inflowing current moving southward (into the box) in the upper layers between station pairs 4 and 6 and outflowing towards the north at the intermediate depth, reaching the bottom, except for

station pair 4. In the middle and eastern parts of the section (station pairs 3 and 5), there is an outflowing current (out of the box, directed northward) over the whole water column, except one spot of positive velocity (into the box) at station pair 3, with thickness of 125 m and a depth between 90 m and 215 m; below that depth there is an outflowing towards the north that reaches down to the bottom. The maximum outflowing occurs at station pair 5 with magnitude of  $0.15 \text{ m s}^{-1}$ . The bottom velocities in section C are small ( $0 \text{ } 10^{-3} \text{ m s}^{-1}$ ). The geostrophic velocities structured in section C shows a cyclonic circulation with northward inflowing RSSW and intermediate GAIW on the eastern side of the section and deeper return flow in the RSOW and RSDW layers at the western end of the section. This feature was described by Sofianos and Johns (2003), who showed the presence of a gyre between latitudes  $14^{\circ}\text{N}$  and  $16^{\circ}\text{N}$  rotating cyclonically during the summer and anticyclonically during the winter (Figure 9-2).

Section F is located fairly close to the Strait of Bab el Mandeb, which can be seen clearly as the four basic water masses (RSSW, GAIW, RSOW and RSDW) involved in the summer circulation (Figure 6-11 and Figure 9-1, right panel). There is a thin layer of outflowing RSSW across the whole section as shown in Figure 9-2, except for an inflowing current (into the box, station pair 11) in the middle of the section. The structure of geostrophic velocity in the section shows anticyclonic features in upper layers (in layers  $\sigma_{\theta} < 24.4$ ), with a strong outflowing current (RSSW) in the surface layer at the western boundary of the section with a maximum of  $0.32 \text{ m s}^{-1}$  (at station pair 13) and an inflowing at station pair 11 with a maximum of  $0.42 \text{ m s}^{-1}$ . Underlying the surface layer, there is an inflowing current of GAIW occupying the whole section (at layer,  $24.4 > \sigma_{\theta} < 27$ ) except for one spot of negative velocity (out of the box, station pair 10). The inflowing layer is thicker against the eastern side of the section with maximum velocity of  $0.22 \text{ m s}^{-1}$  (station pair 7). This indicates that the GAIW flows northward into the Red Sea along the eastern side of the section following its entrance through the Strait of Bab el Mandeb. Conversely, in the RSOW layer, there is a southward current out of the Red Sea concentrated against the western side of the section with a core at a depth between 100 and 150 m and a maximum velocity of  $0.16 \text{ m s}^{-1}$  at a depth of  $\sim 133 \text{ m}$  (station pair 10). This layer of outflowing current has a core of the highest dissolved oxygen value (characteristic of RSOW), as described in section 6.3.3 (Figure 6-5). In this layer there is a return current shifted to the north located at the western and eastern boundaries of the section (at station pairs 7-8 and 11-12). The

deepest layer (RSDW) has a flow pattern similar to the RSOW; the current flows southward with intensification on the western side of the section (station pairs 9-10) and there is cyclonic recirculation toward the north (into the box, station pairs 7-8 and 11-12).

The geostrophic velocities indicate that section F has a lot more structure than section C and that is attributed to the presence of the GAIW at subsurface layer and cyclonic and anticyclonic eddies present in the surface layer. Section C, in comparison, has a clear structure with an inflowing current on the western side of the section and outflow on the eastern side of the section. The surface currents in both boundaries (African and Arabian coasts) of sections C and F are directed to the south-southeast (into the box in section C and out of the box in section F) under the influence of reversing winds of the north-northwesterly winds in the southern half of the Red Sea during the southwest monsoon (June to September). In addition, the subsurface current of GAIW flows along the eastern side of the two sections toward the north. The deep currents of RSOW and RSDW flow southward in both sections towards the Gulf of Aden, with intensification along the western side and recirculation toward the north along the eastern side of both sections. The main noticeable difference between the geostrophic velocity structures in the two sections is the pathway of the southward current that occurs in all layers on the western side of section C, whereas it only occurs on the surface and in the deep layers in section F (RSOW and RSDW). The northward currents mostly occur in all layers on the eastern side of section C, whereas it just occupies the whole subsurface layer (GAIW) and some parts of the deep layers on the eastern side.

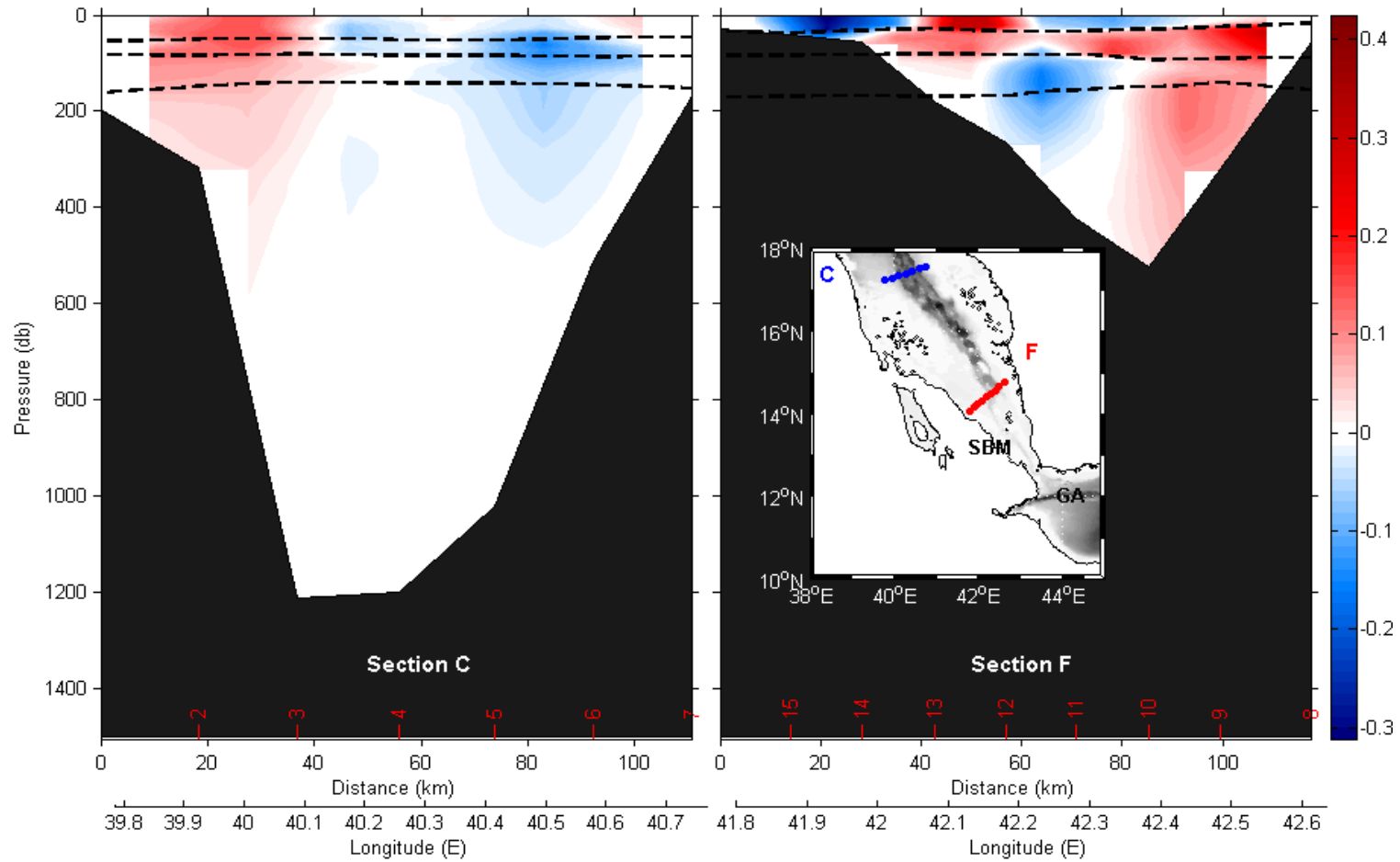


Figure 9-1: Geostrophic velocity (in  $\text{m s}^{-1}$ ) of the inverse model solution, with water mass boundaries (dashed lines). For simplicity the two sections were taken from the west-east direction. Positive velocities (red) are directed into the box and negative velocities (blue) are going out of the box. The station numbers are shown in red at the bottom of each panel. The map indicates the location of the two sections in the southern Red Sea region

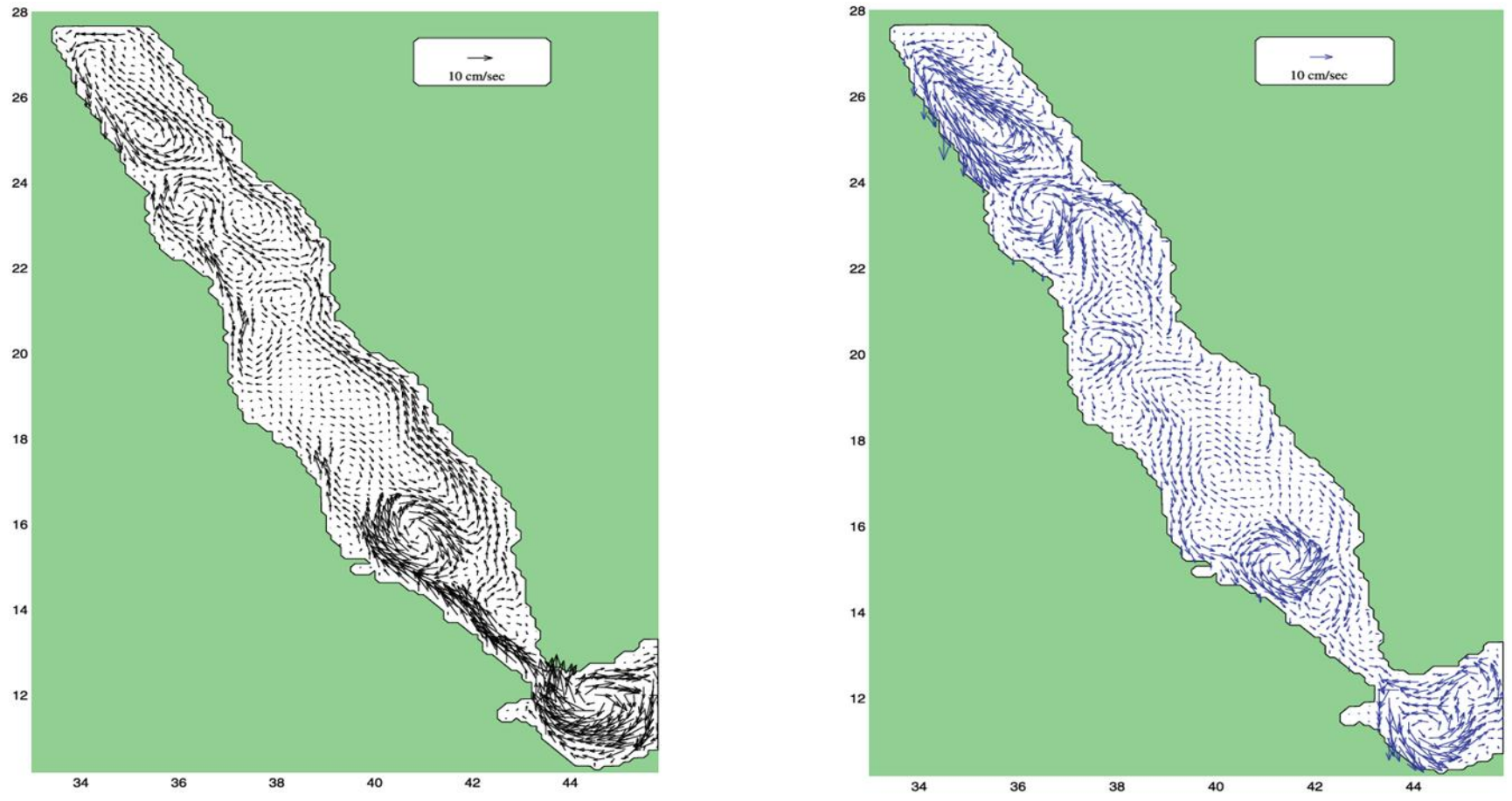


Figure 9-2: Mean winter (left panel) and summer (right panel) surface circulation from MICOM simulation. The results represent the last 9 years of simulation (Sofianos & Johns, 2003)

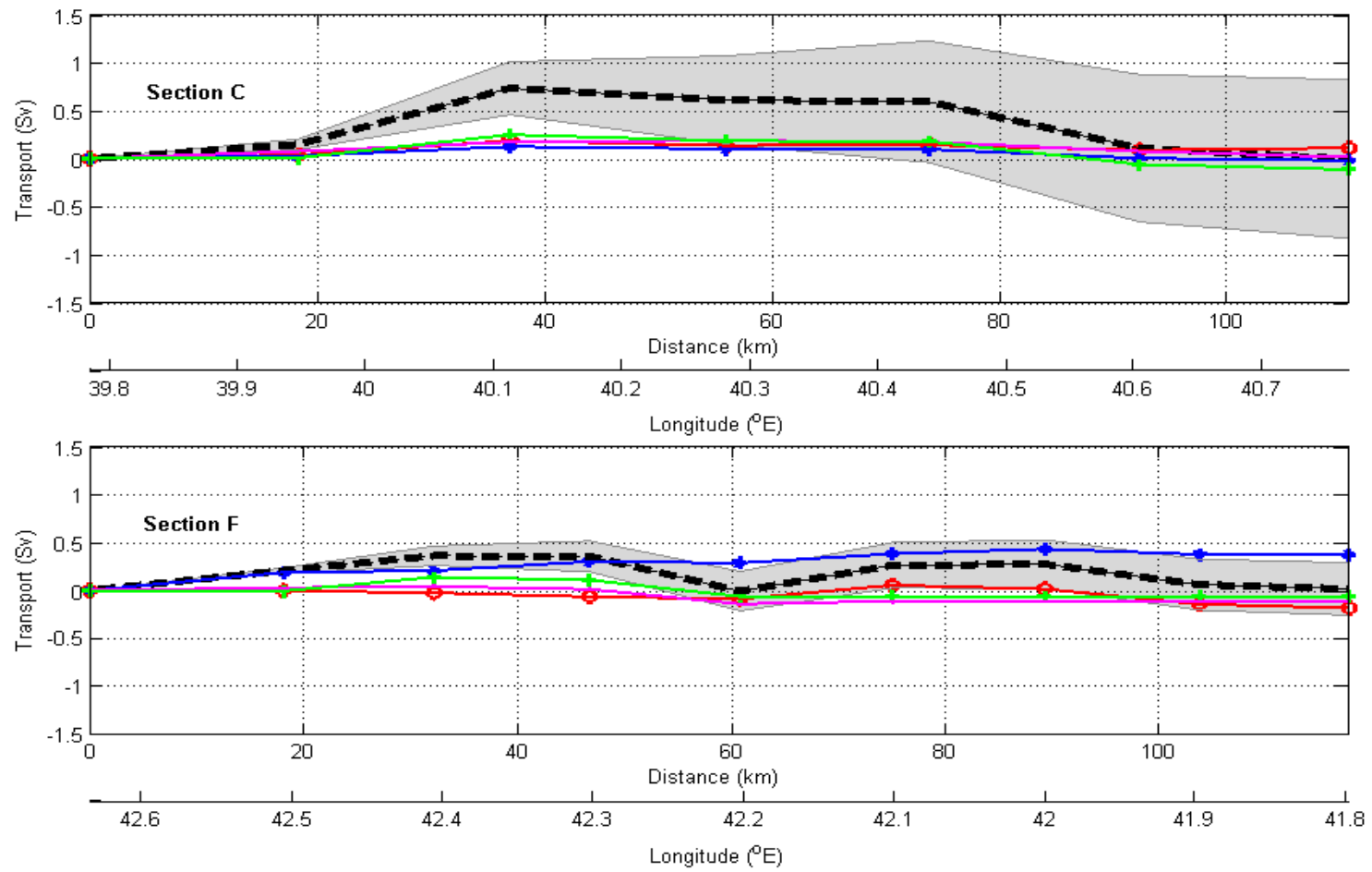


Figure 9-3: Cumulative full-depth volume transport (in Sv, positive into the box) for each section (black dashed lines). Accumulated volume transport for each layer is plotted for RSSW (green), GAIW (blue), RSOW (red) and RSDW (magnetic). The *a posteriori* cumulative error is shown in the grey shaded area

### 9.3 Summer circulation of the southern Red Sea

In this section, the computed transports and circulation in each transect will be described and the pathways and modification of the major water masses traced as they circuit the Red Sea.

#### 9.3.1 Full-depth volume transports

The volume transports across each section (sections C and F) and the transport in each layer are summarised in Table 9-1. The circulation in the water column is considered in three parts: upper, intermediate and deep layers, where the analysis is based on the specified water masses defined in Table 9-1. The upper layer includes the RSSW flows, the intermediate depth includes the inflowing cold and fresh GAIW and the deep layer includes the RSOW toward the Gulf of Aden and RSDW. Figure 9-3 shows that the cumulative volume transports along each section of the box are derived for total full depth and for each layer defined for the inversion calculation.

In section C, the net volume transport through the section is  $0.00 \pm 0.35$  Sv, of which  $0.73 \pm 0.31$  flow southward (into the box, station pairs 1 and 2) and are conveyed by the Red Sea Water (RSW, including RSSW, RSOW and RSDW) and  $0.73 \pm 0.20$  Sv flow northward through station pairs 3 and 6. The southward transport across section C occurs in the whole water column with magnitudes of 0.15 and 0.58 Sv for the full-depth volume transport at station pairs 1 and 2, respectively (Figure 9-3 and 9-4, upper panel). The recirculation outflow moves northward on the eastern side of the section (out of the box, station pairs 3 and 6).

In section F, the net volume transport of  $0.02 \pm 0.21$  Sv is found, including  $0.64 \pm 0.11$  Sv flow northward through the section (into the box, station pairs 7-8 and station pair 11) and  $0.62 \pm 0.16$  Sv flow southward (out of the box, station pairs 9-10 and station pairs 13-14) (Figure 9-3, lower panel).

### 9.3.2 Upper waters

The starting point is to trace the path of warm and saline outflowing RSSW to the Gulf of Aden over the box (Figure 9-4). Looking at the RSSW in section C and then section F just fairly close to the Strait of Bab el Mandeb region (~70 km), the surface layer has a southward current flow along the boundaries of both sections C and F with a recirculation northward flow in the middle of both sections (station pairs 3 and 5 for section C and station pair 10 for section F). The RSSW current is split into two pathways in the upper layer of both boundaries (African and Arabian coasts), with more intensification along the western boundary, as shown in Figure 9-1. These branches are separated by the cyclonic and anticyclonic circulation in section C and F respectively. The surface currents are intensified along the western boundaries of the both sections, as defined to be within the potential density range on the surface  $\langle \sigma_\theta \rangle > 24.4$  (layer 1 as defined in the inversion model) and the total outflows of the RSSW across sections C and F are  $0.10 \pm 0.004$  Sv (northward direction) and  $0.33 \pm 0.05$  Sv (southward direction), respectively. The inflowing surface currents into the box are found to be  $0.21 \pm 0.06$  Sv (station pairs 1=2, 4 and 6 with maximum velocities of  $0.18 \text{ ms}^{-1}$  at station pair 2) and  $0.14 \pm 0$  Sv (station pairs 7 and 10 and station pairs 12 and 14 with maximum velocities of  $0.36 \text{ ms}^{-1}$  at station pair 13) for sections C and F respectively. The surface circulation pattern from the inversion over the box came as expected circulation in the southern of Red Sea, with outflowing intensification of the flow toward the boundaries of the two sections as shown in Figures 9-8b and 9-9b. This is similar to the structure of the flow resulting from the Miami Isopycnic Coordinate Ocean Model (MICOM) simulation for 9 years of mean summer circulation using both seasonal wind and thermohaline forcing to drive the model (Sofianos & Johns, 2003). Unfortunately, the authors do not discuss the lateral transports in the Red Sea.

The inverse model estimate shows a southward net transport of RSSW (out of the box towards the Strait of Bab el Mandeb) with magnitude of  $0.18 \pm 0.08$  Sv in section F, which represents about 68% of the estimate of the summer outflow (surface outflow, from June to September) of  $0.56$  Sv (Patzert, 1974b). This outflowing estimate is fairly similar to the August value of  $0.21$  Sv estimated by Patzert (1972b) from the ship drifts and is slightly lower than the value of  $0.27$  Sv estimated by Maillard and Soliman (1986). The volume transport at the surface is also similar to the outflowing transport value of  $0.22$  Sv (with  $0.21$  derived from Knudsen formulae) estimated by Sofianos et al. (2002) using current meter observation obtained during the 18 month period

between June 1995 and November 1996 (Figure 9-8b and Figure 9-9b). The seasonal variability in the southern Red Sea region is strongest due to reversal winds and the high variability of the flow exchange with the Gulf of Aden through the Strait of Bab el Mandeb. The southern Red Sea region (southward of 20° N) is influenced by monsoon winds; during the summer season (June-September, southwest monsoon), the winds act in opposition to the thermohaline forcing to drive the surface current flow towards the south-southeast into the Gulf of Aden through the Strait of Bab el Mandeb, where it joins the strong atmospheric and oceanic flow directed into the Arabian Sea (Patzert, 1974a).

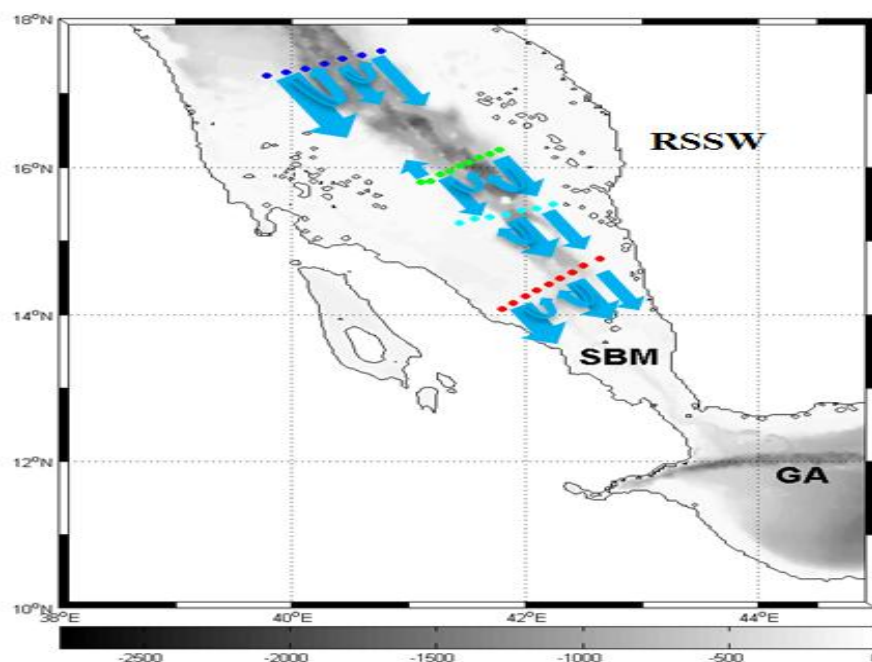


Figure 9-4: Circulation scheme for the southern Red Sea based on results from the geostrophic circulation. The major water masses (see Table 6-1). RSSW represents Red Sea Water mass, SBM the Strait of Bab el Mandeb region and GA the Gulf of Aden region. The dots indicate the hydrographic data from R/V Maurice Ewing (2001) for section C (blue), section D (green), section E (cyan) and section F (red)

### 9.3.3 Intermediate waters

The GAIW inflow (Figure 9-5) takes place between depths of ~30 and ~80 m; it is distinguished by its minima of potential temperature, salinity and oxygen with values of  $\theta \leq 20^{\circ}\text{C}$ ,  $S \leq 37$  and  $O \leq 16 \mu\text{mol/kg}$ . This tongue of the GAIW can be traced as far northward as 18°N (Jones & Browning, 1971; Maillard & Soliman, 1986). The

northward flow of GAIW is concentrated on the eastern side of section F with total inflowing of  $0.44 \pm 0.06$  Sv (station pairs 7-9 and station pairs 11- to 12, with maximum velocities of  $0.16 \text{ ms}^{-1}$  at station pair 1) and there is a recirculation located along the western boundary flowing southward with a total of  $0.07 \pm 0.03$  Sv (station pair 10 and station pairs 13 to 14, with maximum velocities of  $0.22 \text{ ms}^{-1}$  at station pair 13).

GAIW flows northward into the Red Sea along the eastern side of the section following its entrance through the Strait of Bab el Mandeb, as shown in Figures 6-3 (left panel) and 6-11 (Sofianos & Johns, 2007). Continuing northwards, this cold and fresh water flow is found on the eastern side of section C, with total outflow (out of the box, between station pairs 3 and 6) of  $0.14 \pm 0.04$  Sv, and there is return flow southward (into the box, station pairs 1 and 2) with a total of  $0.12 \pm 0.05$  Sv located on the western side of section C (Figure 9-8c and Figure 9-9c).

The inversion results show a northward net volume transport for GAIW with a magnitude of  $0.37 \pm 0.08$  Sv in section F, which is similar to the estimate of 0.33 Sv by Maillard and Soliman (1986) using current meter observation obtained during the summer (July to September) of 1982. It is also similar (within the error bar) to the estimate of 0.29 Sv by Sofianos et al. (2002) based on direct observation of the Strait of Bab el Mandeb. If we look at the thermohaline characteristics of GAIW in the two sections, as described in section 6.3.2, it is clear that the GAIW characteristics are influenced by the vertical mixing with RSSW and RSOW and this increase as it flows northward. These changes were attributed mainly to the lateral stirring and mixing by the strong eddies that occurred in the southern region (Sofianos & Johns, 2007). The inversion results show noticeable differences in the GAIW volume transport between the two sections, with a large reduction of the transport with a magnitude of  $0.35 \pm 0.07$  Sv, which will be discussed in section 9.4 by studying the interior diapycnal mixing between the water masses.

| Water mass | Section C       |                   | Net transport<br>(Sv) | Section F       |                  | Net transport<br>(Sv) |
|------------|-----------------|-------------------|-----------------------|-----------------|------------------|-----------------------|
|            | Inflow          | Outflow           |                       | Inflow          | Outflow          |                       |
| RSSW       | $0.21 \pm 0.06$ | $-0.10 \pm 0.004$ | $0.11 \pm 0.07$       | $0.14 \pm 0.00$ | $-0.33 \pm 0.05$ | $-0.18 \pm 0.08$      |
| GAIW       | $0.12 \pm 0.05$ | $-0.14 \pm 0.04$  | $-0.02 \pm 0.06$      | $0.44 \pm 0.06$ | $-0.07 \pm 0.03$ | $0.37 \pm 0.08$       |
| RSOW       | $0.19 \pm 0.04$ | $-0.17 \pm 0.004$ | $0.02 \pm 0.08$       | $0.07 \pm 0.01$ | $-0.18 \pm 0.09$ | $-0.11 \pm 0.06$      |
| RSDW       | $0.25 \pm 0.16$ | $-0.36 \pm 0.10$  | $-0.11 \pm 0.15$      | $0.15 \pm 0.10$ | $-0.21 \pm 0.08$ | $-0.06 \pm 0.08$      |
| Full-depth | $0.73 \pm 0.31$ | $-0.73 \pm 0.20$  | $0.00 \pm 0.35$       | $0.64 \pm 0.11$ | $-0.62 \pm 0.16$ | $0.02 \pm 0.21$       |

Table 9-1: Volume transports (Sv) for each section (C and F) and for each layer (after the inversion). The sign convection (+) is into the box and (-) is out of the box

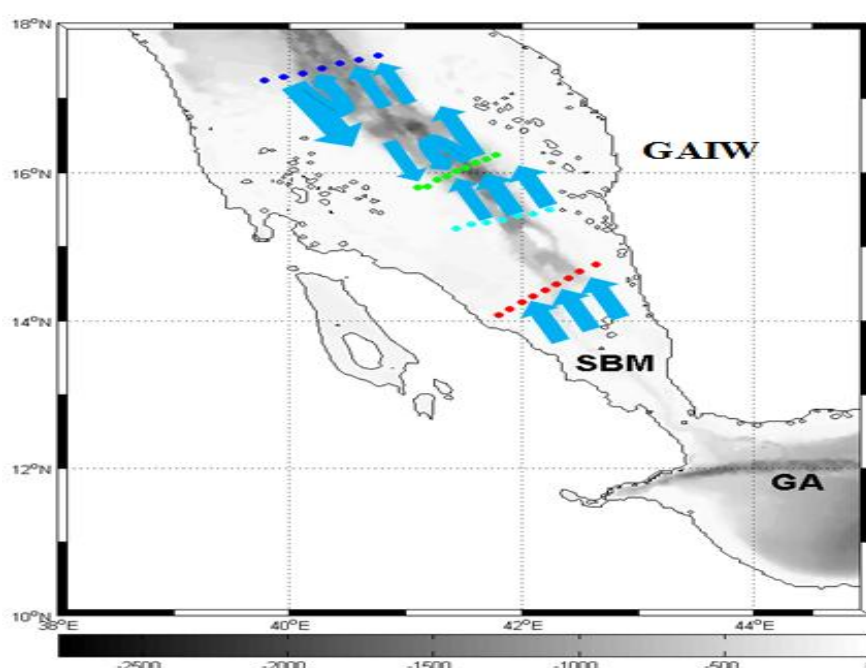


Figure 9-5: As in Figure 9-4 but for Gulf of Aden intermediate water (GAIW)

### 9.3.4 Deep waters

To simplify the description of the circulation in the deep layers, the circulation of the deep water is divided into two parts, namely RSOW and RSDW, which are defined as layers 3 and 4 respectively to be within the potential density range  $27 < \sigma_\theta > 28.33$  for RSOW and  $\sigma_\theta < 28.33$  for RSDW. The RSOW flows southward (Figure 9-6) in the box through section C (into the box, station pairs between 1 and 3) with total inflowing transport of  $0.19 \pm 0.04$  Sv, and a cyclonic recirculation flows northward (out of the box, between station pairs 4 and 6) with a total transport of  $0.17 \pm 0.04$  Sv. The total

net transport of the RSOW through section C is  $0.02 \pm 0.08$  Sv. The RSOW current flows southward along the box, and exits section F (out of the box, station pairs 9 and 10) on the western side (African coast), and due to shallow depth this flow does not exist at station pairs 13 and 14. The total outflowing transport is  $0.18 \pm 0.09$  Sv (station pairs 9 and 10) with a cyclonic returned flow on the eastern side of the section (station pairs 7 and 8), except for station pairs 11 and 12, which have a total transport of  $0.07 \pm 0.01$  Sv (Figures 9-8d and 9-9d). This can be seen clearly in the vertical distribution of the dissolved oxygen, where high dissolved oxygen values are found in both sides of the section and a minimum is found in the middle of the section (Figure 6-5, left panel). The total net transport over the box in RSOW is an outflow with magnitude of  $0.09 \pm 0.06$  Sv. The volume budgets of this layer imply that some of the RSOW is formed in the box by upwelling  $0.09$  Sv of the deep water (RSDW).

Compared with previous outflow RSOW estimates, the estimate of  $0.11 \pm 0.06$  Sv in section F is similar to the estimate by Tragou et al. (1999) ( $0.10$  Sv) applying Knudsen formulae to Patzert (1974b) data, and is also similar (within error range) to the estimates by Sofianos et al. (2002) ( $0.05$  Sv) and to Maillard & Soliman (1986) ( $0.05$  Sv). This estimate of the RSOW is one-third of the annual mean of outflowing of the Red Sea water ( $0.33$  Sv) into the Indian Ocean estimated by Siedler (1969) and Morcos (1970) using Knudsen relations, which was confirmed by Murray and Johns (1997) based on direct velocity observations. The intensity of RSOW changes significantly from the winter to summer seasons due to the effect of the monsoon wind stress and seasonal fluctuations in the buoyancy forcing (Shapiro & Meschanov, 1991). The RSOW from inverse results is about 19% of the rough estimate of the maximum outflow of  $0.57$  Sv in winter provided by Patzert (1974a) and Maillard and Soliman (1986).

The RSOW is mainly discharged in winter to the Indian Ocean and it ceases in summer because the dense outflow transport drops to very low levels (mean  $0.05$  Sv) compared to the magnitude of the RSOW in winter (two times the annual outflow). In winter the dense outflow of RSOW spreads through the Strait of Bab el Mandeb and begins its descent into the Gulf of Aden from 60 to 80 m down to the bottom with high values of temperature ( $22.7^{\circ}\text{C}$ ) and salinity ( $39.50$  psu). The RSOW descends to the intermediate depth between 300 and 900 m after reaching equilibrium in the western Gulf of Aden region, then propagates laterally eastward through the Gulf, where its properties are modified by mixing (Siedler, 1968 ; Maillard & Soliman, 1986; Fedorov

& Meshchanov, 1988; Bower et al., 2000). In the eastern gulf (50° E) of the Arabian Sea, it has a temperature of 11.5-12.5°C and salinity of 35.9-36.15 psu; it sinks to the depths of 600-800 m with density that varies from 27.1 to 27.4 kg m<sup>-3</sup> (Rochford, 1964; Fedorov & Meshchanov, 1988). This core of RSOW enters the open Indian Ocean and spreads southward across the equator; its depth increases progressively down to 900 m at 10°S and reaches 1100 m in the Mozambique Channel at 20-25°S (Wyrтки, 1971; Grundlingh, 1985).

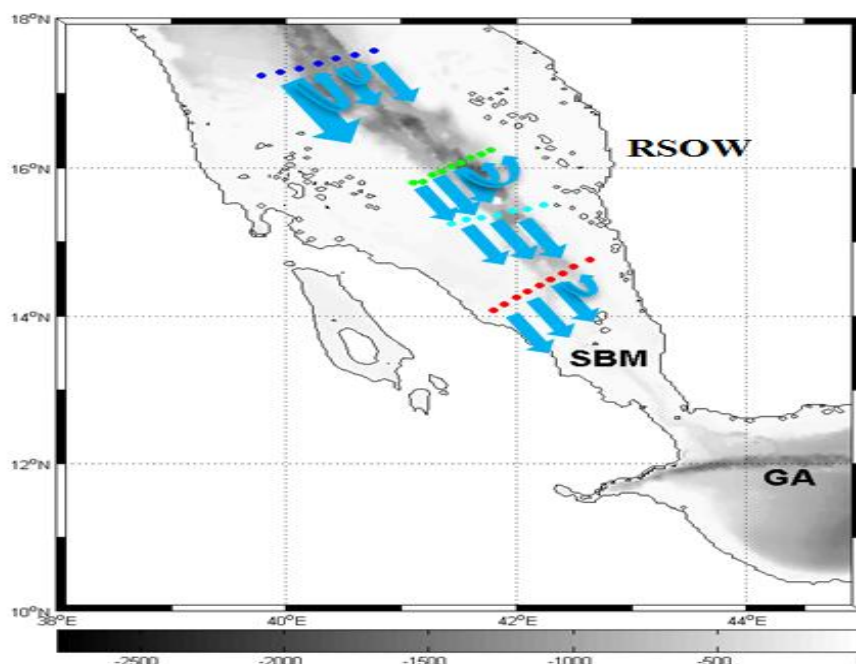


Figure 9-6: As in Figure 9-4 but for Red Sea Outflow Water (RSOW)

In the deep layer (Figure 9-6), the flow of RSDW below  $\sigma_{\theta} < 28.33$  crosses section C on the western side (station pairs 1 and 2) and is similar to the inflowing of the layer above it (RSOW), with a total southward flow of  $0.25 \pm 0.16$  Sv. This flow is completely balanced by  $0.36 \pm 0.10$  Sv of recirculation of deep water on the eastern side (Arabian coast) toward the north (out of the box, between station pairs 3 and 6). The total net transport of RSDW through section C is  $0.11 \pm 0.15$  Sv. Continuing southward, the deep current of RSDW across section F on the western side of the section has a total outflowing of  $0.21 \pm 0.08$  Sv (station pairs 9 and 10) and this flow is partly balanced by  $0.15 \pm 0.10$  Sv of recirculating northward flow (into the box, station pairs 8 and 11). The total net transport of RSDW through section F is  $0.06 \pm 0.08$  Sv. The net transport in the deep water over the box is an outflowing flow with a magnitude of  $0.18 \pm 0.11$  Sv (Figures 9-8e and 9-9e).

The current is influenced by the complex topography of the southern region of the Red Sea, with very wide continental shelves less than 50 m deep on both sides and a deep trench along the main axis of the Red Sea. The inversion results suggest that the densest RSDW flows across section C and recirculates as the slope of the bathymetry increases toward section F from a maximum depth of 1216 m in section C to 528 m in section F, as can be seen in Figure 9-1, and some of the flow upwells to the overlying layer (RSOW). The volume budgets of this layer suggest that some of the RSDW imported within the box might occur by downwelling  $\sim 0.17$  Sv of the overlying RSOW layer. The returned flows of the RSDW joined the cyclonic recirculation loop which feeds the overturning circulation in deep water (460 and 600 m) flowing with slow northward movement. This is related in particular to the old RSDW (characterised by minimum oxygen) as predicted by Cember (1988); the deep water in the northern Red Sea sinks to the bottom level and moves southward until uplifted near the shallow area close to the Strait of Bab el Mandeb to a depth of around 400 m, then flows northward and is mixed with the upper layers.

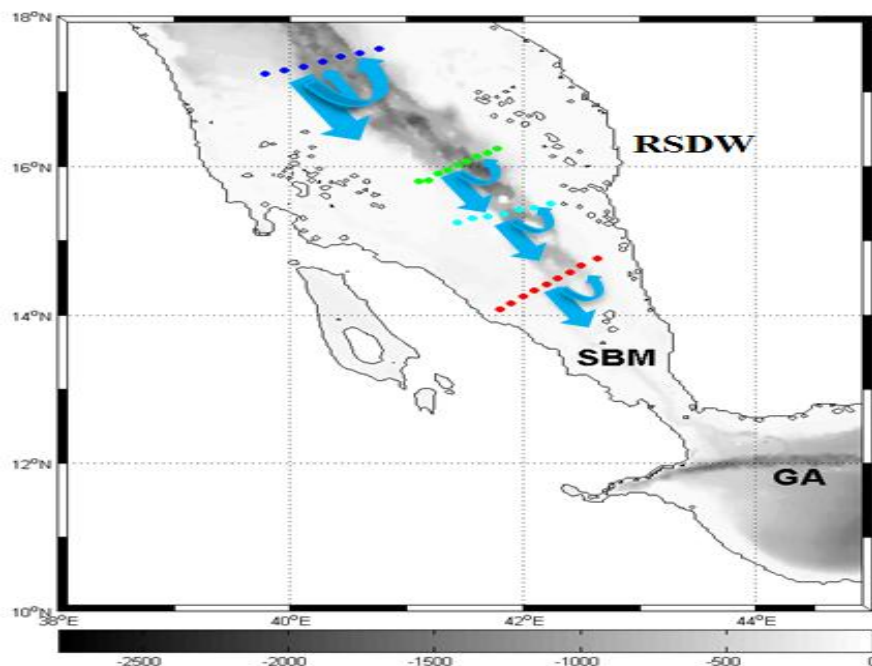


Figure 9-7: As in Figure 9-4 but for Red Sea Deep Water (RSDW)

Integrating the volume transport for each layer in both sections indicates that there is a recirculation northward with magnitude of 0.13 Sv (in the subsurface (GAIW) and deep layers (RSDW) of section C) and southward transport with magnitude of 0.13

Sv (in the surface (RSSW) and deep (RSOW) layers of section C). However, in section F the volume transport indicates that there is southward transport towards the Strait of Bab el Mandeb with magnitude of 0.35 Sv (in the surface (RSSW) and deep (RSOW, RSDW) layers), along with a northward flow of the GAIW with magnitude of 0.37 Sv. The exchange in the upper layers through section F into the Strait of Bab el Mandeb (Figure 9-10) is 0.29 Sv (RSSW and RSOW), if we assume a continuous flow during the year that gives a residence time of ~10 years. As the exchange in the RSDW layer is 0.06 Sv towards the Strait of Bab el Mandeb, this yields a residence time of 69 years for the deep Red Sea water if the volume of the deep water below 300 m of 130000 km<sup>3</sup> is divided by the deep water flow of 0.06 Sv. This result for residence time of the RSDW compared to the renewal times in the literature is within the range of renewal times that vary from a few decades to a century (26 to 320 years) (see Table 1-2). The results of the deep outflowing circulation of 0.06 Sv at section F compared to the rate of the deep water formation are within the range of the annual mean formation rates that vary widely from 0.016 (Kuntz, 1985) to 0.16 Sv (Cember, 1988).

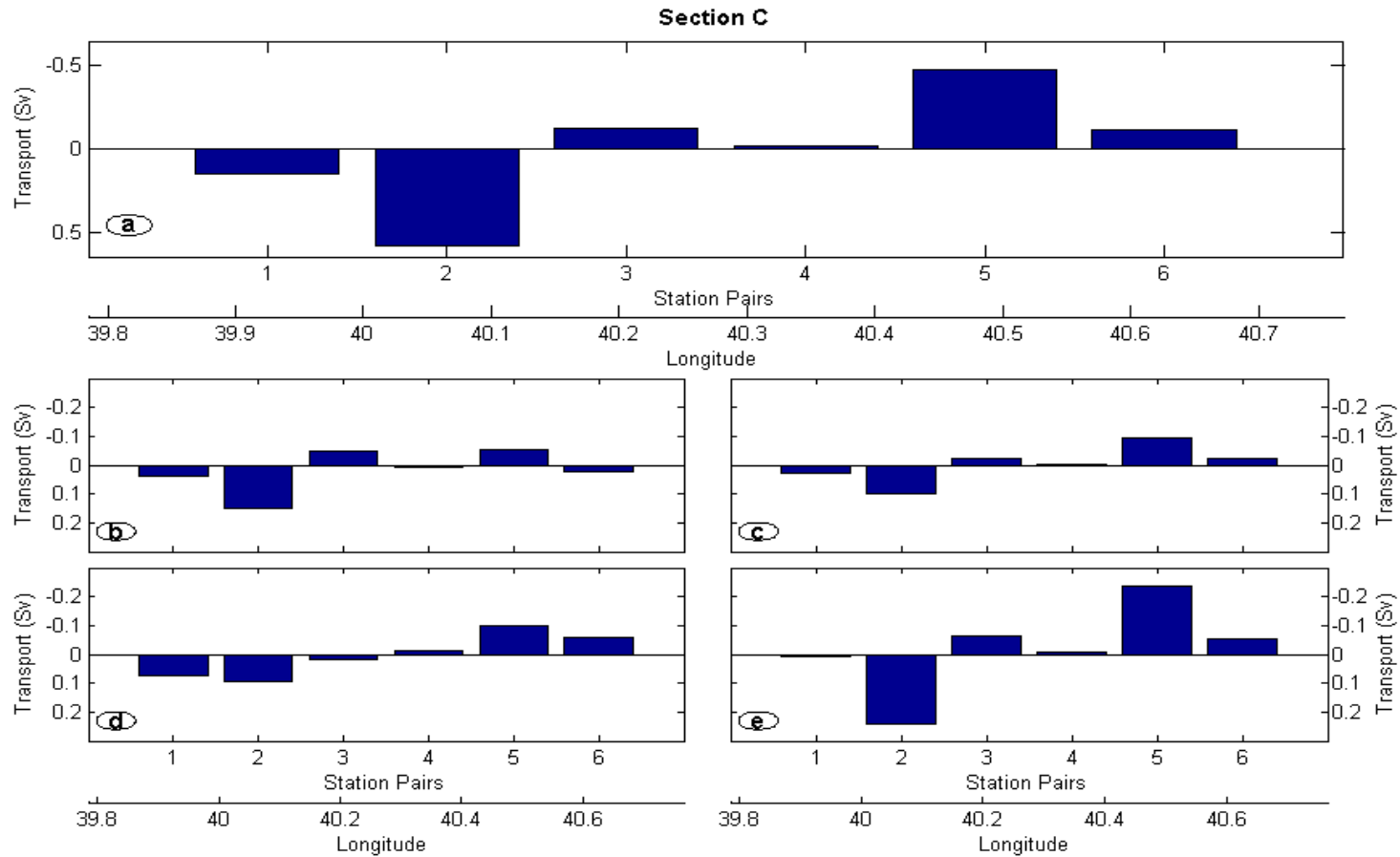


Figure 9-8: Volume transport (Sv) for each station pair at section C, calculated from the standard solution, for a) full-depth volume transports (layer 5), b) present volume transports for RSSW (layer 1,  $\sigma_\theta < 24.4$ ), c) present volume transports for GAIW (layer 2,  $24.4 < \sigma_\theta < 27$ ), d) present volume transports for RSOW (layer 3,  $27 < \sigma_\theta < 28.33$ ) and e) present volume transports for RSDW (layer 4,  $\sigma_\theta > 28.33$ ). Positive values indicate transport directed into the box and negative values indicate transport going out of the box

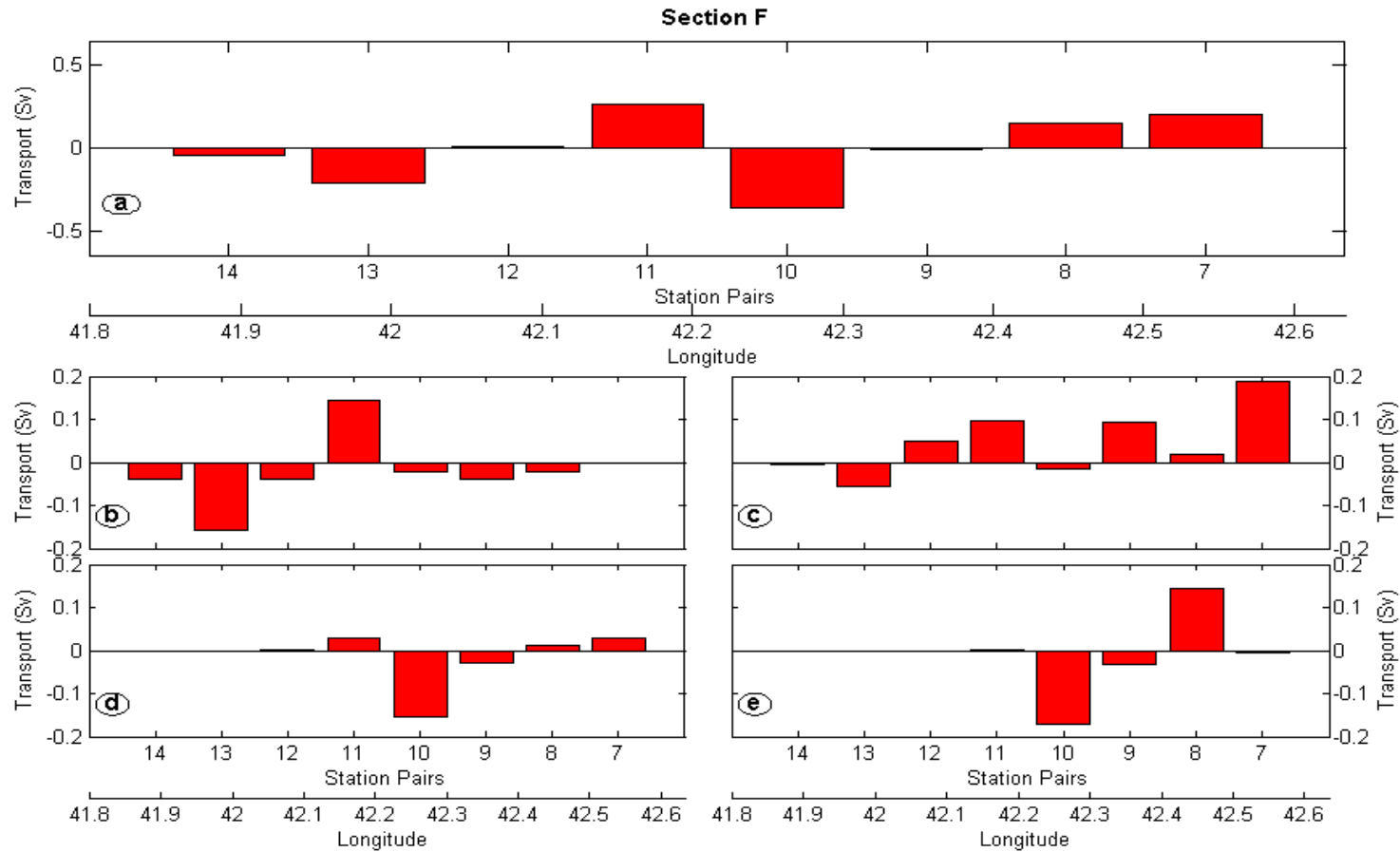


Figure 9-9: Volume transport (Sv) for each station pair in section F, calculated from the standard solution, for a) full-depth volume transports (Layer 5), b) present volume transports for RSSW (layer 1,  $\sigma_\theta < 24.4$ ), c) present volume transports for GAIW (layer 2,  $24.4 < \sigma_\theta < 27$ ), d) present volume transports for RSOW (layer 3,  $27 < \sigma_\theta < 28.33$ ) and e) presents volume transports for RSDW (layer 4,  $\sigma_\theta > 28.33$ ). Positive values indicate transport directed into the box and negative values indicate transport going out of the box

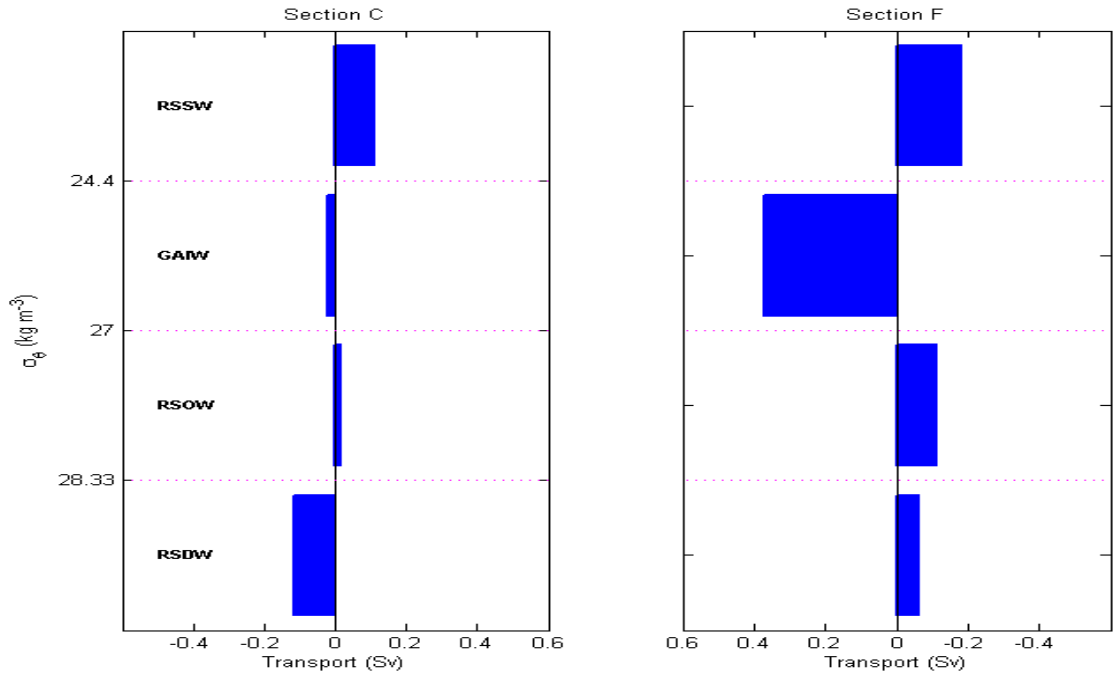


Figure 9-10: Residual for volume transport for each layer of the model in sections C and F. Positive values indicate transport directed northward and negative values indicate transport directed southward

## 9.4 Interior diapycnal mixing

Figures 9-11, 9-12 and 9-13 show the diapycnal velocity for the volume, potential temperature anomaly and salinity anomaly of associated diapycnal transports. As previously mentioned, for the volume, the effective diapycnal velocity is the advective velocity. However, both advection and diffusion contribute to the other property concentrations (heat and salinity). The inverse solution diagnosis gives a small diapycnal velocities ( $o(10^{-6} \text{ m s}^{-1})$ ) over the whole water column (initial diapycnal velocity was assumed to be zero), which is reduced from the *a priori* uncertainty ( $1 \times 10^{-5} \text{ m s}^{-1}$ ). In the RSDW, the magnitudes of the diapycnal volume and salinity velocity are found to be larger than potential temperature with an associated upwelling of 0.07 Sv across the deepest interface ( $\sigma_{\theta} = 28.33$ ) due to mixing in the deep boundary layer. In the water column, the diapycnal velocity in the upper interface ( $\sigma_{\theta} = 24.4$ ) and deep interface ( $\sigma_{\theta} = 28.33$ ) have similar positive magnitudes ( $1.8 \times 10^{-6} \text{ m s}^{-1}$ ), which indicates an upwelling of GAIW towards RSSW (0.08 Sv) and an upwelling of RSDW towards RSOW (0.07 Sv).

The largest velocity across the lower GAIW boundary reflects the large modification of GAIW to RSOW. The accumulated GAIW volume transport across the

box shows a  $0.35 \pm 0.07$  Sv convergence that is balanced by the diapycnal flux export to the adjacent layer. The inversion solution of the GAIW layer shows  $1.8 \times 10^{-6} \text{ m s}^{-1}$  upward velocity across the upper GAIW surface and  $-6.4 \times 10^{-6} \text{ m s}^{-1}$  downward velocity across the lower GAIW surface. These are equivalent to export of 0.07 Sv by upwelling through its upper surface into RSSW and of 0.25 Sv by downwelling through its lower surface into RSOW. Thus expressing the modification of the GAIW might explain the large reduction that occurred in isopycnal GAIW volume transport from 0.37 Sv at F to 0.02 Sv at C. The changes in potential temperature and salinity of GAIW were illustrated in section 6.3.2 as the intermediate cold and fresh water flows across section F toward the north; its characteristics change rapidly due to lateral mixing of the overlying RSSW, warm and saline underlying RSOW and warm and saline water masses. Maillard and Soliman (1986) found the intermediate inflow of the GAIW reaches its northernmost location near  $18^\circ\text{N}$  in October and its flow slows down north of the sill due to the widening of the Red Sea's north where the large eddies begin to take hold. Quadfasel and Baudner (1993) show that the Red Sea circulation is composed of a number of horizontal gyres or eddies distributed along its main axis. The diapycnal export of 0.25 Sv from GAIW into RSOW is a significant net exchange between GAIW and RSOW if we compare it with the lateral transport in the RSOW layer.

The inverse solution shows  $1.8 \text{ m s}^{-1}$  upward velocity across the lower interface between RSOW and RSDW, equivalent to export of 0.07 Sv RSDW upwards through its upper surface into RSOW. This can explain some of the RSOW formed inside the box as suggested by the lateral transport budget of the RSOW.

The accumulated volume transport of the RSDW along the rim of the box shows a  $-0.17 \pm 0.11$  Sv divergence that is balanced by diapycnal fluxes imported from adjacent layers.

As identified by Sloyan and Rintoul (2000) and Naveira Garabato et al. (2003) the effective diffusivity for the potential temperature and salinity flux ( $ED_\theta$ ) can be derived by subtracting the net interior diapycnal volume advection ( $DA_\theta$ ) from the net interior diapycnal potential temperature or salinity ( $DF_\theta$ ):

$$ED_\theta = DF_\theta - DA_\theta \dots (9.1),$$

$$DF_\theta = \omega_\theta^* \times \bar{\theta}^A \times A \dots (9.2) \text{ and}$$

$$DA_\theta = \omega_v^* \times \bar{\theta}^A \times A \dots (9.3),$$

where  $\omega_{\theta}^*$  is the diapycnal velocity for the potential temperature anomaly,  $\omega_v^*$  is diapycnal velocity for the volume,  $A$  is the area of the layer interface and  $\bar{\theta}^A$  is the mean potential temperature anomaly of the interface. The effective diffusion term encompasses all other processes apart from the diapycnal advection, as shown in Figures 9-12 and 9-13. In the solution the diapycnal mixing for the potential temperature and salinity over the box seems to be dominated by the effective diffusion processes through the layer interface. Tandon (2001) provides a detailed review of possible mechanisms that are likely contributing to the effective diffusion term (mixed layer entrainment, vertical motions near fronts, diapycnal eddy stirring). Those processes are likely to occur in the southern Red Sea due to the presence of fronts such as GAIW that affect the circulation and strong eddies activities north of the sill ( $13^{\circ} 44' N$ ).

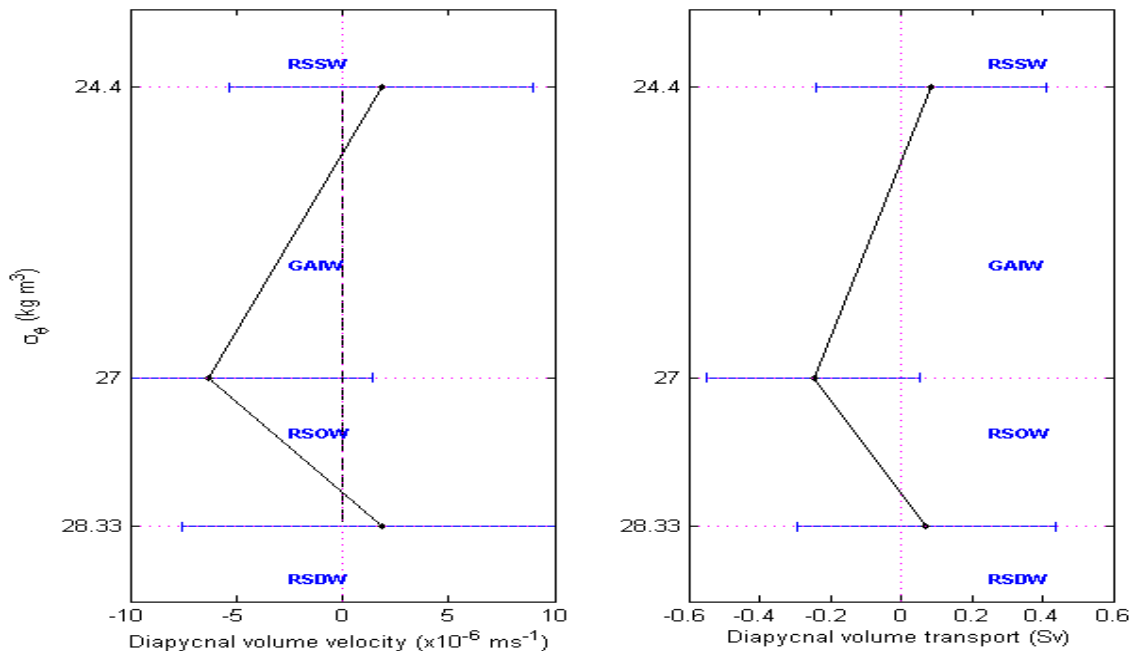


Figure 9-11: Interior diapycnal velocity and associated diapycnal volume transport for the model domain in the solution. Positive velocity or transport is directed upward. Water masses are labelled and their boundaries indicated by horizontal dotted lines. The a posteriori uncertainty is shown by error bar

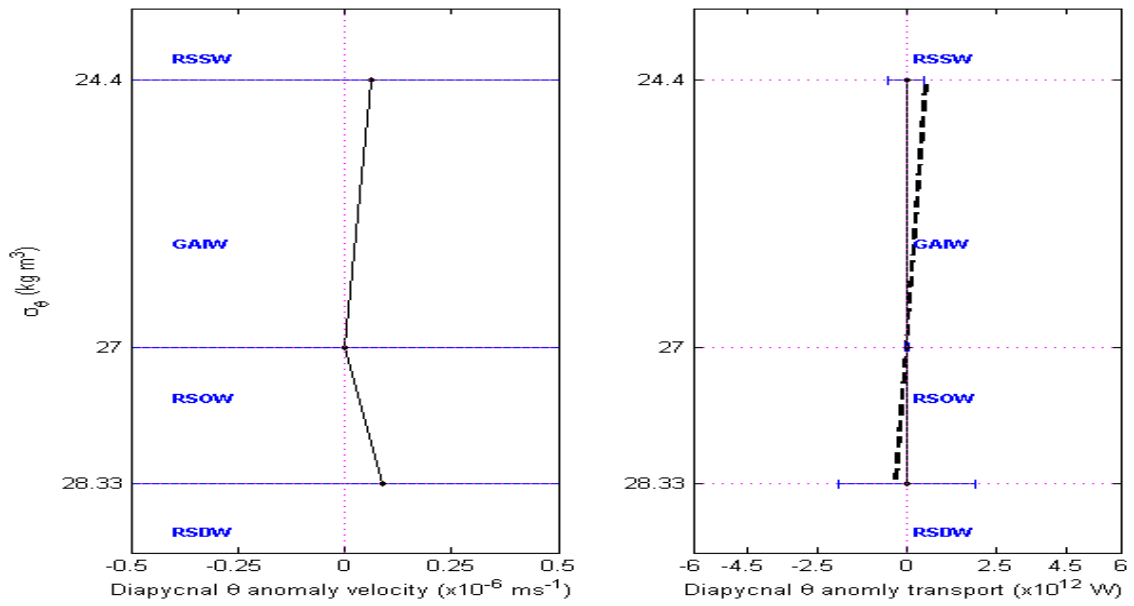


Figure 9-12: Interior diapycnal velocity and associated diapycnal potential temperature anomaly transport for the model domain in the solution. Positive velocity or transport is directed upward. Water masses are labelled and their boundaries indicated by horizontal dotted lines. The black dashed line indicates the conurbation from the effective diffusion where the contribution of the diapycnal volume has been removed. The a posteriori uncertainty is shown by error bar

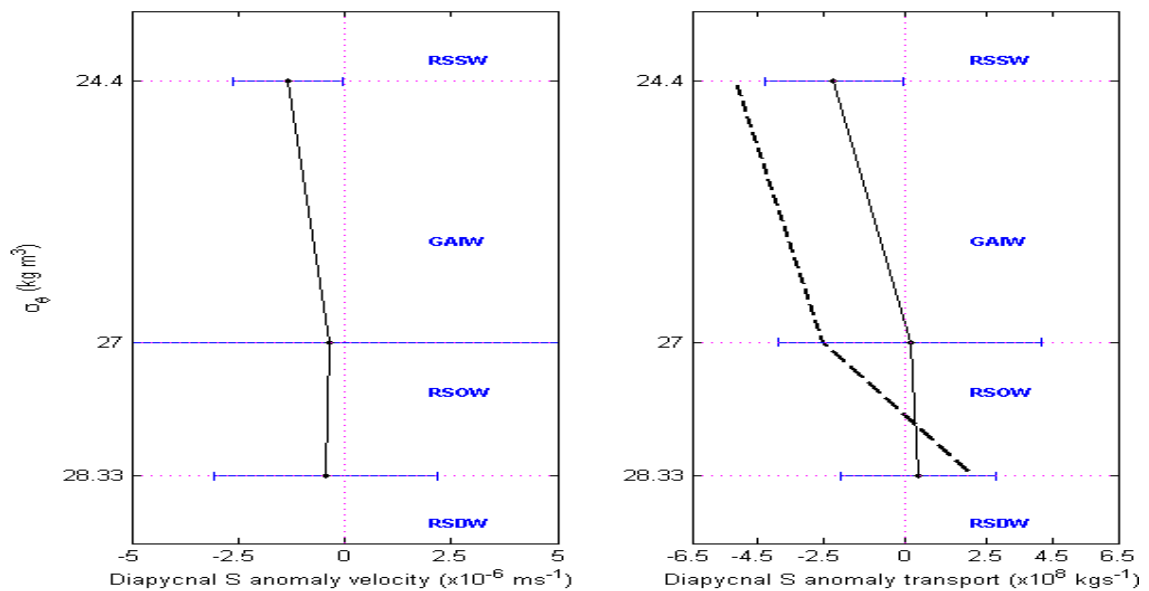


Figure 9-13: Interior diapycnal velocity and associated diapycnal salinity anomaly transport for the model domain in the solution. Positive velocity or transport is directed upward. Water masses are labelled and their boundaries indicated by horizontal dotted lines. The black dashed line indicates the conurbation from the effective diffusion where the contribution of the diapycnal volume has been removed. The a posteriori uncertainty is shown by error bar

## 9.5 Heat and salt fluxes

Some points of interest in the results are the heat and freshwater exchanges between the Red Sea and the Gulf of Aden through the Strait of Bab el Mandeb, discussed in many studies, including those by Thompson (1939), Murray and Johns (1997), Smeed (1997, 2004), Tragou et al. (1999) and Sofianos et al. (2002).

Figures 9-14 show the inversion results for the heat fluxes across sections C and F and over the whole box. There is a southward heat advection in all individual layers (RSSW, GAIW and RSDW) in section C, with magnitudes of 3.71, 0.44 and 1.28 TW ( $\text{TW} = 10^{12} \text{ W}$ ), respectively, except for the RSOW layer, which had a magnitude of 0.12 TW. The large net heat transport (3.71 TW) in the surface layer (RSSW) is expected due to air-sea interaction when the sea surface temperature is highest in the summer season and increases towards the Strait of Bab el Mandeb.

In section F, the net heat transport southward (out of the box) in the upper layers RSSW and GAIW has magnitudes of 5.37 and 6.58 TW, respectively. The net heat loss by advection in the upper layer is expected as a result of the outflowing surface current that is south of the Strait of Bab el Mandeb and the inflowing of the subsurface cold and fresh layer (GAIW) towards the Red Sea (into the box). However, there is a net heat inflowing northwards in the deep layers (RSOW and RSDW) with magnitudes of 0.76 and 0.61 TW, which might be attributed to the recirculation transport in the deep layers. The net heat flux over the whole box in the southern Red Sea region indicates that there is a net heat loss of 7.8 TW in the upper layers (RSSW and GAIW), while there is a net heat gain of 2.52 TW in the deep layers. The total net heat flux over the box is heat lost by advection with magnitude of -5.28 TW.

The estimate of heat exchange in section F towards the Strait of Bab el Mandeb indicates that there is a heat loss by advection with a magnitude of  $23.5 \pm 5.7 \text{ W m}^{-2}$  as that value estimated by Patzert (1974b) with magnitude of  $21.81 \text{ W m}^{-2}$  and with magnitude of  $-22 \text{ W m}^{-2}$  based on data from Sofianos et al. (2002). The seasonal heat exchange by advection between the Red Sea and Gulf of Aden through the Strait of Bab el Mandeb suggests that the annual exchange is small. There is a net heat loss through the strait during summer months by advection as suggested by Patzert (1974b) with an average of  $-17 \text{ W m}^{-2}$  and Tragou et al. (1999) with an average of  $-10 \text{ W m}^{-2}$  whereas there is a net heat gain during the winter by advection.

Figure 9-15 shows the salt fluxes for individual layers across each section (C and F) and over the whole box. In section C, there are net salt transports of  $-0.11 \times 10^9 \text{ kg s}^{-1}$  northwards out of the box in the surface layer (RSSW) and  $-0.16 \times 10^9 \text{ kg s}^{-1}$  in the deep layer (RSDW) while there are net salt transports of  $0.03 \times 10^9 \text{ kg s}^{-1}$  southward into the box in the subsurface layer (GAIW) and  $0.03 \times 10^9 \text{ kg s}^{-1}$  in the deep layer (RSOW).

In section F, there are net salt transports outflowing southward (out of the box) with magnitudes of  $1.02 \times 10^9 \text{ kg s}^{-1}$  in the subsurface (GAIW) and  $0.16$  and  $0.08 \times 10^9 \text{ kg s}^{-1}$  in deep layers (RSOW and RSDW, respectively). In contrast, there is a net salt transport northwards (into the box) with magnitude of  $0.28 \times 10^9 \text{ kg s}^{-1}$  in the surface layer (RSSW). The salt transports over the whole box indicate that there is a net salt gain of  $0.17 \times 10^9 \text{ kg s}^{-1}$  in the surface layer (RSSW) and net salt losses of  $0.98 \times 10^9 \text{ kg s}^{-1}$  in the subsurface (GAIW) and  $0.13$  and  $0.24 \times 10^9 \text{ kg s}^{-1}$  in the deep layers (RSOW and RSDW, respectively). The estimate of salt transport in section F indicates that there is a salt loss with a magnitude of  $0.98 \times 10^9 \text{ kg s}^{-1}$ ; this estimate supported by the analysis of Tragou et al. (1999) which gives a magnitude of  $0.8 \times 10^9 \text{ kg s}^{-1}$  but opposite direction (salt gained).

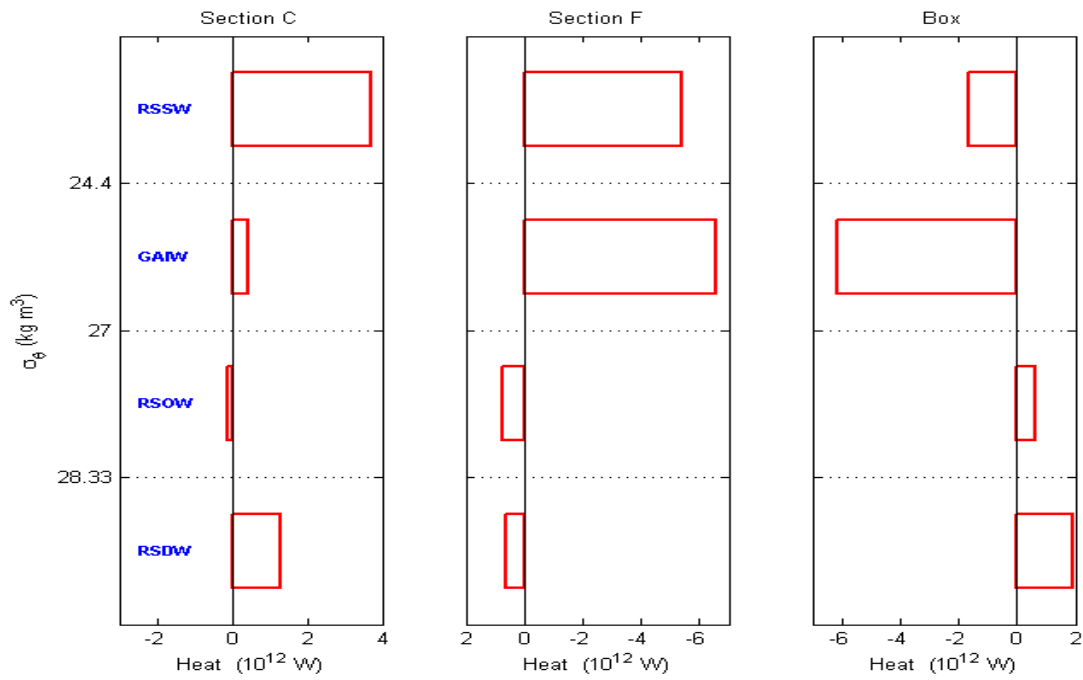


Figure 9-14: Heat fluxes ( $10^{12}$  W) for individual layers in section C (left panel), in section F (middle panel) and over the whole box (right panel). Positive values indicate net heat towards the box

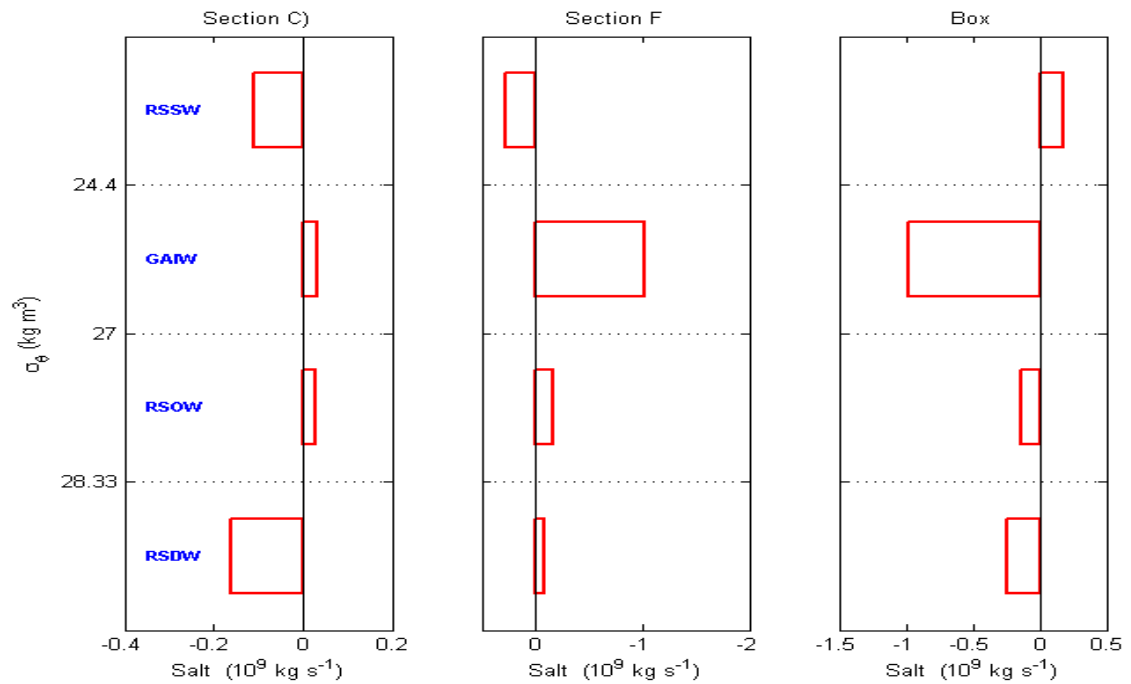


Figure 9-15: Salt fluxes ( $\text{kg s}^{-1}$ ) for individual layers in section C (left panel), in section F (middle panel) and over the whole box (right panel). Positive values indicate net salt towards the box

## 9.6 Conclusion

In this chapter, the steady state lateral circulation in the southern Red Sea region was described for August 2001. The descriptions of the geostrophic transport in the southern part of the Red Sea are given by two synoptic hydrographic sections in the framework of the inverse model. The inverse model confirms the expected qualitative picture of the circulation in the southern Red Sea region and quantitative estimate of the transports that generally accord well with previous estimates for the Strait of Bab el Mandeb. The surface circulation is influenced by the monsoon winds (SW) during the summer season where it acts in opposition to the thermohaline forcing to drive the surface current flow towards the south-southeast through the Strait of Bab el Mandeb. The circulation of the Red Sea is affected by the presence of the GAIW in the intermediate depth with magnitude of 0.37 Sv.

# Chapter 10 Summary and Conclusion

## 10.1 Overview

This thesis has been dedicated to the study of the variations in thermohaline properties in the RSW over a long period dating back to 1889 to see whether there are significant trends toward higher salinity and higher temperature against the background of natural seasonal and interannual variability. The thesis has also included a diagnosis of the circulation of the Red Sea, using synoptic hydrographic measurement together with inverse methods, to provide quantification of summer (August) field fluxes (volume, heat salt) and the southward RSOW export to the Indian Ocean through the Strait of Bab el Mandeb as well as the renewal time for formation of the RSDW.

Most of the studies in the Red Sea have focused on a particular aspect such as shallow thermohaline circulation in the upper layers (e.g. (Tragou & Garrett, 1997), the deep water formation and renewal time (e.g. (Eshel et al., 1994; Woelk & Quadfasel, 1996; Jean-Baptiste et al., 2004) and the exchange with the Indian Ocean through the Strait of Bab el Mandeb. Moreover, some studies have focused on the heat and freshwater budget of the Red Sea (e.g. (Thompson, 1939; Murray & Johns, 1997; Smeed, 1997; Tragou et al., 1999; Sofianos et al., 2002; 2004). However, this work's focus on investigating the Red Sea deep water over time resulted from the lack of literature on this kind of study in relation to the Red Sea.

An inverse box model of the southern Red Sea region is constructed using two synoptic hydrographic sections collected on board the R/V Maurice Ewing during the period from 4 August to 19 August 2001 (Sofianos & Johns, 2007) to quantify the summer field fluxes (volume, heat and salt). The box inverse model is a very useful

technique that can resolve fluxes at the boundaries (hydrographic sections) so that the RSW inflow and outflow can be diagnosed. A detailed description of the geostrophic circulation in the southern Red Sea is diagnosed using a box inverse model. An initial estimate of the circulation in the southern Red Sea based on a priori knowledge is introduced in order to guide the inversion model. Full-depth and layer-specific conservation is applied for the volume, potential temperature and salinity anomalies. Also, the exchange between layers, diapycnal fluxes for volume and potential temperature and salinity anomalies (the anomalies are defined relative to the mean property values along the rim of the box) were explicitly included for the relevant layer interfaces.

The preferred solution was selected such that the equation residuals are required to be zero, within one *a posteriori* standard deviation; also, the solution was required to be within one standard deviation of the *a priori* error estimate. A number of sensitivity tests were performed in order to assess the robustness and stability of the model to its parameters. All these tests were comparable with the selected solution. It is found that the model is sensitive for two main fundamental components including a sufficient number of constraints and including the diapycnal mixing at the interface in the obtained stable solution. However, the modifications in the various parameters as in all the different experiments stayed within the *a posteriori* error of the selection, indicating that the solution is robust to these changes.

## 10.2 Decadal changes in the Red Sea deep water properties

The thermohaline properties of the RSDW were investigated using hydrographic data dating back to 1889. The main results of this study show there are signals of cooling and freshening throughout the entire dataset with magnitudes of  $2 \times 10^{-4} \text{ C}^\circ \text{y}^{-1}$  and  $0.09 \times 10^{-4} \text{ psu y}^{-1}$  respectively. These changes in the thermohaline properties are not statistically significant throughout the entire dataset. The hydrographic data were split into two time periods (pre-1950 and post-1950) to facilitate the comparison between them. The analyses indicate that there is a warming signal for the time period pre-1950 which is statistically significant at a confidence level of 95%. However, the salinity has decreased for this time period with an average of  $-5 \times 10^{-4} \text{ C}^\circ \text{yr}^{-1}$  but these changes in the salinity were not statistically significant.

For the time period post-1950, the analysis shows that both the potential temperature and salinity of the RSDW have decreased the former by an average of 35.5

$\times 10^{-4} \text{ C}^\circ \text{ yr}^{-1}$  and the latter by an average of  $13.8 \times 10^{-4} \text{ psu yr}^{-1}$ . Both of these changes are statistically significant at a confidence level of 95%.

The results suggest that the potential temperature has increased between 1889 and 1950 by as much as  $0.07^\circ\text{C}$  while decreasing between 1950 and 2011 by as much as  $0.12^\circ\text{C}$ . They also suggest that the salinity seems to have decreased between 1889 and 1950 as much as 0.078 psu, while the decrease between 1950 and 2011 was possibly as much as 0.13 psu.

To assess the spatial coherence of the changes in the thermohaline properties of the Red Sea, five sections along the main axis of the Red Sea are analysed. The main results show the differences between the 2001 and 1962 sections, a cooling and freshening for the RSDW along the Red Sea basin with an average of  $-0.25 \pm 0.029 \text{ C}^\circ$  and  $0.018 \pm 0.008 \text{ psu}$  for potential temperature and salinity respectively.

The Red Sea basin was subdivided into seven geographical regions with grids of  $2^\circ$  latitude intervals and using the available high resolution CTD data from 1977 to 2011 in order to distinguish between the spatial variability and basin-wide changes in the thermohaline properties of the RSDW. The results indicate that there is consistent cooling and freshening in all seven regions over the time period between 1977 and 2011. This supports our results regarding long-scale cooling and freshening that occurred in the previous analysis, which implies that the changes are most likely caused by changes in the conditions of formations.

The observations of Woelk and Quadfasel (1996) show new deep water formed during the winter of 1982/83 as can be seen in Figure 3-5c and d. They linked the triggering and the intensity of the convection to the atmospheric forcing like cooling and evaporation over the Gulf of Suez during the winter of 1982/83. However, the NOCS data indicate that the cooling and net evaporation increase over the three source regions for deep water formation and not only over the Gulf of Suez (Figures 3-11 and 3-13). The net heat flux and net evaporation time series over the northern Red Sea, Gulf of Suez and Gulf of Aqaba show that the winters of 1986/1987, 1988/1989, 1989/1990, 1991/1992 and 1999/2000 would also be periods of potentially high renewal of the deep water in the northern Red Sea.

### 10.3 Circulation in the southern Red Sea region

The circulation scheme described in Chapter 9, and illustrated in Figures 9-4, 9-5, 9-6 and 9-7, is summarised here. The initial velocities for the inversion were derived from the geostrophic velocity in the southern part of the Red Sea and are given by two synoptic hydrographic sections in the framework of the inverse model. The inverse model confirms the expected qualitative picture of the circulation in the southern Red Sea region and quantitative estimates of volume transport for the RSSW, GAIW and RSOW are in agreement with previous observations and modelling studies.

The net transport from the standard model suggests a southward inflowing of the RSSW along the box rim towards the Strait of Bab el Mandeb, crossing sections C and F at their boundaries with magnitudes of  $0.11 \pm 0.07$  and  $0.18 \pm 0.08$  Sv respectively. The upper layers in the southern Red Sea region (southward of  $20^\circ\text{N}$ ) are influenced by monsoon winds; during the summer season (June-September, southwest monsoon), the winds act in opposition to the thermohaline forcing. They drive the surface current's flow towards the south-southeast into the Gulf of Aden through the Strait of Bab el Mandeb to join the strong atmospheric and oceanic flow directed into the Arabian Sea (Patzert, 1974a).

Conversely, in the subsurface layers there is a northward inflowing of GAIW into the Red Sea across sections F and C with magnitudes of  $0.37 \pm 0.08$  Sv and  $0.02 \pm 0.06$  Sv respectively. The current in this layer flows northward into the Red Sea along the eastern side of both sections following its entrance through Strait of the Bab el Mandeb. The inversion solution of the GAIW layer shows  $1.8 \times 10^{-6} \text{ m s}^{-1}$  upward velocity across the upper GAIW surface and  $-6.4 \times 10^{-6} \text{ m s}^{-1}$  downward across the lower GAIW surface. These are equivalent to export of 0.07 Sv by upwelling through its upper surface into RSSW and of 0.25 Sv by downwelling through its lower surface into RSOW (Figure 9-11). Thus, the modification of the GAIW might explain the large reduction that occurred in isopycnal GAIW volume transport from 0.37 Sv in section F to 0.02 Sv in section C.

The total outflow of the RSOW is  $0.02 \pm 0.08$  Sv in section C and  $0.11 \pm 0.06$  Sv in section F towards the Gulf of Aden through the Strait of Bab el Mandeb. The intensity of RSOW changes significantly from winter to summer due to the effect of the monsoon wind stress and seasonal fluctuations in the buoyancy forcing (Shapiro & Meschanov, 1991). The volume budget of the box implies that some of the RSOW is formed in the box by upwelling of 0.09 Sv of the deep water (RSDW). The solution

shows an upward diapycnal velocity of  $1.8 \text{ m s}^{-1}$  across the interface of RSOW and RSDW, equivalent to export of  $0.07 \text{ Sv}$  RSDW upwards through its upper surface into RSOW. This can explain some of the RSOW formed inside the box as suggested by the lateral transport budget of the RSOW (Figure 9-11).

The total net transport in the RSDW is  $0.11 \pm 0.15 \text{ Sv}$  flowing northward in section C and  $0.06 \pm 0.08 \text{ Sv}$  flowing southward in section F. The current in this layer is influenced by the complex topography of the southern Red Sea region. The inversion results suggest that the densest RSDW flows across section C and recirculates as the slope of the bathymetry increases toward section F from a maximum depth of 1216 m in section C to 528 m in section F, as can be seen in Figure 9-1. In addition some of the flow upwells to the overlying layer (RSOW). The returned flows of the RSDW join the cyclonic recirculation loop, which feeds the overturning circulation in deep water (460 and 600 m) flowing with slow northward movement. This is related in particular to the old RSDW (characterised by minimum oxygen) as predicted by Cember (1988); the deep water in the northern Red Sea sinks to the bottom level, moves southward until it is uplifted near the shallow area close to the Strait of Bab el Mandeb to a depth of around 400 m and flows northward where it mixes with the upper layers (Figure 10-1).

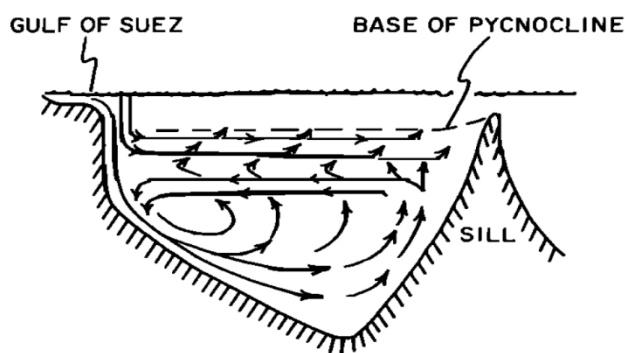


Figure 10-1: Schematic of the general circulation for the RSDW according to Cember (1988)

The flushing time for the RSDW layer is 69 years if we assume continuous outflowing of  $0.06 \text{ Sv}$  in section F towards the Strait of Bab el Mandeb, with the volume of the deep water below 300 m of  $130000 \text{ km}^3$  divided by the deep water flow of  $0.06 \text{ Sv}$ . This flushing time for the RSDW compared to the literature on the flushing time is within the range that varies from a few decades to a few centuries (26 to 320 years) (see Table 1-2). Also, this outflowing value of  $0.06 \text{ Sv}$  is within the annual rate of the RSDW formation, which varies from  $0.04$  to  $0.16 \text{ Sv}$ .

The inversion results show there is heat loss by advection into the Gulf of Aden by a magnitude of  $23.5 \pm 5.7 \text{ W m}^{-2}$  and salt losses by of  $0.98 \times 10^9 \text{ kg s}^{-1}$ .

Beal et al. (2003) investigated the variability of the circulation, water mass and heat and salt fluxes between two zonal hydrographic sections along  $8.5^\circ\text{N}$  in June and September 1995. They show that the RSOW is present near the western boundary of the Somali current ( $\gamma_n = 27.1\text{-}27.6$ ), which supports previous evidence of a possible export of RSOW during the SW monsoon through the interior of the Arabian Sea. The heat loss by advection from the Red Sea into the Gulf Aden is about less than 2% at  $8.5^\circ\text{N}$  in June and less than 7% in September compared to the total heat transport across the section at  $8.5^\circ\text{N}$ . And the salt transport is about less than 25% in June and less than 8% in September. Unfortunately, the magnitude of the heat and salt transport through the Red Sea layer ( $\gamma_n = 27.1\text{-}27.6$ ) across section  $8.5^\circ\text{N}$  is not provided in Beal et al.'s paper.

## 10.4 Conclusion

This study shows that a long trend of cooling and freshening observed in the Red Sea deep water is linked to the convection that occurs intermittently rather than continuously during wintertime in the source of the formation regions.

The box inverse method only quantifies mean steady state circulation in the southern Red Sea, which is limited to the exact time 'snapshot' of the hydrographic sections; therefore another method should be applied. For example, profiling mooring monitoring the inflow and outflow across the Red Sea is the most efficient way to obtain time series and to calculate the fluxes over a long time period.

More observation is needed and a direct current measurement for deep Red Sea water will reduce the uncertainties in the results. Recently two moored meteorological buoys were deployed in the Red Sea by the marine departments of King Abdulaziz University and King Abdullah University for Science and Technology that will help to assess the metrological data and reduce their uncertainties.

# References

- Ahmad, F. & Sultan, S. a. R. 1987. On the heat balance terms in the central region of the Red Sea. *Deep-Sea Research*, 34, 1757-1760.
- Ahmad, F. & Sultan, S. a. R. 1989. Sea surface fluxes and their comparison with the oceanic heat flow in the Red Sea. *Oceanologica ACTA*, 12, 33-36.
- Anotonov, J. I., Levitus, S. & Boyer, T. P. 2004. Climatological annual cycle of ocean heat content. *Geophysical Research Letters*, 31.
- Beal, L., Chereskin, T., Bryden, H. & Ffield, A. 2003. Variability of water properties, heat and salt fluxes in the Arabian Sea, between the onset and wane of the 1995 southwest monsoon. *Deep Sea Research Part II: Topical Studies in Oceanography*, 50, 2049-2075.
- Beal, L. M., Ffoield, A. & Gordon, A. L. 2000. Spreading of Red Sea overflow waters in the Indian Ocean. *Geophysical Research*, 105, 8549-8564.
- Berry, D. I. & Kent, E. C. 2009. A New Air–Sea Interaction Gridded Dataset from ICOADS With Uncertainty Estimates. *Bulletin of the American Meteorological Society*, 90, 645-656.
- Bethoux, J., Gentili, B., Raunet, J. & Tailliez, D. 1990. Warming trend in the western Mediterranean deep water.
- Bethoux, J. P. 1988. Red-Sea geochemical budgets and exchanges with the Indian-Ocean. *Marine Chemistry*, 24, 83-92.
- Bethoux, J. P., Gentili, B. & Tailliez, D. 1998. Warming and freshwater budget change in the Mediterranean since the 1940 s, their possible relation to the greenhouse effect. *Geophysical Research Letters*, 25, 1023-1026.
- Bignami, F., Marullo, S., Santoleri, R. & Schiano, M. E. 1995. Longwave radiation budget in the Mediterranean Sea. *Journal of Geophysical Research*, 100(C2), 2501-2514.

- Bower, A. S., Hunt, H. D. & Price, J. F. 2000. Character and dynamics of the Red Sea and Persian Gulf outflows. *Geophysical Research*, 105C, 6387–6414.
- Boyer, T. & Levitus, S. 1994. Quality control and processing of historical oceanographic temperature, salinity, and oxygen data. *NOAA Technical Report NESDIS 81*. Washington, DC.
- Buchan, A. 1895. Report on oceanic circulation based on the observation made on board H. M. S. "challenger" and other observations report on scientific results of the voyage of H. M. S. "challenger".
- Bunker, A. F., Charnock, H. & Goldsmith, R. A. 1982. A note on the heat balance of the Mediterranean and Red Seas. *Journal of Marine Research*, 40, 73-84.
- Candela, J. 2001. Mediterranean Water and Global Circulation. In: SIEDLER, G., CHURCH, J. & GOULD, J. (eds.) *Ocean Circulation and Climate-Observing and Modelling the Global Ocean*. San Diego: Academic Press.
- Cember, R. P. 1988. On the sources, formation and circulation of Red-Sea deep-water. *Journal of Geophysical Research*, 93, 8175–8191.
- Clark, N. E., Eber, L., Laurs, R. M., Renner, J. A. & Saur, J. F. T. 1974. Heat Exchange Between Ocean and Atmosphere in the Eastern North Pacific for 1961-71. *NMFS SSRF-682*. Washington, D.C.
- Da Silva, A. M., Young, C. C. & Levitus, S. 1994. Atlas of Surface Marine Data 1994. NESDIS 6, ed. United States of America. Department of Commerce.
- Degens, E. & Ross, D. A. 1969. *Hot Brines and Recent Heavy Metal Deposits in the Red Sea*, New York, Springer-Verlag.
- Donohue, K. A., Firing, E. & Beal, L. 2000. Comparison of three velocity sections of the Agulhas Current and Agulhas Undercurrent. *Journal of Geophysical Research*, 105, 28,585-28,593.
- Edwards, A. J. & Head, S. M. 1987. *Key Environments: Red Sea*, Oxford, Pergamon Press.
- Eshel, G., Cane, M. A. & Blumenthal, M. B. 1994. Modes of subsurface, intermediate, and deep water renewal in the Red Sea. *Journal of Geophysical Research*, 99, 15941-15952.
- Fairall, C. W., Bradley, E. F., Rogers, D. P., Edson, J. B. & Young, G. S. 1996. Bulk parameterization of air-sea fluxes for TOGA-COARE. *Journal of Geophysical Research* 101, 3747-3764.

- Fedorov, K. N. & Meshchanov, S. L. 1988. Structure and propagation of the Red Sea water in the Aden Gulf. *Oceanology*, 28, 357–363.
- Fraile-Nuez, E., Plaza, F., Hernández-Guerra, A., Vargas-Yáñez, M. & Lavín, A. 2008. Mass transport in the Bay of Biscay from an inverse box model. *Journal of Geophysical Research*, 113, C06023.
- Friedrichs, M. a. M. 1993. Meridional Circulation in the Tropical North Atlantic. Woods Hole Oceanographic Institution.
- Ganachaud, A. 1999. *Large scale oceanic circulation and fluxes of freshwater, heat, nutrients and oxygen*. PhD, Institute of Technology/Woods Hole Oceanographic Institution Joint Program.
- Ganachaud, A. 2003a. Error budget of inverse box models: The North Atlantic. *Journal of Atmospheric and Oceanic Technology*, 20, 1641-1655.
- Ganachaud, A. 2003b. Large-scale mass transports, water mass formation, and diffusivities estimated from World Ocean Circulation Experiment (WOCE) hydrographic data. *Journal of Geophysical Research*, 108, 3213.
- Ganachaud, A. & Wunsch, C. 2000. Improved estimates of global ocean circulation, heat transport and mixing from hydrographic data. *Nature*, 408, 453-457.
- Ganachaud, A. & Wunsch, C. 2003. Large-Scale Ocean Heat and Freshwater Transports during the World Ocean Circulation Experiment. *Journal of Climate*, 16, 696-705.
- Ganachaud, A., Wunsch, C., Marotzke, J. & Toole, J. 2000. Meridional overturning and large-scale circulation of the Indian Ocean. *Journal of Geophysical Research*, 105, 117-26.
- Grasshoff, K. 1969. Zur Chemie des Roten Meeres und des Inneren Golfs von Aden nach Beobachtungen von F.S. "Meteor" während der Indischen Ozean Expedition 1964/65. Meteor Forschungsergebnisse, Deutsche Forschungsgemeinschaft, Reihe A Allgemeines, Physik und Chemie des Meeres, Gebrüder Bornträger, Berlin, Stuttgart, A6. 1–76.
- Grundlingh, M. L. 1985. Occurrence of Red Sea water in the southwestern Indian Ocean, 1981. *Journal of Physical Oceanography*, 15, 207-212.
- Hastenrath, S. & Lamb, P. J. 1979. *Heat budget atlas of the tropical Atlantic and eastern Pacific Oceans*, Madison University of Wisconsin Press.

- Hernández-Guerra, A., Fraile-Nuez, E., López-Laatzén, F., Martínez, A., Parrilla, G. & Vélez-Belchí, P. 2005. Canary Current and North Equatorial Current from an inverse box model. *Journal of Geophysical Research*, 110, C12019.
- Ivchenko, V., Wells, N., Aleynik, D. & Shaw, A. 2010. Variability of heat and salinity content in the North Atlantic in the last decade. *Ocean Science*, 6, 719-735.
- Jean-Baptiste, P., Fourré, E., Metz, N., TERNON, J. F. & POISSON, A. 2004. Red Sea Deep Waters circulation and ventilation rate deduced from the  $^3\text{He}$  and  $^{14}\text{C}$  tracer fields. *Journal of Marine Systems*, 48, 37-50
- Johnson, D. R., Boyer, T. P., Garcia, H. E., Locarnini, R. A., Baranova, O. K. & Zweng, M. M. 2009. World Ocean Database 2009 Documentation. Maryland: NOAA Printing Office.
- Jones, E. N. & Browning, D. G. 1971. Cold water layer in the southern Red Sea. *Limnology and Oceanography*, 503-509.
- Josey, S. A., Kent, E. C. & Taylor, P. K. 1999. New insights into the ocean heat budget closure problem from analysis of the SOC air-sea flux climatology. *Journal of Climate*, 12, 2856-2880.
- Josey, S. A., Oakley, D. & Pascal, R. W. 1997. On estimating the atmospheric longwave flux at the ocean surface from ship meteorological reports. *Journal of Geophysical Research*, 102, 27961-27,972.
- Josey, S. A., Pascal, R. W., Taylor, P. K. & Yelland, M. J. 2003. A New Formula For Determining the Atmospheric Longwave Flux at the Ocean Surface at Mid-High Latitudes. *Journal of Geophysical Research*, 108(C4).
- Jullion, L. 2008. *Water mass modification in the Southwestern Atlantic*. PhD, University of East Anglia
- Jullion, L., Heywood, K. J., Naveira Garabato, A. C. & Stevens, D. P. 2010. Circulation and water mass modification in the Brazil-Malvinas Confluence. *Journal of Physical Oceanography*, 40, 845-864.
- Kamel, M. & Eid, F. 2005. Heat and salt storages in the offshore water of the Red Sea.
- Krahmann, G. & Schott, F. 1998. Longterm increases in Western Mediterranean salinities and temperatures: anthropogenic and climatic sources. *Geophysical Research Letters*, 25, 4209-4212.
- Kuntz, R. 1985. *Bestimmung der Tiefenwasserzirkulation des Roten Meeres anhand einer Boxmodellauswertung von Tritium-,  $^3\text{He}$ - und Salinitätsdaten*. PhD Thesis, Ruprecht Karls University.

- Levitus, S. 1984. Annual cycle of temperature and heat storage in the World Ocean. *Journal of Physical Oceanography*, 14, 727-746.
- Levitus, S. 1986. Annual cycle of salinity and salt storage in the World Ocean. *Journal of Physical Oceanography*, 16, 322-343.
- Levitus, S. 1987. Rate of change of heat storage of the World Oceans. *Journal of Physical Oceanography* 17, 518-528.
- Levitus, S., Antonov, J. & Boyer, T. 2005. Warming of the world ocean, 1955–2003. *Geophysical Research Letters*, 32.
- Levitus, S., Antonov, J., Boyer, T., Baranova, O., Garcia, H., Locarnini, R., Mishonov, A., Reagan, J., Seidov, D. & Yarosh, E. 2012. World ocean heat content and thermosteric sea level change (0–2000 m), 1955–2010. *Geophysical Research Letters*, 39, L10603.
- Liu, W. T., Katsaros, K. B. & Businger, J. A. 1979. Bulk parameterization of air–sea exchanges of heat and water vapor including the molecular constraints at the interface. *Journal of the Atmospheric Sciences*, 36, 1722–1735.
- Lumpkin, R. & Speer, K. 2007. Global Ocean Meridional Overturning. *Journal of Physical Oceanography*, 37, 2550–2562.
- Lyman, J. M., Willis, J. K. & Johnson, G. C. 2006. Recent cooling of the upper ocean. *Geophysical Research Letters*, 33, L18604.
- Maillard, C. 1974. Eaux intermédiaires et formation d'eau profonde en Mer Rouge. *L'oceanographie physique de la Mer Rouge, Symposium de l'Association Internationale des Sciences Physiques de l'océan*. Paris: CNEXO, 105-134.
- Maillard, C. & Soliman, G. 1986. Hydrography of the Red Sea and exchanges with the Indian Ocean in summer. *Oceanologica Acta*, 9, 249-269.
- Maiya, I. A. 1993. Heat Storage in the Eastern Mediterranean. *Journal of Physical Oceanography* 23, 1259-1263.
- Manins, P. C. 1973. A filling box model of the deep circulation of the Red Sea. *Mémoires Société Royale des Sciences de Liège*, 6, 153-166.
- Mcdonagh, E. L. & King, B. A. 2005. Oceanic fluxes in the South Atlantic. *Journal of Physical Oceanography*, 36, 109–122.
- Mcintosh, P. C. & Rintoul, S. R. 1997. Do Box Inverse Models Work? *Journal of Physical Oceanography*, 27, 291-308.
- Morcos, S. A. 1970. Physical and chemical Oceanography of the Red Sea. *Oceanography Marine Biology Annual Review*, 8, 73-202.

- Morgan, P. P. 1995. Box inverse modelling with DOBOX 4.2. CSIRO Marine lab., Div. of oceanography Hobart.
- Munk, W. & Wunsch, C. 1998. Abyssal recipes II: energetics of tidal and wind mixing. *Deep-Sea Research Part I*, 45, 1977-2010.
- Murray, S. P. & Johns, W. 1997. Direct observations of seasonal exchange through the Bab el Mandab Strait. *Geophysical Research Letters*, 24, 2557-2560.
- Naveira Garabato, A. C., Stevens, D. P. & Heywood, K. J. 2003. Water mass conversion, fluxes, and mixing in the Scotia Sea diagnosed by an inverse model. *Journal of Physical Oceanography*, 33, 2565-2587.
- Neumann, A. C. & Mcgill, D. A. 1961. Circulation of Red Sea in Early Summer. *Deep Sea Research*, 8, 223-235.
- Neumann, J. 1952. Evaporation from the Red Sea. *Israel Exploration*, 2, 153-162.
- Osman, M. M. 1985. Evaporation from coastal water off Port-Sudan. *Journal of the Faculty of Marine Science(KAU)*, 4, 29-37.
- Palmer, M., Gomis, D., Mar Flexas, M., Jordà, G., Jullion, L., Tsubouchi, T. & Naveira Garabato, A. C. 2011. Water mass pathways and transports over the South Scotia Ridge west of 50° W. *Deep Sea Research Part I: Oceanographic Research Papers*.
- Papadopoulos, V. P., Abualnaja, Y., Josey, S. A., Bower, A., Raitzos, D. E., Kontoyiannis, H. & Hoteit, I. 2013. Atmospheric forcing of the winter air-sea heat fluxes over the northern Red Sea. *Journal of Climate*.
- Patzert, W. C. 1972a. Seasonal reversal in Red Sea circulation. *L'oceanographie physique de la Mer Rouge, Symposium de l'Association Internationale des Sciences Physiques de l'océan*. Paris: CNEXO,55-85.
- Patzert, W. C. 1972b. *Sesonal variation in structure and circulation in the Red Sea* PhD, University of Hawaii.
- Patzert, W. C. 1974a. Wind-induced reversal in Red Sea circulation. *Deep-Sea Research*, 21, 109-121.
- Patzert, W. C. 1974b. Volume and heat transports between the Red Sea and Gulf of Aden, and notes on the Red Sea heat budget. *L'oceanographie physique de la Mer Rouge, Symposium de l'Association Internationale des Sciences Physiques de l'océan*. Paris: CNEXO, 191-201.
- Phillips, O. M. 1966. On turbulent convection current and the circulation of the Red Sea. *Deep-Sea Research*, 13, 1149-1160.

- Plaehn, O., Baschek, B., Badewien, T., Walter, M. & Rhein, M. 2002. Important of the Gulf of Aqaba for the formation of bottom water in the Red Sea. *Journal of Geophysical Research*, 107(C8), doi:10.1029/2000JC000342.
- Privett, D. W. 1959. Monthly charts of evaporation from the Indian Ocean (including the Red Sea and the Persian Gulf). *The Quarterly Journal of the Royal Meteorological Society*, 85, 424-428.
- Quadfasel, D. 2001. Red Sea Circulation. In: STEELE, J. A., THORPE, S. A. & TUREKIAN, K. K. (eds.) *Encyclopedia of Ocean Sciences*.
- Quadfasel, D. & Baudner, H. 1993. Gyre-scale circulation cells in the Red Sea. *Oceanologica Acta*, 16, 221-229.
- Reed, R. K. 1977. On estimating insolation over the ocean. *Journal of Physical Oceanography*, 7, 482-485.
- Risien, C. M. & Chelton, D. B. 2008. A global climatology of surface wind and wind stress fields from eight years of QuikSCAT scatterometer data. *Journal of Physical Oceanography*, 38, 2379-2413.
- Robinson, M. K. 1974. Atlas of monthly mean sea surface and subsurface temperature and the depth of the top of the Thermocline. *L'oceanographie physique de la Mer Rouge, Symposium de l'Association Internationale des Sciences Physiques de l'océan*. Paris: CNEXO, 29-54.
- Rochford, D. J. 1964. Salinity maxima in the upper 1000 meters of the north Indian Ocean. *Australian Journal of Marine and Freshwater Research*, 15, 1-24.
- Rohling, E. J. & Bryden, H. L. 1992. Man-Induced Salinity and Temperature Increases in Western Mediterranean Deep Water. *Journal of Geophysical Research*, 97, 11191-11198.
- Shapiro, G. I. & Meschanov, S. L. 1991. Distribution and spreading of Red Sea water and salt lens formation in the northwest Indian Ocean. *Deep-Sea Research*, 38, 21-34.
- Shi, W., Subrahmanyam, B. & Morrison, J. M. 2003. Estimation of heat and salt storage variability in the Indian Ocean from TOPEX/Poseidon altimetry. *Journal of Geophysical Research*, 108(C7).
- Siedler, G. 1968 Schichtungs und Bewegungsverhältnisse am Sudausgang des Roten Meeres. "Meteor" Forsch.-Ergebn Reihe A, 4. 1-67.

- Siedler, G. 1969. General circulation of water masses in the Red Sea. *In*: DEGENS, E. & ROSS, D. A. (eds.) *Hot Brines and Recent Heavy Metal Deposits in the Red Sea*. New York: Springer-Verlag.
- Sloyan, B. M. & Rintoul, S. R. 2000. Estimates of area-averaged diapycnal fluxes from basin-scale budgets. *Journal of Physical Oceanography*, 30, 2320-2341.
- Smeed, D. 1997. Seasonal variation of the flow in the strait of Bab al Mandab. *Oceanologica Acta* 20, 773-781.
- Smeed, D. 2004. Exchange through the Bab el Mandab. *Deep-Sea Research*, 51, 455–474.
- Smeed, D. A. 2000. Hydraulic control of three-layer exchange flows: application to the Bab al Mandab. *Journal of Physical Oceanography*, 30, 2574-2588.
- Smith, S. D. 1980. Wind stress and heat flux over the ocean in gale force winds. *Journal of Physical Oceanography*, 10, 709–726.
- Smith, S. D. 1988. Coefficients for sea surface wind stress, heat flux, and wind profiles as a function of wind speed and temperature. *Journal of Geophysical Research*, 93 (C12), 15467–15472.
- Smith, W. H. F. & Sandwell, D. T. 1997. Global sea floor topography from satellite altimetry and ship depth soundings. *Science*, 277, 1956-1962.
- Sofianos, S. S. & Johns, W. E. 2003. An Oceanic General Circulation Model (OGCM) investigation of the Red Sea circulation: 2. Three-dimensional circulation in the Red Sea. *Journal of Geophysical Research*, 108, 3066.
- Sofianos, S. S. & Johns, W. E. 2007. Observations of the summer Red Sea circulation. *Journal of Geophysical Research*, 112, doi:10.1029 - 2006JC003886.
- Sofianos, S. S., Johns, W. E. & Murray, S. P. 2002. Heat and freshwater budgets in the Red Sea from direct observations at Bab el Mandeb. *Deep-Sea Research Part II: Topical Studies in Oceanography*, 49, 1323-1340.
- Tandon, A. 2001. Water mass transformation due to mixed layer entrainment and mesoscale stirring: In series or parallel? From Stirring to Mixing in a Stratified Ocean: Proc. 'Aha Huliko'a Hawaiian Winter Workshop, Honolulu, HI, University of Hawaii at Manoa. 105-111.
- Taylor, P. K. & Yelland, M. J. 2001. The Dependence of Sea Surface Roughness on the Height and Steepness of the Waves. *Journal of Physical Oceanography*, 31, 572 - 590.

- Thompson, E. F. 1939. The exchange of water between the Red Sea and the Gulf of Aden over the “sill”. *John Murray Expedition 1933–34 Scientific Report*, 2, 105–119.
- Tragou, E. & Garrett, C. 1997. The shallow thermohaline circulation of the Red Sea. *Deep Sea Research Part I: Oceanographic Research Papers*, 44, 1355-1376.
- Tragou, E., Garrett, C., Outerbridge, R. & Gilman, G. 1999. The heat and freshwater budgets of the Red Sea. *Journal of Physical Oceanography*, 29, 2504–2522.
- Tsubouchi, T., Bacon, S., Garabato, A. C. N., Aksenov, Y., Laxon, S., Fahrback, E., Beszczynska-Möller, A., Hansen, E., Lee, C. & Ingvaldsen, R. 2012. The Arctic Ocean in summer: A quasi-synoptic inverse estimate of boundary fluxes and water mass transformation. *Journal of Geophysical Research*, 117, C01024.
- Valentine, H. R., Lutjeharms, J. R. E. & Brundrit, G. B. 1993. The water masses and volumetry of southern Agulhas current region. *Deep-Sea Research*, 40, 1285-1305.
- Ve´lez-Belchi, P., Hernández-Guerra, A., Fraile-Nuez, E. & Benni´Tez-Barrios, V. 2010. Changes in Temperature and Salinity Tendencies of the Upper Subtropical North Atlantic Ocean at 24.5°N. *JOURNAL OF PHYSICAL OCEANOGRAPHY*, 40, 2546-2555.
- Vercelli, E. 1925. Recherche di oceanografia fisica eseguite della R. N. AMMIRAGLIO MAGNAGHI (1923–24). *Part I. Correnti e maree. Annali Idrografici*, 11, 1-188.
- Vercelli, F. 1927. The Hydrographic Survey of the R. N. Amrairaglio Magnaghi in the Red Sea. *Annual Hydrographic* 2, 1- 290.
- Villwock, A. 1994. *ENSO induzierte Variabilität im Indischen Ozean*. PhD, University of Hamburg.
- Wallace, J., Rasmusson, E., Mitchell, T., Kousky, V., Sarachik, E. & Storch, H. V. 1998. On the structure and evolution of ENSO-related climate variability in the tropical Pacific: Lessons from TOGA. *Journal of Geophysical Research*, 103, 14241-14259.
- Webster, P. J., Bradley, E. F., Fairall, C. W., Godfrey, J. S., Hacker, P., Houze Jr., R. A., Lukas, R., Serra, Y., Hummon, J. M., Lawrence, T. D. M., Russell, C. A., Ryan, M. N., Sahami, K. & Zuidema, P. 2002. The Joint Air-Sea Monsoon Interaction Experiment (JASMINE) Pilot Study. *Bulletin of the American Meteorological Society*, 83, 1603-1630.

- Weller, R., Baumgartner, M., Josey, S., Fischer, A. & Kindle, J. 1998. Atmospheric forcing in the Arabian Sea during 1994–1995: Observations and comparisons with climatology and models. *Deep-Sea Research Part II*, 45, 1961–1999.
- Woelk, S. & Quadfasel, D. 1996. Renewal of deep-water in the Red Sea during 1982–1987. *Journal of Geophysical Research*, 101, 18155–18165.
- Wong, A. P. S., Johnson, G. C. & Owens, W. B. 2003. Delayed mode calibration of autonomous CTD profiling float salinity data by  $\theta$ -S climatology. *Journal of Atmospheric and Oceanic Technology*, 20, 308–318.
- Woodruff, S. D., Diaz, H. F., Elms, J. D. & Worley, S. J. 1998. COADS Release 2 Data and Metadata Enhancements for Improvements of Marine Surface Flux Fields. *Physics and Chemistry of the Earth*, 23, 517–526.
- Worley, S. J., Woodruff, S. D., Reynolds, R. W., Lubker, S. J. & Lott, N. 2005. ICOADS release 2.1 data and products. *International Journal of Climatology*, 25, 823–842.
- Wunsch, C. 1978. The North Atlantic general circulation West of 50° W determined by inverse methods. *Reviews of Geophysics*, 16, 583–620.
- Wunsch, C. 1996. *The Ocean inverse circulation inverse problem*, Cambridge University Press.
- Wust, G. 1954. Gesetzmäßige Wechselbeziehungen zwischen Ozean und Atmosphäre in der zonalen Verteilung von Oberflächensalzgehalt, Verdunstung und Niederschlag. *Archives for Meteorology Geophysics and Bioklimatologie*, A 7, 305–328.
- Wyrtki, K. 1971. *Oceanographic Atlas of the International Indian Ocean Expedition*, Washington, D. C, National Science Foundation.
- Wyrtki, K. 1974. On the deep circulation of the Red Sea. *L'oceanographie physique de la Mer Rouge, Symposium de l'Association Internationale des Sciences Physiques de l'océan*. Paris: CNEXO, 135–163.
- Yegorov, N. I. 1950. Calculation of the heat balance of the Red Sea. *Meteorologia idrologia*, 3, 49–56.
- Zemba, J. C. 1991. *The structure and transport of the Brazil Current between 27° and 36°S*. PhD, Massachusetts Institute of Technology/Woods Hole Oceanographic Institution Joint Program.
- Zhang, Y., Rossow, W. B., Lacis, A. A., Oinas, V. & Mishchenko, M. I. 2004. Calculation of radiative fluxes from the surface to top of atmosphere based on

ISCCP and other global data sets: Refinements of the radiative transfer model and the input data. *Journal of Geophysical Research*, 109, D19105, doi:10.1029/2003JD004457.

# Appendix A

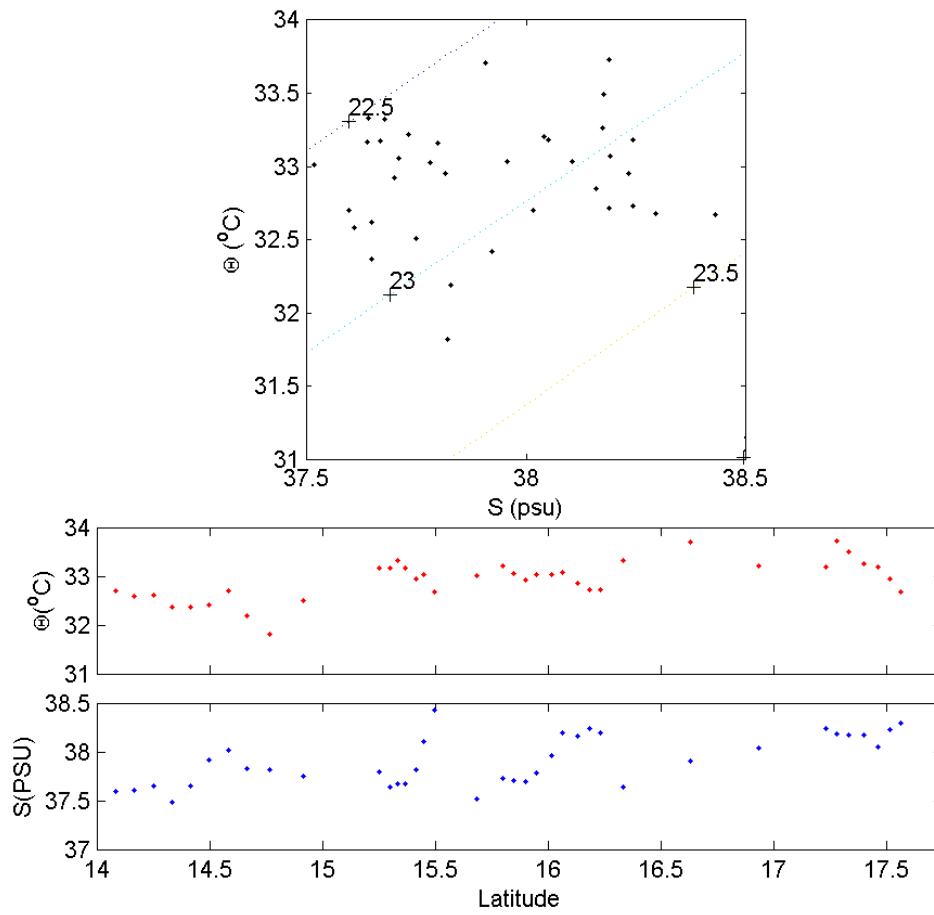


Figure A-1: Potential temperature (°C) and salinity characteristics of the surface waters (upper 10 m) as a function of latitude from section F to section C

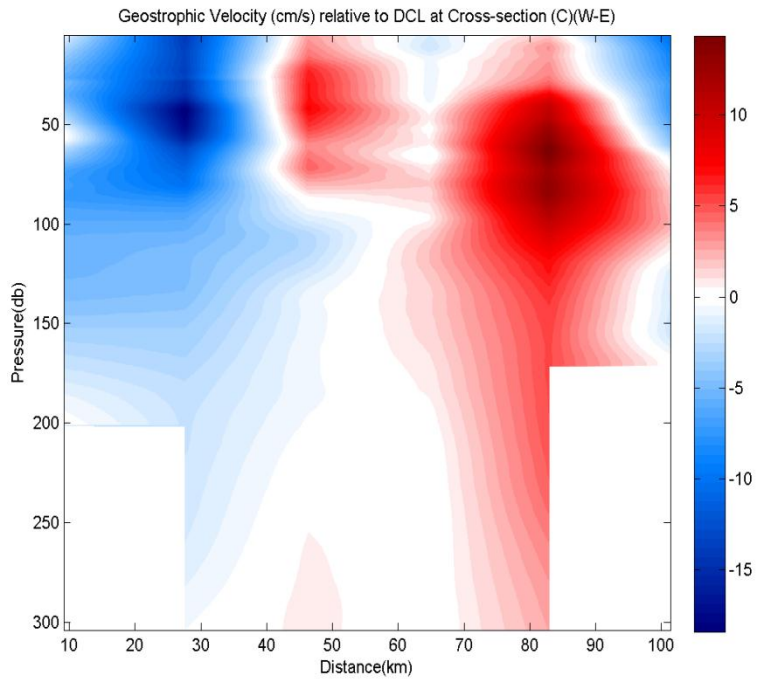


Figure A-2: Geostrophic velocity in section C. Positive (+) values indicate northwards flow and negative (-) values indicate southwards flow

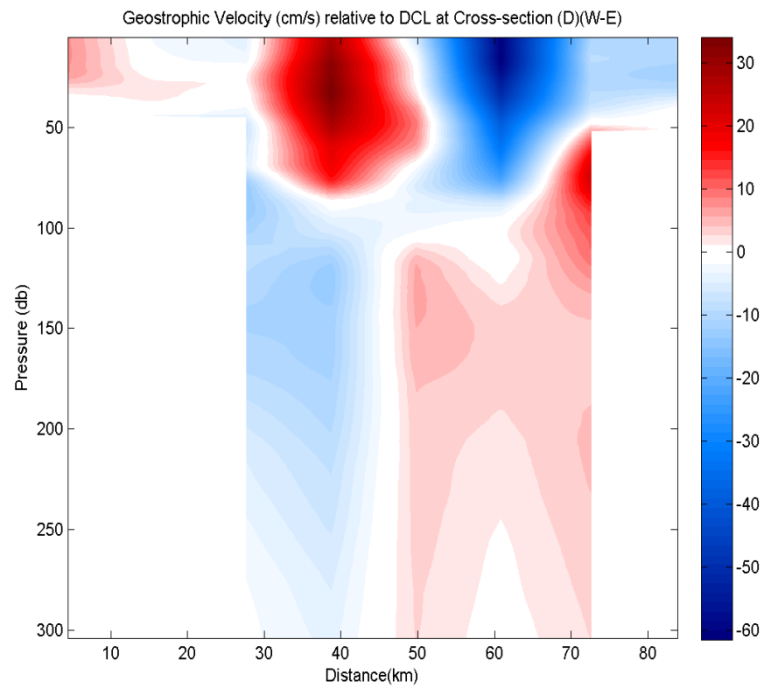


Figure A-3: Geostrophic velocity in section D. Positive (+) values indicate northwards flow and negative (-) values indicate southwards flow

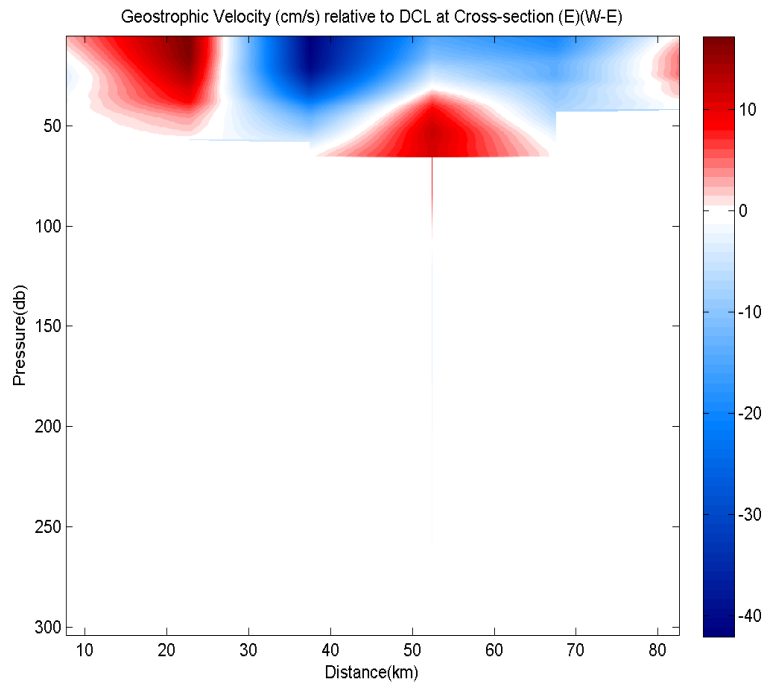


Figure A-4: Geostrophic velocity in section E. Positive (+) values indicate northwards flow and negative (-) values indicate southwards flow

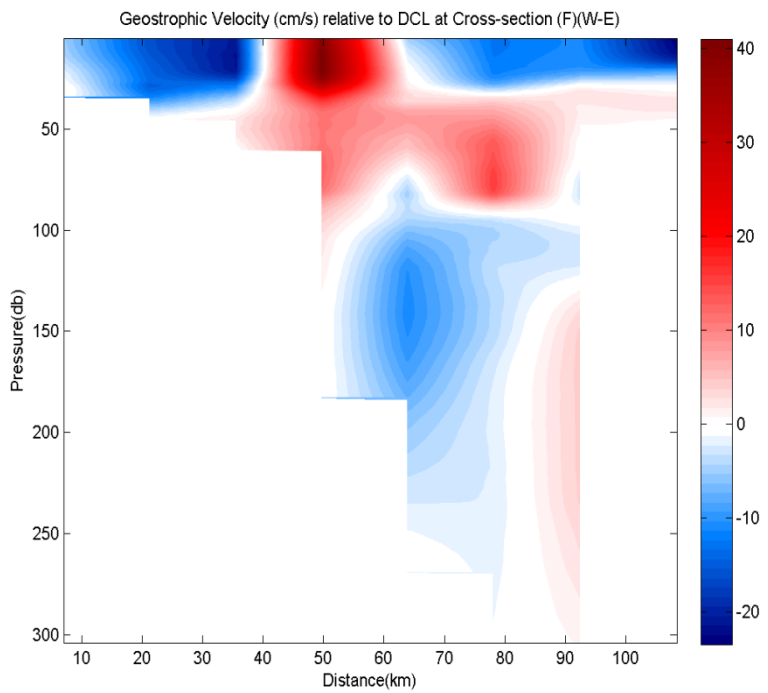


Figure A-5: Geostrophic velocity in section F. Positive (+) values indicate northwards flow and negative (-) values indicate southwards flow